61 /1/2023

JOURNAL OF THEORETICAL AND APPLIED MECHANICS

WARSAW 2023, QUARTERLY, VOLUME 61, INDEX 365238, ISSN 1429-2955

POLISH SOCIETY OF THEORETICAL AND APPLIED MECHANICS ptmts

POLISH SOCIETY OF THEORETICAL AND APPLIED MECHANICS

JOURNAL OF THEORETICAL AND APPLIED MECHANICS

No. 1 • Vol. 61

Quarterly

WARSAW, JANUARY 2023

JOURNAL OF THEORETICAL AND APPLIED MECHANICS
(until 1997 Mechanika Teoretyczna i Stosowana, ISSN 0079-3701)

Beginning with Vol. 45, No. 1, 2007, *Journal of Theoretical and Applied Mechanics* (JTAM) has been selected for coverage in Thomson Reuters products and custom information services. Now it is indexed and abstracted in the following:

- **Science Citation Index Expanded** (also known as SciSearch®)
- **Journal Citation Reports/Science Edition**

* * * * *

Editorial Office

Al. Armii Ludowej 16, room 650; 00-637 Warszawa, Poland
phone (+48) 664 099 345, e-mail: biuro@ptmts.org.pl

www.jtam.pl

* * * * *

Publication supported by Ministry of Science and Higher Education of Poland

Rozwój kwartalnika naukowego *Journal of Theoretical and Applied Mechanics*, ISSN 1429-2955, jest dofinansowany ze środków Ministra Edukacji i Nauki przyznanych z pomocy *de minimis* w ramach programu „Rozwój czasopism naukowych", umowa RCN/SN/0056/2021/1.

JOURNAL OF THEORETICAL AND APPLIED MECHANICS
61, 1, pp. 3-9, Warsaw 2023
https://doi.org/10.15632/jtam-pl/157011

BIOMECHANICAL CRITERION OF DYNAMIC STABILITY BASED ON ZMP FORMULA AND FLASH-HOGAN PRINCIPLE OF MINIMUM JERK

Grzegorz Ilewicz
Warsaw University of Technology, Faculty of Mechatronics, Warsaw, Poland
e-mail: grzegorz.ilewicz@pw.edu.pl
Jerzy Mrozowski, Jan Awrejcewicz, Bartłomiej Zagrodny, Michał Ludwicki
Lodz University of Technology, Faculty of Mechanical Engineering, Lodz, Poland

The main aim of the article is to define a criterion of dynamic stability based on the Flash-Hogan principle and the ZMP method. The gait researches were focused on analysis and observation of the human biomechanism with the optical system Optitrack. The smooth reference trajectory is defined forming a stability pattern. The optimal, due to the minimum jerk criterion, ZMP trajectory is illustrated in the results Section in order to demonstrate the dynamic stability pattern for the needs of rehabilitation in cases of neuromuscular damage or injuries affecting gait stability.

Keywords: biomechanical stability, jerk, Flash-Hogan principle, ZMP, Optitrack

1. Introduction

Stability is the ability to retrieve the state of equilibrium lost as a result of existing destabilizing factors. Loss of stability may be caused by incorrect setting of the foot, impaired control of movements in joints of the lower limb, wrong construction of lower limbs, but also the appearance of a slip phenomenon when foot touches the ground. Maintaining stability requires active involvement of biological motors (actin-myosin systems). The effect of the neuromuscular process is a human gait. An important biomechanical criterion for a human gait is dynamic stability. In biomechanical studies of the equilibrium state, cases of postural stability and locomotion of a human motor system are analyzed. Postural stability is related to a static issue. A biomechanism, by definition, is posturally stable when the projection of its mass center on the support surface is within the designated polygon. The gait, being the subject of work deliberations, is a two-legged and behavioral motor activity occurring with the interaction of human nervous and muscular systems.

Locomotion studies are conducted after adoption of various definitions of stability due to the diverse interpretation of the equilibrium state. A number of methods have also been defined to formulate the criterion of dynamic stability. The most important methods are: ZMP (zero moment point), FRI (foot rotation indicator) and CMP (centroidal moment pivot). In some work, the author assumes that dynamic stability can be determined on the basis of the ZMP method, in a combination with the minimal jerking theory formulated by Flash-Hogan (1985). According to Flash and Hogan, the optimal trajectory characterized by smoothness can be obtained by minimizing the integral criterion, which includes in itself a function of the square of the jerk, which is the third derivative of the displacement. Obtaining such a result for the ZMP trajectory makes it possible to achieve its smoothness.

The biomechanical criterion of dynamic stability in the work is formulated as: a human biomechanical system or biomechatronic human with an exoskeleton is dynamically stable while walking if the time integral has been minimized from the square of the jerk function point of

the ZMP, specified by Flash and Hogan, and the ZMP point is inside the support polygon. Acceptance of the above criterion ensures no jerks in the trajectory of the ZMP, which means lack of the jerk in the biokinematical chain during the walk. The method for solving the case when the minimum ZMP trajectory is not inside the support polygon is to use an algorithm for controlling the dynamics of the biomechanical system with an exoskeleton, which will prevent such a situation or will cause the ZMP trajectory to return inside the support polygon.

The presented work is associated with a significant number of important scientific views. Researchers at various scientific centers have appointed multi-aspect methods for determining the dynamic stability of a gait to find out the properties of the biomechanical system precipitated from the equilibrium. In 1968, Miomir Vukobratović proposed a dynamic stability criterion for bipedal robots, which was applied sixteen years later to construct a WL-10RD biped robot in order to control its dynamics (Vukobratović and Borovac, 2004). The article gives various interpretations of the ZMP method. An elementary work in determining the stability for bipedal robots using the ZMP method is in the work (Vukobratović and Juričić, 1968). The examination method of static (postural) stability, defined as GCOM criterion in reference to the ZMP method, was analyzed in the work (Mrozowski *et al.*, 2008) by using an optical system consisting of two perpendicularly arranged cameras. The graphs show the course of ZMP and GCOM trajectories. In the following work, it is proposed to increase the accuracy of measuring the trajectory of the spatial model using six digital cameras and the Optitrack system.

The use of three principles of determining the dynamic stability, i.e. ZMP (zero moment point), FRI (foot rotation indicator), CMP (centroidal moment pivot) in robotics and biomechanics of gait is described in a complex way in the work (Popovic *et al.*, 2005).

The works (Bruijn *et al.*, 2012; Gouwanda and Muraledharan, 2012) describe the dynamic stability of a gait based on analysis of the maximum of Lapunov's exponent. The normal gait and a gait with an attached knee orthosis joint were examined. Gyroscopic sensors connected to s computer using a wireless network were used to measure the trajectory. These sensors are an alternative to optical systems because during a gait test, however, it is compulsory to make numeric integration of the measurement signal.

Analytical formulas defining dynamic stability based on the correlation of the trajectory of the generalized center of gravity and the trajectory of the assumed points of the feet during normal walking were also introduced (Antipov *et al.*, 2018).

The application of the finite difference method for approximation of time derivatives of the displacement during gait is described in the work (Ilewicz and Wojnarowski, 2012). Papers (Zatziorsky, 1998; Zatziorsky and Seluyanov, 1983) present some ways of obtaining the mass parameters of the human body.

Modeling of human walking patterns has been described in work (Kazemi and Ozgoli, 2019). In this report, Pontryagin's minimum principle was applied in order to obtain a smoother trajectory.

The key studies in the area of minimum jerk are the papers (Flash and Hogan, 1995; Flash *et al.*, 2003).

Engelbrecht (2001) describes the use of mechanical minimum principles in a motor control. It describes the principle of Flash-Hogan's minimum jerk and the principle of Uno's minimal change of the moment.

The application of the minimum jerk principle and the minimum moment principle are shown in the article (Fligge *et al.*, 2015). The methods discussed were used to find a way to generate a trajectory for a biped robot.

The principle of minimum jerk was used, stating that the trajectory of minimum jerk movement on the surface of a sphere should be geodetic. A mechatronic robot for studying the interaction of a human-machine system was used in the study (Sha *et al.*, 2006).

The simultaneous use of the ZMP criterion and the minimum jerk to generate a smooth trajectory of a bipedal robot is described in (Suleiman, 2016).

Arisumi *et al.* (2008) dealt with problems of dynamic stability related to transport of objects with the use of robotic systems. In the article (Xiang and Arefeen, 2020) an optimization problem of the dynamic human system and the load being lifted is described.

The aim of this work is to achieve s criterion of dynamic stability based on the Flash--Hogan principle and the ZMP method. The accepted criterion is universal for various gait cases, however, its usefulness in the case of a gait with the assistance of a supporting exoskeleton is particularly evident. A premise for the adopted goal is to say that the optimization of human body movements is a difficult issue that can be accomplished by using a supporting exoskeleton with an optimal ZMP trajectory generator. It is also stated that the movement along a smoother ZMP trajectory reduces wear of the musculoskeletal system, thus the exoskeleton with the applied trajectory of the optimal ZMP can be used for early rehabilitation of injured patients. Scientific researches (experimental and numerical) were carried out to seek for the criterion of dynamic stability.

2. Materials and methods

The article focuses on obtaining a new method for determining dynamic stability. It was assumed that the criterion sought would be based on the ZMP method. Coordinates of the ZMP point on the surface were obtained on the basis of an experimental study using an optical system. It is then demanded from the trajectory generator that the generated trajectory of the ZMP point would be as smooth as possible. The above assumption will be fulfilled by using one of the principles of the minimum mechanics of the so-called Flash-Hogan's jerks theory (Flash and Hogan, 1985). The principle resulting from this theory is called the principle of the minimum jerk. A series of experimental tests were carried out with the usage of the Optitrack research equipment consisting of six digital optical sensors in order to register the motion. The image from optical sensors was recorded at 120 Hz. Despite the right preparation of the experimental environment, it was necessary to correct the obtained trajectories by interpolating the appearing discontinuities (their cause was a momentary lack of visibility of the marker by the optical system) in positions by using parabolic polynomials. To determine the trajectory of the ZMP point, Ha and Choi's model (Ha and Choi, 2007), consisting of the lower limbs and torso was used

$$\begin{aligned} X_{ZMP}(t) &= \frac{\sum_{i=1}^{5} m_i(\ddot{y}_i + g)x_i - \sum_{i=1}^{5} m_i \ddot{x}_i y_i}{\sum_{i=1}^{5} m_i(\ddot{y}_i + g)} \\ Z_{ZMP}(t) &= \frac{\sum_{i=1}^{5} m_i(\ddot{y}_i + g)z_i - \sum_{i=1}^{5} m_i \ddot{z}_i y_i}{\sum_{i=1}^{5} m_i(\ddot{y}_i + g)} \end{aligned} \tag{2.1}$$

where: m_i is mass of the link i, x, y, z are coordinates of the center of the mass of the link i.

A criterion of dynamic stability was proposed, based on finding the minimum of the function of the square of jerk for the trajectory of the ZMP. Such an assumption gives an opportunity to state that the optimal trajectory can be found, therefore, there is no unexpected displacement of the ZMP point on the walking surface. This corresponds to minimal jerks of the human biokinematical chain and minimization of the usage of the musculoskeletal system. The jerk is referred to as the third displacement derivative. It informs how fast the force will change over time according to the equation

$$\frac{\partial F(\dot{x}, x, t)}{\partial t} = \frac{\ddot{x} F}{\partial \dot{x}} + \frac{\dot{x} \partial F}{\partial x} + \frac{\partial F}{\partial t} = mj \tag{2.2}$$

where x is displacement, $\dot{x}$ – velocity, $\ddot{x}$ – acceleration, $\dddot{x} = j$ – jerk, m – mass.

To determine the trajectory of the minimum ZMP jerk, one of the minimum mechanical principles developed by Flash and Hogan (1985) is used. It postulates that the integral

$$\int_0^t \dddot{x}^2 \, dt \to \min \tag{2.3}$$

where $\dddot{x}$ is jerk of ZMP point, reaches the minimum value. Then, the optimal trajectory of the ZMP point is achieved. Most researchers, dealing with motor control, believe that this principle reflects biological utility of the biomechanism. After solving Euler-Lagrange's equation, the smooth trajectory equation of the ZMP point is obtained

$$x(t)_{ZMP} = c_5 t^5 + c_4 t^4 + c_3 t^3 + c_2 t^2 + c_1 t + t_0 \tag{2.4}$$

where c_i are polynomial coefficients.

Polynomial coefficients (2.4) are gained from the equation

$$\begin{bmatrix} 0 & 0 & 0 & 0 & 0 & 1 \\ t^5 & t^4 & t^3 & t^2 & t & 1 \\ 0 & 0 & 0 & 0 & 1 & 0 \\ t^4 & t^3 & t^2 & t & 1 & 0 \\ 0 & 0 & 0 & 1 & 0 & 0 \\ t^3 & t^2 & t & 1 & 0 & 0 \end{bmatrix} \begin{bmatrix} c_5 \\ c_4 \\ c_3 \\ c_2 \\ c_1 \\ c_0 \end{bmatrix} = \begin{bmatrix} a \\ b \\ 0 \\ 0 \\ 0 \\ 0 \end{bmatrix} \tag{2.5}$$

where a, b are boundary conditions.

Todorov-Jordan's algorithm is a numerical modification of the theory given by Flash-Hogan and describes the problem of optimal control assuming various cost functions such as maximizing smoothness by minimizing jerks. Todorov and Jordan used a numerical approach to obtain velocity profiles in perfect harmony with the experiment. Their numerical algorithm is based on minimizing the jerk along the trajectory. The algorithm assumes that the trajectory of the ZMP point is given, and only space of velocity profiles is minimized. The Flash-Hogan algorithm requires both trajectory and velocity to be calculated. Details of Todorov-Jordan's algorithm are given in (Todorov and Jordan, 1998).

3. Results

Based on Todorov-Jordan's algorithm, the important trajectories were obtained in the Matlab environment. The trajectories of the ZMP point during normal gait of various qualities obtained by the optical system are illustrated in Figs. 1 to 3. The trajectories of the minimum jerk shown with the red line are the trajectories that give the result of minimal jerks of the biokinematical chain during the gait. During the gait with an exoskeleton, some jerks may appear during realization of the rehabilitation algorithm (braking, acceleration), whose influence on the ZMP trajectory can be leveled based on the Flash-Hogan principle and the used algorithm. This gives a positive effect of the smooth and rhythmic movement of the patient in the exoskeleton.

The used algorithm also gives the possibility of global smoothing of the ZMP trajectory for various smoothing filter coefficients while minimizing the jerk phenomenon (Todorov and Jordan, 1998; Meirovitch *et al.*, 2016). Figures 1 to 3 illustrate the smoothing for a variety of smoothing coefficients λ. For $\lambda = 1$, the trajectory is a straight line and it strongly deviates from the trajectory of the minimum jerk. By increasing the value of the smoothing factor, it increases the accuracy of matching the optimal trajectory to the ZMP trajectory points. Figure 2 illustrates the ZMP trajectory for the coefficient λ equal to 12. There is an improvement in the smoothness of the ZMP trajectory.

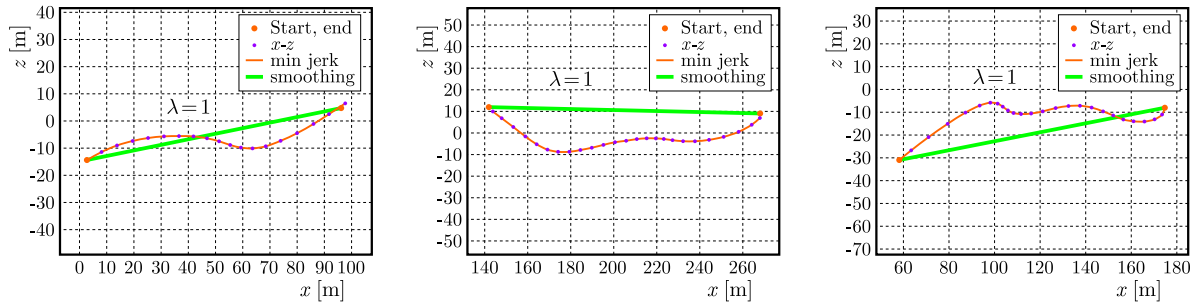

Fig. 1. Optimal ZMP trajectory for the coefficient $\lambda = 1$

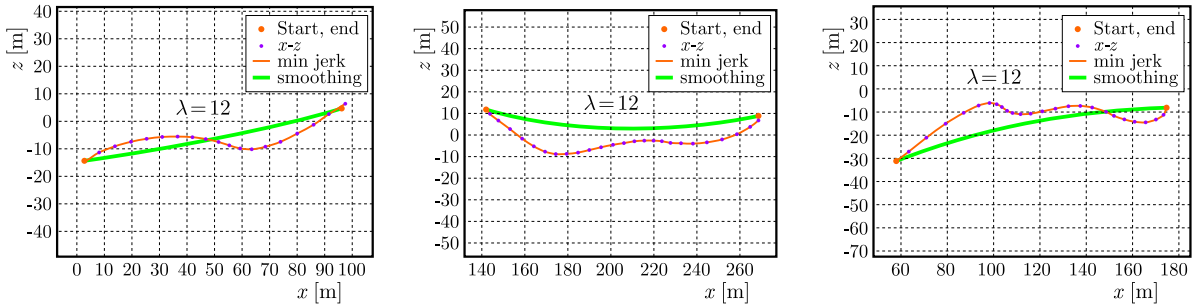

Fig. 2. Optimal ZMP trajectory for the coefficient $\lambda = 12$

For the value of the lambda smoothing filter equal to 36 (Fig. 3), a simultaneous effect of minimizing the emerging or might occurring jerk and matching the smoothed trajectory to the trajectory of the ZMP is obtained, whereas the trajectory becomes smooth.

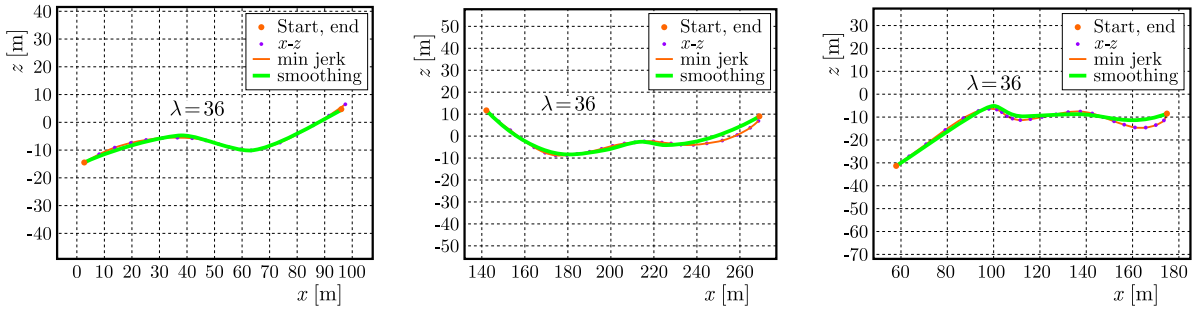

Fig. 3. Optimal ZMP trajectory for the coefficient $\lambda = 36$

The errand of the optimal ZMP trajectory to the exoskeleton control system will allow one to obtain better dynamic characteristics of the biokinematical chain during the gait. This will also result in increasing the coordination of the structure of human movements. From the point of biomechanics, it is stated that the movement on the optimal trajectory will minimize the usage of the musculoskeletal system. Undoubtedly also, for this reason, it can be applied to the exoskeleton control system for the early rehabilitation of injured patients.

4. Discussion

The obtained model determining the dynamic stability criterion can be added to the structure of the exoskeleton control system and enable smooth, rhythmic and coordinated gait by a smooth regulation of servomotors that drive individual degrees of freedom. Obtaining such an effect will give favorable effects of rehabilitation enabling the rehabilitated patient's gait to be adjusted with

the help of an exoskeleton to the predetermined ZMP patterns, which can be described as optimal or, from a medical point of view, to be correct. The conducted research works made it possible to determine the innovative criterion of dynamic stability on the basis of Flash-Hogan's jerk principle. The adopted dynamic stability criterion specifies that human biomechanism during gait is dynamically stable in the case when the integral function, containing the square of the ZMP point jerk, is minimized and the ZMP point is within the designated support polygon. The trajectory of the ZMP point, after obtaining the minimum of integral criterion (2.3), becomes smooth and no jerks are observed in it. The obtained method of determining the dynamic stability gives the possibility to apply it to the exoskeleton control program, therefore, it is a significant innovation in relation to the exoskeleton control models created in research and development centers around the world. The obtained effect also gives the possibility of using it in the process of rehabilitation of patients, due to the fact that after applying the algorithm to the exoskeleton control system, the rehabilitated patient's movement can be forced in trajectories of various smoothness and thus, achieve the desired therapeutic effects. Not without significance is also the fact that the movement along the optimal trajectory will minimize wear of the musculoskeletal system, so that the exoskeleton could be used for early rehabilitation of the patient after the operation or injury.

5. Conclusions

The work proposes an innovative formulation of the criterion of dynamic stability. The outcome of applying Flash-Hogan's minimum principle is an optimal trajectory of the ZMP point, for the integral squared jerk criterion. ZMP trajectories that deviate from the trajectory of the minimum jerk and those which are not inside the support polygon are not being considered to be optimal dynamic, so that the criterion of dynamic stability defined in this work is not met for them. Optimality of the ZMP trajectory reflects the lack of jerks in the biokinematic chain during a human walk. Conducting rehabilitation activities can be used to move toward the trajectory of the ZMP of a patient with a damaged nervous system or trauma of the musculoskeletal system to the given optimal trajectory. Rehabilitation research, which may be conducted in the future using this criterion, rely on determining the optimal ZMP trajectory and the patterns that allow gradual approach to its quality. It is evident that this type of rehabilitation can be carried out with the help of an exoskeleton that emables sooner return to normal dynamic stability during the gait. The function of this interactive medical robot with a rehabilitated patient, after losing the ability to remain stable, will also take place with the lack of jerks resulting from actions of the mechatronic system of the exoskeleton during contact with the ground.

References

1. Antipov V., Postolny A., Yatsun A., Jatsun S., 2018, The control algorithm of the lower limb exoskeleton synchronous gait, *MATEC Web of Conferences*, **161**

2. Arisumi H., Miossec S., Chardonnet J., Yokoi K., 2008. Dynamic lifting by whole body motion of humanoid robots, *2008 IEEE/RSJ International Conference on Intelligent Robots and Systems, IEEE*, 668-675

3. Bruijn S., Bregman D., Meijer O., Beek P., Dieën J., 2012, Maximum Lyapunov exponents as predictors of global gait stability: A modeling approach, *Medical Engineering and Physics*, **34**, 4, 428-436

4. Engelbrecht S., 2001, Minimum principles in motor control, *Journal of Mathematical Physiology*, **45**, 497-542

5. Flash T., Hogan N., 1985, The coordination of arm movements: An experimentally confirmed mathematical model, *The Journal of Neuroscience*, **5**, 7, 1688-1703
6. Flash T., Hogan N., Richardson N., 2003, Optimization principles in motion control, [In:] *The Handbook of Brain Theory and Neural Network*, 2d ed., MIT Press, Cambridge, 827-831
7. Fligge N., McIntyre J., van der Smagt, 2012, Minimum jerk for human catching movements in 3D, *The Fourth IEEE RAS/EMBS. International Conference on Biomedical Robotics and Biomechatronics*
8. Gouwanda D., Muraledharan S., 2012, Local gait dynamic stability of individuals with knee brace and ankle brace, *IEEE EMBS International Conference on Biomedical Engineering and Sciences*
9. Ha T., Choi C., 2007, An effective trajectory generation method for bipedal walking, *Robotics and Autonomous Systems*, **55**, 10, 795-810
10. Ilewicz G., Wojnarowski J., 2012, Anthropometrical model of human gait, *International Journal of Applied Mechanics and Engineering*, **17**, 4, 1139-1148
11. Kazemi J., Ozgoli S., 2019, Real-time gait planner for human walking using a lower limb exoskeleton and its implementation on exoped robot, *Robotics and Autonomous Systems*, **116**, 1-23
12. Meirovitch Y., Bennequin D., Flash T., 2016, Geometrical invariance and smoothness maximization for task-space movement generation, *IEEE Transactions on Robotics*, 32, 4, 837-853
13. Mrozowski J., Awrejcewicz J., Bamberski P., 2008, Analysis of stability of the human gait, *Journal of Theoretical and Applied Mechanics*, **45**, 1, 91-98
14. Popovic M., Goswami A., Herr H., 2005, Ground reference points in legged locomotion: definitions. biological trajectories and control implications, *The International Journal of Robotics Research*, **24**, 12, 1013-1032
15. Sha D., Patton J., Mussa-Ivaldi, 2006, Minimum jerk reaching movements of human arm with mechanical constraints at endpoint, *International Journal of Computers, Systems and Signals*, **7**, 1
16. Suleiman W. 2016, Inverse kinematics: new method for minimum jerk trajectory generation whole-body control for robots in the real world, *IROS14 Workshop*, Chicago
17. Todorov E., Jordan M., 1998, Smoothness maximization along a predefined path accurately predicts the speed profiles of complex arm movement, *Journal of Neurophysiology*, **80**, 696-714
18. Vukobratović M., Borovac B., 2004, Zero-moment point thirty five years of its life, *International Journal of Humanoid Robotics*, **1**, 1, 157-173
19. Vukobratović M., Juričić D., 1968, Contribution to the synthesis of biped gait, *Proceedings of IFAC Symposium. Technical and Biological Problem on Control*, Erevan, USSR
20. Xiang Y., Arefeen A., 2020, Two-dimensional team lifting prediction with floating-base box dynamics and grasping force coupling, *Multibody System Dynamics*, **50**, 2, 211-231
21. Zatziorsky V., 1998, *Kinematics of Human Motion*, Human Kinetics, Champaign. IL, USA
22. Zatziorsky V., Seluyanov V., 1983, The mass and inertia characteristics of the mass segments of the human body, *Biomechanics. Human Kinetics*, **8b**, 4b, 1152-115

Manuscript received April 20, 2022; accepted for print September 30, 2022

JOURNAL OF THEORETICAL AND APPLIED MECHANICS
61, 1, pp. 11-22, Warsaw 2023
https://doi.org/10.15632/jtam-pl/157084

ANALYTICAL SOLUTION FOR ONE-DIMENSIONAL CONSOLIDATION OF UNSATURATED SOILS UNDER DYNAMIC LOAD

Zhi-Yi Liu
Lanzhou University of Technology, School of Civil Engineering, Lanzhou, China, and
Hexi University of Technology, School of Civil Engineering, Zhangye, China
e-mail: liuzhiyibeijing@163.com

Yu Song
Lanzhou University of Technology, School of Civil Engineering, Lanzhou, China
e-mail: 591546531@qq.com

Feng-Xi Zhou
Lanzhou University of Technology, School of Civil Engineering, Lanzhou, China, and
Engineering Research Center of Disaster Mitigation in Civil Engineering of Ministry of education, Lanzhou, China
Corresponding author, e-mail: geolut@163.com

Li-Ye Wang
Lanzhou University of Technology, School of Civil Engineering, Lanzhou, China
e-mail: gwly1024@163.com

Firstly, in this paper, based on the theory of the porous elastic medium and combined with the effective stress principle of unsaturated soil, a set of governing equations is established to describe consolidation of the unsaturated soil. Secondly, an analytical expression under any dynamic loads is obtained with the help of Laplace integral transformation. Finally, analysis of numerical examples under specific boundary conditions is made to discuss one--dimensional consolidation characteristics under harmonic loads and the influence of factors on the consolidation characteristics of unsaturated soil, such as excitation frequency and initial saturation.

Keywords: unsaturated soil, consolidation characteristics, dynamic load, analytical solution, numerical calculation

1. Introduction

Under an external load, the pore fluid is slowly discharged out of soil, and the process of gradual compression of soil is called soil consolidation. Consolidation characteristics of soil under complex conditions are of great significance to the actual construction process and operation stage of a project. For example, due to the effect of vehicle vibration load, long-term consolidation and deformation of the roadbed has a decisive impact on safety, durability, later operation and maintenance of the project in highway or railway engineering. Therefore, the ability to describe accurately the consolidation and deformation characteristics of soil is of great significance to present engineering.

At present, scholars have done a series of research on the problem of static and dynamic consolidation of the saturated soil foundation from different aspects (Pan *et al.*, 2006; Xie *et al.*, 2008, 2014; Toufigh and Ouria, 2009; Wang *et al.*, 2017a,b; Shi *et al.*, 2018). Compared with saturated soil, unsaturated soil not only contains the solid phase and liquid phase, but also contains a certain amount of the gas phase. It is widely present in arid, semi-arid areas and soil above the groundwater level. The research on consolidation of unsaturated soil began in the

1960s, when Fredlund and Rahardjo (1993) considered the continuity of pore water and pore gas, and established a relatively complete consolidation equation of unsaturated soil based on three-phase coupling characteristics. When discussing the problem of one-dimensional consolidation, the pore water dissipation equation is similar to the Terzaghi consolidation theory, but in the derivation process many assumptions that are inconsistent with the actual situation are introduced, such as constant total stress and so on. Since then, the analysis of the consolidation of unsaturated soil had achieved a series of results whether in terms of theoretical analysis (Sheng *et al.*, 2019; Qin *et al.*, 2010; Su and Xie, 2010; Ho *et al.*, 2014; Lo *et al.*, 2016; Wang *et al.*, 2017, 2018) or numerical simulation (Chen *et al.*, 1999; Yin and Ling, 2007; Huang *et al.*, 2009; Pedroso and Farias, 2011). However, in the research on the consolidation theory of unsaturated soil, most of the load forms imposed on the soil are dead loads or cyclic loads. In contrast, analytical solutions under the action of other dynamic loads are rarely reported in the literature. Based on the elastic theory of unsaturated porous media, this paper considers a function of three-phase coupling in unsaturated soil and establishes the consolidation equation under any dynamic loads. The Laplace integral transformation is used to finally obtain an explicit analytical solution for the problem of one-dimensional consolidation. Numerical examples under specific boundary conditions are used to discuss the law of influence of consolidation characteristics of the soil, frequency and saturation under harmonic loads.

2. Governing equation

Without considering the body force, the momentum balance equation of unsaturated porous media can be expressed as (Lo *et al.*, 2002)

$$R_{11}\Big(\frac{\partial \mathbf{u}_a}{\partial t}-\frac{\partial \mathbf{u}_s}{\partial t}\Big)=\theta_a\nabla P_a \qquad R_{22}\Big(\frac{\partial \mathbf{u}_w}{\partial t}-\frac{\partial \mathbf{u}_s}{\partial t}\Big)=\theta_w\nabla P_w \qquad \nabla\cdot\boldsymbol{\sigma}=\rho\ddot{\mathbf{u}}_s \tag{2.1}$$

where $\mathbf{u}_a$, $\mathbf{u}_w$ and $\mathbf{u}_s$ represent the displacement vectors of gas, water and solid soil skeletons, respectively; θ_a and θ_w represent the volume fractions of gas and water, respectively, and there are $\theta_a=S_a\varphi$, $\theta_w=S_w\varphi$, where S_a and S_w are the saturation of gas and water, respectively, φ is porosity of the soil; P_a and P_w are pore gas pressure and pore water pressure, respectively; $R_{11}=-[\theta_a^2\eta_1/k_s]k_{ra}$ is the viscous coupling coefficient of the solid phase and gas; $R_{22}=-[\theta_w^2\eta_2/k_s]k_{rw}$ is the viscous coupling coefficient of the solid phase and water, where η_1 and η_2 are viscosity coefficients of gas and water, respectively; k_s is the inherent permeability of porous media, k_{ra} and k_{rw} describe the relative permeability of gas and water, respectively; $\boldsymbol{\sigma}$ is the total stress tensor.

Unsaturated soil theory based on the suction stress between solid particles and the effective stress can be expressed as

$$\boldsymbol{\sigma}=\boldsymbol{\sigma}'-(P_a+\sigma^s)\boldsymbol{\delta} \tag{2.2}$$

where $\boldsymbol{\sigma}'$ is the effective stress tensor; σ^s – suction stress between solid particles, which is a function related to the matrix suction and other factors, $\boldsymbol{\delta}$ – unit tensor. Regarding the expression of inter-particle attraction, domestic and foreign scholars have given different forms (Lu *et al.*, 2010; Chen *et al.*, 1993; Jiang *et al.*, 2004). According to current needs, this paper adopts the suction stress function with an explicit expression (Lu *et al.*, 2010), namely

$$\sigma^s=\begin{cases} P_a-P_w & \text{for} \quad P_a-P_w\leqslant 0 \\ -S_e(P_a-P_w) & \text{for} \quad P_a-P_w\geqslant 0 \end{cases} \tag{2.3}$$

where $S_e=(S_w-S_r)/(S_s-S_r)$ is the effective saturation, S_s – complete saturation, and S_r – residual saturation.

Combining the deformation of the solid framework and the pore fluid, the stress-strain relationship can be obtained (Lo *et al.*, 2014)

$$\boldsymbol{\sigma} = 2G\mathbf{e} + \Big[\Big(a_{11} - \frac{2}{3}G\Big)e + a_{12}\varepsilon_a + a_{13}\varepsilon_w\Big]\boldsymbol{\delta} \tag{2.4}$$

and

$$-\theta_a P_a = a_{12}e + a_{22}\varepsilon_a + a_{23}\varepsilon_w \qquad -\theta_w P_w = a_{13}e + a_{23}\varepsilon_a + a_{33}\varepsilon_w \tag{2.5}$$

where $\mathbf{e} = (\nabla\mathbf{u}_s + \nabla\mathbf{u}_s^{\mathrm{T}})/2$ is the strain tensor of the framework; $e = \nabla\mathbf{u}_s$ is the volumetric strain of the solid-phase framework; $\varepsilon_a = \nabla\mathbf{u}_a$ and $\varepsilon_w = \nabla\mathbf{u}_w$ are volumetric strains of gas and water, respectively; G is the shear modulus of the porous medium; $\boldsymbol{\sigma}$ is the unit tensor; a_{ij} $(i, j = 1, 2, 3)$ are coefficients of elasticity.

Combining Eqs. (2.2), (2.3) and (2.4), we can get

$$\boldsymbol{\sigma} = 2G\mathbf{e} + \Big[\Big(a_{11} - \frac{2}{3}G + A_1a_{12} + A_2a_{13}\Big)e + (a_{12} + A_1a_{22} + A_2a_{23})\varepsilon_a + (a_{13} + A_1a_{23} + A_2a_{33})\varepsilon_w\Big]\boldsymbol{\delta} \tag{2.6}$$

where $A_1 = (1 - S_e)/\theta_a$ and $A_2 = S_e/\theta_w$.

Through simultaneous Eqs. (2.5), the solution can be

$$\varepsilon_a = d_1e + d_2P_a + d_3P_w \qquad \varepsilon_w = d_4e + d_5P_a + d_6P_w \tag{2.7}$$

where

$$d_1 = \frac{a_{12}a_{23} - a_{13}a_{23}}{a_{23}^2 - a_{22}a_{33}} \qquad d_2 = \frac{\theta_a a_{33}}{a_{23}^2 - a_{22}a_{33}} \qquad d_3 = \frac{-\theta_w a_{23}}{a_{23}^2 - a_{22}a_{33}}$$
$$d_4 = \frac{a_{12}a_{22} - a_{12}a_{23}}{a_{23}^2 - a_{22}a_{33}} \qquad d_5 = \frac{-\theta_a a_{23}}{a_{23}^2 - a_{22}a_{33}} \qquad d_6 = \frac{\theta_w a_{22}}{a_{23}^2 - a_{22}a_{33}}$$

Take divergence on both the left and right-hand sides of Eqs. (2.1), and substitute Eqs. (2.7) into it, then the coupled diffusion equation can be obtained

$$\begin{aligned} d_2\frac{\partial P_a}{\partial t} + d_3\frac{\partial P_w}{\partial t} + (d_1 - 1)\frac{\partial e}{\partial t} &= \frac{\theta_a}{R_{11}}\nabla^2 P_a \\ d_5\frac{\partial P_a}{\partial t} + d_6\frac{\partial P_w}{\partial t} + (d_4 - 1)\frac{\partial e}{\partial t} &= \frac{\theta_w}{R_{22}}\nabla^2 P_w \end{aligned} \tag{2.8}$$

Substitute Eqs. (2.7) into Eq. (2.6) to eliminate ε_a and ε_w, the total stress expression can be obtained as

$$\boldsymbol{\sigma} = 2\mathbf{G}e + (H_1e + H_2P_a + H_3P_w)\boldsymbol{\delta} \tag{2.9}$$

the coefficients in Eq. (2.9) are

$$\begin{aligned} H_1 &= a_{11} - \frac{2}{3}G + A_1a_{12} + A_2a_{13} + (a_{12} + A_1a_{22} + A_2a_{23})d_1 + (a_{13} + A_1a_{23} + A_2a_{33})d_4 \\ H_2 &= (a_{12} + A_1a_{22} + A_2a_{23})d_2 + (a_{13} + A_1a_{23} + A_2a_{33})d_5 \\ H_3 &= (a_{12} + A_1a_{22} + A_2a_{23})d_3 + (a_{13} + A_1a_{23} + A_2a_{33})d_6 \end{aligned}$$

Finally, by combining Eqs. $(2.1)_3$ and (2.9), a balance equation expressed by skeleton displacement, pore pressure and pore water pressure can be obtained

$$G\nabla^2\mathbf{u}_s + (H_1 + G)\nabla e + H_2\nabla P_a + H_3\nabla P_w = \rho\ddot{\mathbf{u}}_s \tag{2.10}$$

Based on the above derivation process, it is found that Eqs. (2.8) and (2.10) are three phase-coupling partial differential equations, which can be used to describe the consolidation of unsaturated soil.

3. Analytical solution of the one-dimensional dynamic consolidation problem

Consider the unsaturated soil layer as shown in Fig. 1, where thickness of the soil layer is h, and there is a dynamic load $f(t)$ acting on the surface, $e_{xx} = e_{yy} = 0$, $e = e_{zz} = \partial w/\partial z$.

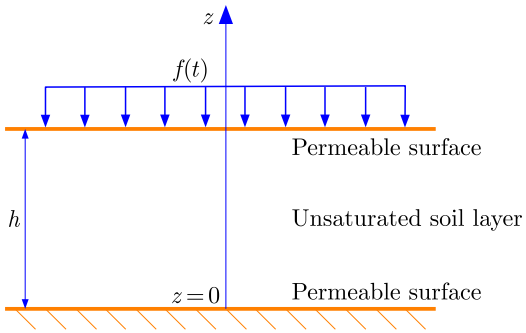

Fig. 1. Calculation model of unsaturated soil under the dynamic load $f(t)$

So control Eqs. (2.8) and (2.10) can be written as

$$\begin{aligned} q_1\frac{\partial P_a}{\partial t} + q_2\frac{\partial P_w}{\partial t} &= b_1\frac{\partial^2 P_a}{\partial z^2} + \gamma_1\frac{\partial f(t)}{\partial t} \\ q_3\frac{\partial P_a}{\partial t} + q_4\frac{\partial P_w}{\partial t} &= b_2\frac{\partial^2 P_w}{\partial z^2} + \gamma_2\frac{\partial f(t)}{\partial t} \end{aligned} \tag{3.1}$$

and

$$\frac{\partial w}{\partial z} = -\frac{f(t)}{2G+H_1} - \frac{H_2}{2G+H_1}P_a - \frac{H_3}{2G+H_1}P_w \tag{3.2}$$

where b_2/q_4 represents the diffusion coefficient of pore water pressure, called the consolidation coefficient, and is often expressed by the symbol c_v. The coefficients q_1, q_2, q_3, q_4, b_1, b_2, γ_1, γ_2 are respectively

$$q_1 = d_2 - \frac{H_2(d_1-1)}{2G+H_1} \qquad q_2 = d_3 - \frac{H_3(d_1-1)}{2G+H_1} \qquad q_3 = d_5 - \frac{H_2(d_4-1)}{2G+H_1}$$

$$q_4 = d_6 - \frac{H_3(d_4-1)}{2G+H_1} \qquad b_1 = \frac{\theta_a}{R_{11}} \qquad b_2 = \frac{\theta_w}{R_{22}}$$

$$\gamma_1 = \frac{d_1-1}{2G+H_1} \qquad \gamma_2 = \frac{d_4-1}{2G+H_1}$$

Since the exhaust and drainage cannot be completed at the moment of applying the dynamic load $f(t)$, it is considered that the content of water and gas remains the same. From Eqs. (3.1), we get

$$\int_0^{0^+} b_1\frac{\partial^2 P_a}{\partial z^2}\,dt = \int_0^{0^+} b_2\frac{\partial^2 P_w}{\partial z^2}\,dt = 0 \tag{3.3}$$

The formula: integral limit 0 and 0^+, respectively, represents the time before and after the load is applied.

From Eq. (3.2), we get

$$\frac{\partial w(z,0^+)}{\partial z} = -\frac{f(t)_{0^+}}{2G+H_1} - \frac{H_2}{2G+H_1}P_a - \frac{H_3}{2G+H_1}P_w \tag{3.4}$$

Combining Eqs. (3.3) and (2.8), we find

$$\begin{aligned}(d_1-1)\frac{\partial w(z,0^+)}{\partial z}+d_2P_a(z,0^+)+d_3P_w(z,0^+)=0\\(d_4-1)\frac{\partial w(z,0^+)}{\partial z}+d_5P_a(z,0^+)+d_6P_w(z,0^+)=0\end{aligned}\tag{3.5}$$

Substituting Eq. (3.4) into Eqs. (3.5), respectively, the initial conditions of the problem can be obtained as

$$P_a(z,0^+)=r_1f(t)_{0^+}\qquad P_w(z,0^+)=r_2f(t)_{0^+}\tag{3.6}$$

where

$$r_1=\frac{(1-d_4)q_2-(1-d_1)q_4}{(2G+H_1)(q_1q_4-q_2q_3)}\qquad r_2=\frac{(1-d_1)q_3-(1-d_4)q_1}{(2G+H_1)(q_1q_4-q_2q_3)}$$

Assume that the soil layer can both drain and exhaust on both sides at $z=0$ and $z=h$, and the boundary conditions are

$$P_a(0,t)=P_w(0,t)=0\qquad P_a(h,t)=P_w(h,t)=0\tag{3.7}$$

Without loss of generality, it is assumed that the pore gas pressure $P_a(z,t)$, pore water pressure $P_w(z,t)$ and the Fourier series form $\partial f(t)/\partial t$ are

$$P_a(z,t)=\sum_{n=0}^{\infty}P_{an}(t)\sin(\lambda_nz)\qquad P_w(z,t)=\sum_{n=0}^{\infty}P_{wn}(t)\sin(\lambda_nz)\tag{3.8}$$

and

$$\frac{\partial f(t)}{\partial t}=\sum_{m=0}^{\infty}B_m(t)\sin(\lambda_mz)\tag{3.9}$$

where $\lambda_m=m\pi/h$, P_{an}, P_{wn} and B_m are functions related to time t.

Combining Eqs. (3.8) and (3.1), we get

$$\begin{aligned}\sum_{n=0}^{\infty}[q_1P'_{an}(t)+q_2P'_{wn}(t)+b_1\lambda_n^2P_{an}(t)]\sin(\lambda_nz)=\gamma_1\sum_{m=0}^{\infty}B_{am}(t)\sin(\lambda_mz)\\\sum_{n=0}^{\infty}[q_3P'_{an}(t)+q_3P'_{wn}(t)+b_2\lambda_n^2P_{wn}(t)]\sin(\lambda_nz)=\gamma_2\sum_{m=0}^{\infty}B_{wm}(t)\sin(\lambda_mz)\end{aligned}\tag{3.10}$$

Using the orthogonality of trigonometric functions and Eq. (3.1), we can see that the number of terms in m and n are equal, so that we obtain

$$\begin{aligned}q_1P'_{an}(t)+q_2P'_{wn}(t)+b_1\lambda_n^2P_{an}(t)=\gamma_1B_{an}(t)\\q_3P'_{an}(t)+q_4P'_{wn}(t)+b_2\lambda_n^2P_{wn}(t)=\gamma_2B_{wn}(t)\end{aligned}\tag{3.11}$$

Considering the initial conditions in Eqs. (3.6), integrating Eqs. (3.8) one arrives at

$$\begin{aligned}P_{an}(0)=\frac{2}{h\lambda_n}r_1f(t)_{0^+}[1-\cos(n\pi)]\\P_{wn}(0)=\frac{2}{h\lambda_n}r_2f(t)_{0^+}[1-\cos(n\pi)]\end{aligned}\tag{3.12}$$

Using Laplace integral transformation, Eqs. (3.11) can be written as follows

$$\begin{bmatrix} P_{an}(s) \\ P_{wn}(s) \end{bmatrix} = \frac{1}{X}\left(\begin{bmatrix} sq_4 + b_2\lambda_n^2 & -sq_2 \\ -sq_3 & sq_1 + b_1\lambda_n^2 \end{bmatrix} \begin{bmatrix} q_1 & q_2 \\ q_3 & q_4 \end{bmatrix} \begin{bmatrix} P_{an}(0) \\ P_{wn}(0) \end{bmatrix} + \begin{bmatrix} sq_4 + b_2\lambda_n^2 & -sq_2 \\ -sq_3 & sq_1 + b_1\lambda_n^2 \end{bmatrix} \begin{bmatrix} \gamma_1 B_{an}(s) \\ \gamma_2 B_{wn}(s) \end{bmatrix} \right) \tag{3.13}$$

where $X = \Delta s^2 + \lambda_n^2(b_1q_4 + b_2q_1)s + b_1b_2\lambda_n^4$ and $\Delta = q_1q_4 - q_2q_3$.

Solving Eq. (3.13), we get

$$\begin{aligned} P_{an}(s) &= \frac{s}{s^2+\beta_n^2}P_{an}(0) + \frac{b_2\lambda_n^2 q_1}{\beta_n\Delta}\frac{\beta_n}{s^2+\beta_n^2}P_{an}(0) + \frac{b_2q_2\lambda_n^2}{\Delta\beta_n}\frac{\beta_n}{s^2+\beta_n^2}P_{wn}(0) \\ &\quad + \frac{q_4\gamma_1}{\Delta}\frac{s}{s^2+\beta_n^2}B_{an}(s) + \frac{b_2\lambda_n^2\gamma_1}{\beta_n\Delta}\frac{\beta_n}{s^2+\beta_n^2}B_{an}(s) - \frac{q_2\gamma_2}{\Delta}\frac{s}{s^2+\beta_n^2}B_{wn}(s) \\ P_{wn}(s) &= \frac{b_1q_3\lambda_n^2}{\Delta\beta_n}\frac{\beta_n}{s^2+\beta_n^2}P_{an}(0) + \frac{s}{s^2+\beta_n^2}P_{wn}(0) + \frac{b_1\lambda_n^2 q_4}{\beta_n\Delta}\frac{\beta_n}{s^2+\beta_n^2}P_{wn}(0) \\ &\quad - \frac{\gamma_1 q_3}{\Delta}\frac{s}{s^2+\beta_n^2}B_{an}(s) + \frac{q_1\gamma_2}{\Delta}\frac{s}{s^2+\beta_n^2}B_{wn}(s) + \frac{\gamma_2 b_1\lambda_n^2}{\Delta\beta_n}\frac{\beta_n}{s^2+\beta_n^2}B_{wn}(s) \end{aligned} \tag{3.14}$$

where $\beta_n^2 = (1/\Delta)\lambda_n^2(b_1q_4 + b_2q_1)s + (1/\Delta)b_1b_2\lambda_n^4$.

Using Laplace inverse transformation, Eqs. (3.14) can be expressed in the time domain

$$\begin{aligned} P_{an}(t) &= P_{an}(0)\cos(\beta_n t) + \frac{b_2q_1\lambda_n^2}{\beta_n\Delta}P_{an}(0)\sin(\beta_n t) + \frac{b_2q_2\lambda_n^2}{\Delta\beta_n}P_{wn}(0)\sin(\beta_n t) \\ &\quad + \frac{q_4\gamma_1}{\Delta}\cos(\beta_n t)B_{an}(t) + \frac{b_2\gamma_1\lambda_n^2}{\beta_n\Delta}\sin(\beta_n t)B_{an}(t) - \frac{q_2\gamma_2}{\Delta}\cos(\beta_n t)B_{wn}(t) \\ P_{wn}(t) &= \frac{b_1q_3\lambda_n^2}{\Delta\beta_n}P_{an}(0)\sin(\beta_n t) + P_{wn}(0)\cos(\beta_n t) + \frac{b_1q_4\lambda_n^2}{\beta_n\Delta}P_{wn}(0)\sin(\beta_n t) \\ &\quad - \frac{q_3\gamma_1}{\Delta}\cos(\beta_n t)B_{an}(t) + \frac{q_1\gamma_2}{\Delta}\cos(\beta_n t)B_{wn}(t) + \frac{b_1\lambda_n^2\gamma_2}{\beta_n\Delta}\sin(\beta_n t)B_{wn}(t) \end{aligned} \tag{3.15}$$

Combining Eqs. (3.2), (3.8) and (3.15), the settlement expression of the unsaturated soil layer under any dynamic load can be finally obtained

$$\begin{aligned} S(t) &= -\int_0^h \frac{\partial w}{\partial z}\,dz = \frac{H_2}{2G+H_1}\sum_{n=0}^{\infty}\frac{1-\cos(n\pi)}{\lambda_n}P_{an}(t) + \frac{f(t)h}{2G+H_1} \\ &\quad + \frac{H_3}{2G+H_1}\sum_{n=0}^{\infty}\frac{1-\cos(n\pi)}{\lambda_n}P_{wn}(t) \end{aligned} \tag{3.16}$$

4. Numerical example analysis

As a numerical example, consider the following simple harmonic load on the surface of the soil layer

$$f(t) = \frac{P^*}{2}[1 + \cos(\omega t)] \tag{4.1}$$

where $P^*/2$ and ω, respectively, represent the amplitude and frequency of the harmonic load.

Then the analytical expression of settlement deformation is

$$S(t) = -\int_0^h \frac{\partial w}{\partial z}\, dz = \frac{H_2}{2G+H_1}\sum_{n=0}^{\infty}\frac{1-\cos(n\pi)}{\lambda_n}P_{an}(t) + \frac{P^*h[1+\cos(\omega t)]}{2(2G+H_1)} + \frac{H_3}{2G+H_1}\sum_{n=0}^{\infty}\frac{1-\cos(n\pi)}{\lambda_n}P_{wn}(t) \tag{4.2}$$

The specific expressions of each variable in Eq. (4.2) are shown in Appendix A.

The one-dimensional consolidation equation of unsaturated soil considering the pore liquid phase and pore gas phase and their mutual coupling effects is derived and solved by the Laplace transform. Numerical analysis is carried out on the present calculation example under the action of a simple harmonic load. The law of influence of the excitation frequency, initial saturation and depth on the one-dimensional consolidation deformation and characteristics of unsaturated soil is discussed. Among them, physical characteristic parameters of unsaturated soil used in the numerical examples, such as elastic coefficient, matrix suction and permeability coefficient of the fluid phase are all related to saturated soil. Therefore, the expressions of specific parameters are detailed in Appendix B. When considering a one-dimensional unsaturated clay layer, the calculated parameter values are shown in Table 1.

Table 1. Basic physical parameters of clay

Parameter type	Symbol	Numerical value
Porosity	φ	0.475
Fitting parameter	ζ	$1.168\,\mathrm{m}^{-1}$
Fitting parameter	n	1.165
Inherent permeability	k_s	$1.699\cdot10^{-14}\,\mathrm{m}^2$
Shear modulus	G	$2.4\cdot10^6\,\mathrm{Pa}$
Gas bulk modulus	K_1	$1.45\cdot10^5\,\mathrm{Pa}$
Bulk modulus of water	K_2	$2.25\cdot10^9\,\mathrm{Pa}$
Solid bulk modulus	K_s	$3.5\cdot10^{10}\,\mathrm{GPa}$
Consolidation bulk modulus	K_b	$4.5\cdot10^6\,\mathrm{Pa}$
Density of water	ρ_w	$997\,\mathrm{kg/m}^3$
Coefficient viscosity of gas	η_1	$18\cdot10^{-6}\,\mathrm{Pa{\cdot}s}$
Coefficient viscosity of water	η_2	$0.001\,\mathrm{Pa{\cdot}s}$
Acceleration of gravity	g	$9.8\,\mathrm{m/s}^2$
Pore connectivity parameter	η	1.165

Figure 2 shows the influence of the excitation frequency on deformation under different initial saturations. Figures 2a,b,c and 2d are change curves of settlement under different excitation frequencies when the initial saturation S_w is 0.65, 0.75, 0.85 and 1,00, respectively. In addition, dimensionless depth, dimensionless pore water pressure and dimensionless time are defined as z/h and $T = (c_v/h^2)t$. Firstly, the settlement curves under different saturations are discussed separately, and it is found that when the excitation frequency is 0 Hz the settlements show a steady development, which is shown as a consolidation curve under a constant load. When the excitation frequencies are 0.1 Hz and 10 Hz, the settlement curves show obvious dynamic load characteristics, and with an increases of the excitation frequency, the transient response frequency of the settlement also accelerates.

By comparing the calculation results of the initial saturation S_w of 0.65, 0.75 and 0.85 in the unsaturated state with the calculation results in the saturated state ($S_w = 1.00$), it is found that when the excitation frequency $\omega = 0$ Hz, the time for saturated soil clay to reach consolidation

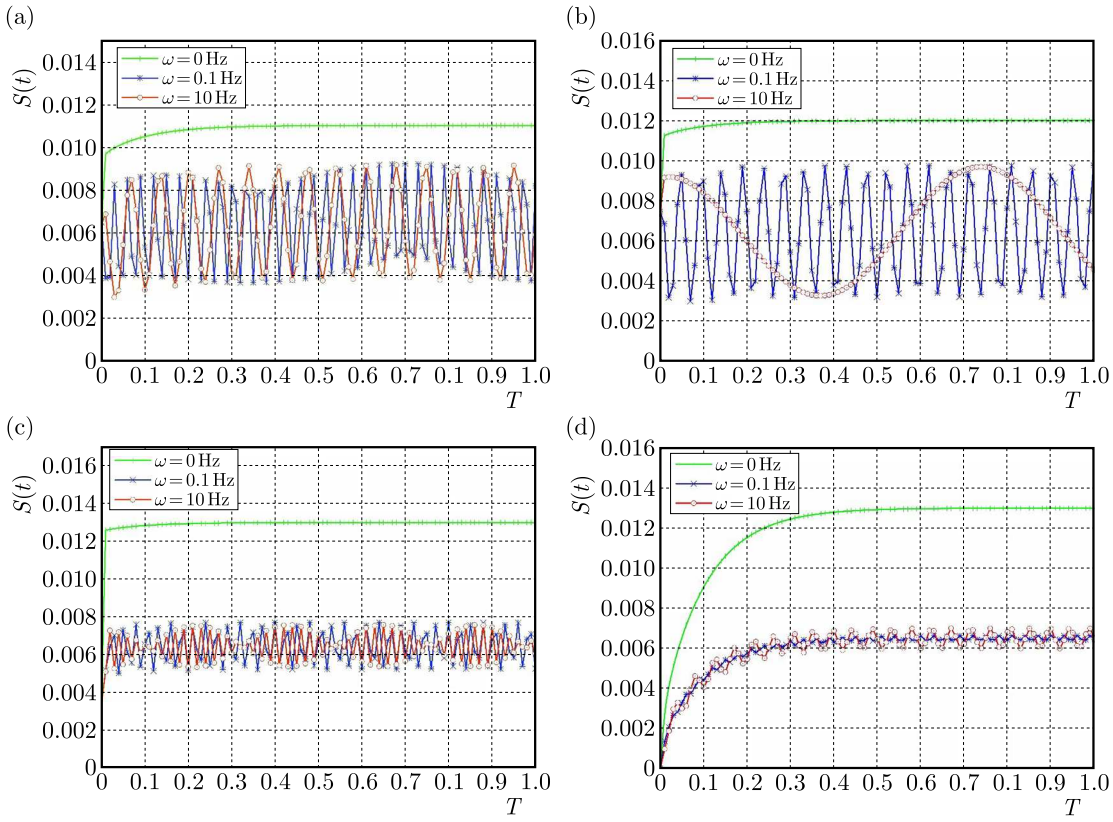

Fig. 2. Influence curves of the frequency on deformation under different saturations: (a) $S_w = 0.65$, (b) $S_w = 0.75$, (c) $S_w = 0.85$, (d) $S_w = 1.00$

stability is significantly longer than that for unsaturated soil clay. When the excitation frequency ω is 0.1 Hz and 10 Hz, the amount of sedimentation at a certain moment decreases with an increase of the initial saturation. In addition, the transient response lasts longer in saturated clay, while the initial saturation is higher, the transient response will disappear more quickly in unsaturated clay. All in all, the value of settlement under the constant load ($\omega = 0$) is always greater than that under the cyclic load ($\omega > 0$). However, for the settlement under the dynamic load it is difficult to maintain stability during the load-bearing period, and the effect of saturation on consolidation deformation is also significantly far from the load frequency.

Figure 3 shows the change curve of pore water pressure P_w/P^* along the soil depth z/h when the dimensionless time T is 10^{-5}, 10^{-3} and 10^{-1}, respectively. Figures 3a,b,c and 3d show the distribution curve when the initial saturation is 0.65, 0.75, 0.85 and 1.00, respectively. In addition, the dimensionless frequency is $\Omega = \omega h^2/c_v$, and the dimensionless frequency is calculated $\Omega = 10^7$ according to specific conditions.

It can be observed from Fig. 3 that under the unsaturated condition, the pore water pressure in the area near the top and bottom of the soil layer has different degrees of oscillation, but this situation does not appear in the saturated state. The reason for this phenomenon is that the frequency of the applied dynamic load is different for different saturation, which causes a change of pore water pressure at the boundary. At the dimensionless frequency $\Omega = 10^7$, when the saturation S_w is 0.65, 0.75 and 0.85, the corresponding excitation frequencies ω are 0.013 Hz, 0.042 Hz and 0.114 Hz, respectively. When the soil is saturated, the corresponding excitation frequency ω is 857 Hz. Therefore, given a dimensionless frequency due to the difference in soil saturation makes the excitation frequency vary greatly. This phenomenon strongly depends on the size of the excitation frequency.

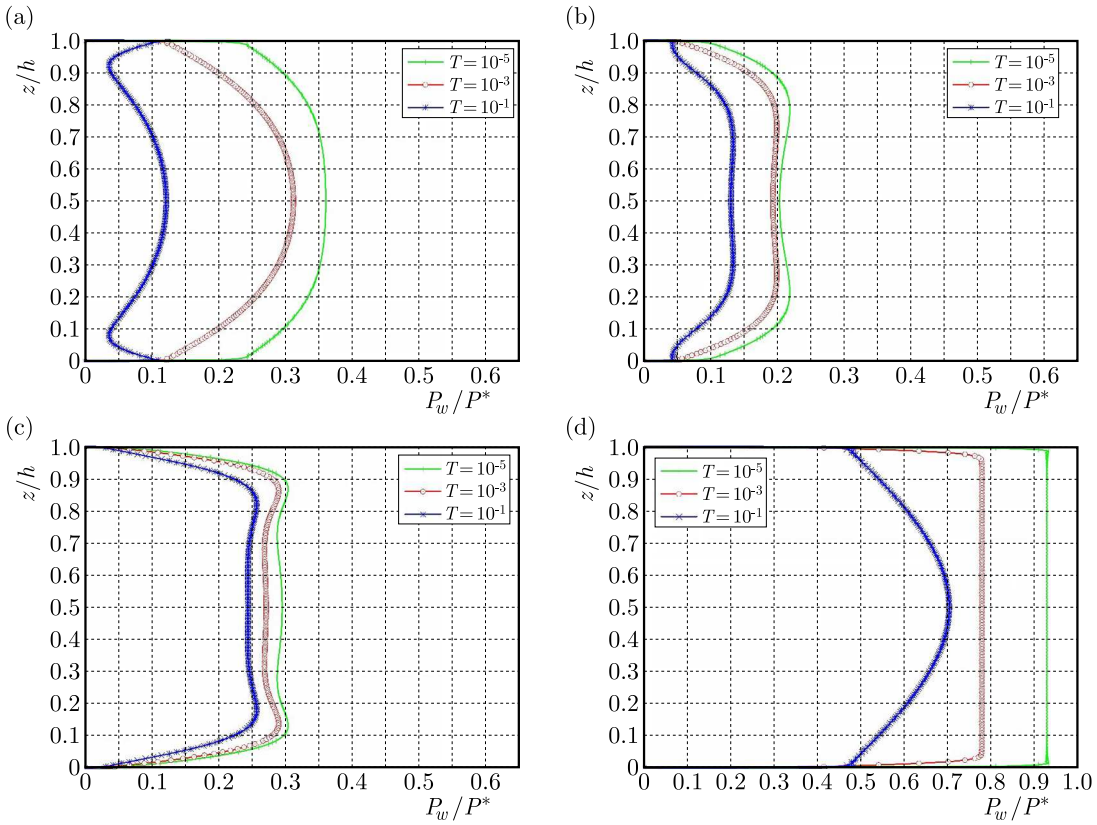

Fig. 3. Distribution law of pore water pressure and depth under complex conditions: (a) $S_w = 0.65$, (b) $S_w = 0.75$, (c) $S_w = 0.85$, (d) $S_w = 1.00$

5. Conclusion

Based on the theory of porous elastic media, an effective stress formula of unsaturated soil expressed by suction stress is adopted, and a analytical solution of one-dimensional consolidation of unsaturated soil under dynamic load is obtained by the Laplace transformation. In addition, specific numerical analysis and discussion of one-dimensional consolidation behavior of unsaturated clay under specific boundary conditions of a simple harmonic load are carried out. It is clear that the excitation frequency of the simple harmonic load and the initial saturation of the soil affects consolidation settlement. The results show that the settlement of soil under the constant load is always greater than the settlement under the dynamic load. For the dynamic load, the settlement at a certain moment decreases with an increase of saturation, and the transient response under the dynamic load is also closely related to the load frequency and saturation. Moreover, pore water pressure exhibits an obvious oscillation phenomenon in the area near the drainage boundary and an oscillatory trend in the unsaturated soil under the dynamic load.

Acknowledgement

This research was supported by the National Natural Science Foundation of China (51978320 and 11962016) and by the Foundation for Innovation Groups of Basic Research in Gansu Province (20JR5RA478). The authors are grateful to the reviewers for their insightful and constructive comments.

Appendix A

The Fourier coefficient of a simple harmonic load Eq. (4.1) is

$$B_m(t) = \frac{P^*\omega[\cos(m\pi) - 1]}{m\pi}\sin(\omega t) = Y_m \sin(\omega t) \tag{A.1}$$

Combine Eq. (3.15) to get

$$\begin{aligned} P_{an}(t) &= (D_1 + G_1)\mathrm{e}^{-C_1 t} + (D_2 + G_2)\mathrm{e}^{-C_2 t} + G_5\cos(\omega t) + G_6\sin(\omega t) \\ P_{wn}(t) &= (D_3 + G_3)\mathrm{e}^{-C_1 t} + (D_4 + G_4)\mathrm{e}^{-C_2 t} + G_7\cos(\omega t) + G_8\sin(\omega t) \end{aligned} \tag{A.2}$$

The coefficients in Eqs. (A.2) are

$$C_1 = \frac{\lambda_n^2}{2}\left(\frac{q_1 b_2 + q_4 b_1}{\Delta} + \sqrt{\frac{1}{\Delta} + (q_1 b_2 + q_4 b_1)^2 - \frac{4 b_1 b_2}{\Delta}}\right)$$

$$C_2 = \frac{\lambda_n^2}{2}\left(\frac{q_1 b_2 + q_4 b_1}{\Delta} - \sqrt{\frac{1}{\Delta} + (q_1 b_2 + q_4 b_1)^2 - \frac{4 b_1 b_2}{\Delta}}\right)$$

$$D_1 = \frac{1}{C_1 - C_2}\Big[P_{an}(0)\Big(C_1 - \frac{q_1 b_2 \lambda_n^2}{\Delta}\Big) - \frac{q_2 b_2 \lambda_n^2}{\Delta} P_{wn}(0)\Big]$$

$$D_2 = \frac{1}{C_1 - C_2}\Big[P_{an}(0)\Big(\frac{q_1 b_2 \lambda_n^2}{\Delta} - C_2\Big) + \frac{q_2 b_2 \lambda_n^2}{\Delta} P_{wn}(0)\Big]$$

$$D_3 = \frac{1}{C_1 - C_2}\Big[P_{wn}(0)\Big(C_1 - \frac{q_4 b_1 \lambda_n^2}{\Delta}\Big) - \frac{q_3 b_1 \lambda_n^2}{\Delta} P_{an}(0)\Big]$$

$$D_4 = \frac{1}{C_1 - C_2}\Big[P_{wn}(0)\Big(\frac{q_4 b_1 \lambda_n^2}{\Delta} - C_2\Big) + \frac{q_3 b_1 \lambda_n^2}{\Delta} P_{an}(0)\Big]$$

$$G_1 = \frac{\omega M_2 - C_1 M_1}{(C_2 - C_1)(C_1^2 + \omega^2)} \qquad G_2 = \frac{C_2 M_1 - \omega M_2}{(C_2 - C_1)(C_1^2 + \omega^2)}$$

$$G_3 = \frac{\omega M_4 - C_1 M_3}{(C_2 - C_1)(C_1^2 + \omega^2)} \qquad G_4 = \frac{C_2 M_3 - \omega M_4}{(C_2 - C_1)(C_1^2 + \omega^2)}$$

$$G_5 = \frac{M_1(C_1 C_2 - \omega^2) - \omega M_2(C_1 + C_2)}{(C_1^2 + \omega^2)(C_2^2 + \omega^2)} \qquad G_6 = \frac{M_1\omega(C_1 + C_2) + M_2(C_1 C_2 - \omega^2)}{(C_1^2 + \omega^2)(C_2^2 + \omega^2)}$$

$$G_7 = \frac{M_3(C_1 C_2 - \omega^2) - \omega M_4(C_1 + C_2)}{(C_1^2 + \omega^2)(C_2^2 + \omega^2)} \qquad G_8 = \frac{M_3\omega(C_1 + C_2) + M_4(C_1 C_2 - \omega^2)}{(C_1^2 + \omega^2)(C_2^2 + \omega^2)}$$

where

$$M_1 = \frac{(q_4 Y_{an} - q_2 Y_{wn})\omega}{\Delta} \qquad M_2 = \frac{b_2 \lambda_n^2 Y_{an}}{\Delta} \qquad M_3 = \frac{(q_1 Y_{wn} - q_3 Y_{an})\omega}{\Delta}$$

Appendix B

In the model of unsaturated soil, the relationship among physical, mechanical parameters and the saturation is as follows.

Coefficient of linear elasticity (Lo *et al.*, 2005)

$$
\begin{aligned}
a_{11} &= \frac{K_s}{N_3}\{(1-\varphi)N_1[K_1K_2 + K_1N_2S_a + K_2N_2(1-S_a)] \\
&\quad + K_bK_s\varphi[K_1(1-S_a) + K_2S_1 + N_2]\} \\
a_{12} &= a_{21} = \frac{N_1K_sK_1S_a(K_2+N_2)}{N_3} \qquad a_{13} = a_{31} = \frac{N_1K_s\varphi K_2(1-S_a)(K_1+N_2)}{N_3} \\
a_{22} &= \frac{K_1S_a^2\varphi}{N_3}\Big[K_s^2\varphi\Big(K_2 + \frac{N_2}{S_a}\Big) + \frac{K_2N_1N_2}{S_a}(1-S_a)\Big] \\
a_{23} &= a_{32} = -\frac{K_1K_2\varphi S_a(1-S_a)(N_1N_2 - \varphi K_s)}{N_3} \\
a_{33} &= \frac{K_2(1-S_a)\varphi}{N_3}\Big[K_s^2\varphi\Big(K_1 + \frac{N_2}{1-S_a}\Big) + \frac{K_1N_1N_2S_a}{1-S_a}\Big]
\end{aligned}
$$

where K_b is the bulk modulus of the soil skeleton; K_1, K_2 and K_s respectively represent the bulk modulus of air, water and solid soil particles. Among them, the parameters N_1, N_2 and N_3 are defined as

$$
\begin{aligned}
&N_1 = K_s(1-\varphi) - K_b \qquad N_2 = \frac{dp_c}{dS_a}S_a(1-S_a) \\
&N_3 \equiv N_1[K_1N_2S_a + K_1K_2 + K_2N_2(1-S_a)] + K_s^2[K_1(1-S_a) + N_2 + K_2S_a]
\end{aligned}
\tag{B.1}
$$

where p_c is the suction matrix. In the V-G model (Genuchten, 1980)

$$
S_e = [1 + (\zeta h_c)^n]^{-m} \tag{B.2}
$$

where n, m and ζ are fitting parameters, $m = 1 - (1/n)$.

Combining Eq. (B.2) the expression for N_2 can be obtained

$$
N_2 = \frac{\rho_w g}{mn\zeta}\frac{S_aS_w}{S_s - S_r}\Big[\Big(\frac{1-S_r}{S_s-S_r} - \frac{S_a}{S_s-S_r}\Big)^{-1/m} - 1\Big]^{(1/n)-1}\Big(\frac{1-S_r}{S_s-S_r} - \frac{S_a}{S_s-S_r}\Big)^{-1-(1/m)} \tag{B.3}
$$

The relative permeability of pore gas and water (Wang *et al.*, 2017) is

$$
k_{ra} = (1-S_e)\Big(1 - \sqrt[m]{S_e}\Big)^{2m} \qquad k_{ra} = S_e^{\eta}\Big[1 - \Big(1 - \sqrt[m]{S_e}\Big)^m\Big]^2 \tag{B.4}
$$

where η represents a parameter related to pore connectivity.

References

1. Chen Z.H., Xie D.Y., Liu Z. D., 1993, Consolidation theory of unsaturated soil based on the theory of mixture, *Applied Mathematics and Mechanics*, **14**, 137-150
2. Chen Z.H., Zhou H.Q., Fredlund D.G., 1999, Nonlinear model for unsaturated soils and its application, *Chinese Journal of Geotechnical Engineering*, **21**, 603-608
3. Fredlund, Rahardjo D.G., 1993, *Soil Mechanics for Unsaturated Soils*, New York: John Wiley and Sons
4. Genuchten van M. Th., 1980, A closed-form equation for predicting the hydraulic conductivity of unsaturated soils, *Soil Science Society of America Journal*, **44**, 892-898
5. Ho L., Fatahi B., Khabbaz H., 2014, Analytical solution for one-dimensional consolidation of unsaturated soils using eigenfunction expansion method, *International Journal for Numerical and Analytical Methods in Geomechanics*, **38**, 1058-1077

6. Huang M.S., Yang C., Cui Y.J., 2009, Elasto-plasticity bounding surface model for unsaturated soils under cyclic loading, *Journal of Geotechnical Engineering*, **31**, 817-823

7. Jiang M.J., Leroueil S., Konrad J.M., 2004, Insight into shear strength functions of unsaturated granulates by DEM analyses, *Computers and Geotechnics*, **31**, 473-489

8. Lo W.C., Sposito G., Chu H., 2014, Poroelastic theory of consolidation in unsaturated soils, *Vadose Zone Journal*, **13**, 1-12

9. Lo W.C., Sposito G., Lee J.W., Chu H.H., 2016, One-dimensional consolidation in unsaturated soils under cyclic loading, *Advances in Water Resources*, **91**, 122-137

10. Lo W.C., Sposito G., Majer E., 2002, Immiscible two-phase fluid flows in deformable porous media, *Advances in Water Resources*, **25**, 1105-1117

11. Lo W.C., Sposito G., Majer E.L., 2005, Wave propagation through porous media containing two immiscible fluids, *Water Resources Research*, **41**, 199-207

12. Lu N., Godt J.W., Wu D.T., 2010, A closed-form equation for effective stress in unsaturated soil, *Water Resources Research*, **46**, 567-573

13. Pan X.D., Cai Y.Q., Xu C.J., Zhang Y.F., 2006, One-dimensional consolidation of viscoelastic saturated soil under cyclic load, *Rock and Soil Mechanics*, **27**, 272-276

14. Pedroso D.M., Farias M.M., 2011, Extended Barcelona basic model for unsaturated soils under cyclic loadings, *Computers and Geotechnics*, **38**, 731-740

15. Qin A.F., Sun D.A., Tan Y.W., 2010, Semi-analytical solution to one-dimensional consolidation in unsaturated soils, *Applied Mathematics and Mechanics*, **31**, 215-226

16. Sheng J.S., Ting W., Yu Q.G., 2019, Equivalent consolidation deformation properties and one--dimensional analysis method of unsaturated soil, *Chinese Journal of Geotechnical Engineering*, **31**, 1037-1045

17. Shi G., Liu Z.Y., Li Y.H., 2018, One-dimensional rheological consolidation analysis of soft clay considering non-darcy seepage under cyclic load, *Rock and Soil Mechanics*, **39**, 530-537

18. Su W.X., Xie K.H., 2010, Analytical solution of one-dimensional consolidation of unsaturated soil by mixed fluid method, *Rock and Soil Mechanics*, **31**, 2661-2665

19. Toufigh M.M., Ouria A., 2009, Consolidation of inelastic clays under rectangular cyclic loading, *Soil Dynamics and Earthquake Engineering*, **29**, 356-363

20. Wang L., Sun D.A., Li P.C., Xie Y., 2017a, Semi-analytical solution for one-dimensional consolidation of fractional derivative viscoelastic saturated soils, *Computers and Geotechnics*, **83**, 30-39

21. Wang L., Sun D.A., Qin A.F., 2017b, General semi-analytical solutions to one-dimensional consolidation for unsaturated soils, *Applied Mathematics and Mechanics (English Edition)*, **38**, 831-850

22. Wang L., Xu Y.F., Xia X.H., Sun D.A., 2018, Semi-analytical solutions to two-dimensional plane strain consolidation for unsaturated soil, *Computers and Geotechnics*, **101**, 100-113

23. Xie K.H., Huang D.Z., Wang Y.L., Deng Y.B., 2014, Analytical theory for one-dimensional consolidation of soil induced by time-dependent pumping and loading, *Marine Georesources and Geotechnology*, **32**, 328-350

24. Xie K.H., Xie X.Y., Li X.B., 2008, Analytical theory for one-dimensional consolidation of clayey soils exhibiting rheological characteristics under time-dependent loading, *International Journal for Numerical and Analytical Methods in Geomechanics*, **32**, 1833-1855

25. Yin Z.Z., Ling H., 2007, Simplified computation of one-dimensional consolidation for partially saturated soils, *Journal of Geotechnical Engineering*, **29**, 633-637

Manuscript received May 25, 2022; accepted for print October 1, 2022

JOURNAL OF THEORETICAL AND APPLIED MECHANICS
61, 1, pp. 23-36, Warsaw 2023
https://doi.org/10.15632/jtam-pl/157464

ANALYSIS OF ABNORMAL VIBRATIONS OF CRUDE OIL EFFLUX PUMPS USING ANSYS

Tianqi Wang
Xian Shiyou University, Mechanical Engineering College, Xi'an, China, and
Xidian University, The School of Mechano-Electronic Engineering, Xi'an, China
Corresponding author, e-mail: wangtianqi@xsyu.edu.cn

Lei Xie
Cementing Company Downhole Service Company CCDC, Chengdu, China

Hongsheng Yu, Xiuliang Wei
Changqing Oilfield Second Oil Transmission Office, Xianyang, China

Pengmin Dong,Tianyi Zhao
Xian Shiyou University, Mechanical Engineering College, Xi'an, China

In this study, abnormal vibrations of 1 pump fluid in a crude oil efflux station in the Changqing Oilfield was investigated. Kinetic simulation was applied to flow fields in the crude oil efflux pump using Ansys to determine trends of the impeller static pressure, speed, total pressure, wall pressure of the impeller, outlet pressure and pressure on the pump shell and to identify the reasons behind the abnormal vibrations. The results indicated that the axial vibration amplitude of the pump could be reduced from 1.3 mm down to 0.68 mm if the operation parameters of the external control oil pump were set as 2500-2550 r/min and 325-335 m^3/h, respectively.

Keywords: abnormal vibrations, internal flow field, Ansys

1. Introduction

Impellers of a centrifugal pump are typically subject to highly complex 3D flows. Here, the fluid speed is distributed over several orders of magnitude; unidirectional flows and cross flow of multiphase flows are observed; separated flow, backflow and secondary flow also occur due to the effects of impeller rotation and surface curvature. As a result, fluid flows in an impeller can be extremely complicated (Shen, 2007). Considering the immaturity of existing testing methods, several researchers have used computational fluid dynamics (CFD) to numerically simulate characteristics of internal flows in the impeller of a centrifugal pump for impeller modeling and design, which has become an important research method in the modern pump technology (Chen *et al.*, 2014; Yu, 2008). Majidi (2005) solved an unsteady 3D viscous flow in the impeller and volute of a centrifugal pump using CFD methods. Benra and Dohmen (1966) investigated an unsteady flow field of a single-blade centrifugal pump using numerical simulation. The results showed that the lift increased in direct proportion with the flow. Boehning *et al.* (2011) investigated the effects of the volute structure on the radial force of a blood pump by using transient numerical methods. The results showed that a dual-volute structure could effectively reduce the radial force compared with the circumferential volute. Barrio *et al.* (2011) calculated the radial force of the impeller of a centrifugal pump under undesigned flow conditions by using a transient numerical method and found that the radial force was 40-70% of that under steady conditions, while the radial force under unsteady conditions was closer to the experimental

results. Mele *et al.* (2014) investigated correlation of vibrations and unsteady flows in a pump under different speeds using both experimental and simulation methods. The results showed that flow-induced vibrations increased with increasing pump speed and were significantly related to pump efficiency.

In this study, the speed and pressure variations were simulated, and by combining the simulation results with the vibration condition of the centrifugal pump during operation, a flow range that could reduce vibration was obtained to guide the actual production.

A crude oil pump group consists of feeding pumps, efflux pumps, heating furnaces, oil storage tanks, reverse feeding pumps and other components. The two feeding pumps and three efflux pumps were double-suction centrifugal pumps purchased from the Hunan Tane Ocean Pump Co., Ltd. (China). The oil pump had a lift of 480 m, a flow of 500 m^3/h, a rated speed of 2980 r/min, a maximum allowed working pressure of 8.8 MPa, a bearing model of 7316B/DB, and a rated motor power of 800 kW. To increase the pump lift, 1 feeding pump worked in tandem with 1 and 2 efflux pumps during the operation of the pump group. The actual working speed and flow of the efflux pumps ranged from 2400 to 2750 r/min and about 350 m^3/h, while the rated speed and flow of the efflux pumps were 2980 r/min and 500 m^3/h, respectively.

The three efflux pumps at the oil efflux station were put into operation on September 15, 2015, and the accumulated operation time until the end of June 2019 was 23,835 hours for 1 efflux pump, 25,511 hours for 2 efflux pump and 23,509 hours for 3 efflux pump, all of which have been operating alternately for nearly four years. For 1 efflux pump, cavitation occurred during operation, the impeller in the pump shell had indications of being subjected to cavitation, and there was obvious crackling sound from the inside. Uninterrupted monitoring for the past five years indicated that vibration at the low-pressure end of 1 efflux pump has become increasingly large, and the transient vibration tested on February 24, 2020 exceeded 9.0 mm/s. After the mode of operation was adjusted using different methods, the vibration perpendicular to the axial direction at the low-pressure end of the pump often exceeded 7.1 mm/s.

With regard to vibrations of an oil pump, this paper proposed a rational speed and flow range using Ansys based on the change law of the flow field and fluid pressure in the pump, to guide the actual production and reduce the vibration amplitude of the pump so as to ensure unhindered production.

2. The pump model

2.1. Geometric parameters of the pump model

A double-suction centrifugal pump was used as the model in this study. This pump had a designed flow of $q_v = 500\,m^3$/h, designed lift of $H = 480$ m, designed speed of $n = 2980$ r/min, specific speed of $n_s = 40$, designed efficiency of $\eta = 78\%$, blade number of $z = 6$, impeller inlet diameter of $D_0 = 180$ mm, impeller outlet diameter of $D_2 = 541$ mm, and impeller outlet width of $b_2 = 21.1$ mm. Additionally, $q_v = 357\,m^3$/h, and speed $n = 2554$ r/min.

2.2. Meshing of the pump model

The centrifugal pump model was simplified using SolidWorks 2019 and fluid domains were selected in SpaceClaim. Figure 1 shows the established model.

The model consists of inflow runners, rotors, guide vanes, volutes, outflow runners and other components. To ensure the overall quality of the mesh and shorten the computational time, all the overflow components were divided using unstructured meshes in this paper. Each component was structurally divided into blocks to pre-generate the mesh, and by adjusting the distribution

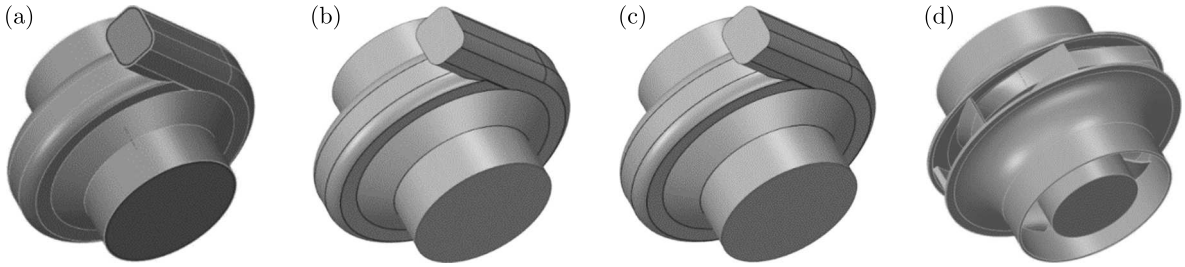

Fig. 1. 3D model of the centrifugal pump: (a) volute fluid domain, (b) pump shell fluid domain, (c) impeller fluid domain, (d) impeller

of nodes and the number of nodes, the mesh domain of each overflow component was encrypted in the targeted manner (Zhao *et al.*, 2005).

The boundary conditions were determined for meshing in FLUENT, with the impeller fluid having 956,000 elements and the shell fluid domain having 1.245 million elements. Figure 2 shows the developed mesh.

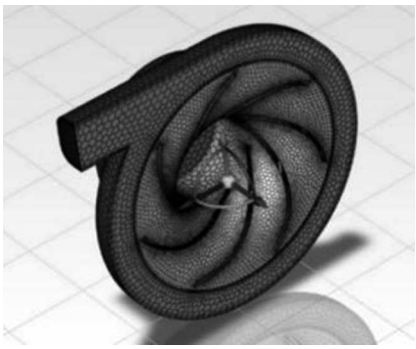

Fig. 2. Model meshing

2.3. Boundary conditions

Given the designed flow and lift of the target pump, the inlet boundary condition was set as the mass flow inlet, and the outlet boundary condition was set as a pressure outlet. Numerical simulation results were used to calculate the corresponding lift and efficiency. The rotating boundary was set as the rotor, the non-slip boundary condition was set as the wall, and the standard wall function was used for the near-wall region (Han *et al.*, 2004). Due to the complex working conditions of the pump station, and influenced by many factors such as pipelines, valves, feeding pumps and discharges, the measured data were averaged in this study. Table 1 lists the specific boundary conditions.

Table 1. Boundary conditions

Inlet pressure [(MPa]	Flow rate at inlet [kg/s]	Speed [r/min]	Center-of-mass coordinates of impeller model	Gravitational acceleration [m/s^2]
0.6134	single inlet, 49.603, two inlets, 99.206	2554.44	$X = -0.0541268$ $Y = -0.0281454$ $Z = 0.413535$	9.81

2.4. Selection of the turbulence model

The SST k-ω turbulence model is used to convert between the k-ω model for the near--wall region and the k-ω model for the far-field region using a blending function. It combines the accuracy of the k-ω model for calculating viscous flows in the near-wall region with the reliability of the k-ω model for calculating free flows in the far-field region. The advantage of this model is that it considers turbulent shear stresses and can obtain accurate results even when flow separation occurs. In this study, the SST k-ω turbulence model was chosen for computation. Herein, the pressure term adopted the second-order central difference format; the momentum term and the turbulent viscosity correction were computed using the second-order windward format. The speed and pressure in the flow field were coupled using the Simple algorithm (Wang, 2004).

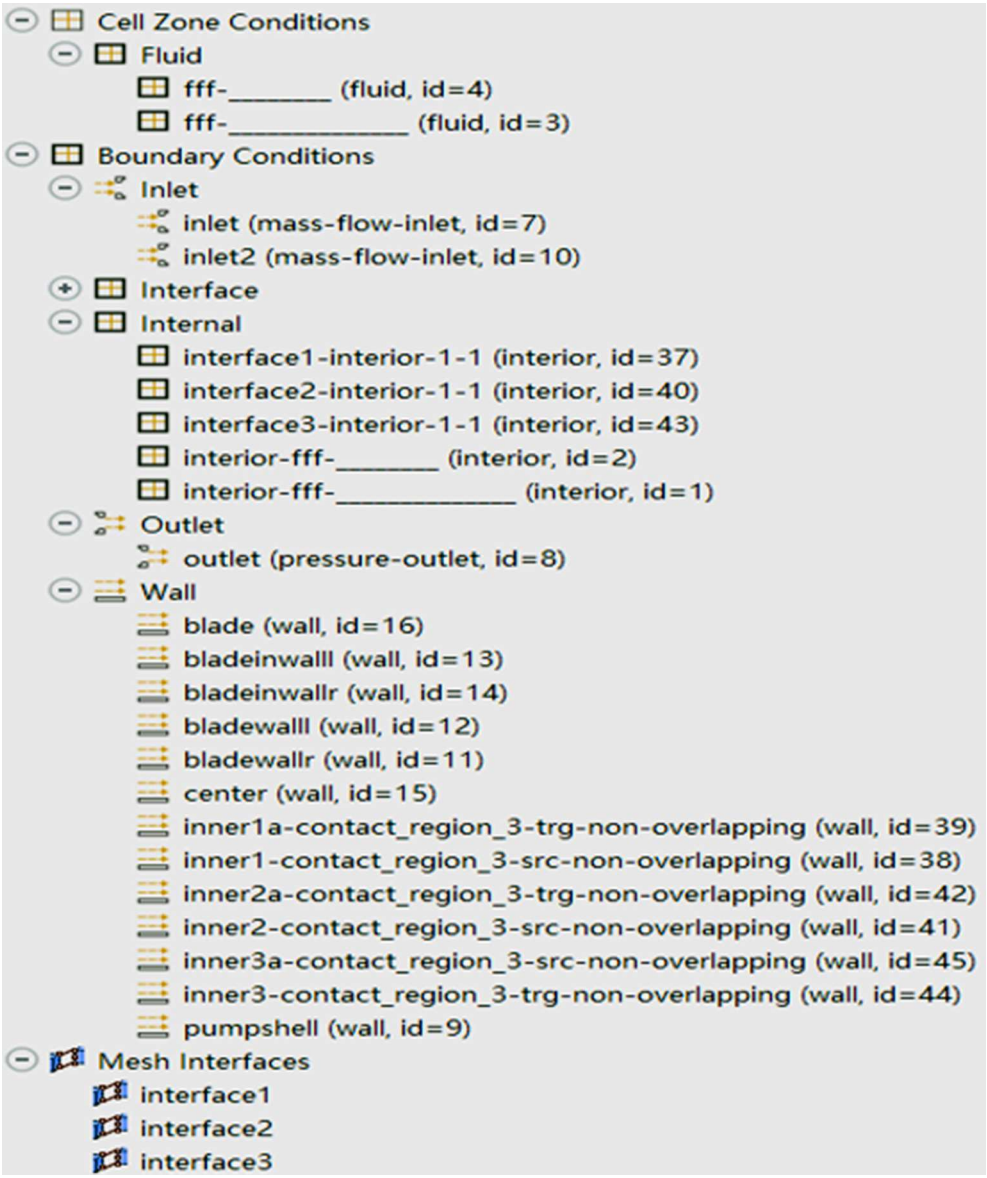

Fig. 3. Boundary condition settings

Mass flow inlet conditions were used for the inlet, and the data were exchanged between the overflow components of the pump using interfaces. The inflow and outflow runner walls of the model pump and the cavity walls of the pump were set as stationary walls. The walls of the blade

and the impeller that rotate with the impeller were set as rotational boundaries. The no-slip boundary conditions were used for solid walls, and the standard wall function was used for near walls. The convection term was discretized using the second-order windward scheme, the diffusion term was discretized based on a central difference format with the second-order accuracy, and the speed and pressure were coupled by the Simple algorithm. To ensure convergence, the monitoring residual value was set to 10^{-5}. Figure 2 shows the developed mesh. The boundary conditions are set in Fig. 3.

2.5. Mesh-independent verification

To exclude the influence of the total number of meshes on the results, 56 sets of meshes with different amounts were divided for mesh-independent verification. The lift of the centrifugal pump was used as a dependent variable for the mesh-independent verification. When the lift fluctuation was less than 1%, the meshes were considered to meet the computational requirements. Meanwhile, by considering both the computational time and resources required for numerical computation, 2.2 million elements were finally selected as the computational requirement. Figure 4 shows the trend of curve change, between 2.1 and 2.3 it is gentle and stable, so 2.2 was selected.

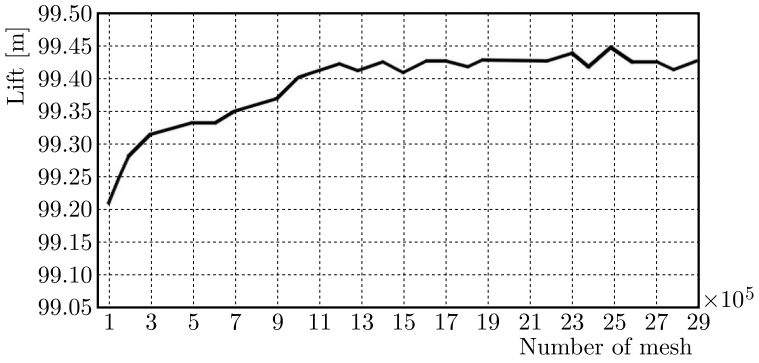

Fig. 4. Relationship between lift and mesh

3. Fluid analysis

3.1. Unstable flow characteristics in the centrifugal pump

A centrifugal pump comprises impellers and volutes. The complex structure and flow patterns result in the formation of unstable unsteady turbulence flows. When a centrifugal pump operates, the internal flows of the pump have many unstable flow characteristics, such as backflow at the impeller inlet, a wake-jet structure of the impeller outlet, and induced vibrations and noise. These unsteady flow characteristics determine the operating performance of the centrifugal pump.

3.1.1. Backflow

Backflow generally occurs at the inlet and outlet of the impeller. The backflow at the impeller inlet is mainly caused by an uneven force of high-speed rotating blades on the internal fluid. Due to the centrifugal force during operation, a pressure difference exists between the fluid flow at the outer edge of the inlet and the fluid in the inlet pipe near the shaft. The pressure at the outer edge is higher than that at the shaft, thus resulting in the fluid backflow from the impeller inlet to the inlet pipe (Zhu, 2008). Figure 5 shows the schematic of the backflow.

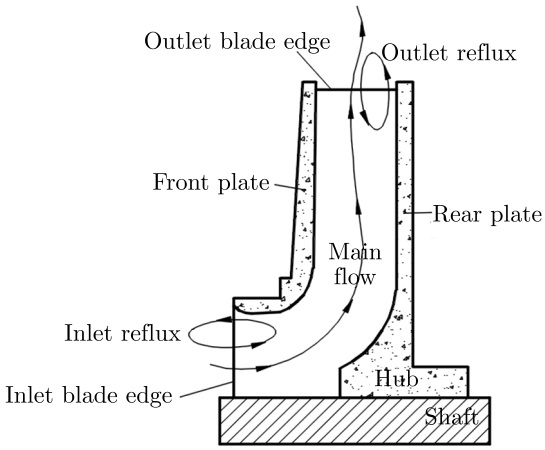

Fig. 5. Schematic of backflows at the inlet and outlet of the centrifugal pump

3.1.2. Wake-jet structure

As mentioned above, the flow rate near the blade pressure surface accelerates, while the fluid flow near the blade suction surface slows down, resulting in a wake-jet structure. A jet zone with a relatively high flow rate and almost zero viscosity exists near the blade pressure surface, while the wake zone with a relatively low flow rate is near the blade suction surface (Zhang, 2001). Figure 6 shows the wake-jet structure.

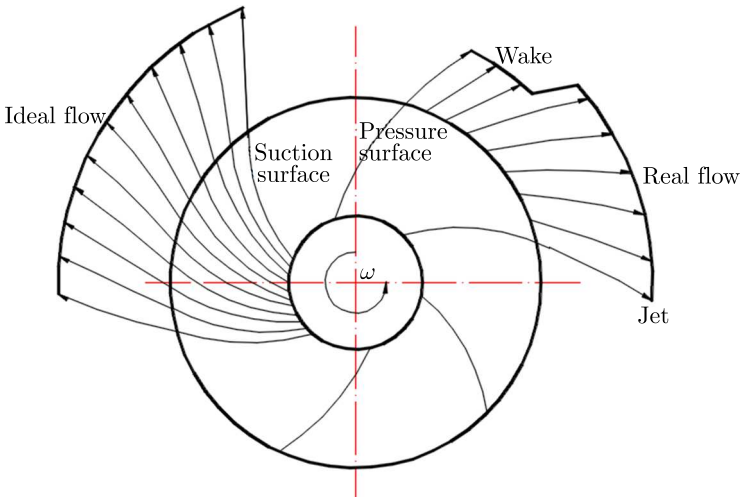

Fig. 6. Wake-jet structure in the sub-impeller

3.2. Analysis of streamlines

Fluent has a wide range of analytical functions and a series of flow models including those for asteady flow, laminar flow, turbulent flow and unsteady flow. The computation and display of streamlines is a fundamental technique in the visualization of flow fields. In this study, the CFD computational mesh was divided into tetrahedral cells first, and the topological relation between the adjacent tetrahedra was set. Subsequently, the "compass" method based on the tetrahedral side method was used for fast point location, and an adaptive step numerical integration method was used to trace the streamlines directly in the physical space. By doing so, the conversion between the physical space, computational space and resulting errors were avoided, and the accuracy and efficiency of streamline tracing were improved (Zhang, 2007). After the computation was completed, Ansys was used to generate streamlines.

Figure 7 shows the distribution of streamlines in the flow field. As observed, the fluid flows in from the fluid domain inlet, and at this point, the streamline is distributed in a regular and orderly manner. After rotation of the impeller, the flow pattern of the streamline changes, and the streamline moves in a spiral shape and flows out from the outlet. The fluid in the pump cavity accelerates, and the fluid in the impeller shows a gradient distribution in terms of the flow rate. Since diameter of the outlet is smaller than that of the inlet, the flow speed at the outlet is significantly higher than that at the inlet. Additionally, the presence of a wake-jet structure and boundary layer separation in the flow runner will lead to increased hydraulic losses, low pump efficiency, and even vibrations.

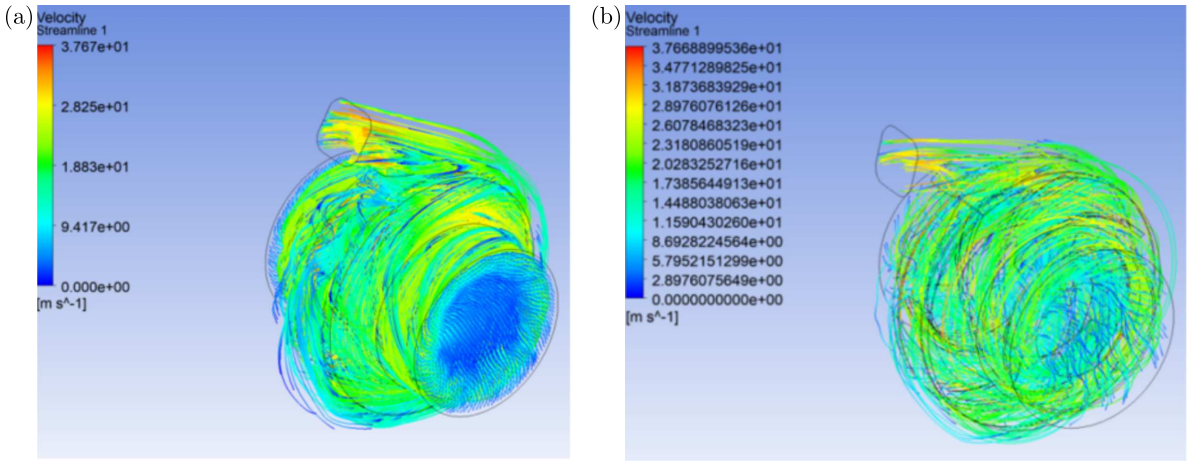

Fig. 7. Distribution of streamlines in the flow field: (a) distribution of the encrypted streamline, (b) distribution of the unencrypted streamline

3.3. Numerical analysis of the impeller

3.3.1. Static pressure

Figure 8 shows the distribution of impeller pressure. As observed, the absolute pressure at the root of the blade in the suction inlet section is lower than that at the blade edge, and the pressure at this position is the same as the outlet pressure of the feeding pump (about 6.4 kPa), which facilitates normal suction of the fluid flowing out from the feeding pump. The pressure at the blade edge is 1.3 MPa, and the pressure gradually increases from the root to the edge of the blade. Given that the blade edge and discharge outlet are closely positioned, the fluid can flow smoothly from the suction inlet to the discharge outlet under low-pressure suction. In summary, the impeller shows good suction and discharge capacity.

3.3.2. Speed

Figure 9 shows the distribution of impeller speed. As observed, the blade edge speed increases from the root to the end surface with a maximum speed of 75.1 m/s, and the speed at the suction inlet section is lower than that at the blade edge. The inlet flow rate is calculated as

$$v = \frac{Q}{S} = \frac{357.14}{3600 \cdot (0.09)^2 \cdot \pi} = 3.90 \,\frac{\mathrm{m}}{\mathrm{s}} \tag{B.1}$$

where Q is the average inlet flow at the centrifugal pump and S is the area of the inlet section with a diameter of 180 mm.

Therefore, the fluid with a relatively low flow rate can be significantly increased after flowing through the impeller. Nevertheless, due to the influence of the secondary flow in the impeller

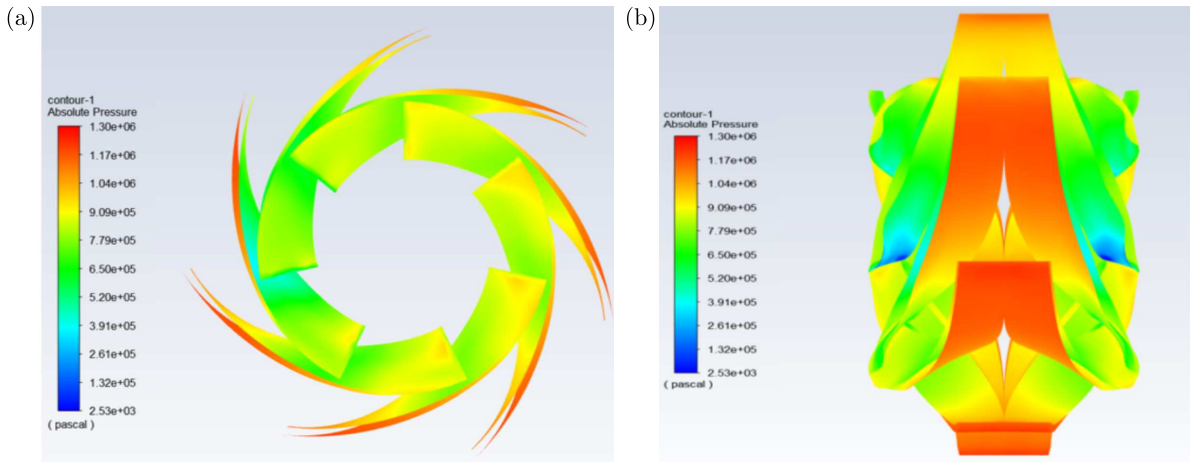

Fig. 8. Distribution cloud of impeller pressure: (a) front view, (b) side view

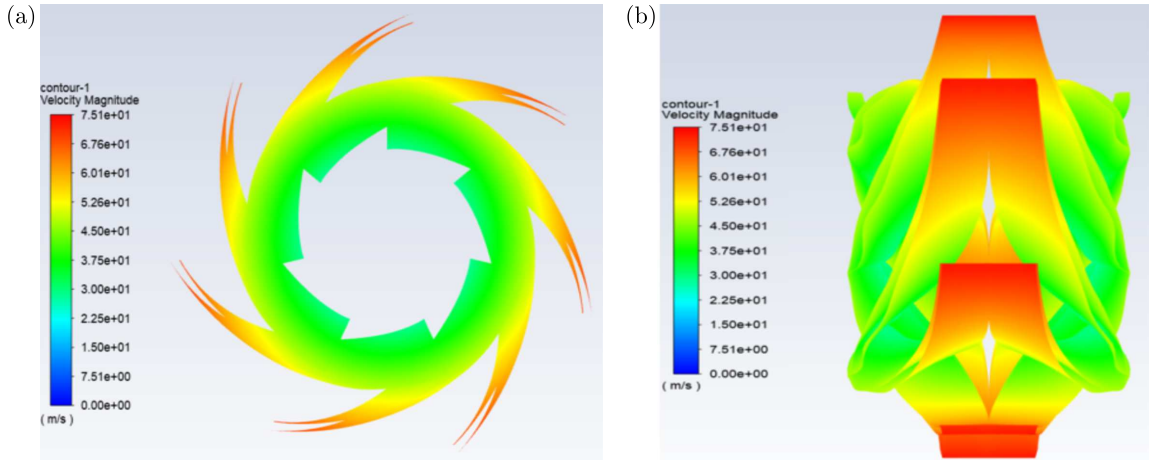

Fig. 9. Distribution cloud of impeller speed: (a) front view, (b) side view

flow runner, high-energy fluid microclusters are clustered at the blade pressure surface, which accelerates the fluid flow rate and thus reduces the possibility of boundary layer separation at the blade pressure surface. On the other side, the low-energy fluid microclusters enter the boundary layer near the suction surface of the blade, which reduces the flow rate near the suction surface, makes the boundary layer thicker and intensifies boundary layer separation at the suction surface of the blade (Wang *et al.*, 2022), which also becomes a triggering factor for pump vibrations.

3.3.3. Total pressure

Figure 10 illustrates the distribution of total pressure on the impeller.

As observed, the total pressure at the impeller blade surface is higher than that at the blade edge and shows an increasing trend from the root to the edge of the blade. Since the total pressure is the sum of static pressure and dynamic pressure, the dynamic pressure at the blade edge is higher than that at the root and its value is the highest, which is also consistent with the trend of speed distribution. The lower part of Fig. 10b shows that the pressure at the outlet is much higher than in other parts after the fluid flows across the impeller of the centrifugal pump. As shown in Fig. 10a, the work done by the blade on the fluid is not uniform, boundary layer separation occurs in the fluid in the impeller flow runner, and a separation vortex is formed in the flow runner. Boundary layer separation may cause vibrations, thus leading to low pump efficiency.

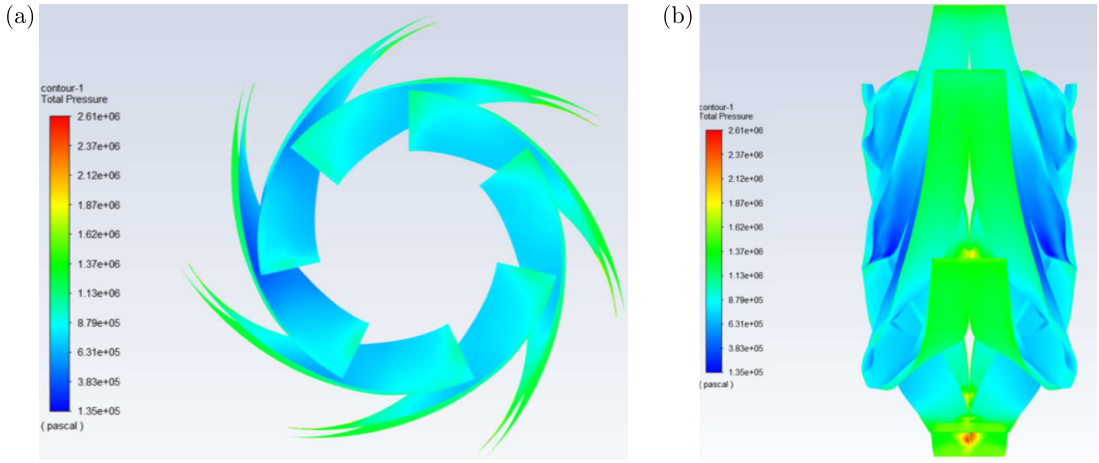

Fig. 10. Distribution cloud of total pressure on the impeller: (a) front view, (b) side view

3.3.4. Analysis of impeller inner wall

Figure 11 shows the distribution of the impeller inner wall pressure. As observed, the pressure distribution in the inner profile of the impeller is basically the same as that in the blade. Since the blade pressure distribution may be described in terms of absolute pressure, the outer profile is described in terms of the surface pressure (static pressure). As observed, the maximum and minimum pressures were 1.2 MPa and 4.0 kPa, respectively. This is partly a result of the combined effect of the impeller centrifugal force and the lifting force. The center of the impeller is the suction zone where the pump sucks the fluid, and the edge is the discharge zone for lifting the liquid pressure for discharge, which forms the work done in the fluid (Chu *et al.*, 2009).

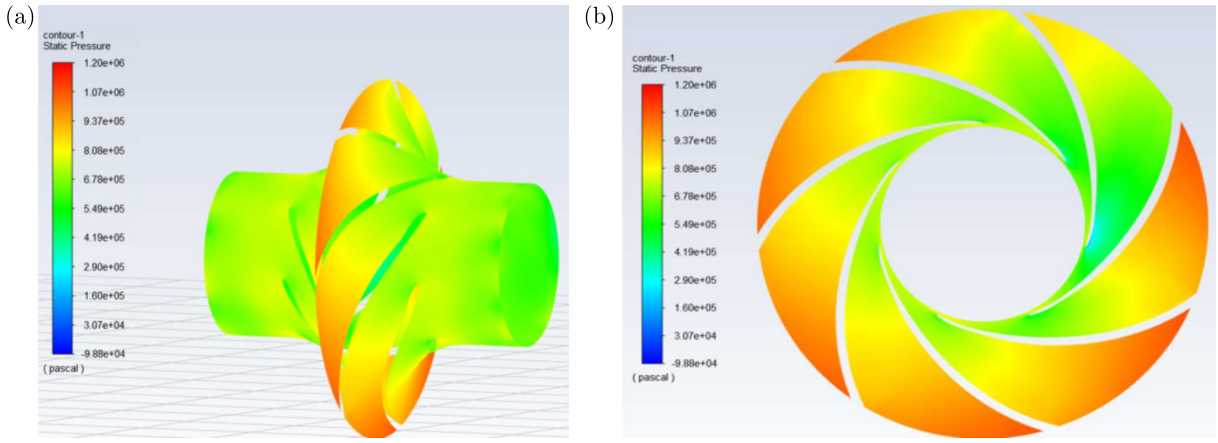

Fig. 11. Distribution cloud of pressure on the inner wall of the impeller

3.3.5. Pressure on the inner wall of the pump

Figure 12 shows the distribution of pressure on the inner wall of the pump. As observed, the maximum and minimum pressures were 1.2 MPa and 4.0 kPa, respectively. This is partly a result of the combined effect of the impeller discharge pressure and the pump shell. Thus, as the impeller radius increases, the pressure also increases, while the local pressure increases significantly due to the outlet backflow.

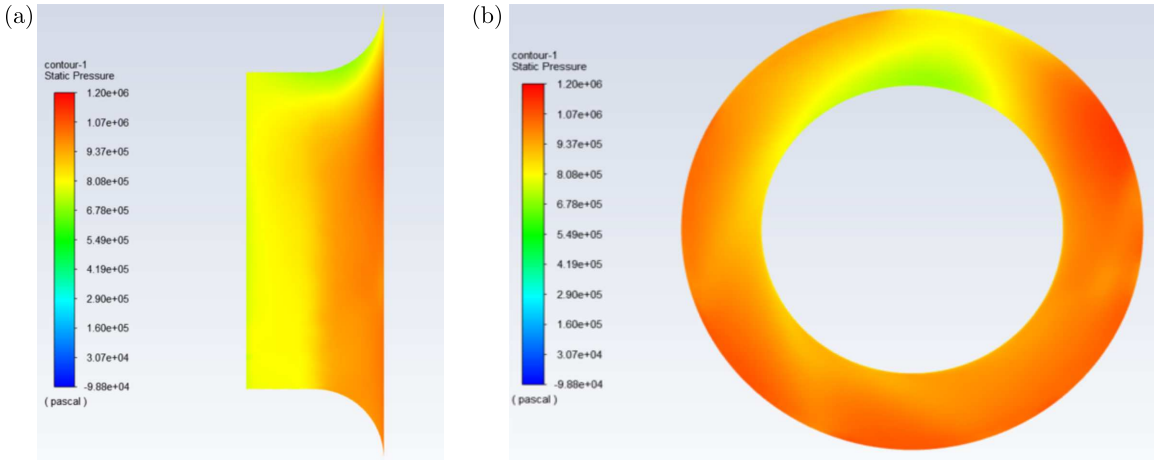

Fig. 12. Distribution cloud of pressure on the inner wall of the pump

3.3.6. Outlet analysis

Figure 13 shows the distribution of the efflux pump outlet pressure. The centrifugal rotation and backflow at the discharge outlet cause backflow near the bottom of the pump cavity. As a result, the bottom has a relatively low flow rate due to the impact of speed and pressure, while the centrifugal force at the top is relatively high, resulting in higher kinetic energy and higher total pressure at the top than at the bottom (Archard, 1953). The outlet pressure was calculated to be 1.3 MPa according to the surface average. The backflow at the impeller outlet is due to the combined effect of non-uniform fluid flows at the outlet and turbulent flows in the volute. The absolute speed of a portion of the fluid is greater than the flow rate in the volute, so this part of the fluid will hit the fluid in the volute with a relatively high kinetic energy. This fluid will be subjected to secondary work in the impeller and will consume more energy, while the flow rate of the rest of the fluid will be lower and will be pressed back into the impeller. Thus, a severe backflow may induce pump vibrations and lead to low pump efficiency.

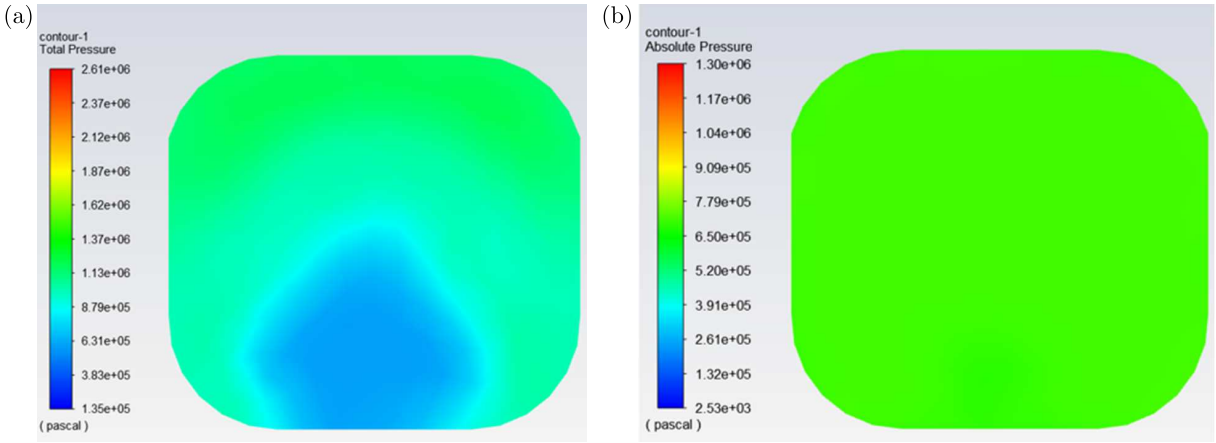

Fig. 13. Distribution cloud of outlet pressure of the output pump

3.3.7. Analysis of the pump shell

Figure 14 shows the distribution of pressure on the pump shell. The center of the pump shell is influenced by the centrifugal lifting force, cavity volume and outlet diameter. The pressure at the center is significantly higher than the suction inlets on both sides, and the pressure decreases

symmetrically along the center surface under the influence of the pump impeller, eventually dropping down to the inlet suction pressure (Chen *et al.*, 2017). The fluid flows in from the inlet negative pressure zone (pressure is relatively low) and flows out of the pump cavity along the tangential direction after the work done by the impeller. Figures 15 and 16 show the cross-section of the shell.

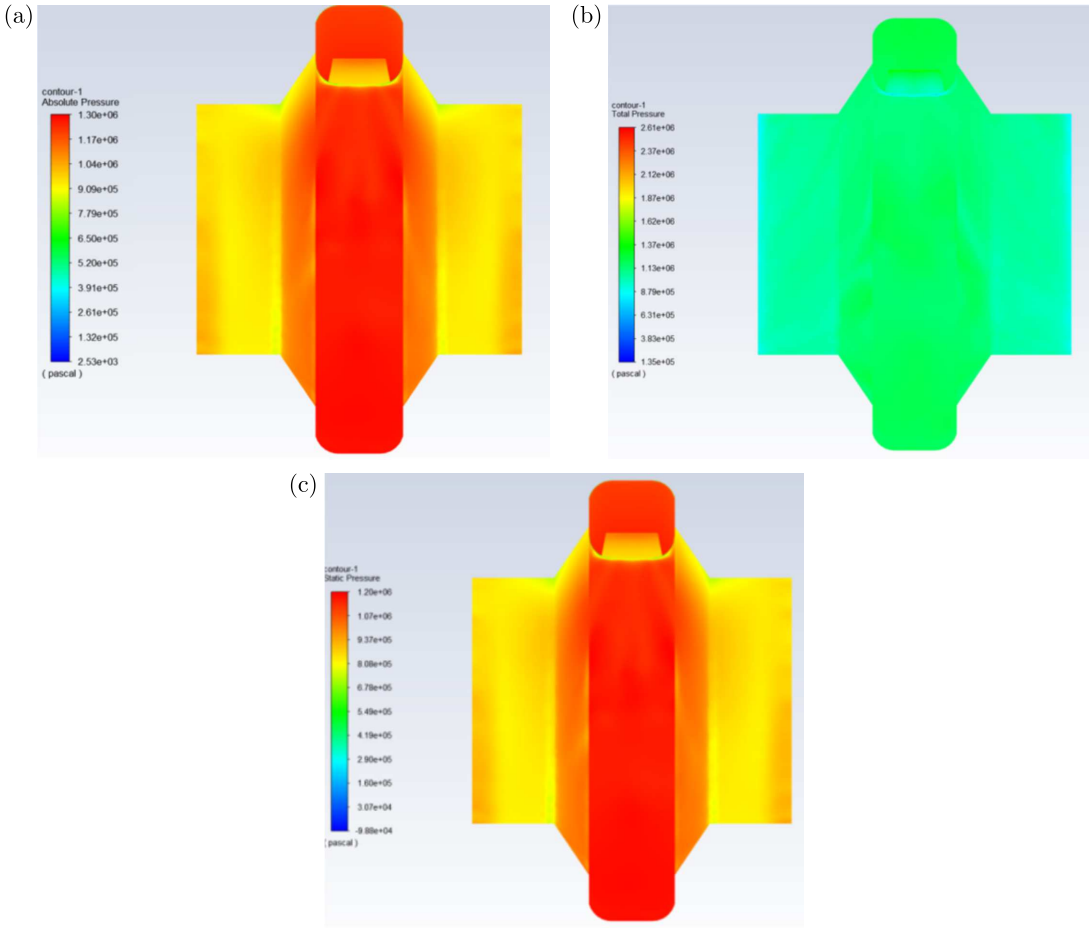

Fig. 14. Distribution cloud of pressure on the pump shell: (a) absolute pressure, (b) total pressure, (c) static pressure

After the centrifugal pump is started, the pump shaft will drive the impeller to facilitate a high-speed rotational movement, forcing the pre-filled fluid between the blades to rotate. Under the action of the inertial centrifugal force, the fluid moves radially from the center of the impeller to the outer circumference. In the process of flowing through the impeller, the fluid will gain energy, resulting in an increased static pressure energy as well as an increased flow rate. When the fluid flows out of the impeller into the pump shell, the flow rate decelerates with a gradual expansion of the flow runner in the shell. In this process, a part of the kinetic energy is converted into static pressure energy, and finally, the fluid flows into the discharge pipe along the tangential direction. While the fluid is thrown from the center of the impeller to the periphery, a low-pressure zone will be formed in the center of the impeller, and the fluid is sucked into the center of the impeller under the action of the total potential energy difference between the liquid surface in the storage tank and the center of the impeller. Depending on continuous operation of the impeller, the liquid will be continuously sucked and discharged. The mechanical energy absorbed by the liquid in the centrifugal pump may be observed in the form of an increase of static pressure energy (Blais *et al.*, 2016; Li *et al.*, 2019).

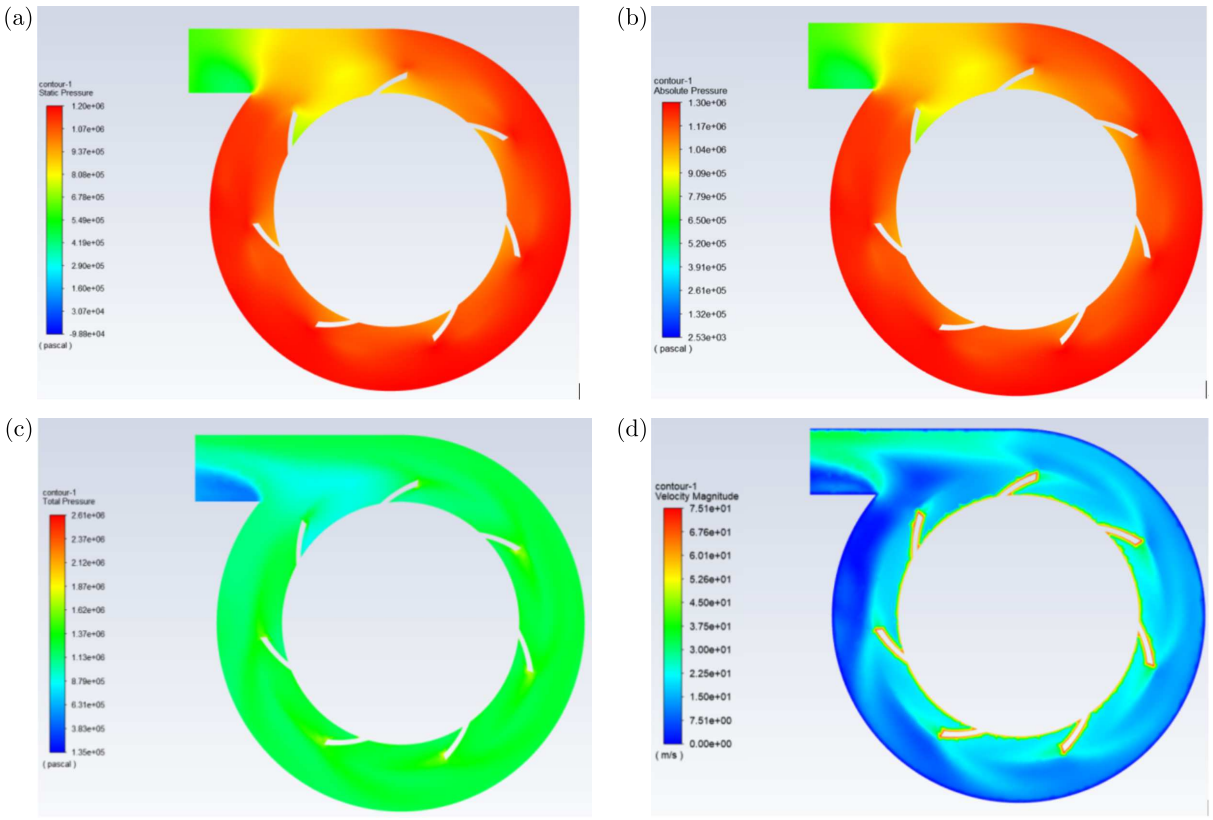

Fig. 15. Vertical center cross-section of the pump shell: (a) distribution of static pressure, (b) distribution of total pressure (difference between the pressure and the static pressure is one atmosphere), (c) total pressure, (d) speed vectorgraph

Based on the results of the simulation analysis of pressure variation, the following operational verification parameters were obtained (Table 2). The results indicated that when the speed and flow rate of the efflux pump was 2300-2550 r/min and 325-335 m^3/h, the maximum vibration value was less than 1.3 mm/s, respectively.

Table 2. 1 pump verification parameters under actual working conditions (high-pressure end)

1 efflux pump [r/min]	Output volume [m^3/h]	Axial vibration [mm]
2519	331	0.68
2575	334	0.91
2325	332	1.05
2475	333	1.03
2525	331	1.08
2550	354	1.18
2450	355	1.1
2400	356	1.3

4. Conclusions

Based on the results of the simulation analysis of pressure variation, the following operational verification parameters were obtained.

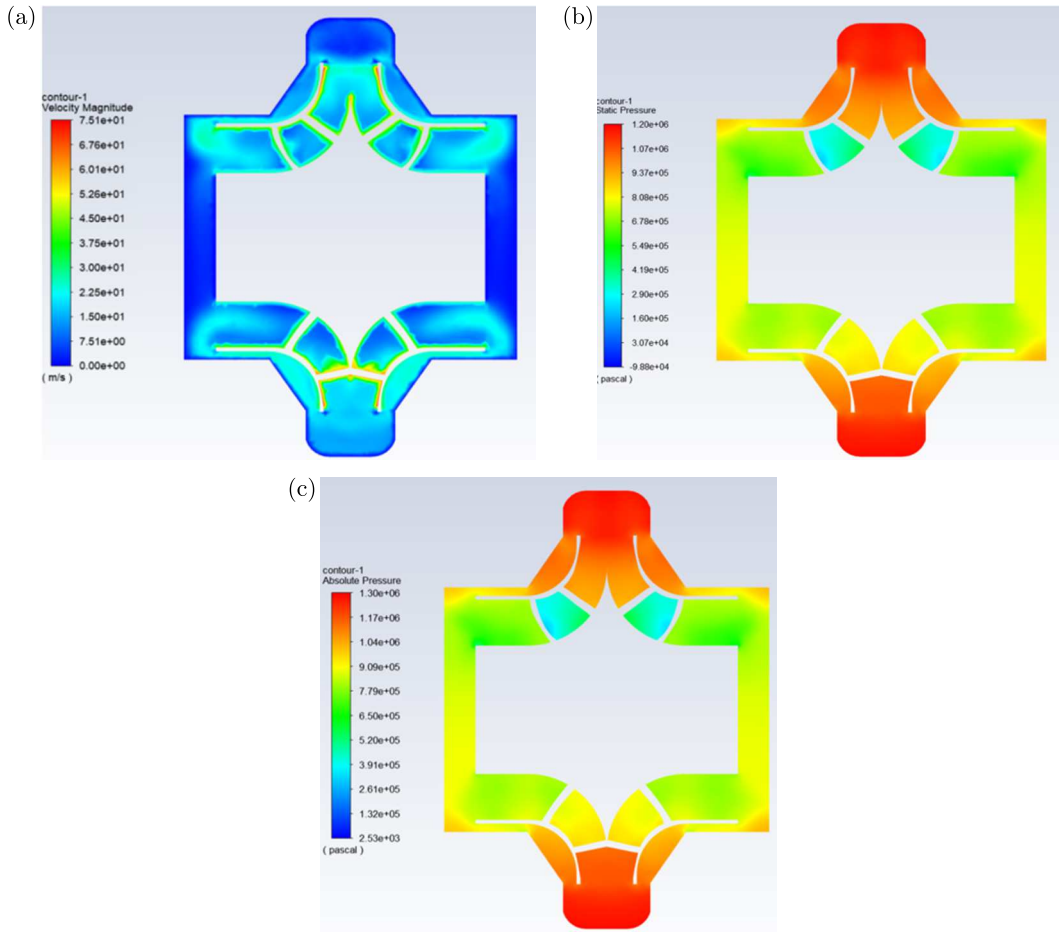

Fig. 16. Horizontal center cross-section of the pump shell: (a) speed vectorgraph, (b) static pressure, (c) absolute pressure

In summary, the pump axial vibration was minimized down to 0.68 mm/s, and the speed and output volume of 1 efflux pump were 2519 r/min and 331 m^3/h, respectively. The abnormal vibrations of the efflux pump during operation were investigated by kinetic simulation of the flow fields in the efflux pump using Ansys. A rational speed and flow rate range through parameter verification was proposed to guide the current production. The results indicated that when the speed and flow rate of the efflux pump was 2500-2550 r/min and 325-335 m^3/h, respectively, the vibrations of the efflux pump could be significantly decreased. The vibration value was reduced to 1.3 mm/s, which is 85.6% lower than the original instantaneous needle movement (9 mm/s) and less than 4.5 mm/s allowable for pump vibration. The normal production can be guaranteed.

Acknowledgment

The research was supported by Shaanxi Natural Science Basic Research Program (2022JM-150).

References

1. Archard J.F., 1953, Contact and rubbing of flat surfaces, *Journal of Applied Physics*, **24**, 8, 981-988
2. Barrio R., Fernández J., Blanco E., Parrondo J., 2011, Estimation of radial load in centrifugal pumps using computational fluid dynamics, *European Journal of Mechanics – B/Fluids*, **30**, 3, 316-324

3. Benra F.K., Dohmen H.J., 1966, Investigation on the time-variant flow in a single-blade centrifugal pump, *Louisiana History the Journal of the Louisiana Historical Association*, **7**, 3, 207-220

4. Blais B., Lassaigne M., Goniva C., Fradette L., Bertrand F., 2016, Development of an unresolved CFD DEM model for the flow of viscous suspensions and its application to solid-liquid mixing, *Journal of Computational Physics*, **318**, 201-221

5. Boehning F., Timms D.L., Amaral F., Oliveira L., Graefe R., Hsu P.-L., Schmitz-Rode T., Steinseifer U., 2011, Evaluation of hydraulic radial forces on the impeler by the volute in a centrifugal rotary blood pump, *Artificial Organs*, **35**, 8, 818-825

6. Chen G.M., Schott D.L., Lodewijks G., 2017, Sensitivity analysis of DEM prediction for sliding wear by single iron ore particle, *Engineering Computations*, **34**, 6, 2031-2053

7. Chen J.Q., Yu J.C., Liu M.L., 2014, *Ansys Fluent Technical Foundation and Engineering Application* (in Chinese), Beijing, China Petrochemical Press, 11-20

8. Chu K.W., Wang B., Yu A.B., Vince A., 2009, CFD-DEM modelling of multiphase flow in dense medium cyclones, *Powder Technology*, **193**, 3, 235-247

9. Han Z.Z., Wang J., Lan X.P., 2004, *Example and Application of Fluid Engineering Simulation*, Beijing: Beijing Institute of Technology Press, 15-60

10. Li Y., Liu S., Hu X., 2019, Research on rotating speed's influence on performance of Deep-Sea lifting motor pump based on DEM CFD, *Marine Georesources and Geotechnology*, **37**, 8, 979-988

11. Majidi K., 2005, Numerical study of un-steady flow in a centrifugal pump, *Journal of Turbomachinery*, **127**, 2, 363-371

12. Mele J., Guzzomi A., Pan J., 2014, Correlation of centrifugal pump vibration to unsteady flow under variable motor speed, *Mechanics and Industry*, **15**, 6, 525-534

13. Shen Z.Z., 2007, *Analysis and Numerical Simulation of Liquid-Solid Two-Phase Flow in Radial Impeller* (in Chinese), Changsha University of Technology, Changsha, 23-40

14. Wang F.J., 2004, *Computational Fluid Dynamics Analysis*, Beijing: Tsinghua University Press, 23-50

15. Wang T.T., Zhi J.C., Yang J.R., Xie R.Z., Yu L.M., Cui N.B., 2022, Numerical simulation of flow field and wear in centrifugal pump based on CFD-DEM, *Journal of Hunan Agricultural University (Natural Sciences)*, **48**, 2, 235-241

16. Yu Y., 2008, *Fluent Introduction and Advanced Tutorial* (in Chinese), Beijing Institute of Technology Press, 25-60

17. Zhang J.F., 2007, *Study on Numerical Prediction and Design Method of Full Flow Field of Centrifugal Pump with Splitter Blades*, Jiangsu: Jiangsu University, 100-152

18. Zhang K.W., 2001, *Principles of Fluid Mechanics*, China Machine Press, 125-160

19. Zhao Q.S., Li C.H., Wang B., 2005, Three-dimensional modeling design for centrifugal spiral casing based on Pro/E (in Chinese), *Journal of Shenyang Agricultural University*, **36**, 2, 241-243

20. Zhu Z.C., 2008, *Theory and Design Application of Low Specific Speed High Speed Centrifugal Pump*, Beijing: China Machine Press, 60-100

Manuscript received July 6, 2022; accepted for print October 3, 2022

JOURNAL OF THEORETICAL AND APPLIED MECHANICS
61, 1, pp. 37-47, Warsaw 2023
https://doi.org/10.15632/jtam-pl/157556

STUDY ON THE STRESS INTENSITY FACTOR OF A COMPACT SPECIMEN UNDER THE PRE-COMPRESSED LOAD CONDITION

Dongquan Wu, Zixiang Liu, Dinghe Li

Sino-European Institute of Aviation Engineering, Civil Aviation University of China, Tianjin, China

Corresponding author Dongquan Wu, e-mail: dqwu@cauc.edu.cn

Zhiqiang Zhang

Aviation Engineering Institute, Civil Aviation University of China, Tianjin, China

Jianguo Chen

The 18th Research Institute of China Electronics Technology Group Corporation, Tianjin, China

Structural components are often operated under combined stress conditions (primary and secondary stresses), but the stress levels generated by residual stress (or secondary stress) is hardly ever evaluated. Hence, stress intensity factors at the crack tips of a compact tension (CT) specimen under a pre-compressed load condition are analyzed using the finite element method. Then, the average residual stress intensity factor is calculated and analyzed. As the crack length a_0/W increases, the average residual stresses σ_{ave}/σ_0 grows under the same pre-compression load. σ_{ave}/σ_0 increases rapidly at a low range of the pre-compression load but tends to a constant in a high range of the load. The distribution of the average residual stress intensity factors K_{ave} and σ_{ave}/σ_0 of the CT specimen with same crack length under different pre-compression loads have the same tendency. Additionally, the distribution of K_{ave} and K_{FEM} under different pre-compression loads are also similar. Nevertheless, K_{ave} estimated by the average residual stress is too conservative and not accurate, and the method is complex, which depends on the analysis of simulation. Therefore, a simple method for calculating Mode I stress intensity factor K for this model is presented. A group of examples is presented to verify the accuracy of the method.

Keywords: pre-compressed load, residual stress, CT specimen, stress intensity factor, finite element method

1. Introduction

The stress intensity factor (SIF) K is used to describe stress intensity or the stress state generated by a remote load or residual stresses near the crack tip in studies related to fracture mechanics (Anderson, 2005). It is usually determined for homogeneous, linear elastic materials and materials that exhibit small-scale yielding at the crack tip. The magnitude of K depends on sample geometry, size and location of the crack, magnitude and model distribution of loads acting on the material. Since the introduction of the SIF (Tada *et al.*, 2000), there have been various investigations regarding K under the primary load condition. Three modes of the SIF under different types of loads have been discussed (Rooke and Percy, 1976), and Mode I is the most common load type encountered in engineering design. Moreover, several of examples of SIFs are investigated in detail (Rooke and Percy, 1976; Sih *et al.*, 1974; Sneddon, 1946; Isida, 1966; Sih and Macdonald, 1974; Erdogan, 1962), such as in infinite plate with uniform uniaxial stress (Rooke and Percy, 1976) and infinite plate (Sneddon, 1946), etc. The American Society for Testing and Materials (ASTM) has proposed fracture toughness testing standard for different specimen modes (ASTM, 2013). The specific calculation equations of Mode I SIF for different specimens are listed in Ref. (Bower, 2009), especially the compact tension (CT) specimen, which

is a common type of specimen. However, the aforementioned studies are conducted considering the primary load, but in-service components invariably develop residual stress introduced during fabrication or service processes (Chen *et al.*, 2013) (usually by thermal gradients or non-uniform plastic deformation) which may cause fracture failure. Hence, it is significant to propose computation equations to predict the SIF under the residual stress condition. Webster *et al.* (2011) obtained K of the residual stress by estimating residual stress distributions. Zhao *et al.* (2013) used this method to analyse K of the residual stress. However, the SIF is overestimated due to the residual stress field, which results in an excessively pessimistic defect assessment. To analyze the effect of residual stress on the SIF, a simple and repeatable technique of obtaining the residual stress is the pre-compression on a specific specimen (CT specimen) (Chen *et al.*, 2013; Zhao *et al.*, 2013; Xu *et al.*, 2016; Song *et al.*, 2015a,b; Shirahatti *et al.*, 2014). A tensile residual stress field in the vicinity of the crack tip can be introduced by loading a pre-compressed specimen beyond the yield strength and then unloading it (Zhao *et al.*, 2013; O'Dowd *et al.*, 2005; Turski *et al.*, 2008). Therefore, in this study, the technique of pre-compressing the CT specimen is used to investigate the effect of residual stress on the SIF. It is significant to make an appropriate prediction and derive computation equations of the SIF resulting from the residual stress.

In this study, the finite-element (FE) method was carried out to assess the effects of local tensile residual stress on the SIF. The residual stress was generated by pre-compressing the CT specimen and then unloading it. The average residual stress intensity factor was calculated and analyzed. The law of change of the SIF varied with the pre-compression load, thickness and crack length of the pre-compressed CT specimen were concluded. An analysis with a series of original computation equations was proposed to predict the SIF of the CT specimen with pre-compressed residual stress. Finally, the suitability and accuracy of the analytical method were studied and validated by comparing them with a range of examples.

2. Finite element models and material properties

2.1. Finite element models

In this study, a three-dimensional finite element (3D FE) model of the CT specimen is employed. A tensile residual stress field in the vicinity of the crack tip can be introduced by loading the pre-compressed specimen beyond the yield strength and then unloading it. This technique was previously developed by Zhao *et al.* (2013), O'Dowd *et al.* (2005), Turski *et al.* (2008).

Figure 1 shows geometry of a specified CT specimen. Thickness, width, crack depth and notch root radius of the specimen respectively are $B = 10\,\text{mm}$, $W = 20\,\text{mm}$, $a_0/W = 0.5$ and $r = 0.20\,\text{mm}$, respectively. Only a half of the symmetric CT geometry is modelled. And the loading process is achieved by the movement of an analytical rigid shell, which is used as the punch tool. The rigid shell is constrained in the horizontal and rotational directions but free to move in the vertical direction during the loading process. The crack is inserted at the end of the notch tip after the pre-compression. Hard contact of contact control, finite sliding of sliding formulation and surface to surface of the discretization method are used in the pre-compression process. Firstly, the residual stress filed could be simulated by using the elastic-plastic finite element model, then the residual stress intensity factor can be obtained when the residual stress filed is loaded in the elastic finite element model.

Figure 2a depicts the FE mesh for the CT specimen, and the local fine mesh distribution around the crack tip is shown in Fig. 2b. The smallest element size is $15\,\mu\text{m}$, which is approximately one third of the average grain size of P92 steel (which is about $40\,\mu\text{m}$ to $50\,\mu\text{m}$). The model in Fig. 2 contains 8802 eight-node linear grid reduced integration elements (C3D8R) and 11060 nodes. All analyses are carried out using ABAQUS code (Hibbitt *et al.*, 2014).

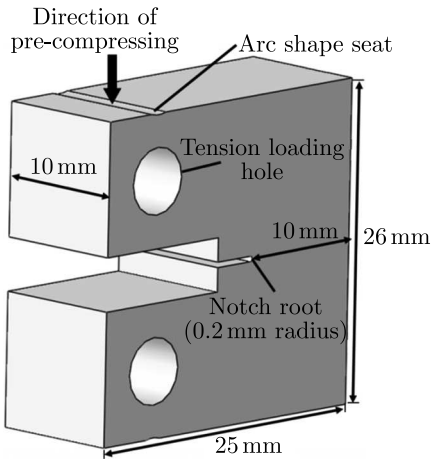

Fig. 1. Geometry of the notched compact tension (CT) specimen

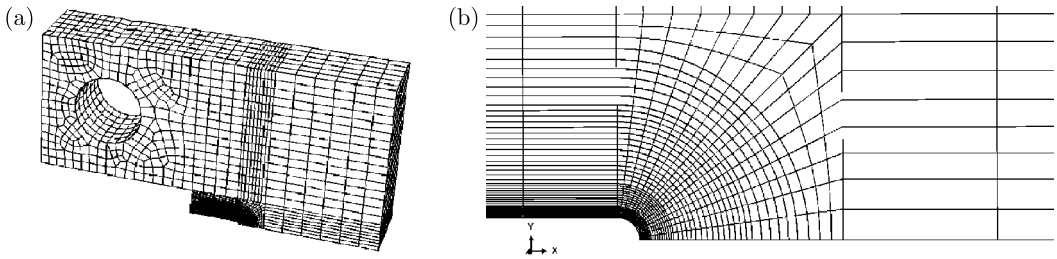

Fig. 2. Finite element model of the notched CT specimen: (a) meshes in the whole model, (b) local fine meshes around the crack tip

Different thicknesses of CT specimen, i.e. 10, 15, 25 and 30 mm, and different crack depth ratios a_0/W (a_0 and W are the initial crack depth and width, respectively) are employed. The specific geometric parameters of CT specimens are listed in Table 1.

Table 1. Geometric parameters of CT specimens used in the FEM

Specimen thickness B [mm]	Crack depth a_0/W	Pre-compressed load P [N]
10 15 20 25 30	0.3	200-20000
10 15 20 25 30	0.4	200-20000
10 15 20 25 30	0.5	200-20000
10 15 20 25 30	0.6	200-20000
10 15 20 25 30	0.7	200-20000

2.2. Material properties

The isotropic hardening model and mechanical properties of P92 steel are used. The power--hardening stress-strain relation (Song *et al.*, 2015a) at room temperature is expressed as follows

$$\sigma = \begin{cases} E\varepsilon & \sigma \leqslant \sigma_0 \\ K_P \varepsilon^{n_p} & \sigma > \sigma_0 \end{cases} \tag{B.1}$$

where E is Young's modulus of 206000 MPa. n_p is strain-hardening exponent of 0.155, σ_0 is the yeilding stress of 320 MPa, and K_p is the strain-hardening coefficient of 861 MPa (Zhao *et al.*, 2012).

3. FEM results and a method of average stress intensity factor predictions

Webster *et al.* (2011) and Zhao *et al.* (2013) obtained an average stress intensity factor K_{ave} of the residual stress by estimating average residual stress distributions. The average stress intensity factor K_{ave} is calculated by

$$K_{ave} = \sigma_{ave}\sqrt{2\pi r_{ave}} \tag{B.1}$$

where σ_{ave} is the average residual stress ahead of the crack tip, r_{ave} the average distance of residual stress distributions ahead of the crack tip.

Figure 3 shows the residual stress distribution ahead of the crack tip of the CT specimen with thickness $B = 10\,\text{mm}$, crack length $a_0/W = 0.3$, and pre-compression load $P = 5000\,\text{N}$. The residual stress σ_{22} is normalised by σ_0, and we could obtain the average residual stress intensity factor $K_{ave} = 224.22\,\text{MPa·mm}^{-1/2}$. Similarly, we could calculate K_{ave} values under different load levels and specimen sizes.

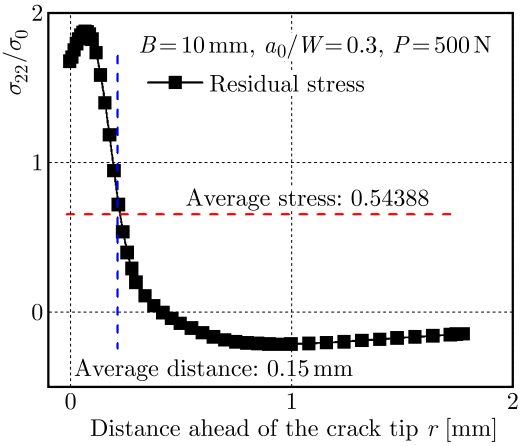

Fig. 3. The distribution of residual stress and average stress ahead of the crack tip

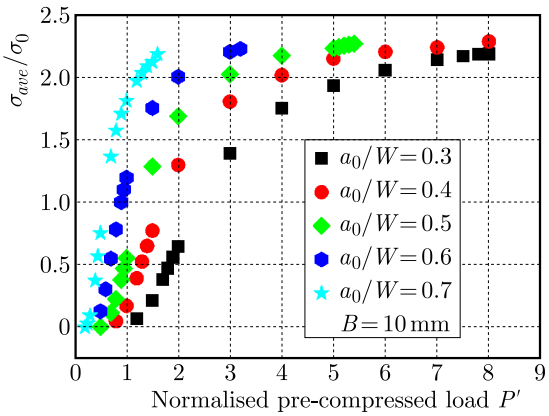

Fig. 4. Comparision of the average stress distribution under different crack depth a_0/W, specimen thickness $B = 10\,\text{mm}$

Figure 4 depicts distribution of the average residual stresses σ_{ave}/σ_0 of the CT specimen with thickness $B = 10\,\text{mm}$ and different crack length under different pre-compression loads. The pre-compression load P is normalised as $P' = P\,\text{N}$. It is clearly seen that as the crack length a_0/W increases, the average residual stresses σ_{ave}/σ_0 grows under the same pre-compression load. In addition, σ_{ave}/σ_0 increases rapidly at a low range of the pre-compression load but tends to a constant in a high range of the load.

Figure 5 compares the simulated stress intensity factors K_{FEM} (which are directly obtained by using the history output variables from FE results) and the average residual stress intensity factors K_{ave} of the CT specimen with thickness $B = 10\,\text{mm}$ and different crack length under the different pre-compression loads. The distribution of K_{ave} and σ_{ave}/σ_0 with the same crack length under different pre-compression loads have the same tendency. Additionally, the distribution of K_{ave} and K_{FEM} for different pre-compression loads are also similar. It is indicated that the average stress intensity factor K_{ave} of the residual stress estimated by the average residual stress could underestimate the residual stress intensity factor, but it is much too conservative and not accurate, which may endanger in-service components. Moreover, the prediction method of the residual stress intensity factor is complex and it needs analysis of simulation. Therefore, a simple and accurate method is needed to predict the residual stress intensity factor.

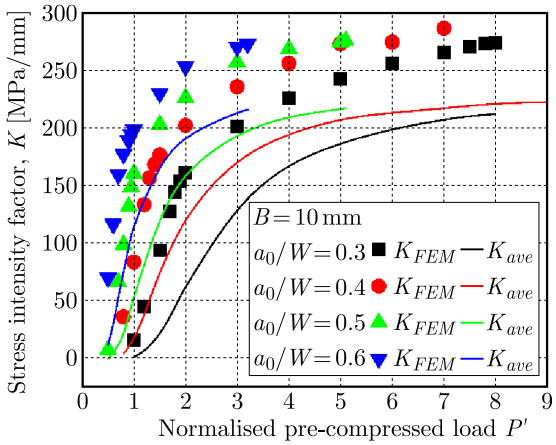

Fig. 5. Comparision of stress intensity factors between the FEM solutions and the results calculated by the average stresses

4. Methodology

The results of the normalised SIF under different specimen thickness B and different crack depth a_0/W are listed in Fig. 6. To simplify the analysis, the parameters are normalised as follows: $K' = K$ [MPa·m$^{-1/2}$], and $B' = B$ [mm]. It is found from Fig. 6 that K' increases rapidly in the low range of P' and smoothly increases in the high range of P'. The change rules of the K'-P' line may be related to the change rules of the residual stress, because the SIF is a vital term in the stress distribution near the crack tip (Tada, 2000). Moreover, for the same specimen, thickness B, K' line moves left and upward as the crack depth a_0/W increases. In addition, for the same crack depth a_0/W, the K'-P' line moves right and downward as the specimen thickness B increases.

By comparing several types of function expressions, a perfect relationship between K' and P' is approximated to a complex exponential function (Fig. 6), which can be expressed by the following equation

$$K' = a\mathrm{e}^{bP'} + c\mathrm{e}^{dP'} \tag{B.1}$$

K' is the normalised SIF ($K' = K$ [MPa·m$^{-1/2}$]) and P' is the normalised pre-compressed load ($P' = P$ [N]). Additionally, a, b, c and d are parameters related to the normalised specimen thickness B' ($B' = B$ [mm]) and crack depth a_0/W. All parameters for different geometrical conditions are obtained by fitting the curves, as seen in Fig. 6.

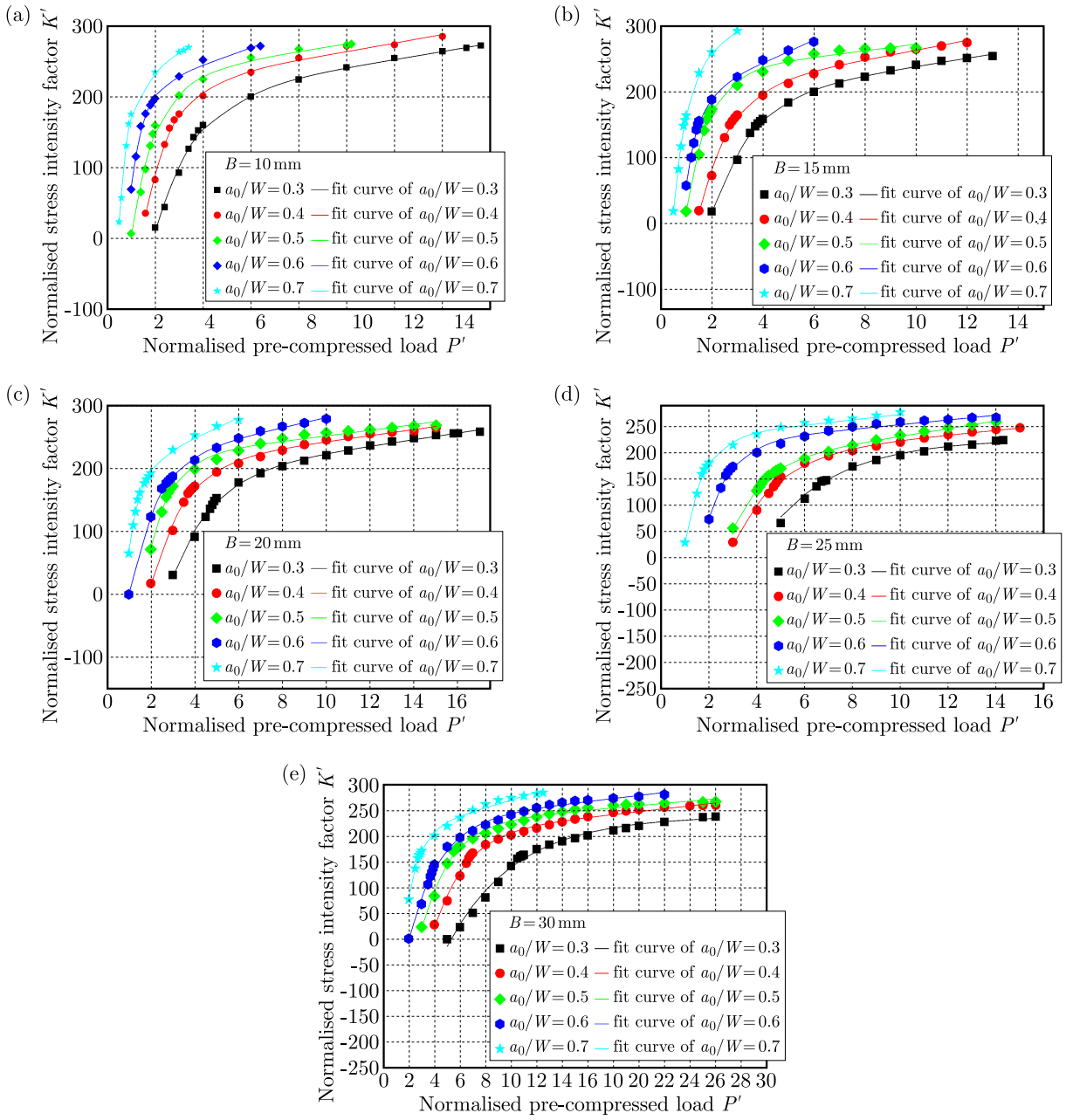

Fig. 6. Comparision of K' solutions under different crack depth a_0/W, (a) specimen thickness $B = 10\,\text{mm}$, (b) $B = 15\,\text{mm}$, (c) $B = 20\,\text{mm}$, (d) $B = 25\,\text{mm}$, (e) $B = 30\,\text{mm}$

Figure 7 shows the fitted curves of parameters (a, b, c and d) and the normalised specimen thickness B' under different crack depths a_0/W. It is obvious that a-B' and c-B' curves are linear, whereas b-B' and d-B' curves are approximately quadratic. The fitted curves can be expressed as follows

$$\begin{aligned} a &= a_1 + a_2 B' \qquad & b &= b_1 + b_2 B + b_3 B'^2 \\ c &= c_1 + c_2 B' \qquad & d &= d_1 + d_2 B + d_3 B'^2 \end{aligned} \tag{B.2}$$

It is indicated that as the crack depth increases, a-B' and b-B' curves move upward but c-B' and d-B' curves move downward. The variation trend in the fitted curves is constantly related to the crack depth a_0/W. Therefore, it is important to analyse the relationship between the parameters a_1, a_2, b_1, b_2, b_3, c_1, c_2, d_1, d_2 and d_3 and a_0/W.

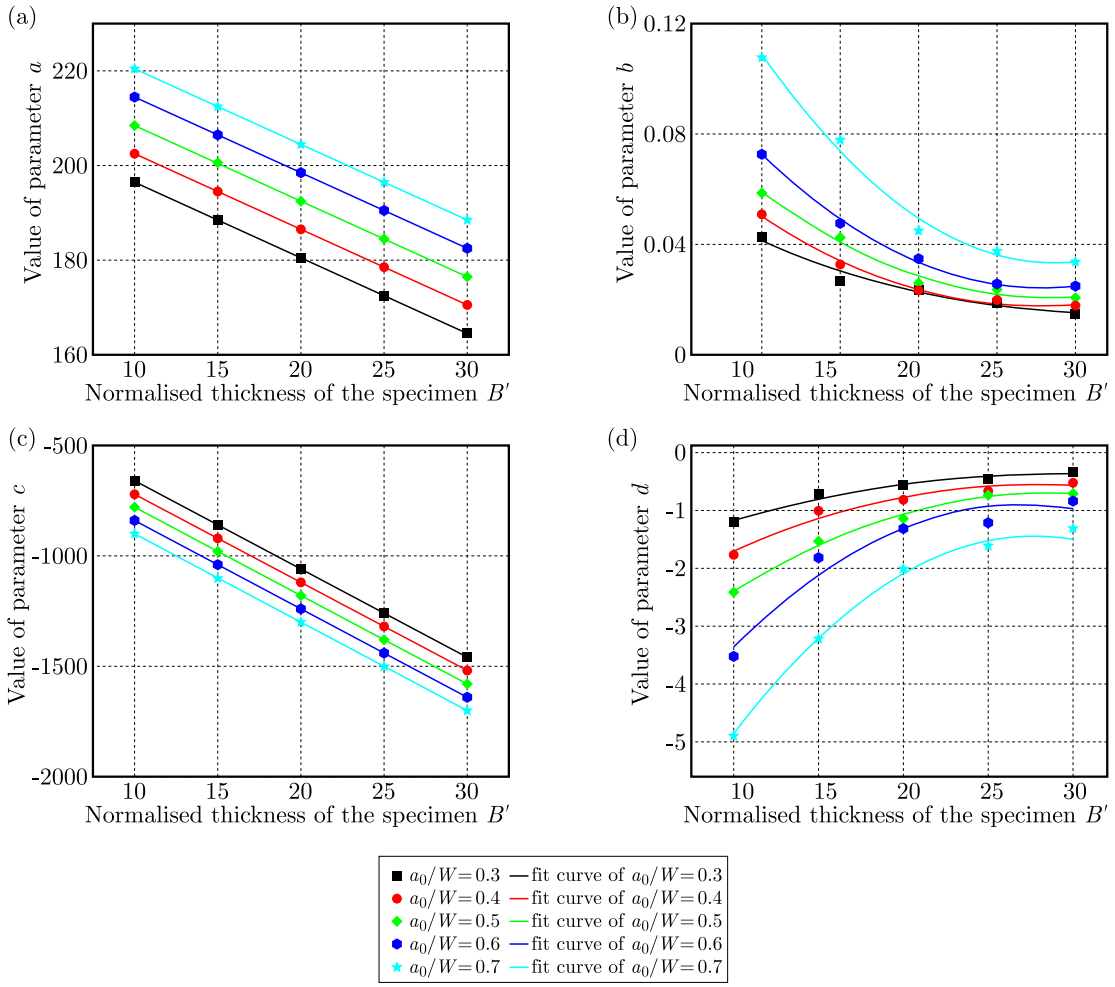

Fig. 7. Fitted curve of parameters and normalised specimen thickness B', (a) parameters a and B', (b) b and B', (c) c and B', (d) d and B'

Figure 8 shows the fitted curve of parameters a_1, a_2, b_1, b_2, b_3, c_1, c_2, d_1, d_2, d_3 and the crack depth a_0/W. It can be concluded that a_1-B' and c_1-B' curves show a good linear relationship, a_2-B' and c_2-B' curves are horizontal, and the other curves are approximately quadratic. The fitted curves can be expressed as follows

$$
\begin{aligned}
&a_1 = a_{11} + a_{12}\frac{a_0}{W} \qquad a_2 = -1.6 \qquad b_1 = b_{11} + b_{12}\frac{a_0}{W} + b_{13}\frac{a_0}{W}^2 \\
&b_2 = b_{21} + b_{22}\frac{a_0}{W} + b_{23}\frac{a_0}{W}^2 \qquad b_3 = b_{31} + b_{32}\frac{a_0}{W} + b_{33}\frac{a_0}{W}^2 \\
&c_1 = c_{11} + c_{12}\frac{a_0}{W} \qquad c_2 = -40 \qquad d_1 = d_{11} + d_{12}\frac{a_0}{W} + d_{13}\frac{a_0}{W}^2 \\
&d_2 = d_{21} + d_{22}\frac{a_0}{W} + d_{23}\frac{a_0}{W}^2 \qquad d_3 = d_{31} + d_{32}\frac{a_0}{W} + d_{33}\frac{a_0}{W}^2
\end{aligned}
\tag{B.3}
$$

All the coefficients a_1, a_2, b_1, b_2, b_3, c_1, c_2, d_1, d_2 and d_3 obtained by fitting the curves shown in Fig. 8 are listed in Table 2.

By substituting the coefficients into Eqs. (4.3) and substituting these equations into Eqs. (4.2), we could obtain a general equation to predict the SIF of the CT specimen under the

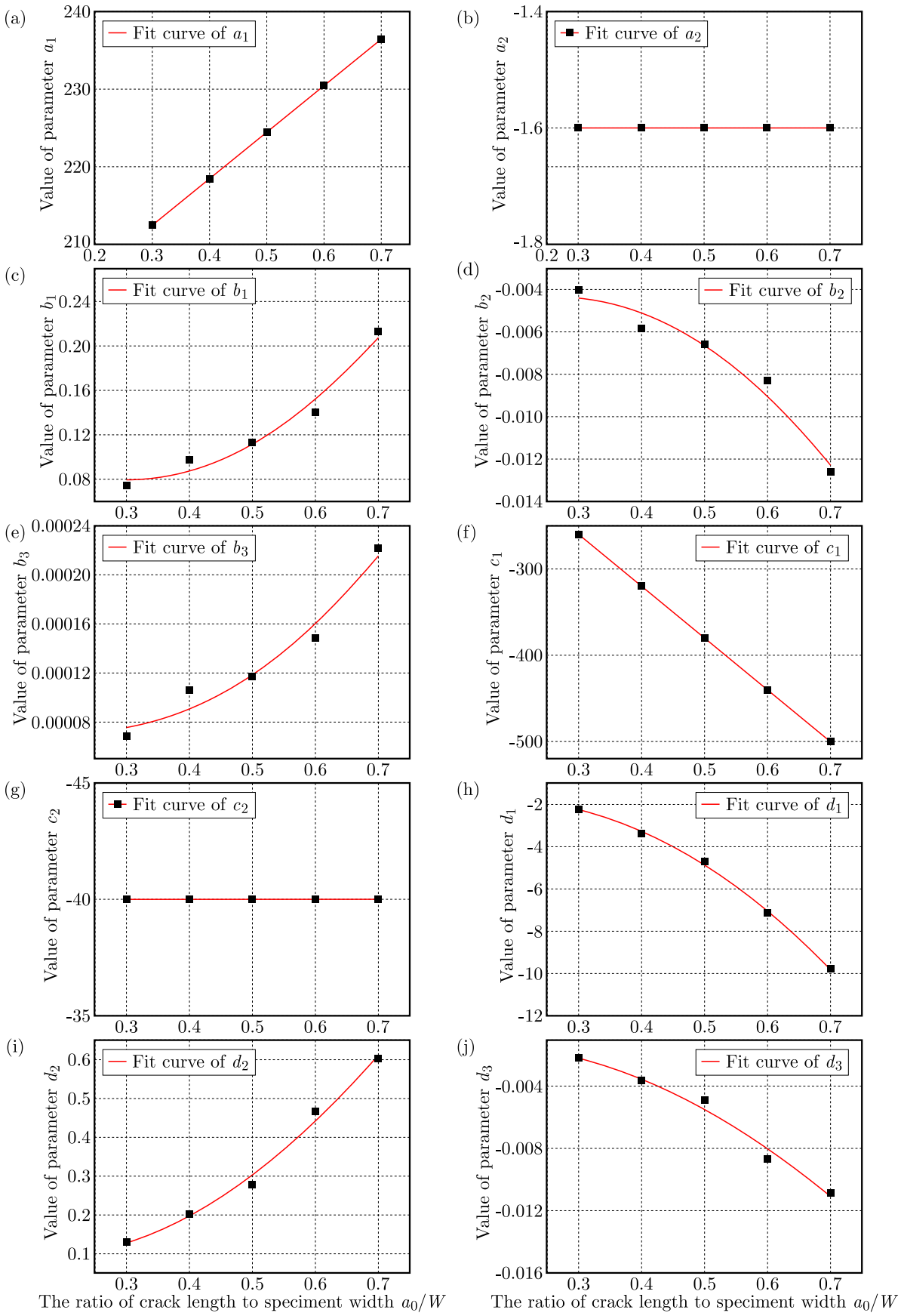

Fig. 8. Fitted curve of coefficients and normalised crack depth a_0/W: (a) a_1, (b) a_2, (c) b_1, (d) b_2, (e) b_3, (f) c_1, (g) c_2, (h) d_1, (i) d_2, (j) d_3

Table 2. Coefficients of the fitted curves in Fig. 8

a_{11}	a_{12}	a_2	b_{11}	b_{12}	b_{13}
194.5	60	−1.6	0.15075	−0.47518	0.79486
b_{21}	b_{22}	b_{23}	b_{31}	b_{32}	b_{33}
−0.0075	0.02322	−0.0429	0.00011	−0.00031	0.00066
c_{11}	c_{12}	c_2	d_{11}	d_{12}	d_{13}
−80	−600	−40	−2.831	10.815	−29.73
d_{21}	d_{22}	d_{23}	d_{31}	d_{32}	d_{33}
0.11576	−0.467	1.67914	−0.0015	0.00658	−0.0289

pre-compressed condition wherein only the following two variables are involved: specimen thickness B and crack depth a_0/W. The rearranged functions can be expressed as follows

$$\begin{aligned} K' = &\Big(a_{11} + a_{12}\frac{a_0}{W} + a_2 B'\Big)\exp\Big\{\Big[b_{11} + b_{12}\frac{a_0}{W} + b_{13}\Big(\frac{a_0}{W}\Big)^2 \\ &+ \Big(b_{21} + b_{22}\frac{a_0}{W} + b_{23}\Big(\frac{a_0}{W}\Big)^2\Big)B + \Big(b_{31} + b_{32}\frac{a_0}{W} + b_{33}\Big(\frac{a_0}{W}\Big)^2\Big)B'^2\Big]P'\Big\} \\ &+ \Big(c_{11} + c_{12}\frac{a_0}{W} + c_2 B'\Big)\exp\Big\{\Big[d_{11} + d_{12}\frac{a_0}{W} + d_{13}\Big(\frac{a_0}{W}\Big)^2 \\ &+ \Big(d_{21} + d_{22}\frac{a_0}{W} + d_{23}\Big(\frac{a_0}{W}\Big)^2\Big)B + \Big(d_{31} + d_{32}\frac{a_0}{W} + d_{33}\Big(\frac{a_0}{W}\Big)^2\Big)B'^2\Big]P'\Big\} \end{aligned} \tag{B.4}$$

5. Verification of the function

To validate the function, we compare the SIFs between the FE method results, the calculated solutions obtained by this function and the average residual stress intensity factors. The follwing two cases of CT specimens with different geometry are chosen for the study under the pre-compressed condition:

- Case 1: specimen thickness $B = 18\,\text{mm}$ and the crack depth $a_0/W = 0.35$;
- Case 2: specimen thickness $B = 28\,\text{mm}$ and the crack depth $a_0/W = 0.65$.

First, according to Eq. (4.4), we can obtain specific calculation equations for specimens of each geometry under the pre-compressed condition. After substituting different normalised pre-compressed loads P' into the equations, the data of the normalised SIF K' can be obtained.

It can be seen from Fig. 9 that the calculated solutions are a good fit to the FE solutions, and the function is more appropriate and larger than the average residual stress intensity factors. In conclusion, this approach is satisfactory and accurate in enabling the engineering estimates for fracture related problems.

6. Conclusions

The finite-element method is applied to assess the effects of local tensile residual stress on the stress intensity factor. A simple method for calculating Mode I stress intensity factor of residual stress is presented. The main results obtained are summarized as follows:

- As the crack length a_0/W increases, the average residual stresses σ_{ave}/σ_0 grows, under the same pre-compression load. σ_{ave}/σ_0 increases rapidly at the low range of the pre-compression load but tends to a constant value in the high range of load.

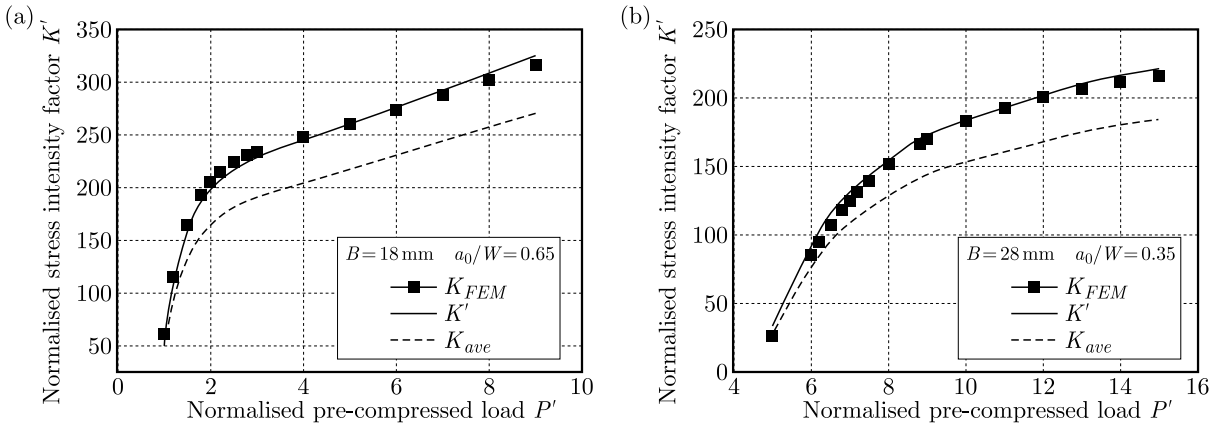

Fig. 9. Comparison of K' between the FE solutions, average results and calculated solutions: (a) specimen thickness $B = 18\,\mathrm{mm}$, crack depth $a_0/W = 0.35$, (b) $B = 28\,\mathrm{mm}$, $a_0/W = 0.65$

- The distributions of average residual stress intensity factors K_{ave} and σ_{ave}/σ_0 of the CT specimen with the same crack length under different pre-compression loads have the same tendency. Additionally, the distribution of K_{ave} and K_{FEM} under different pre-compression loads are also similar. Nevertheless, K_{ave} estimated by the average residual stress is too conservative and not accurate. The method is complex and needs analysis of simulation results.
- A simple method for calculating Mode I stress intensities for the CT specimen under the pre-compressed condition is proposed. The approach is very easy and simple, which consists of two variables only if the geometry is defined: specimen thickness B and the crack depth a_0/W. A comparison between the calculation and FE solutions suggests that the approach is satisfactory and accurate in estimating Mode I stress intensities for the CT specimen under the pre-compressed condition for engineering fracture related problems.

Acknowledgements

The author would like to acknowledge the support from the Fundamental Research Funds for the Central Universities (grant No. 3122021083).

References

1. Anderson T.L., 2005, *Fracture Mechanics: Fundamentals and Applications*, CRC Press
2. ASTM, 2013, Standard Test Method for Measurement of Creep Crack Growth Times and Rates in Metals, 27
3. Bower A.F., 2009, *Applied Mechanics of Solids*, CRC Press
4. Chen L.Y., Wang G.Z., Tan J.P., Xuan F.Z., Tu S.T., 2013a, Effects of residual stress on creep damage and crack initiation in notched CT specimens of a Cr-Mo-V steel, *Engineering Fracture Mechanics*, **97**, 80-91
5. Erdogan F., 1962, On the stress distribution in plates with collinear cuts under arbitrary loads, *Proceedings of the Fourth US National Congress of Applied Mechanics*, **1**, 547-574
6. Hibbitt, Karlsson & Sorensen, Inc, 2014, ABAQUS version 6.14
7. Isida M., 1966, Stress intensity factors for the tension of an eccentrically cracked strip, *ASME, Journal of Applied Mechanics*, **33**, 3, 674-675
8. Nikbin K.M., 2004, Justification for meso-scale modeling in quantifying constraint during creep crack growth, *Materials Science and Engineering: A*, **365**, 107-113

9. O'Dowd N.P., Nikbin K.M., Biglari F.R., 2005, Creep crack initiation in a weld steel: effects of residual stress, *Proceedings of 2005 ASME Pressure Vessels and Piping Division Conference*, Denver, Colorado, USA, 843-851
10. Rooke D.P., Percy D.J., 1976, *Compendium of Stress Intensity Factors*, HMSO Ministry of Defence, Procurement Executive
11. Shirahatti A.M., Hossain S., Smith D.J., 2014, The effect of combined applied and residual stress on creep crack initiation in stainless steel, *Procedia Engineering*, **86**, 669-676
12. Sih G.C., Macdonald B., 1974, Fracture mechanics applied to engineering problems-strain energy density fracture criterion, *Engineering Fracture Mechanics*, **6**, 2, 361-386
13. Sih G.C., Paris P.C., Erdogan F., 1974, Crack-tip stress intensity factors for the plane extension and plate bending problems, *Journal of Applied Mechanics*, **29**, 306-312
14. Sneddon I.N., 1946, The distribution of stress in the neighbourhood of a crack in an elastic solid, *Proceedings of the Royal Society A*, **187**, 1009, 229-260
15. Song X.M., Wang G.Z., Tu S.-T., Xuan F.Z., 2015a, Effects of residual stress on creep crack initiation and growth of Cr-Mo-V steel in cracked C(T) specimen, *Procedia Engineering*, **130**, 1770-1778
16. Song X.M., Wang G.Z., Xuan F.Z., Tu S.T., 2015b, Investigation of residual stress effects on creep crack initiation and growth using local out-of-plane compression, *Engineering Fracture Mechanics*, **149**, 45-57
17. Tada H., Paris P.C., Irwin G.R., 2000, *The Stress Analysis of Cracks Handbook*, American Society of Mechanical Engineers
18. Turski M., Bouchard P.J., Steuwer A., Withers P.J., 2008, Residual stress driven creep cracking in AISI Type 316 stainless steel, *Acta Materialia*, **56**, 3598-3612
19. Webster G.A., Davies C.M., Nikbin K.M., 2011, Prediction of creep crack growth in the presence of residual stress, *Materials at High Tempertures*, **28**, 3, 165-171
20. Xu M., Chen J., Lu H., Xu J., Yu C., Wei X., 2016, Effects of residual stress and grain boundary character on creep cracking in 2.25Cr-1.6W steel, *Materials Science and Engineering: A*, **659**, 188-197
21. Zhao L., Jing H., Xu L., An J., Xiao G., 2012, Numerical investigation of factors affecting creep damage accumulation in ASME P92 steel welded joint, *Materials Design*, **34**, 566-575
22. Zhao L., Jing H., Xu L., Han Y., Xiu J., 2013, Effect of residual stress on creep crack growth behavior in ASME P92 steel, *Engineering Fracture Mechanics*, **110**, 233-248

Manuscript received September 20, 2022; accepted for print October 10, 2022

JOURNAL OF THEORETICAL AND APPLIED MECHANICS
61, 1, pp. 49-63, Warsaw 2023
https://doi.org/10.15632/jtam-pl/157571

IMPACT OF MATERIAL NONLINEARITY OF DAM-FOUNDATION ROCK SYSTEM ON SEISMIC PERFORMANCE OF CONCRETE GRAVITY DAMS

Djamel Ouzandja
Laboratory of Materials and Mechanics of Structures (LMMS), Department of Civil Engineering, University of Msila, Algeria
e-mail: djamel.ouzandja@univ-msila.dz

Mokhtar Messaad
Laboratory of Hydraulic Developments and Environment LAHE, University of Biskra, Algeria
e-mail: mokhtar.messaad@univ-biskra.dz

Amina T. Berrabah
Department of Civil Engineering and Public Works, Faculty of Technology, University Belhadj Bouchaib, Ain Temouchent, Algeria
e-mail: a.taharberrabah@gmail.com

Mohamed Belhrizi
Consultant, Antony, France
e-mail: mohambel@free.fr

This paper shows the impact of material nonlinearity of a dam-foundation rock system on seismic performance of Oued Fodda concrete gravity dam, located at northwestern side of Algeria. For the purpose, a three-dimensional dam-foundation rock system finite element model is employed in analyses. The hydrodynamic interaction between reservoir water and dam-foundation system is implicitly taken into consideration by the Westergaard approach using surface finite elements added to dam-fluid and foundation-fluid interfaces. The concrete material model is used to present the cracking of dam concrete under a seismic load the using smeared crack approach based on the Willam and Warnke failure criterion. The materially nonlinear analysis for both dam concrete and foundation rock is performed using Drucker--Prager model. According to numerical results, tensile stresses and maximum strains reduce significantly in the materially nonlinear model. In addition, the cracking areas in the dam decrease also when material nonlinearity characteristics of the dam-foundation rock system is considered in analyses.

Keywords: concrete gravity dam, dynamic dam-foundation rock interaction, Drucker-Prager model, cracking, nonlinear earthquake analysis, finite element method

1. Introduction

The dynamic response analysis of concrete gravity (CG) dams is influenced by a number of factors; among them there is soil-structure interaction, fluid-structure interaction and material nonlinear performance of a dam-foundation rock system itself. Burman *et al.* (2008) studied the response of CG dams to seismic loading considering foundation rock nonlinearity. The results illustrated that nonlinear behavior of foundation rock affected the dam response. The influence of materially nonlinear properties of Sariyar gravity dam exposed to near-fault seismic movements was performed by Akköse and Şimeşk (2010). The study demonstrated that the concrete dam nonlinearity gave a significant impact on the dam-water-foundation system response. Burman *et al.* (2010) presented seismic analysis of a dam-foundation system considering the effect

of materially nonlinear foundation domain. The taking into account of the nonlinear material response of foundation rock generates higher displacements and stresses in the dam compared to the results extracted from linear analysis. Wang *et al.* (2015) used linear and nonlinear computation approaches to study seismic behavior of CG dams considering the effect of integrated duration. Ouzandja and Tiliouine (2015) investigated the effect of conditions of contact at the dam-foundation interface on seismic behavior of Oued Fodda CG dam employing linear and nonlinear analyses. Their results showed that nonlinear analysis led to lower responses. Yazdani and Alembagheri (2017) utilized material and geometric nonlinearities to study the seismic response of Pine Flat dam. Khazaei-Poul and Zerva (2018) conducted nonlinear seismic analyses of CG dams considering the influence of foundation rock.

In three-dimensional (3D) models, Wang *et al.* (2012) investigated seismic nonlinear performance of CG dams including dam-foundation interaction. An earthquake nonlinear analysis of roller-compacted concrete (RRC) dams was presented by Kartal (2012) considering the friction contact formulation at the dam-foundation-reservoir interface. The results indicated that displacements increase in the materially nonlinear response, whereas the principal stress components decrease, in contrast, under hydrodynamic pressure. Hariri-Ardebili (2014) revealed the effect of foundation rock nonlinearity on the stability of concrete dams subjected to earthquakes. His study showed that considering the nonlinear model of foundation rock increases the response and damaged area in the dam. Arici *et al.* (2014) and Yilmazturk *et al.* (2015) presented nonlinear seismic studies on a RCC dam using 2D and 3D models. The results illustrated that 3D analysis of the dam was significantly different from that resulted from 2D analysis. This comparative study revealed the necessity and importance of taking into account 3D analysis as these gravity structures are constructed in relatively narrow canyons for seismic safety assessment. A materially nonlinear analysis of CG dams considering the dynamic fluid-structure interaction was performed by Ouzandja *et al.* (2017). Wang *et al.* (2017) studied seismic damage of Guandi gravity dam using hard and soft contact models. The study was based on transient nonlinear seismic analyses. A linear and nonlinear earthquake performance of Cine RCC dam was investigated by Kartal and Karabulut (2018). Larger tensile stresses were noticed in linear analysis according to their study. Moradloo *et al.* (2018) studied seismic damage of arch concrete dams through transient nonlinear analysis. Their results manifested that the index of displacement failure was more conservative and impractical in the assessment of seismic damage than the index of tensional failure. Karabulut and Kartal (2020) exposed the impact of boundary conditions on earthquake response of a RCC dam in linear and nonlinear analyses. They found that the dam performance increases under effects of viscous boundary conditions. The influence of earthquake epicenter distance on the fracture response of concrete dams was examined by Karalar and Çavuşli (2020). The study demonstrated that the dam nonlinear seismic response depends on the epicenter distance of the earthquake. Pirooznia and Moradloo (2021) presented seismic cracking of concrete arch dams using a nonlinear dynamic model considering dam-reservoir interaction.

The current paper exhibits the impact of material nonlinearity of a dam-foundation rock interaction system on the response of CG dams during earthquake. To this end, a 3D finite element model of the dam-foundation rock system is employed in different analyses using the ANSYS software (2018). Oued Fodda CG dam, located in Chlef town at northwestern Algeria, is chosen in this study. The added mass approach (Westergaard, 1933) is used to model the hydrodynamic effect of the reservoir fluid using 3D surface finite elements that are applied on the dam-fluid and foundation-fluid interfaces. The concrete material model, available with element Solid65, is used to predict seismic cracking of dam concrete due to a multiaxial stress state using the smeared crack approach based on the Willam and Warnke (1975) failure criterion. The Drucker-Prager criterion (Drucker and Prager, 1952) is selected in a materially nonlinear response for the dam-foundation rock coupled system.

2. Drucker-Prager model

The Drucker-Prager model (Drucker and Prager, 1952) is widely used in finite element numerical modeling codes, especially dedicated to geotechnical and geomechanical applications. This model represents a simple approach of materials behavior with internal friction, coherent or not (soils, rocks, concrete and various granular materials). The Drucker-Prager criterion is a generalization of the von Mises criterion for materials with internal friction. The failure surface representing the von Mises criterion is a cylinder parallel to the trisector of the principal stress space. And that representing Drucker-Prager criterion is a cone with a circular section admitting the same axis as the symmetry axis (Fig. 1) (Chen and Mizuno (1990). The equation of this surface can be expressed as

$$f = \alpha I_1 + \sqrt{J_2} - k \tag{B.1}$$

where α and k are constants that depend on the angle of internal friction φ and cohesion c of the material presented by

$$\alpha = \frac{2\sin\varphi}{\sqrt{3}(3-\sin\varphi)} \qquad k = \frac{6c\cos\varphi}{\sqrt{3}(3-\sin\varphi)} \tag{B.2}$$

in Eq. (2.1), I_1 is the first stress tensor invariant of σ_{ij} written as follows

$$I_1 = \sigma_{11} + \sigma_{22} + \sigma_{33} \tag{B.3}$$

and J_2 is the second invariant of the deviatoric stress tensor s_{ij} formulated by

$$J_2 = \frac{1}{2} s_{ij} s_{ij} \tag{B.4}$$

where s_{ij} is the deviatoric stresses given as follows

$$s_{ij} = \sigma_{ij} - \delta_{ij}\sigma_m \qquad i,j = 1,2,3 \tag{B.5}$$

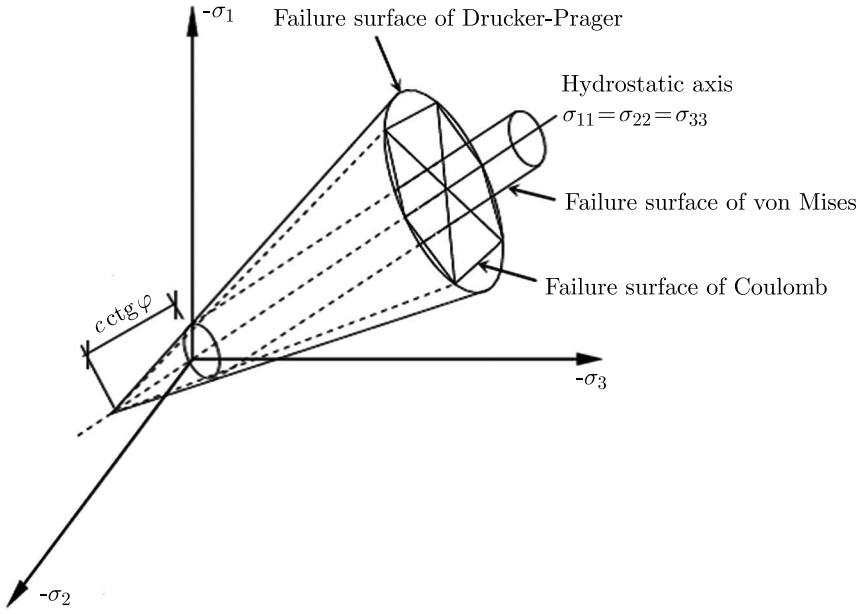

Fig. 1. Failure surface of Coulomb, Drucker-Prager and von Mises (Chen and Mizuno, 1990)

In Eq. (2.5), δ_{ij} is the Kronecker delta, which is equal to 1 for $i = j$; 0 for $i \neq j$, and σ_m is the mean stress given as

$$\sigma_m = \frac{I_1}{3} = \frac{\sigma_{11} + \sigma_{22} + \sigma_{33}}{3} = \frac{\sigma_{ii}}{3} \tag{B.6}$$

If the terms in Eq. (2.5) are determined by Eq. (2.6) and replaced in Eq. (2.4), the second invariant of the deviatoric stress tensor can be presented as follows

$$J_2 = \frac{1}{6}[(\sigma_{11} - \sigma_{22})^2 + (\sigma_{22} - \sigma_{33})^2 + (\sigma_{33} - \sigma_{11})^2] + \sigma_{12}^2 + \sigma_{13}^2 + \sigma_{23}^2 \tag{B.7}$$

3. Numerical model

3.1. Material properties

The numerical application treats Oued Fodda CG dam existing in Chlef territory at the northwest of Algeria, which is classified as high seismic activity zone in the national seismic code. This region suffered a strong earthquake known as the 1980 El Asnam earthquake (M7) that destroyed more than 70% of the city. The studied dam-foundation system is shown in Fig. 2.

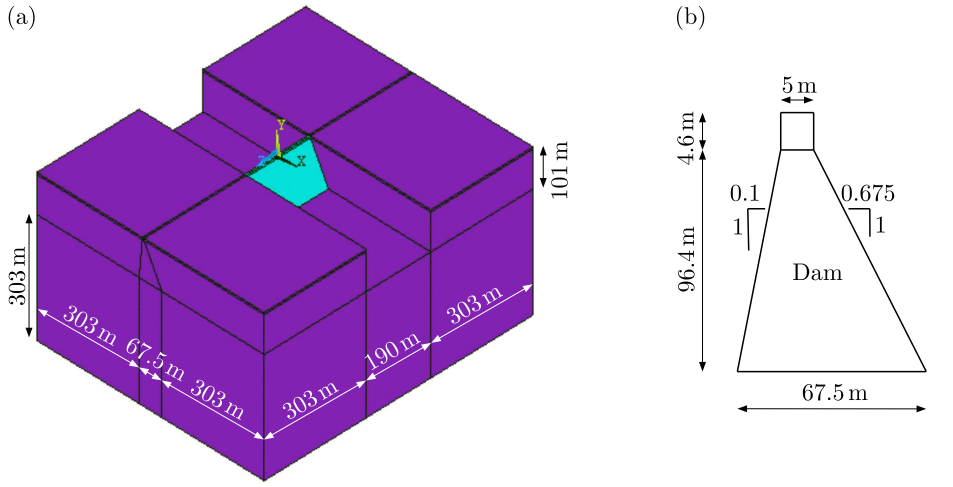

Fig. 2. Geometry of Oued Fodda dam-foundation rock system: (a) dam-foundation rock system, (b) dam

Mechanical properties of dam-foundation system materials are summarized in Table 1. Nonlinear analyses for both dam concrete and foundation rock are defined using the Drucker-Prager model (Drucker and Prager, 1952) (Table 1). The tensile and compressive strengths of dam concrete are 2.2 MPa and 24.1 MPa, respectively.

Table 1. Mechanical properties of the concrete dam and its foundation rock

Material properties	Material	
	Concrete dam	Foundation rock
Modulus of elasticity [MPa]	24600	20000
Poisson's ratio	0.20	0.33
Mass density [kg/m^3]	2640	2000
Cohesion [MPa]	2.7	1.9
Angle of internal friction	37	28

3.2. Dam-foundation rock system discretization

The dam-foundation rock system is discretized with a 3D finite element model illustrated in Fig. 3 using ANSYS computer Code (2018). The model exhibits 39750 finite elements, among them 2700 solid elements (Solid65) employed for the dam, and 37050 solid elements (Solid45) considered for the foundation rock. The hydrodynamic effect of the reservoir fluid is modeled employing the Westergaard (1933) approach. This method, which is an approximate approach, replaces the fluid with mass distributed uniformly on the dam-fluid and foundation-fluid interfaces, i.e., the fluid is represented as structural masses added to that of the dam and foundation. In this study, 3D surface finite elements (Surf154) are used to model the added mass approach, resulting in 900 elements.

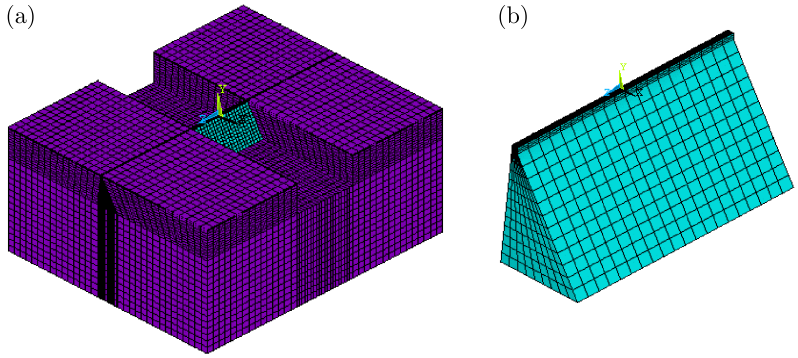

Fig. 3. Finite element discretization of Oued Fodda dam-foundation rock system: (a) dam-foundation rock system, (b) dam

4. Nonlinear seismic analyses of Oued Fodda dam-foundation rock system

This work shows the earthquake nonlinear response of Oued Fodda dam-foundation rock system. The dam region incurred a severe earthquake, 1980 El Asnam earthquake (M7), which caused significant material and human losses. However, there was available only seismic replica record of this earthquake. The stream direction was subjected to the horizontal component of the seismic replica record with peak ground acceleration (PGA) of 0.132 g, which was scaled by factor 2.5 to attain to a PGA of 0.33 g (Fig. 4) equal roughly to the evaluated PGA of the 1980 El Asnam earthquake (M7).

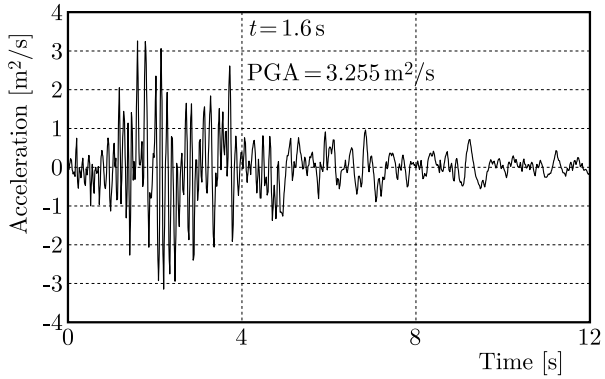

Fig. 4. Horizontal component of the 1980 El Asnam earthquake replica record after scaling operation of 2.5

Two different models are provided in earthquake analysis: the first model prescribes that the dam concrete is modeled using element Solid65 based on the smeared crack approach, whereas

the foundation rock is presumed to be elastic linear. The second model presents that the dam concrete is modeled using element Solid65 based on the smeared crack approach, while both the dam and foundation rock are modeled by an elastic-plastic model. The horizontal displacements, principal stress and strain components as well as cracking response resulted from the first and second models and are compared to each other.

4.1. Displacements

Figure 5 exhibits the distribution of horizontal displacements in upstream and downstream faces along the dam crest in the first and second models. The envelopes of maximum horizontal displacements of the dam during earthquake are presented in Fig. 6 for both two models. As can be shown from Figs. 5 and 6 that the horizontal displacements obtained from the second model are lower than those ones from the first model. Therefore, the material nonlinearity of the dam-foundation rock coupled system can lead to a decrease in the displacement response of the dam.

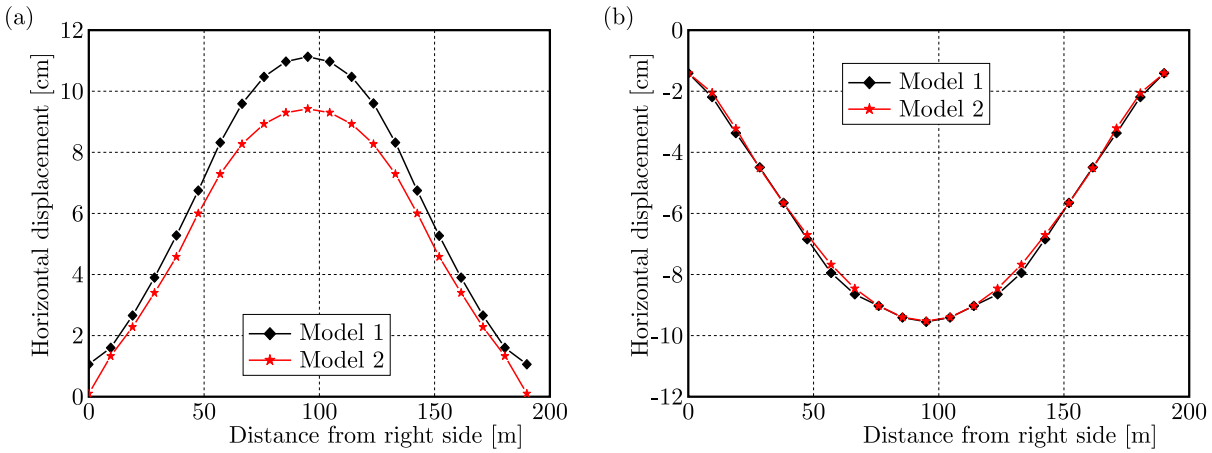

Fig. 5. Distribution of horizontal displacements in two faces along the dam crest: (a) downstream face, (b) upstream face

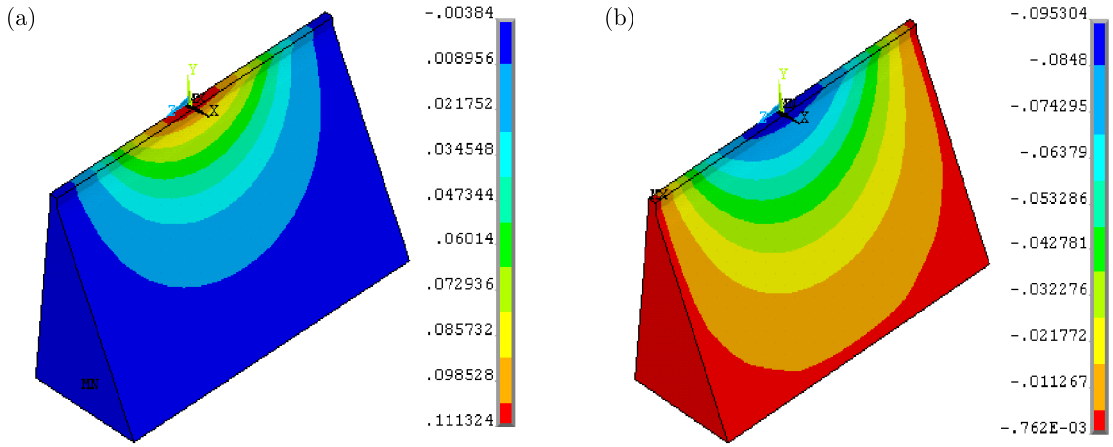

Fig. 6. Envelopes of maximum horizontal displacements for the dam, [m]: (a) model 1, (b) model 2

Figure 7 compares the horizontal displacement time history at the upstream middle crest located along the dam central axis, in which the maximum displacement at the crest decreases from 11.13 cm in the first model to 9.53 cm in the second one. This indicates a 14% reduction for the crest displacement amount in the second model. The horizontal displacement time history at

the heel and toe located along the dam symmetry central axis is plotted in Fig. 8. It is evident that the displacement time histories for both heel and toe of the dam in the first and second models are similar to each other, which the maximum displacement of 1.68 cm at the heel and 1.58 cm at the toe.

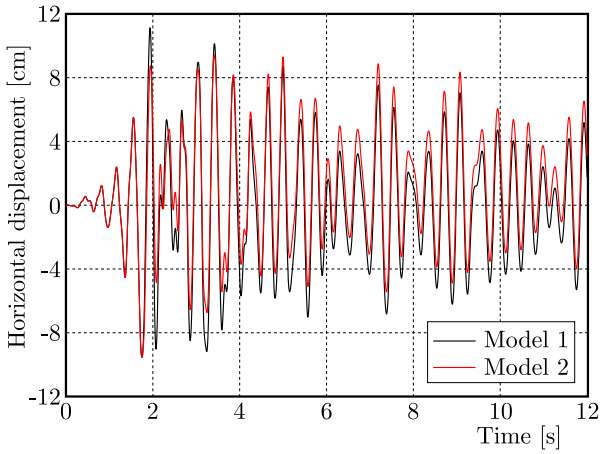

Fig. 7. Horizontal displcement time history at the dam crest for two models 1 and 2

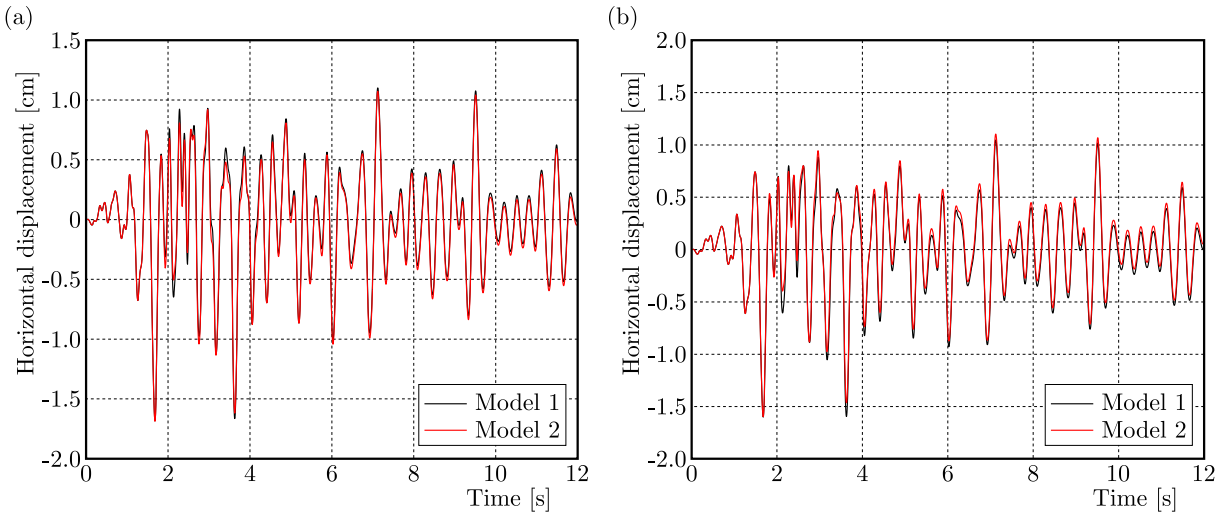

Fig. 8. Horizontal displacement time history at the heel and toe of the dam: (a) at the dam heel, (b) at the dam toe

4.2. Principal stresses

The envelopes of maximum principal tensile and compressive stresses in the upstream face of the dam appear in Figs. 9 and 10, respectively, for the two models. On the other hand, Figs. 11 and 12 show also the envelopes of principal stress components in the downstream face. As can be seen, the tensile stresses resulted from the second model are much lower than those from the first model, while the values of compressive stresses are convergent to each other. It is observed that the maximum principal stress components occur at right and left upper lateral extremities and middle bottom parts for both upstream and downstream faces in the two models.

The time history of principal stresses at the dam middle heel is presented in Fig. 13, in which the maximum principal tensile stress reduces from 11254.74 kN/m^2 in the first model to 3747.09 kN/m^2 in the second one. This denotes a decrease of 67% for the amount of principal tensile stress in the second model. In contrast, the value of maximum compressive stress is

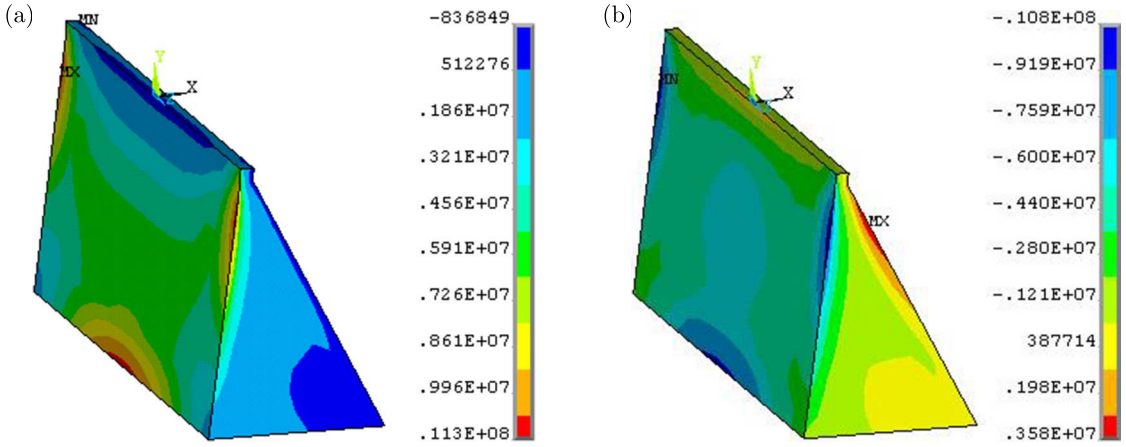

Fig. 9. Envelopes of maximum principal tensile stresses in the dam upstream face, [Pa]: (a) model 1, (b) model 2

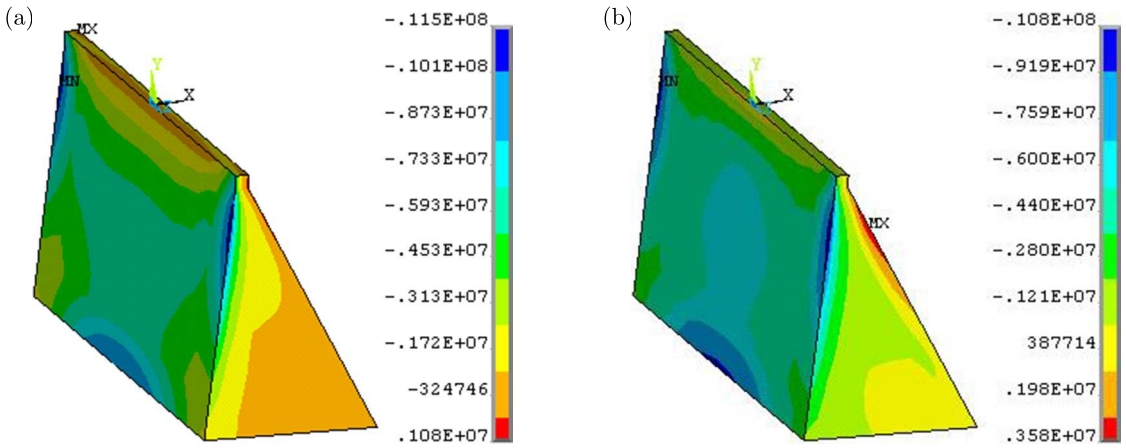

Fig. 10. Envelopes of maximum principal compressive stresses in the dam upstream face, [Pa]: (a) model 1, (b) model 2

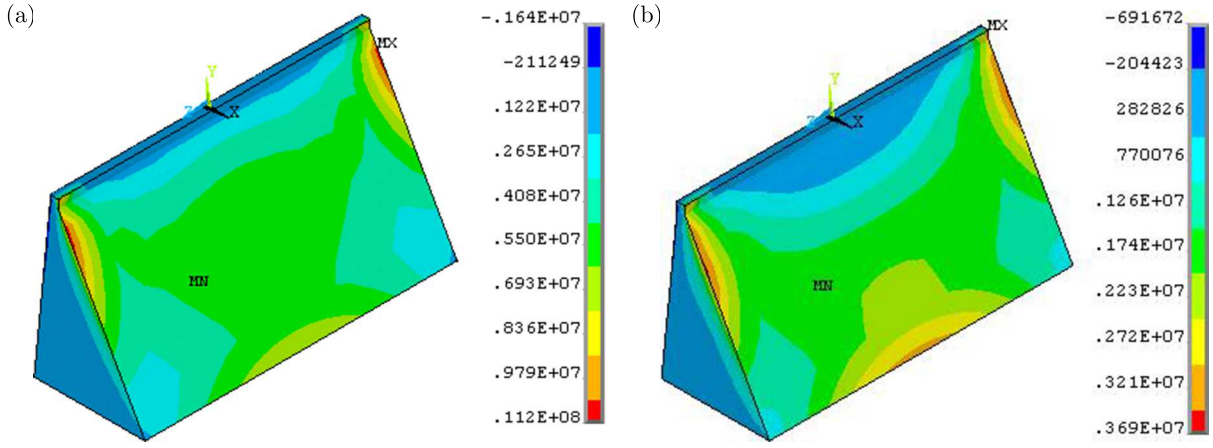

Fig. 11. Envelopes of maximum principal tensile stresses in the dam downstream face, [Pa]: (a) model 1, (b) model 2

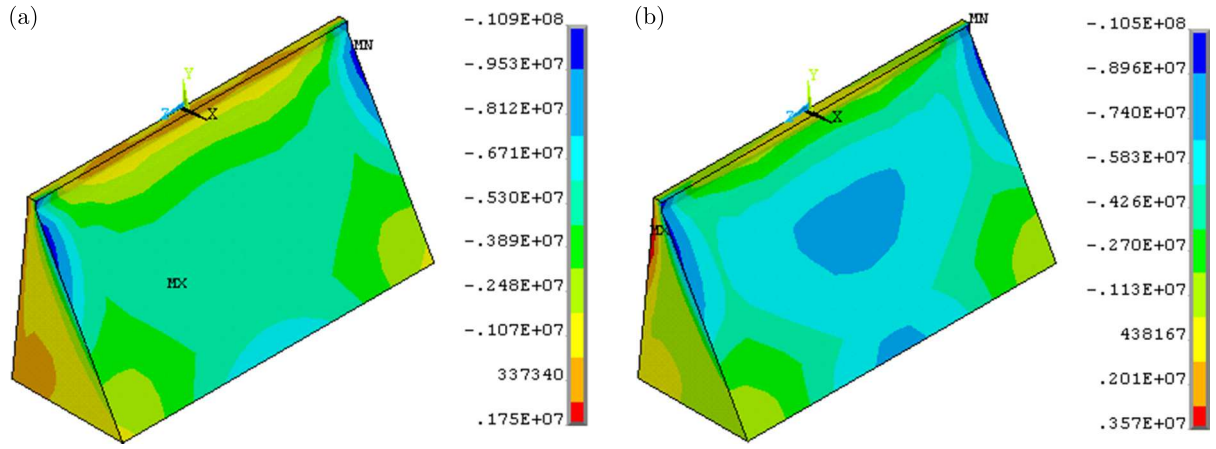

Fig. 12. Envelopes of maximum principal compressive stresses in the dam downstream face, [Pa]: (a) model 1, (b) model 2

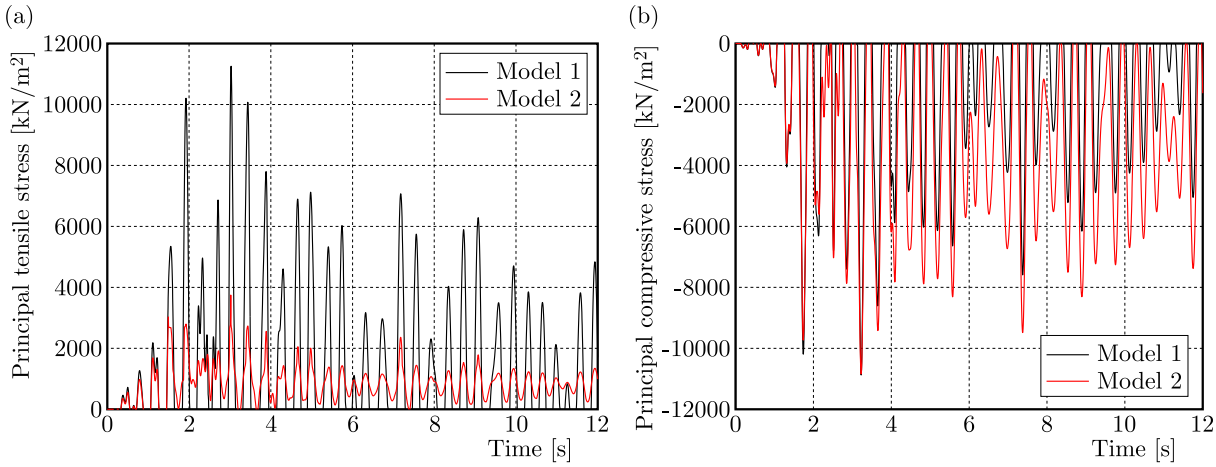

Fig. 13. Time history of principal stresses at the dam heel: (a) principal tensile stress, (b) principal compressive stress

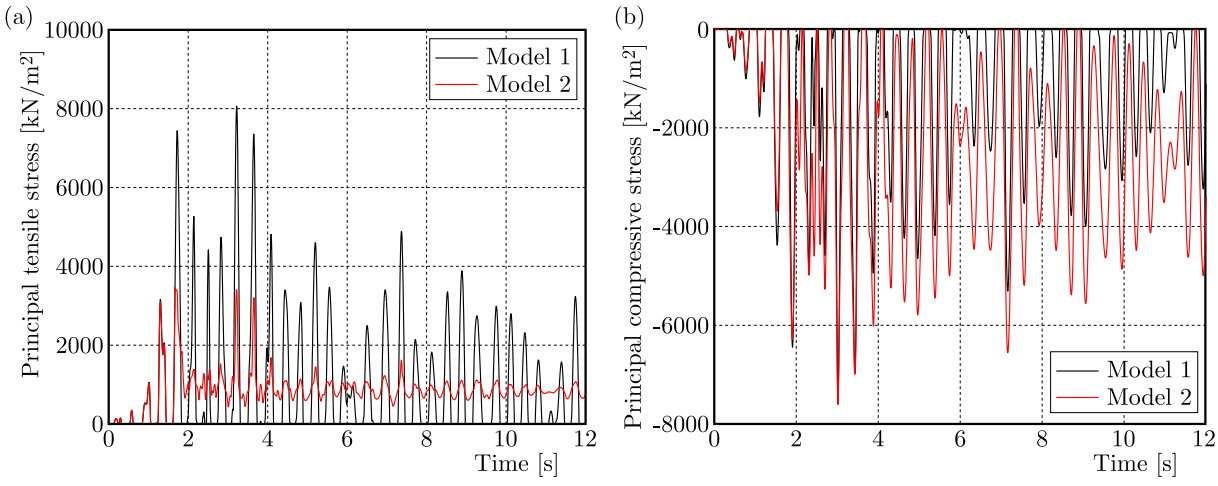

Fig. 14. Time history of principal stresses at the dam toe: (a) principal tensile stress, (b) principal compressive stress

convergent in the two models and equal to $-10874.37\,\mathrm{kN/m^2}$. According to Fig. 14 illustring the time history of maximum principal stresses at the middle toe, the maximum principal tensile stress decreases from $8065.77\,\mathrm{kN/m^2}$ in the first model to $3457.57\,\mathrm{kN/m^2}$ in the second analysis, i.e, a diminution of 43% for the amount of principal tensile stress in the second model. In contrast, the value of maximum compressive stress is convergent in the two models and equal to $-7604.92\,\mathrm{kN/m^2}$.

4.3. Principal strain

The envelopes of maximum and minimum principal strains in the dam upstream face are depicted in Figs. 15 and 16, respectively, for both two models. On the other hand, Figs. 17 and 18 illustrate also the envelopes of principal strain components in the downstream face. As can be shown, the maximum principal strains found from the second model are much lower than those from first one, whereas the values of minimum strains are convergent to each other. It is obvious that the maximum principal strain components appear where the maximum principal stress components occur.

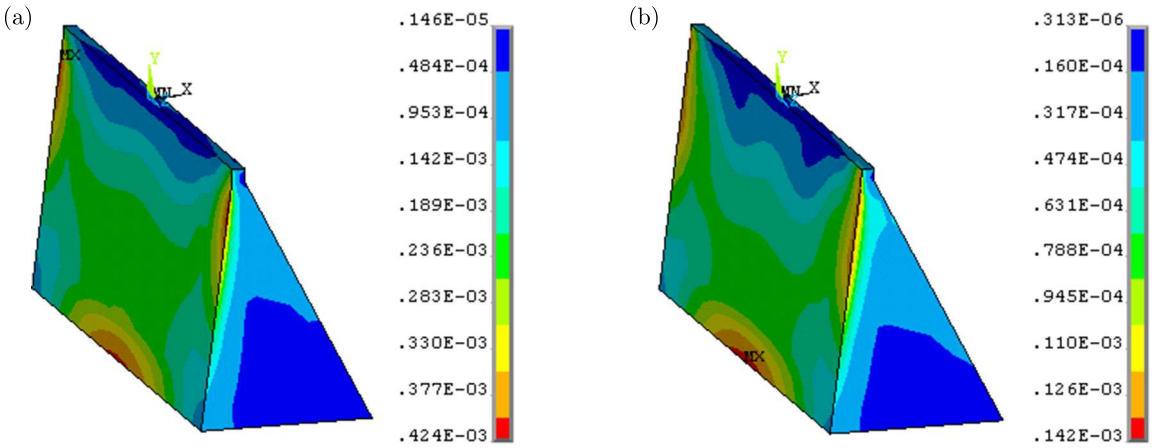

Fig. 15. Envelopes of maximum principal strain in the dam upstream face, [m/m] : (a) model 1, (b) model 2

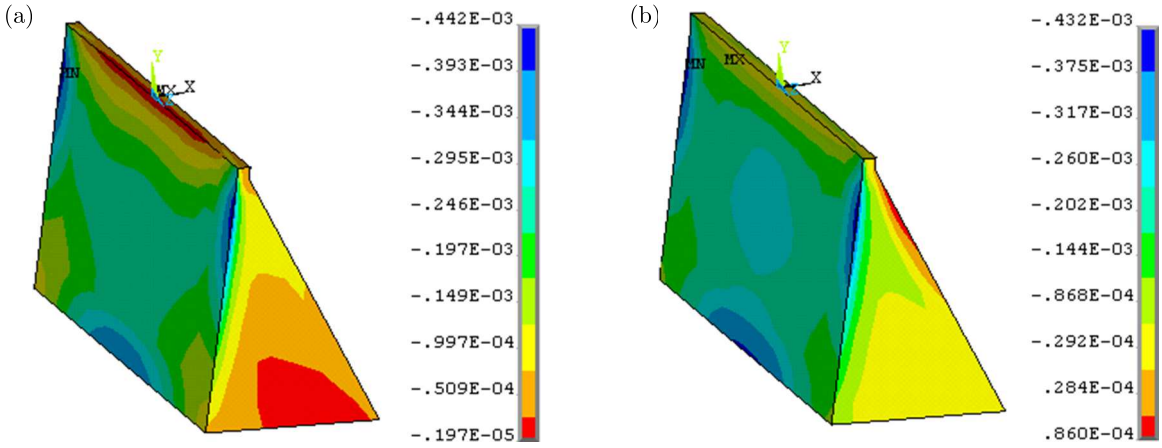

Fig. 16. Envelopes of minimum principal strain in the dam upstream face, [m/m]: (a) model 1, (b) model 2

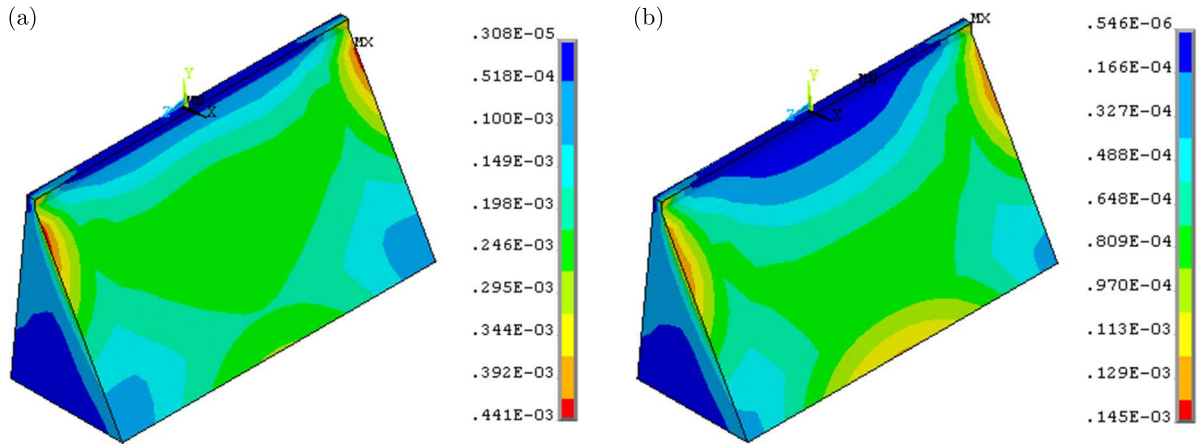

Fig. 17. Envelopes of maximum principal strain in the dam downstream face, [m/m]: (a) model 1, (b) model 2

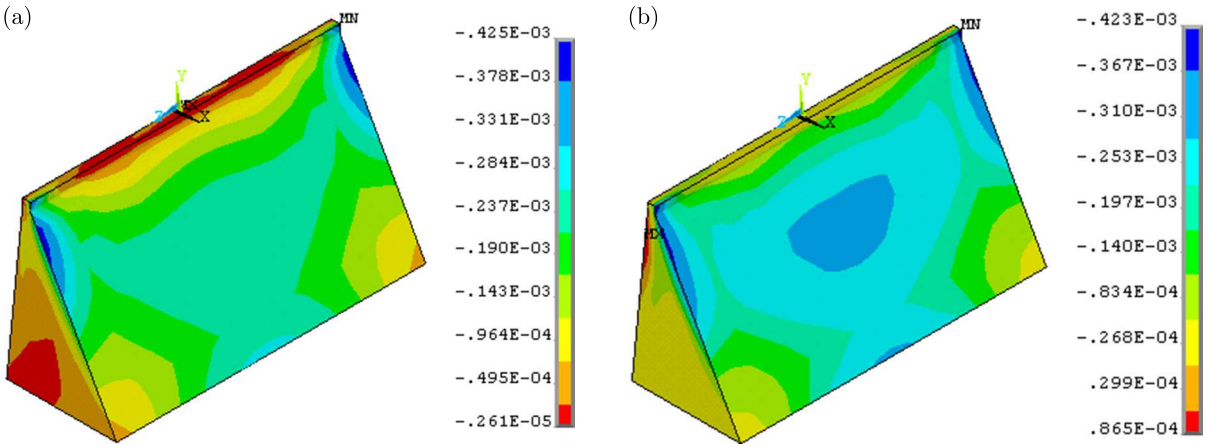

Fig. 18. Envelopes of minimum principal strain in the dam downstream face, [m/m]: (a) model 1, (b) model 2

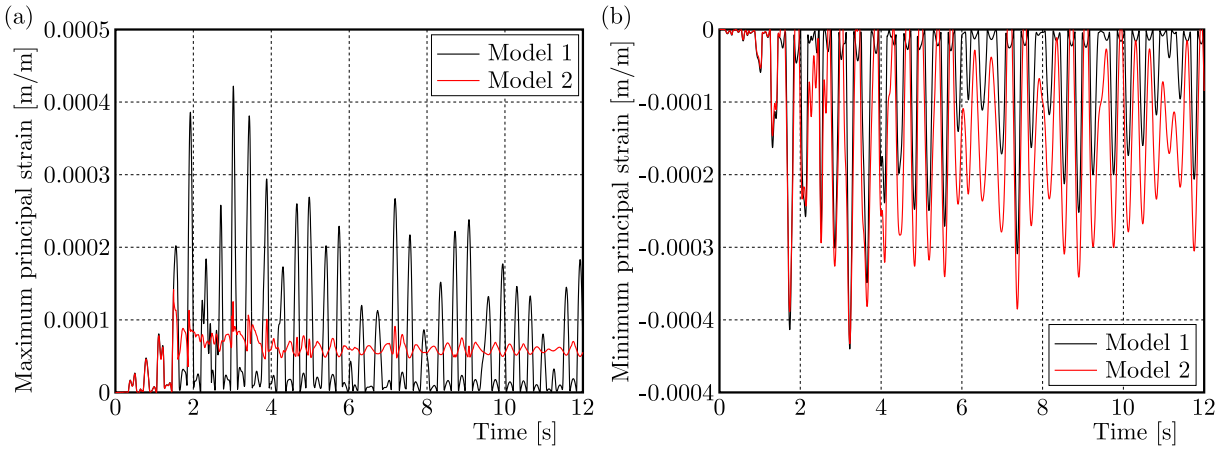

Fig. 19. Time history of principal strains at the dam heel: (a) maximum principal strain, (b) minimum principal strain

The time history of principal strains at the dam heel is compared in Fig. 19, in which the maximum principal strain decreases from 0.422‰ in the first model to 0.141‰ in the second one. In contrast, the value of minimum strain is convergent in the two models and is equal to −0.437‰. According to Fig. 20 representing the time history of principal strains at the toe, the maximum principal strain reduces from 0.313‰ in the first model to 0.130‰ in the second one. In contrast, the value of minimum strain is convergent in the two models and is equal to −0.318‰.

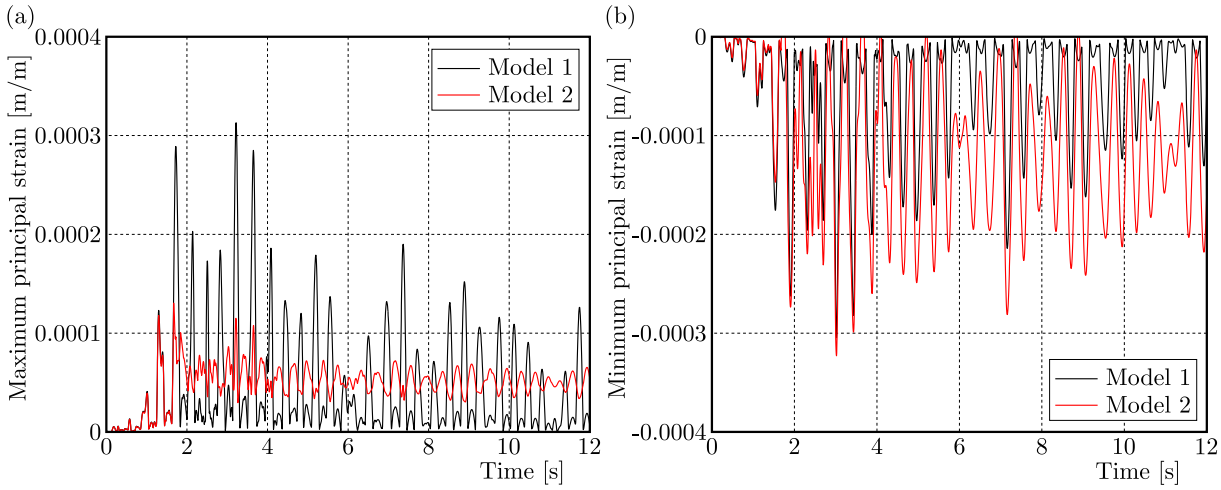

Fig. 20. Time history of principal strains at the dam toe: (a) maximum principal strain, (b) minimum principal strain

4.4. Cracking profiles

The final cracking profiles in upstream and downstream faces of Oued Fodda dam are shown in Figs. 21 and 22, respectively, for both models. As may be seen, cracks occur in tensioned parts in two models, where the maximum tensile stresses appear. In the second model, the cracks occur at the right and left upper lateral extremities and middle bottom parts for both upstream and downstream faces, while the cracking includes large parts on upstream and downstream faces in the first model according to the distribution of maximum principal tensile stresses into the dam faces (see Figs. 9a and 11a). These big cracked areas affect significantly stability and safety of the dam structure. In general, the materially nonlinear properties of the dam and foundation rock can significantly reduce damage areas in the dam body.

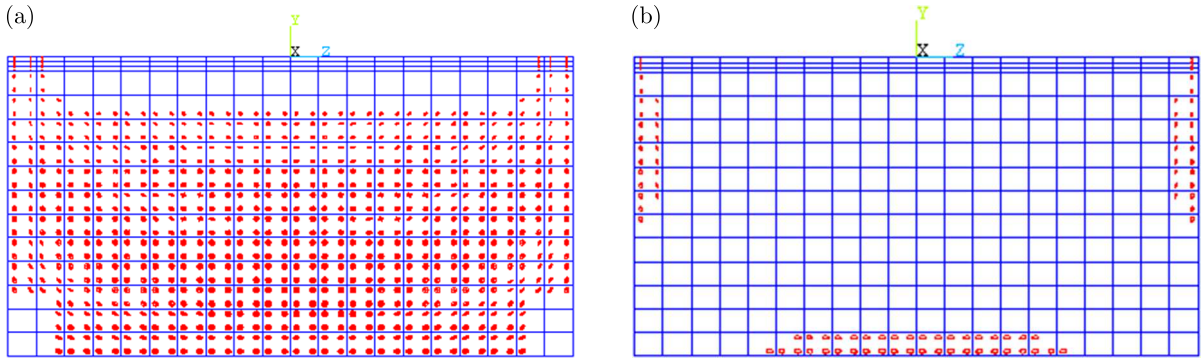

Fig. 21. Cracking profile in the dam upstream face: (a) model 1, (b) model 2

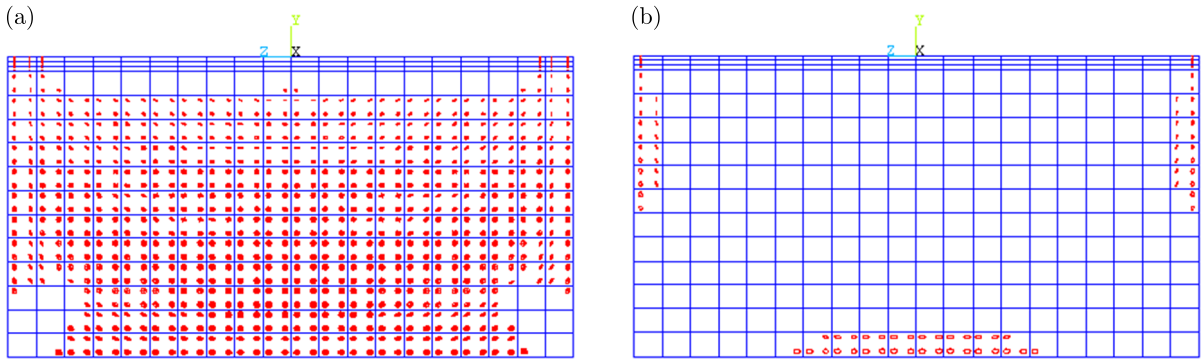

Fig. 22. Cracking profile in the dam downstream face: (a) model 1, (b) model 2

5. Conclusions

The current study presents the effect of material nonlinearity of both the dam and foundation rock on the earthquake response of Oued Fodda dam. The hydrodynamic interaction between the reservoir water and dam-foundation system is modeled by the Westergaard approach using 3D surface finite elements. The Drucker-Prager criterion is employed in materially nonlinear analysis for the dam-foundation rock coupled system. From this numerical investigation, one can obtain the following inferences:

1. The tacking into account the materially nonlinear model of the dam-foundation rock coupled system can:
   - lead to a decrease in the horizontal displacements of the dam,
   - significant decrease in the tensile stresses and maximum strains in the dam,
   - reduction of cracked areas in the dam body.
2. The dam real behavior is obtained in the second model, which is a more realistic model, compared to the first one.
3. The results obtained from this study demonstrate the need for a substantially nonlinear model of the coupled dam-foundation rock system in order to assess the design and to predict the dam reliable earthquake performance.
4. The material nonlinearity should be taken into account in numerical analyses to achieve more reliable and practical findings.

According to this study, taking into account the materially nonlinear model of the dam--foundation coupled system can have an impact on displacements, magnitude of tensile stresses and failure zones in concrete of the dam. In order to achieve reliable, accurate and realistic findings of the seismic performance of the dam-foundation coupled system, it has therefore become crucial and necessary to do substantially nonlinear analysis.

References

1. Akköse M., Şimşek E., 2010, Non-linear seismic response of concrete gravity dams to near--fault ground motions including dam-water-sediment-foundation interaction, *Applied Mathematical Modelling*, **34**, 11, 3685-3700

2. ANSYS, 2018, Theory User's Manual, Swanson Analysis Systems Inc., Canonsburg, PA, USA

3. Arici Y., Binici B., Aldemir A., 2014, Comparison of the expected damage patterns from two- and three-dimensional nonlinear dynamic analyses of a roller compacted concrete dam, *Structure and Infrastructure Engineering*, **10**, 3, 305-315

4. Burman A., Maity D., Sreedeep S., 2010, Iterative analysis of concrete gravity dam-nonlinear foundation interaction, *International Journal of Engineering, Science and Technology*, **2**, 4, 85-99

5. Burman A., Reddy B.V., Maity D., 2008, Seismic analysis of concrete gravity dams considering foundation flexibility and nonlinearity, *Proceedings of the 12th International Conference on Computational Methods and Advances in Geomechanics (IACMAG)*, Goa, India.

6. Chen W.F., Mizuno E., 1990, *Nonlinear Analysis in Soil Mechanics*, Elsevier, Amsterdam

7. Drucker D.C., Prager W., 1952, Soil mechanics and plastic analysis or limit design, *Quarterly of Applied Mathematics*, **10**, 2, 157-165

8. Hariri-Ardebili M.A., 2014, Impact of foundation nonlinearity on the crack propagation of high concrete dams, *Soil Mechanics and Foundation Engineering*, **51**, 2, 72-82

9. Karabulut M., Kartal M.E., 2020 Seismic analysis of Roller Compacted Concrete (RCC) dams considering effect of viscous boundary conditions, *Computers and Concrete*, **25**, 3, 255-266

10. Karalar M., Çavuşli M., 2020, Seismic effects of epicenter distance of earthquake on 3D damage performance of CG dams, *Earthquakes and Structures*, **18**, 2, 201-213

11. Kartal M.E., 2012, Three-dimensional earthquake analysis of roller-compacted concrete dams, *Natural Hazards and Earth System Sciences*, **12**, 7, 2369-2388

12. Kartal M.E., Karabulut M., 2018, Earthquake performance evaluation of three-dimensional roller compacted concrete dams, *Earthquakes and Structures*, **14**, 2, 167-178

13. Moradloo J., Naserasadi K., Zamani H., 2018, Seismic fragility evaluation of arch concrete dams through nonlinear incremental analysis using smeared crack model, *Structural Engineering and Mechanics*, **68**, 6, 747-760

14. Ouzandja D., Tiliouine B., 2015, Effects of dam-foundation contact conditions on seismic performance of concrete gravity dams, *Arabian Journal for Science and Engineering*, **40**, 11, 3047-3056

15. Pirooznia A., Moradloo A.J., 2021, Seismic fracture analysis of concrete arch dams incorporating the loading rate dependent size effect of concrete, *Structural Engineering and Mechanics*, **79**, 2, 169-198

16. Khazaei-Poul M., Zerva A., 2018, Nonlinear dynamic response of concrete gravity dams considering the deconvolution process, *Soil Dynamics and Earthquake Engineering*, **109**, 324-338

17. Wang G., Wang Y., Lu W., Yu M., Wang C., 2017, Deterministic 3D seismic damage analysis of Guandi concrete gravity dam: A case study, *Engineering Structures*, **148**, 263-276

18. Wang G., Wang Y., Lu W., Zhou W., Zhou C., 2015, Integrated duration effects on seismic performance of concrete gravity dams using linear and nonlinear evaluation methods, *Soil Dynamics and Earthquake Engineering*, **79**, 223-236

19. Wang H., Feng M., Yang H., 2012, Seismic nonlinear analyses of a concrete gravity dam with 3D full dam model, *Bulletin of Earthquake Engineering*, **10**, 6, 1959-1977

20. Westergaard H.M., 1933, Water pressures on dams during earthquakes, *Transactions of the American Society of Civil Engineers (ASCE)*, **98**, 2, 418-433

21. Willam K.J., Warnke E.D., 1975, Constitutive model for the triaxial behavior of concrete, *Proceedings of International Association for Bridge and Structural Engineering*, **19**, 174, ISMES, Bergamo, Italy

22. Yazdani Y., Alembagheri M., 2017, Nonlinear seismic response of a gravity dam under near--fault ground motions and equivalent pulses, *Soil Dynamics and Earthquake Engineering*, **92**, 621-632

23. Yilmazturk S.M., Arici Y., Binici B., 2015, Seismic assessment of a monolithic RCC gravity dam including three dimensional dam-foundation-reservoir interaction, *Engineering Structures*, **100**, 137-148

Manuscript received August 7, 2022; accepted for print October 26, 2022

JOURNAL OF THEORETICAL AND APPLIED MECHANICS
61, 1, pp. 65-76, Warsaw 2023
https://doi.org/10.15632/jtam-pl/157479

ANALYTICAL STUDY ON THE CUTTING FORCE AND RESIDUAL STRESS IN WHIRLWIND MILLING OF A LARGE SCREW

Qin Guo
Industrial Center, Nanjing Institute of Technology, Nanjing, Jiangsu, China
e-mail: 453094252@qq.com
Yulin Wang, Bin Zhou
School of Mechanical Engineering, Nanjing University of Science and Technology, Nanjing, Jiangsu, China

The finite element method (FEM) is developed to simulate a discontinuous cutting in the whirlwind milling. Firstly, a simplified arc-cutting model for simulating the actual circular cutting, and a plane-cutting model for simplification were both developed and verified by experiments. Then, the effects of cutting parameters on the cutting force and residual stress were effectively investigated based on the plane-cutting model. Moreover, a plane-second--cutting model was further developed. It showed that a minor decrease of cutting force and a higher maximum compressive stress were generated in the second cutting. Those results were conducive to predict and improve the whirlwind milling.

Keywords: whirlwind milling (WM), cutting force, residual stress, finite element method (FEM)

1. Introduction

Among different cutting methods, the Whirlwind Milling (WM) (Wang *et al.*, 2020b) is one of the most efficient and environmental ways, especially for processing a large screw. Properties of the surface and the sub-surface of a machined screw are known to depend on cutting parameters and physical states. Thus, the cutting force and residual stress were chosen to reflect the state of cutting and surface (Cao *et al.*, 2019; Bobzin *et al.*, 2021). The favor cutting force can improve machined surface quality and tool life. Residual compressive stress can suppress fatigue failure of the product and prolong fatigue life. Combining with experiments, the Finite Element Method (FEM) (Kundrák *et al.*, 2021) can describe the changing process of some physical quantities with time in the processing as realistically and intuitively as possible. For the cutting force and residual stress, the FEM with experiments were used to study and improve the whirlwind milling.

Previous studies analyzed the cutting force and residual stress. Wang *et al.* (2020b) proposed linear and nonlinear cutting force models based on cutting coefficients in helical milling. Zhou and Ren (2020) modeled the shear cutting force based on unequal division in the parallel-sided shear zone in orthogonal cutting. Wang *et al.* (2019) presented a cutting force model based on the geometrical and mechanical nature of the tool and workpiece. Salonitis *et al.* (2015) predicted the residual stress profile as a function of process parameters and the thermo-mechanical response in grind-hardening of AISI 1045 steel. Masmiati *et al.* (2016) predicted a mathematical model of residual stress, cutting force and surface roughness in end milling. Son *et al.* (2015) studied deformation and residual stress. The prediction methods, such as an analytical model and finite element analysis, were verified by firing and cooling experimental results.

The FEM is regarded as a useful method to study the cutting process. It can provide the information of the cutting force, residual stress, chip morphology and so on (Cai *et al.*, 2019).

Kara *et al.* (2016) applied FEM to predict cutting temperatures in orthogonal turning of AISI 316L stainless steel. Huang *et al.* improved the thermal model by FEM which can provide a more clear description of temperature distribution in the workpiece. Chang *et al.* (2017) performed FEM simulations of hard turning aluminum 2024-T3 to predict the distribution of residual stresses. Huang *et al.* (2015) proposed FEM based analytical model of the stress field to calculate the residual stress. Tounsi and El Wardany (2015) conducted four cutting simulations of titanium alloy Ti6Al4V. The results showed that the tangential force of the last three cuttings were almost the same as the first one, and the normal force was significantly smaller than that of the first cutting. For whirlwind milling, Yan *et al.* (2018) proposed a time-varying heat source modeling method and analyzed transient temperature in the cutting zone.

For WM, the technology has been applied in precision machining. But due to technical confidentiality and other reasons, there are few paper reported on the basic theory and cutting mechanism. Lee *et al.* (2008) modeled the tool-nose trajectory by the internal and external WM method and predicted the over-cut amount of the screw surface. Zanger *et al.* (2017) modeled the surface profile of a screw in dry WM. Han and Liu (2014) analyzed the theoretical machining error by dividing the scallop height into axial and cross-sectional errors. Wang *et al.* (2020a) applied an analytical approach to investigate WM forming errors, including circularity error, scallop height and surface roughness. With the help of cutting experiments, Guo *et al.* (2020a) investigated firstly the effect of cutting parameters on three characteristic parameters of the residual stress, then developed a prediction model of residual stress by the response surface methodology (Guo *et al.*, 2019), and finally minimized the tangential cutting force by optimizing cutting parameters (Guo *et al.*, 2020b).

The above researches have made great contribution to study the cutting process. However, the cutting depth in some models was assumed to be constant, which did not represent the machining characterics of whirlwind milling. Additionally in WM, the tests of cutting force and residual stress are difficult, complicated, time-consuming, and almost unpractical under every cutting parameter. Thus, the paper would develop different FEM models for simulating different thermo-mechanical processes in whirlwind milling. These work would be helpful to optimize the whirlwind milling parameters and improve the machined surface integrity of screw.

2. Finite element model

2.1. Simplified geometry model of whirlwind milling

The whirlwind milling in Fig. 1 is a complicated cutting process. For simulating, some simplifications and assumptions are made as follows:

(1) The workpiece is assumed to be fixed during the cutting process since rotational speed of the tools is much higher than that of workpiece.
(2) The small lead angle (around 2.28°) is neglected. The small lead angle has little influence on simulation results, so it can be ignored in a arc-cutting model.
(3) The first cutting is assumed to be accomplished and ignored due to chips different from those of the following cutting.

Due to the fact that the screw in whirlwind milling generates chips with arc-characteristics. Therefore, it is necessary to establish an arc-cutting model. Figure 1 shows the geometric forming process in which the number of tools on the whirling ring is n_d, workpiece rotational speed N_w, whirling ring rotational speed N_t, workpiece radius r, tool noses' circular radius R, eccentricity e for the segment O_wO_t. The parameter d is formed by the first cutting process. The cutting depth

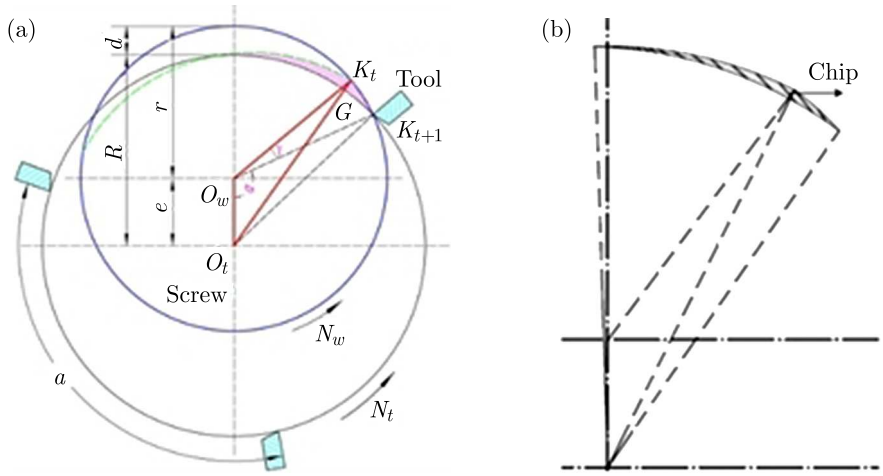

Fig. 1. Simplified geometry model of (a) cutting principle and (b) chip of whirlwind milling

changes during one cutting process. The maximum cutting depth h_{max} during one cut after the first one satisfies

$$h_{max} = \sqrt{r^2 + e^2 - 2er\cos(\alpha + \gamma)} - R \tag{B.1}$$

Here γ and α are calculated as follows

$$\gamma = 360 N_w \frac{\Delta t}{60} \tag{B.2}$$

In Eq. (2.2), γ is the rotation angle of the workpiece from the beginning of cutting process K_n to the beginning of cutting process K_{n+1} $(n \geqslant 2)$ while Δt is the time interval, which can be calculated as

$$\Delta t = \frac{60}{n_d N_t} \tag{B.3}$$

2.2. Settings and configurations of the FEM models

The Abaqus software was used to model the cutting. The arc-cutting model was established based on the plane strain assumption to simulate the whirlwind milling. The workpiece was of AISI 52100 steel, and the tools of PCBN. The material properties are shown in Table 1.

The Johnson-Cook constitutive model was used to describe the flow stress under high temperature, high strain and high strain rate in whirlwind milling. The Johnson-Cook failure model in Eq. (2.4) and parameters in Table 2 were adopted to describe the chip separation

$$\begin{aligned} w &= \sum \frac{\Delta \overline{\varepsilon}}{\varepsilon_f} \\ \varepsilon_f &= \left(d_1 + d_2 e^{d_3 \frac{\sigma_p}{\sigma_e}}\right)\left(1 + d_4 \ln \frac{\dot{\varepsilon}}{\dot{\varepsilon}_0}\right)\left(1 + d_5 \frac{T - T_r}{T_m - T_r}\right) \end{aligned} \tag{B.4}$$

where $\Delta \overline{\varepsilon}$ is the equivalent plastic strain increment, ε_f is the failure strain, d_1-d_5 are failure parameters measured by tensile torsion tests, $\dot{\varepsilon}_0$ is the reference strain rate.

In the study, a revised Coulomb equation was used to describe the friction between the tool and the chip. The expression was shown as

$$\tau = \begin{cases} \mu\sigma_n & \tau < \tau_{max} \quad \text{(in sliding area)} \\ \tau_{max} & \tau > \tau_{max} \quad \text{(in sticking area)} \end{cases} \tag{B.5}$$

Table 1. Material properties of PCBN and AISI52100

Physical characteristics	Workpiece-GCr15	Temperature [K]	Tool-PCBN
Density [kg/m^3]	7812	–	3480
Elasticity modulus [MPa]	2.17E+0o5	–	7.2E+005
Poisson's ratio [–]	0.3	–	0.3
Thermal conduction [W/(mK)]	46.6	–	79.54
Coefficient of expansion [K^{-1}]	1.14E-005	373	5.6E-006
	1.24E-005	473	
	1.34E-005	573	
	1.30E-005	673	
	1.17E-005	773	
Specific heat capacity [J/(kgK)]	552	318	500
	788	798	
	724	1254	

Contact of properties GCr15-PCBN	Tangential properties – coefficient of friction	0.2	
	Normal properties	Hard contact	
	Heat conduction	Conductance	Clearance
		28000	0
		0	0.001

Table 2. Shear failure criterion parameters of Johnson-Cook model

Failure parameters	d_1	d_2	d_3	d_4	d_5
Value	0.0368	2.34	−1.484	0.0035	0.411

where μ is the friction coefficient of the sliding zone, τ_{max} is the shear yield stress, σ_n is the normal stress of the tool-chip contact surface. In the study, the value of μ is assigned to be 0.35, the value of τ_{max} is 570 MPa, which can achieve good agreements with the experiments in terms of the cutting force and residual stress distribution.

The mesh is an important part in the finite element simulation, and the quality of the mesh would directly determine the accuracy of simulation results. The CPE4RT element was selected for the chip, the joint and workpiece. The CPE3RT element was selected for the cutting tool. The workpiece was considered to be isotropic while the tool was assumed to be rigid. The boundary conditions were set as follows: the upside of the workpiece was free while the rest sides were fixed, as shown in Fig. 2. The velocity was assigned on the rigid body reference point of the tool

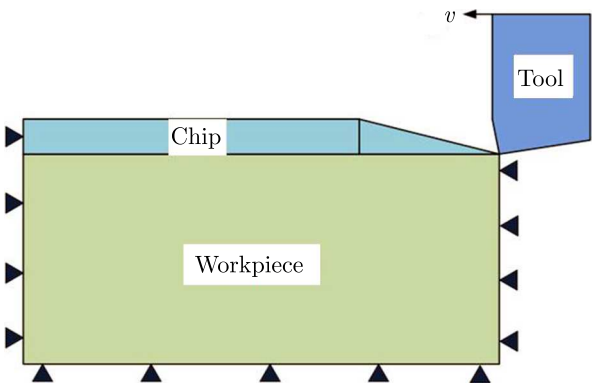

Fig. 2. Sketch of FEM

so that the tool moved straightly or circumferentially. The initial temperature of the workpiece and tool was 22°C. Only the upside of the workpiece exchanged heat fluxes with the environment if a cool-down step was set.

3. Finite element model validation

To validate the arc-cutting model, experiments were conducted. The validation experiments are shown in Fig. 3a. The cutting parameters were selected as cutting speed of 3.33 m/s, rake angle of −7°, a clearance angle of 5° and h_{max} of 0.062 mm. In Fig. 3b, a 3D piezoelectric force sensor was chosen, and the data was recorded using a standard quartz dynamometer (Kistler 9602A3) allowing measurements from −1 to 1 KN. By a team self-developed testing system (Ni *et al.*, 2012), the WM cutting forces were acquired as shown in Fig. 3c. During the data collecting, see Fig. 3d, the sampling frequency of data was set at 5000 Hz. The force signals acquired were analyzed for a cutting time of 1.5 s.

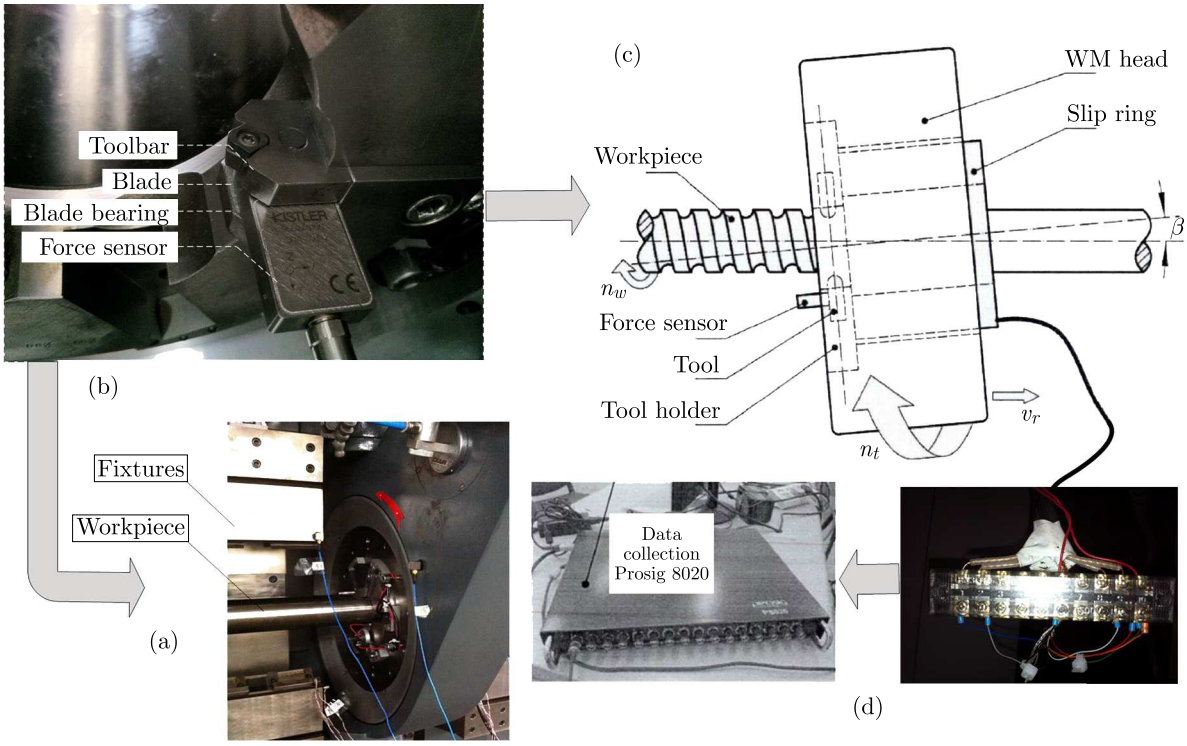

Fig. 3. Validation of cutting force experiments

In simulation, some simplifications and assumptions in the arc-cutting model were made. The tool edge was simplified and assumed as a sharp one, the tool as a rigid body by neglecting the energy absorption and deformation which was used to simulate the actual circular cutting. To reduce difficulties of building the arc-cutting model, a simplified plane-cutting model was developed. It simplified an equal-depth cutting depth, and could avoid effectively the complex mesh distortion appearing in the arc-cutting model. In addition, the plane-cutting model considered the tool wear and absorption of mechanical and thermal energy, thus could simulate the actual thermo-mechanical process.

For the tangential force F_t and radial force F_r, comparisons between the experiments and simulations are listed in Table 3. The results indicated that the predicted cutting forces in the arc-cutting model agreed well with the experiments. However, the predicted cutting force was 9.3% smaller than the experimental one in the radial direction and 3.6% smaller in the tangential

direction. The arc-cutting model, therefore, resulted in a small drop of the cutting force. While for the plane-cutting model, the cutting force was 3.1% smaller than the experimental one in the tangential direction and 21.6% smaller in the radial direction.

Table 3. Values and errors of the experiment and simulation

	Experiments	Arc-cutting simulation	Plane-cutting simulation
Tangential force F_t [N]	151.2	145.7	146.5
Radial force F_r [N]	57.9	52.5	45.34
Error of F_t		3.6%	3.1%
Error of F_r		9.3%	21.6%

Through the comparison in Fig. 4, it could be found that the predicting accuracy of the arc-cutting model was higher than of the plane-cutting model. Although, the error of the plane--cutting model was much larger, especially in predicting the radial force. The error of the tangential force between the arc-cutting and plane-cutting model was only 0.5%, which could be ignored for the tangential cutting force. Therefore, for improving the calculation efficiency, the plane cutting model was used to simulate the screw in whirlwind milling.

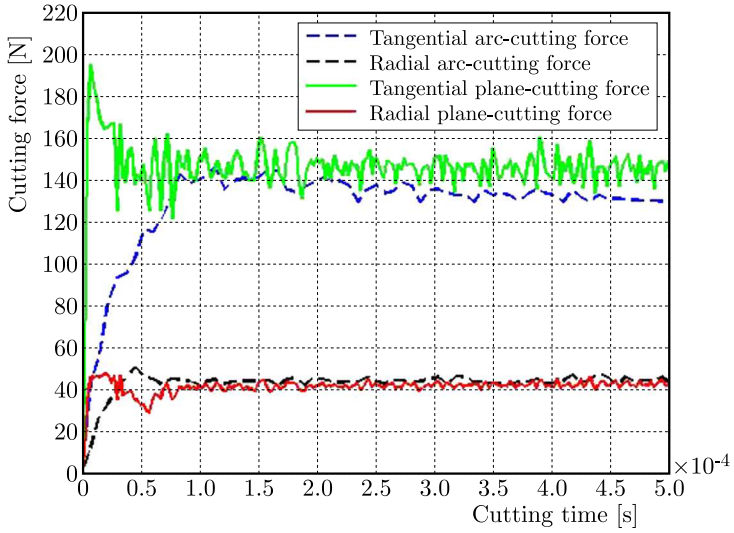

Fig. 4. Comparison of cutting forces between arc-cutting and plane-cutting

4. Simulation results

Due to the features of incremental forming with multi-tools in whirlwind milling, the vibration, temperature and residual stress of one cutting had important effects on the subsequent cutting. Therefore, the adjacent cuttings were simulated by employing the plane-cutting model.

4.1. Simulation of the cutting force and residual stress in the first cutting

The single-factor sets of simulations, assigned in Table 4, were designed to study the effects of cutting parameters.

The predicted cutting forces under different cutting parameters were calculated and illustrated. Figure 5 shows relationships between cutting parameters and cutting forces. As the cutting depth increased, the tangential force varied from 110 N to 210 N, and the radial force from 40 N to 60 N. The tangential force increased more rapidly because it is the main cutting force for forming. As the cutting speed increased from 1 m/s to 5 m/s in Fig. 6, the tangential

Table 4. Investigated cutting parameters

h_{max} [mm]	Cutting speed [m/s]	Rake angle	Clearance angle
0.06, 0.08, 0.10, 0.12	3	−7°	5°
0.08	1, 2, 3, 4, 5	−7°	5°
0.08	3	±7°, ±5°, 0	5°

force decreased at first and then increased slowly while the radial force kept approximately the same magnitude. Figure 7 shows the tendency that tangential and radial cutting forces change with different rake angles. As the rake angles increased, the radial force changed from 5 N to 45 N while the tangential force increased insignificantly. Hence, the rake angle was the main influence factor of the radial forces.

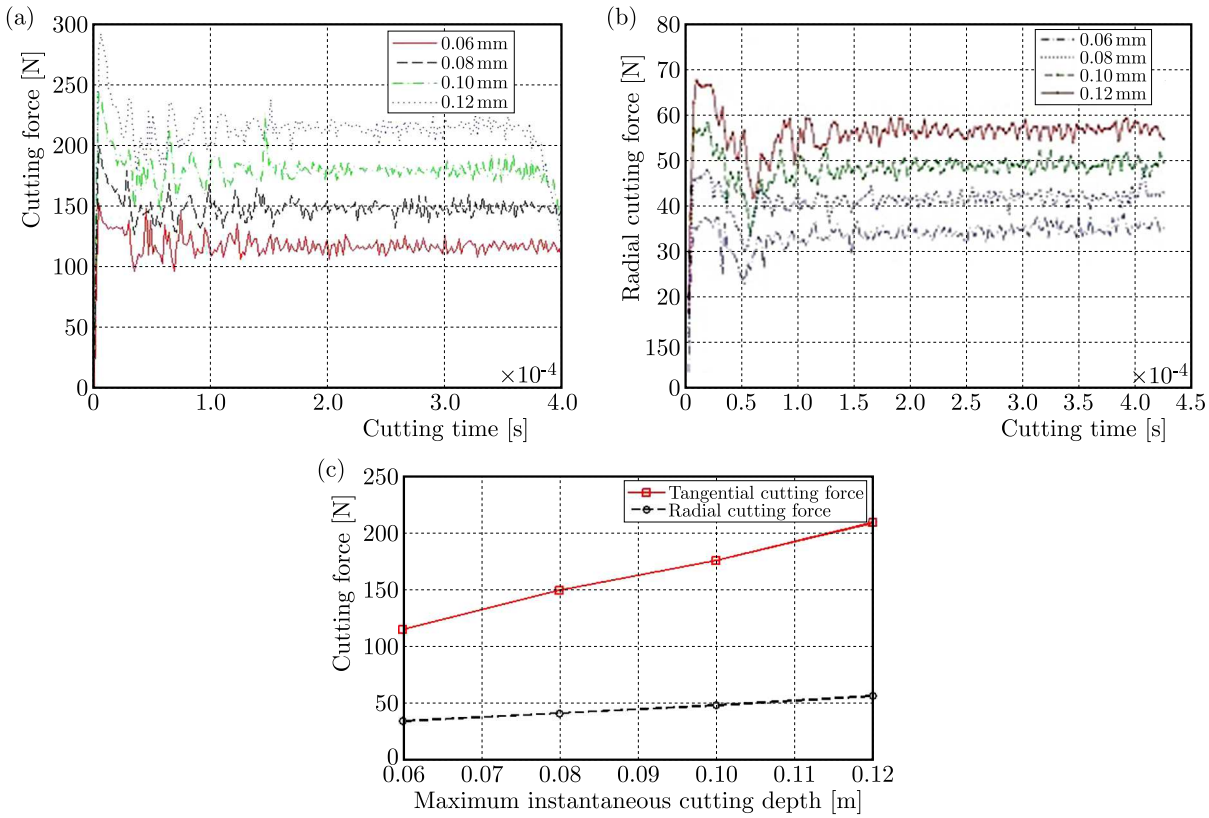

Fig. 5. Variation of (a) tangential, (b) radial cutting force and (c) comparisons under different cutting depths

The residual stresses have significant effects on the quality and life of machined parts. The simulation process was divided into several steps: (1) cutting; (2) retracting tools; (3) transforming constraint; (4) cooling of the workpiece to room temperature. For investigating the influence of cutting depth, three values 0.08 mm, 0.10 mm, 0.12 mm were constructed to predict the residual stress. The other cutting parameters were fixed, as the cutting speed at 3.33 m/s, rake angle at −7° and clearance angle at 5°, respectively.

For simulation, the workpiece was assumed to be residual stress free before the first cut. Figure 8 shows the distribution of residual normal stress S_{11} under different cutting depths. It could be found that the residual stress generated a peak at a certain depth below the machined surface and then decreased gradually to a stable state, fluctuating within a little amplitude. The residual stresses were tested by X-350A Stress Analyzer. A Cr Ka radiation was applied to scan the 211 peak of α-Fe steel. Every layer was successively removed by electrochemical etching to

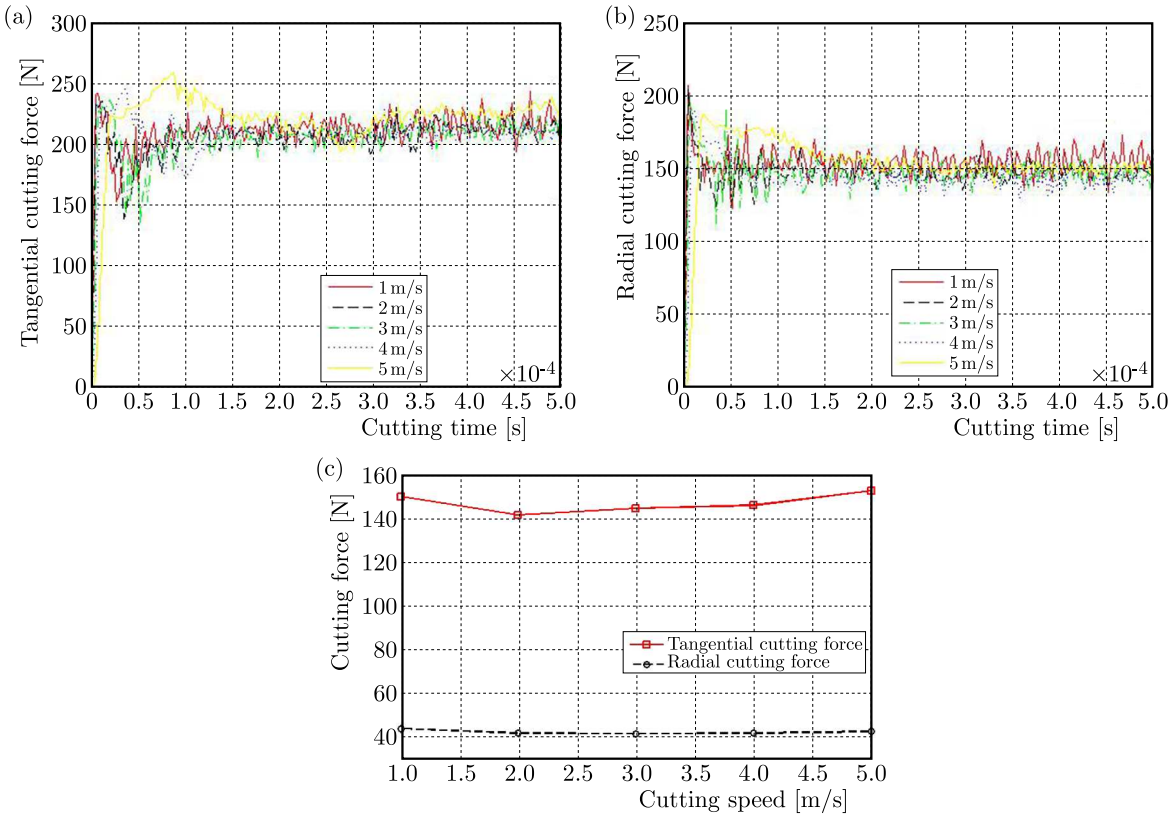

Fig. 6. Variation of (a) tangential, (b) radial cutting force and (c) comparisons under different cutting speeds

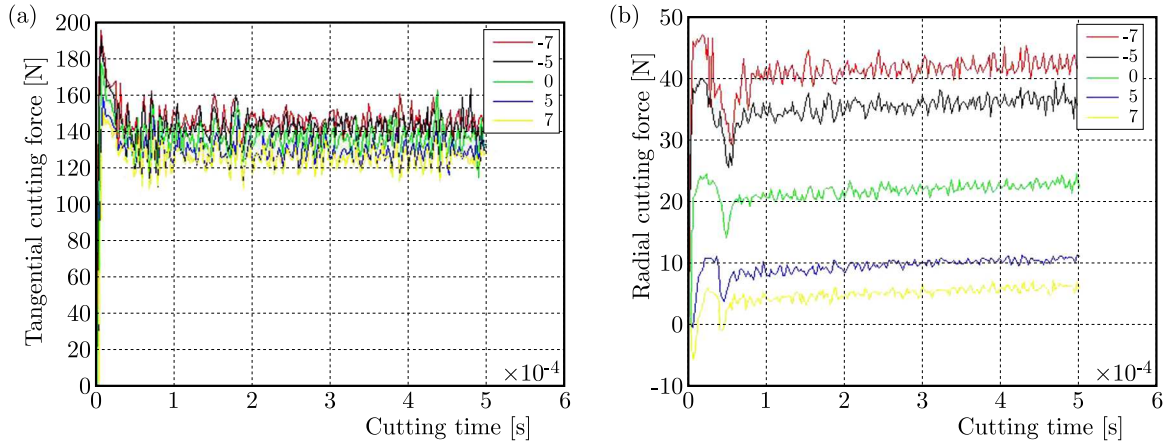

Fig. 7. Variation of (a) tangential and (b) radial cutting force under different rake angles

avoid additional alternation. The tube voltage was set as at 27 kV, and the current 7.5 mA. A 1 mm collimator was used to minimize divergence of the X-ray beam. Under the cutting depth of 0.08 mm, the predicted maximum residual stress was -333 MPa, which was verified by tested data in Fig. 9.

In Table 5, the residual stress S_{11} under three cutting depths was compared. Consistently, as the cutting depth increased, the maximum residual stress and depth of the steady state both increased correspondingly. In the case of cutting depth 0.12 mm, the residual stress reached a peak value of -372 MPa at 0.06 mm below the machined surface and a stable state at depth of 0.24 mm.

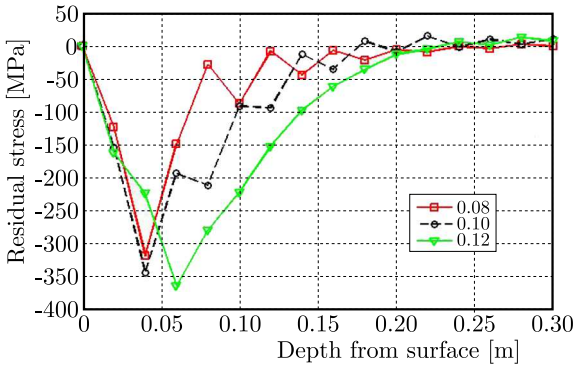

Fig. 8. Variation law of residual stress under different cutting depths

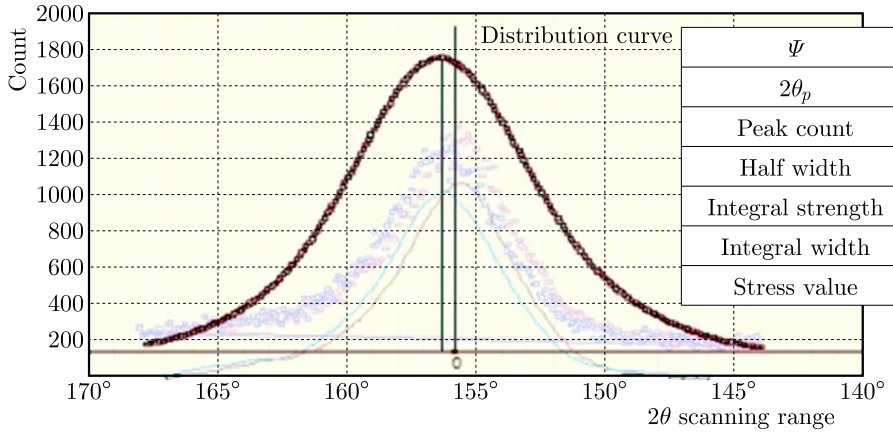

Ψ	0°	45.0°
$2\theta_p$	155.799°	156.338°
Peak count	1066	1012
Half width	5.14°	5.35°
Integral strength	6348.8	6316.6
Integral width	5.96°	6.24°
Stress value	-344 MPa	

Fig. 9. Tested residual stress under cutting depth of 0.08 mm

Table 5. Residual stress under different depths

Cutting depth [mm]	Maximum residual stress [MPa]	Depth of maximum residual stress [mm]	Depth of steady state [mm]
0.08	−333	0.04	0.10
0.10	−347	0.04	0.18
0.12	−372	0.06	0.24

4.2. Simulation of the cutting force and residual stress in the second cutting

For the FEM modeling of the second cutting, the physical state of the machined surface after unloading in the previous cutting was used as the initial condition for the next cutting. Two unloading steps were implemented after each cut: (1) releasing the cutting force; (2) cooling the workpiece down to the room temperature. As depicted in Fig. 10, the next and previous cutting were under the same cutting parameters, that is for the maximum depth 0.08 mm, rake angle −7°, clearance angle 5° and cutting speed 3 m/s. Steps were made as follows step 1 for the first cut (0.06 s), step 2 for the second cut (0.04 s), step 3 for retracting tools, and step 4 for cooling the workpiece down to the room temperature (3 s).

The cutting forces in Fig. 11a decreased slightly and were more stable in the next cutting process. The tangential force decreased by about 3%, and the radial force by about 2%. The residual stress S_{11} in Fig. 11b reached a peak of −333 MPa at 0.04 mm below the machined surface in the first cutting, while compared to that of −351 MPa at 0.045 mm in the second cutting process. The result indicated that the second-cutting process would increase the max-

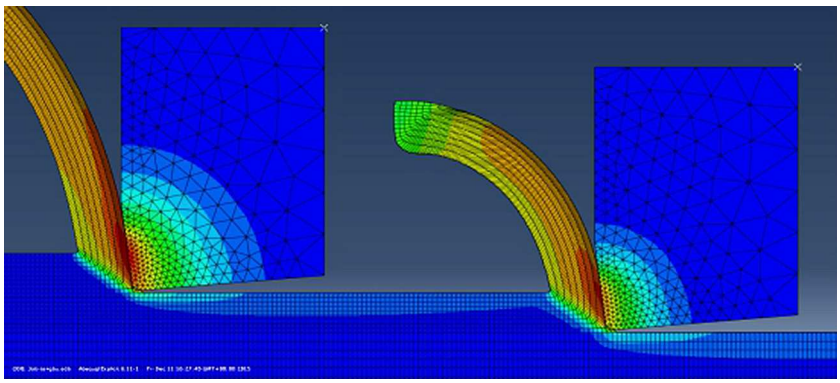

Fig. 10. The cutting morphology under the next cutting and precious cutting

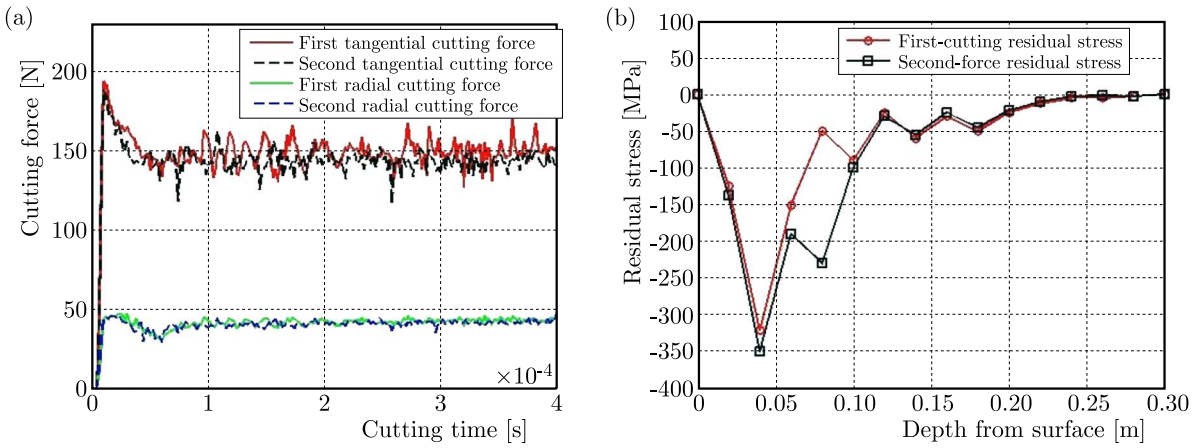

Fig. 11. Comparison of (a) cutting forces, (b) residual stress between the next and previous cutting

imum compressive stress and its distance from the machined surface. Moreover, the depth of compressive stress distribution also increased in the second cutting process.

5. Conclusion

Considering the periodic amplitude-variation of the cutting depth, the FEM models, namely the arc-cutting model, plane-cutting model and plane-second-cutting model, have been developed to analyze the thermo-mechanical process in whirlwind milling of a screw. The effects of cutting parameters on the cutting force and residual stress have been analyzed. Conclusions can be drawn as follows:

- The arc-cutting and plane-cutting FEM model were developed to study the whirlwind milling. The arc-cutting model was used for simulating the actual circular cutting, and the plane-cutting model for simplification and efficient computation. Both models were verified to be effective in predicting the tangential force, while the precision of the plane-cutting model was slightly lower than that of the arc-cutting model for predicting the radial force. Due to the fact that the tangential force is dominant for forming, combined with high efficiency of prediction, the plane-cutting model was preferred to analyze the whirlwind milling.
- The cutting force increased rapidly with the cutting depth, but slowly with the cutting speed and rake angle. The maximum depth of the cut was the dominant factor on the cutting force. The maximum residual stress value as well as depth of the maximum compressive stress layer increased correspondingly with the cutting depth.

- In the plane-second-cutting model, the second cut lowered the cutting force but generated a larger maximum residual stress at a deeper distance. These results would be helpful to optimize the cutting parameters and improve the machined surface integrity in the screw whirlwind milling.

References

1. Bobzin K., Brögelmann T., Maier H. J., Heidenblut T., Kahra C., Carlet M., 2021, Influence of residual stresses in hard tool coatings on the cutting performance, *Journal of Manufacturing Process*, **69**, 340-350
2. Cai S., Yao B., Feng W., Cai Z., 2019, An improved cutting force prediction model in the milling process with a multi-blade face milling cutter based on FEM and NURBS, *International Journal of Advanced Manufacturing Technology*, **104**, 2487-2499
3. Cao P., Zhu Z., Guo X., Wang X., Fu C., Zhang C., 2019, Cutting force and cutting quality during tapered milling of glass magnesium board, *Applied Sciences*, **9**, 12, 2533
4. Chang Y.Y., Sun T., Wang H.C., 2017, Experimental and FEM study of residual stresses during ultra-precision turning of aluminum 2024-T3, *Experimental Techniques*, **42**, 2, 223-231
5. Guo Q., Xie J., Yang W., Xu Y., Wang Y., 2020a, Comprehensive investigation on the residual stress of large screws by whirlwind milling, *International Journal of Advanced Manufacturing Technology*, **106**, 843-850
6. Guo Q., Xu Y., Wang M., Yang W., Wang Y., 2020b, Studies on residue stress and deformation behavior of GC_{r15} subjected to whirlwind milling, *International Journal of Precision Engineering and Manufacturing*, **21**, 3
7. Guo Q., Wang M., Xu Y., Wang Y., 2019, Minimization of surface roughness and tangential cutting force in whirlwind milling of a large screw, *Measurement*, **152**, 3, 107256
8. Han Q.Q., Liu R.L., 2014, Theoretical modeling and error analysis for CNC whirling of the helical surfaces of custom screws using common inserts, *Proceedings of the Institution of Mechanical Engineers, Part C Journal of Mechanical Engineering Science*, **228**, 11, 1948-1957
9. Huang K., Yang W., 2016, Analytical model of temperature field in workpiece machined surface layer in orthogonal cutting, *Journal of Materials Processing Technology*, **229**, 375-389
10. Huang K., Yang W., Chen Q., 2015, Analytical model of stress field in workpiece machined surface layer in orthogonal cutting, *International Journal of Mechanical Sciences*, **103**, 127-140
11. Kara F., Aslantaş K., Çiçek A., 2016, Prediction of cutting temperature in orthogonal machining of AISI 316L using artificial neural network, *Applied Soft Computing*, **38**, 64-74
12. Kundrák J., Karpuschewski B., Pálmai Z., Felhö C., Makkai T., Borysenko D., 2021, The energetic characteristics of milling with changing cross-section in the definition of specific cutting force by FEM method, *CIRP Journal of Manufacturing Science and Technology*, **32**, 12, 61-69
13. Lee M.H., Kang D.B., Son S.M., Ahn J.H., 2008, Investigation of cutting characteristics for worm machining on automatic lathe – comparison of planetary milling and side milling, *Journal of Mechanical Science and Technology*, **22**, 12, 2454-2463
14. Masmiati N., Sarhan A.A.D., Hassan M.A.N., Hamdi M., 2016, Optimization of cutting conditions for minimum residual stress, cutting force and surface roughness in end milling of S50C medium carbon steel, *Measurement*, **86**, 253-265
15. Ni S.Y., Zhu H.Y., Li Y., 2012, A cutting force and temperature measuring device of arbor-type rotary milling cutter, *CN 102554702 A*.

16. Salonitis K., Kolios A., 2015, Experimental and numerical study of grind-hardening-induced residual stresses on AISI 1045 steel, *International Journal of Advanced Manufacturing Technology*, **79**, 9-12, 1443-1452

17. Son Y.K., Lee K.H., Yang K.S., Ko D.C., Kim B.M., 2015, Prediction of residual stress and deformation of enameled steel, *International Journal of Precision Engineering and Manufacturing*, **16**, 7, 1647-1653

18. Tounsi N., El-Wardany T., 2015, Finite element analysis of chip formation and residual stresses induced by sequential cutting in side milling with microns to sub-micron uncut chip thickness and finite cutting edge radius, *Advances in Manufacturing*, **3**, 4, 309-322

19. Wang L., He Y., Wang Y.L., Li Y.F., Liu C., Wang S.L, Wang Y., 2020a, Analytical modeling of material removal mechanism in dry whirling milling process considering geometry, kinematics and mechanics, *International Journal of Mechanical Sciences*, **172**, 105419

20. Wang H., Wang J.Y., Zhang J.M., Tao K., Wu D., 2020b, Identification and analysis of cutting force coefficients in the helical milling process, *Journal of Advanced Mechanical Design, Systems, and Manufacturing*, **14**, 1

21. Wang J., Zuo J, Shang Z, Fan X., 2019, Modeling of cutting force prediction in machining high-volume SiCp/Al composites, *Applied Mathematical Modelling*, **70**, 1-17

22. Wang Y., Yin C., Li L., Zha W., Pu X., Wang Y., Wang J., He Y., 2020c, Modeling and optimization of dynamic performances of large-scale lead screws whirl milling with multi-point variable constraints, *Journal of Materials Processing Technology*, **276**, 116392

23. Yan H.E., Liu C., Yufeng, L.I., Wang L., Wang Y., 2018, Transient thermal and analytical model of whirling process based on time-varying heat source in machining screw, *Journal of Mechanical Engineering*

24. Zanger F., Sellmeier V., Klose J., Bartkowiak M., Schulze V., 2017, Comparison of modeling methods to determine cutting tool profile for conventional and synchronized whirling, *Procedia CIRP*, **58**, 222-227

25. Zhou J., Ren J., 2020, Predicting cutting force with unequal division parallel-sided shear zone model for orthogonal cutting, *International Journal of Advanced Manufacturing Technology*, **107**, 42014211

Manuscript received June 18, 2022; accepted for print October 24, 2022

JOURNAL OF THEORETICAL AND APPLIED MECHANICS
61, 1, pp. 77-87, Warsaw 2023
https://doi.org/10.15632/jtam-pl/157583

COMPARATIVE EVALUATION OF WEAR BEHAVIOR OF TRIBO-PAIRS IN RECIPROCATING PUMPS WITH MULTIPLE MATERIALS UNDER DIFFERENT CONDITIONS

Ran Li
Graduate School, China Coal Research Institute, Beijing, China, and
Beijing Tianma Intelligent Control Technology Co., Ltd. Beijing, China

Wenshu Wei, Hao Liu
Beijing Tianma Intelligent Control Technology Co., Ltd. Beijing, China

Dalong Wang
School of Mechanical Electronic and Information Engineering, China University of Mining and Technology Beijing, Beijing, China; e-mail: wangdl@student.cumtb.edu.cn

Jian Ye, Shoubin Li, Wei Wang, Huigang Wu
Beijing Tianma Intelligent Control Technology Co., Ltd. Beijing, China

In the study of wear behavior of tribo-pairs in reciprocating pumps, the tribo-pairs can be considered as contact pairs consisting of a disc and pin. In this paper, pin-on-disc wear tests were carried out by using two types of cast iron pin specimens with different materials. Additionally, the effects of the lubrication condition, test load, diamond-like carbon (DLC) coating and plateau honing cross-hatch pattern on wear behavior of the tribo-pairs were investigated. Experimental results based on surface topography analysis and scanning electron micrograph (SEM) analysis show that the lubricant and DLC coating have a positive effect on wear resistance of test specimens. Disc specimens of three material types (i.e. ISO 185/JL/250, tin-bronze, zirconia) are able to show good anti-wear behavior. The tribo-pairs composed of spheroidal graphite cast irons as well as implementation of the plateau honing cross hatch on disc specimens have no significant effect on the wear resistance. The Archard model was used to estimate abrasive wear under dry conditions, which was over-predicted compared to the experimental results.

Keywords: reciprocating pump, tribo-pairs, cast iron pin, wear behavior, wear resistance

1. Introduction

Tribo-pairs in reciprocating pumps consist of crossheads and crosshead bushings, which are often subjected to reverse loads during normal service operation (Li *et al.*, 2021). A potential failure of tribo-pairs is usually associated with destructive debris produced by wear. Due to fragility of the crosshead, it is critical to use compatible materials for the crossheads and crosshead bushings to improve wear resistance. It is therefore important and necessary to understand and be able to predict wear behavior of high-speed tribo-pairs of reciprocating pumps (Miller, 1987). Several standard test methods are available for measuring the friction coefficient and wear performance of tribo-pairs, such as ASTM D6425 and DIN 51834 (ASTM, 2010; Woydt and Ebrecht, 2003).

Cast iron is widely used in the manufacturing of many reciprocating pump parts, such as crankshaft case, crossheads, crosshead bushings, etc. Numerous studies have been carried out on the wear behavior of different cast irons. Mohamadzadeh *et al.* (2009) reported on sliding wear behavior of a gray cast iron surface remelted by tungsten inert gas. Saeidi *et al.* (2016) studied the effect of laser surface texturing on friction behavior and lifetime of grey cast iron

reciprocating under starved lubrication conditions. Through development of fractional factorial design, five geometrical texture parameters (feature depth, diameter, length, area fraction and sliding direction) were studied using a design of experiments (DoE), and the reciprocal sliding tests were carried out for a cast iron-steel tribo-pair at a pressure of 24 MPa and a frequency of 6 Hz. Ausserer *et al.* (2016) investigated the influence of various industrially used gases (Ar, N_2, CO_2 and air) on tribological behavior of steel-steel contacts. Cabanettes *et al.* (2015) proposed to map variations in roughness of a cylinder liner by using confocal 3D measuring equipment, and computed tailor made parameters extracting honing texture information. Khanlari *et al.* (2018) conducted a series of ball (WC)-on-plate reciprocating sliding wear tests under moderate and extreme sliding induced stress conditions to illustrate how 58Ni39Ti-3Hf responds as compared to 60NiTi. In addition, to fully understand the reasons causing divergence in the wear response of both materials, they investigated and compared mechanical and micro-tribological properties of these two alloys by means of indentation, hardness and scratch tests. Carrera-Espinoza *et al.* (2016) evaluated tribological properties at the surface of borided and unborided steel employing the ball-on-flat method with sliding reciprocating wear tests, using an Al2O3 ball as the counterpart. In addition, they evaluated coefficients of friction (CoFs) on the boride layers from sliding reciprocating wear tests for dry and lubricated conditions. Ayyagari *et al.* (2018) evaluated reciprocating sliding wear behavior of two high entropy alloys, CoCrFeMnNi and Al0.1CoCrFeNi, in dry and marine environments. Onuoha *et al.* (2016) evaluated sliding wear resistance of TiC cermets in a reciprocating motion using a WC-Co counter face sphere paired against the TiC cermets. Kim *et al.* (2018) compared lubricity of sliding cylinder liner surfaces under different plateau honing marks by friction and wear tests with reciprocating motion. Balarini *et al.* (2020) investigated the influence of both reciprocating and unidirectional rotating tribotests on the tribological performance of MoDTC-containing oils. Dang *et al.* (2020) first systematically studied the effect of Mo element concentration on the crystal lattice constant, microhardness and reciprocating dry sliding friction and wear properties of face-centered cubic (FCC) single phase based CoCrFeNiMo high entropy alloys (HEAs). Liu *et al.* (2021) studied tribological behavior of two types of DLC coatings deposited on GCr15 substrates. Okubo *et al.* (2021) investigated tribological properties of DLC network nanostructures in contact with DLC/steel in a formulated engine oil. Many studies (Malburg *et al.*, 1993; Jocsak *et al.*, 2005; Gore *et al.*, 2011) have shown that the plateau honing cross hatch surface finish method can effectively reduce friction and wear. Kim *et al.* (2021) investigated performance and side effects of uneven plateau-honed surfaces, and conducted friction, wear and failure tests to compare the the performance of the plateau-honed surfaces with different levels of roughness and different profiles.

In this paper, the results of pin-on-disc wear tests carried out on two types of cast iron pin specimens (i.e. ISO 1083/JS/600-3, ISO 185/JL/250) and disc specimens made of different materials under dry, lubrication and DLC coating conditions, were presented. Moreover, the effects of lubrication conditions, test loads, DLC coating and plateau honing cross-hatch patterns on wear behavior of tribo-pairs were investigated. The results of the wear tests were determined on the basis of the friction coefficient and wear weight. Surface topography analysis and scanning electron micrograph (SEM) analysis were conducted on the surface of the test disc, which was helpful to reveal the wear mechanism of test specimens.

2. Experiments

The test specimens of pin and disc used in this paper are shown in Fig. 1. The test pin has a diameter of 15 mm and a height of 22 ± 0.05 mm; the test disc has a diameter of 24 mm and a height of 7.85 ± 0.05 mm. The test pin specimens are made of two basic materials, namely

spheroidal graphite cast iron (ISO 1083/JS/600-3) and grey cast iron (ISO 185/JL/250). Some ISO 1083/JS/600-3 test pin specimens were deposited by DLC coating. Six materials were used for test specimens of disc, namely ISO 1083/JS/400-18, ISO 1083/JS/500-10, ISO 185/JL/250, grey cast iron (L161), tin-bronze and zirconia. The material properties of L161, tin-bronze, zirconia are shown in Table 1.

Fig. 1. Test specimens of pin and disc

Table 1. Material properties of L161, tin-bronze, zirconia [wt%]

Materials	L161	Tin-bronze	Materials	Zirconia
C	2.9-3.7	–	CaO	0.0074
Si	1.8-2.6	0.005	MgO	0.0096
Mn	0.5-1.0	–	K_2O	0.00058
P	0.1-0.4	1.5	Na_2O	0.0011
S	< 0.12	0.08	Fe_2O_3	0.0052
Cr	0.1-0.4	–	SiO_2	0.36
Cu	0.3-0.5	81.0-85.0	Al_2O_3	0.75
B	0.03-0.08	–	TiO_2	0.014
Sn	–	6.3-7.5	ZrO_2	92.54
Pb	–	6.0-8.0	Y_2O_3	5.84
Zn	–	2.0-4.0		
Al	–	0.005		

The DLC coating was deposited on the test disc using a non-equilibrium magnetron sputtering process, including two layers of Cr/WC on the bottom and TAC on the top. The L161 test disc was made using a complete liner whose inner surface was plateau honed in a 45° cross-hatch pattern. The test disc specimen and its position in the complete liner are shown in Fig. 2. The unhoned surface of the pieces cut from the complete liner was machined flat to assist in the installation of the test disc.

The SRV® IV test apparatus was used in this study. Figure 3 shows the test chamber of the SRV® IV test apparatus. The apparatus consists mainly of the upper specimen holder, lower specimen holder, swing arm and the pressure sensor. The upper and lower specimen holders are designed to accommodate the pin and disc specimens, respectively. The swing arm is used for providing vibratory movements of the pin specimens. The pressure sensors are used to interpret the test data. The constant test parameters, i.e., a frequency of 50 Hz, temperature of 50°C, stroke of 1 mm, test duration of 1 h, were applied to the wear test.

Three groups of wear tests were designed and performed under ISO-VG 220 lubricant and dry conditions with test loads of 30 N and 100 N, respectively. The first group of tests was designed for investigating the effect of DLC coatings on friction and wear behavior for the ISO 1083/JS/600-3 test pin specimens sliding against ISO 1083/JS/400-18 and ISO 185/JL/250 test

Fig. 2. Representation of L161 disc specimens made from the complete liner

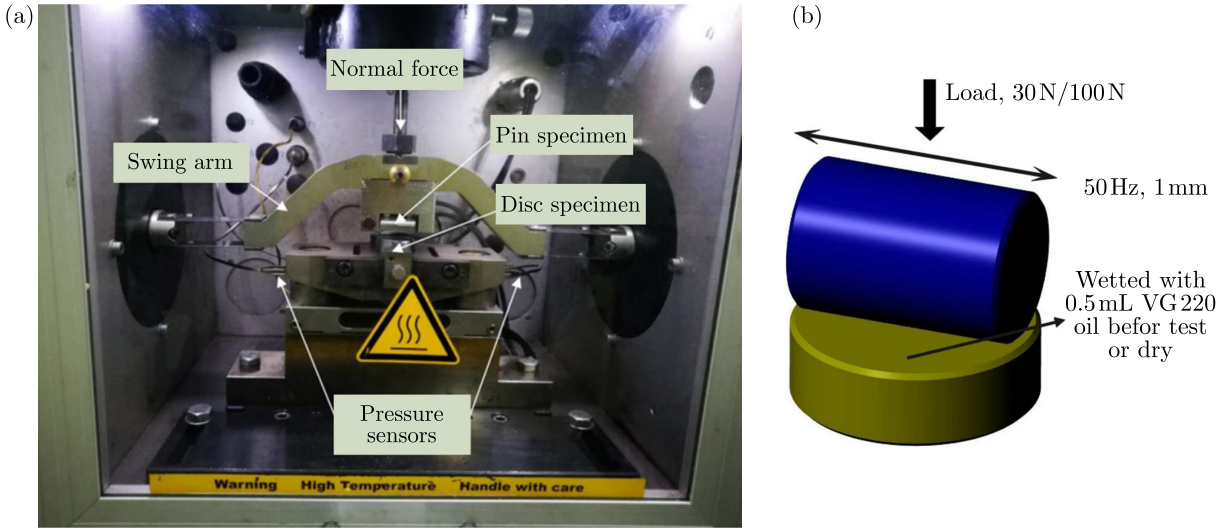

Fig. 3. (a) Test chamber of the SRV® IV test apparatus, (b) schematic representation of the pin-on-disc test specimens

disc specimens. The second and third groups of tests were designed for studying friction and wear behavoir for the ISO 1083/JS/600-3 and ISO 185/JL/250 test pin specimens sliding against different materials, which aims at distinguishing the more suitable tribo-pairs in reciporcating pumps.

3. Results and analysis

3.1. Test results of the friction coefficient and wear weight

Figure 4 shows the typical result for variation in friction coefficients of the ISO 185/JL/250 sliding against ISO 185/JL/250. An electronic balance with accuracy of 0.01 mg was used to measure wear weight of the test discs. The wear rate $W+s$ [mm^3/Nm] of materials, as proposed by previous studies (Zhang *et al.*, 2015; Yin *et al.*, 2021), is given by

$$W_s = \frac{\Delta m}{\rho N L} \tag{B.1}$$

where ρ is density of the worn material, N is the normal load, L is the total sliding distance, and Δm is the wear weight.

Table 2 summarises the test results expressed by the friction coefficient of all specimens and the wear weight and wear rates of the test discs. As can be seen from Table 2, the friction

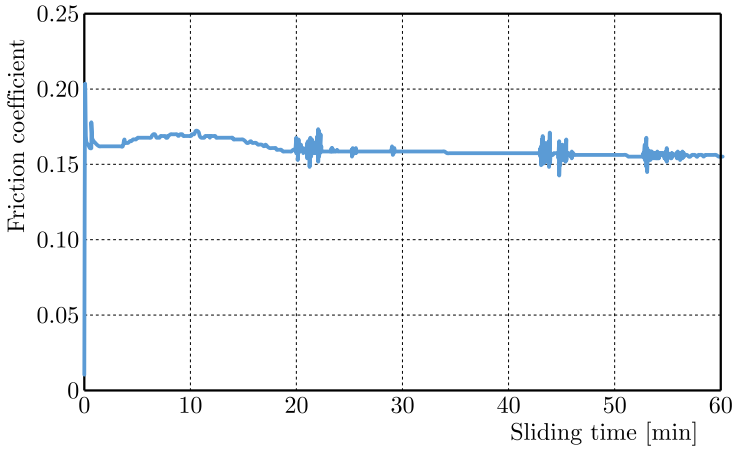

Fig. 4. Variation in friction coefficients of the ISO 185/JL/250 sliding against ISO 185/JL/250

Table 2. Test conditions and test results

Test gr.	Pin specimen	Disc specimen	Lubrication	Normal force [N]	COF	Wear weight [mg]	W_s [10^{-6} mm^3/Nm]
1	ISO 1083/JS/600-3	ISO 1083/JS/400-18	Dry	30	1.088	2.88	37.558
		ISO 185/JL/250	Dry	30	1.023	3.98	54.194
	ISO 1083/JS/600-3 with DLC coating	ISO 1083/JS/400-18	Dry	30	0.567	1.78	23.213
		ISO 485/JL/250	Dry	30	0.496	2.08	28.322
	ISO 1083/JS/600-3 with DLC coating	ISO 1083/JS/400-18	Dry	100	0.678	14.7	57.512
		ISO 185/JL/250	Dry	100	0.601	3.12	12.745
2	ISO 1083/JS/600-3	ISO 1083/JS/400-18	VG 220	100	0.175	0.11	0.430
		ISO 185/JL/250	VG 220	100	0.16	0.19	0.776
		ISO 1083/JS/500-10	VG 220	100	0.166	0.26	1.017
		L161	VG 220	100	0.157	0.59	2.410
		Tin-bronze	VG 220	100	0.167	0	0
		Zirconia	VG 220	100	0.155	0.04	0.190
3	ISO 185/JL/250	ISO 185/JL/250	VG 220	100	0.163	0.37	1.511
		L161	VG 220	100	0.164	0.38	1.552
		Tin-bronze	VG 220	100	0.163	0	0
		Zirconia	VG 220	100	0.164	0.08	0.380

coefficients of ISO 1083/JS/600-3 test pins with DLC coating and without DLC coating vary from 0.496 to 1.088 under the dry condition, and the friction coefficients for both ISO 1083/JS/600-3 and ISO 185/JL/250 test pins sliding against different test discs are almost the same, i.e. by a value of 0.16 under the lubrication condition. For the lubraication condition, the smallest wear rates are obtained for the tin-bronze and zirconia test discs sliding aginst both the ISO 1083/JS/600-3 and ISO 185/JL/250 test pins.

3.2. Test results of the surface profile

In order to investigate the effect of the DLC coating and lubrication conditions on wear of the test discs, the surface profile of the specimens was analyzed in detail using the white light interferometry method. This method can measure the rough surface profile of an object, as shown in Figs. 5 and 6, which are the surface profiles of ISO 185/JL/250 and ISO 1083/JS/400--18 test disc specimens under different working conditions. Figure 5a shows the surface profile of an ISO 185/JL/250 test disc specimen tested with an ISO 1083/JS/600-3 test pin specimen

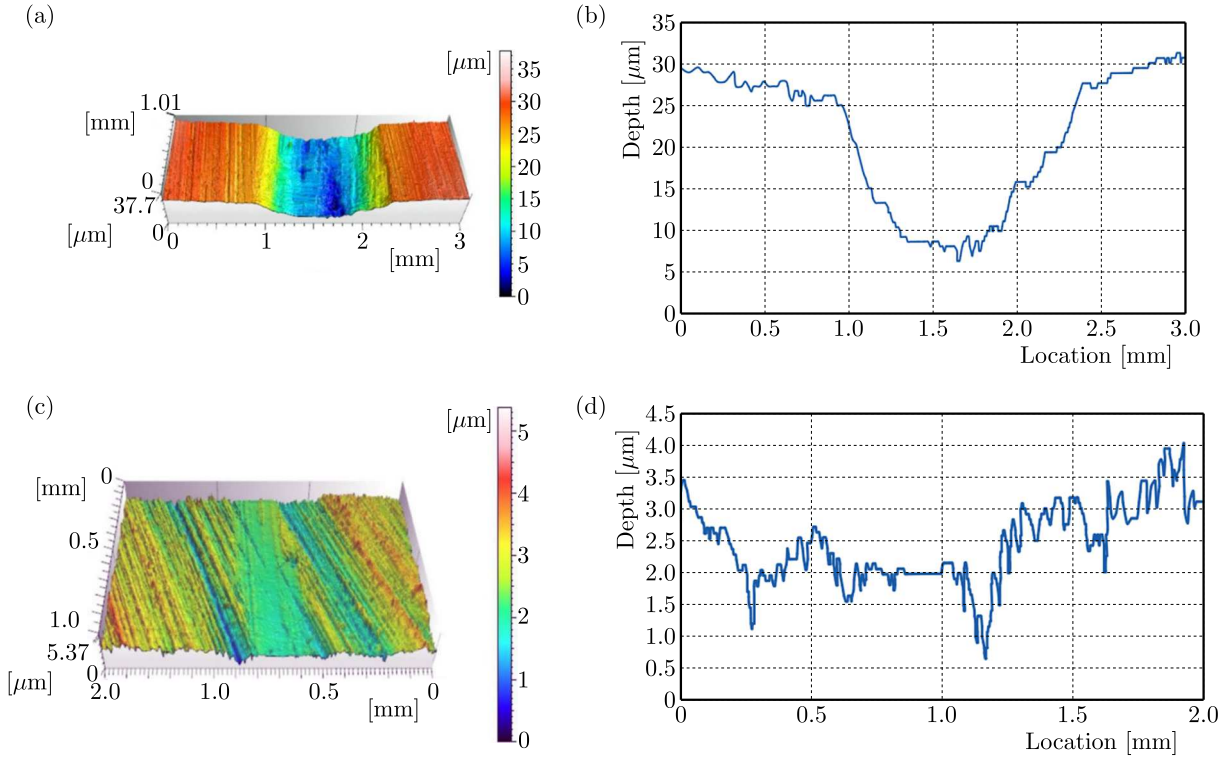

Fig. 5. The profiles of ISO 185/JL/250 test discs under different conditions: (a) 3D profile under dry condition, (b) 2D profile in depth under dry condition, (c) 3D profile under lubrication condition, (d) 2D profile in depth under lubrication condition

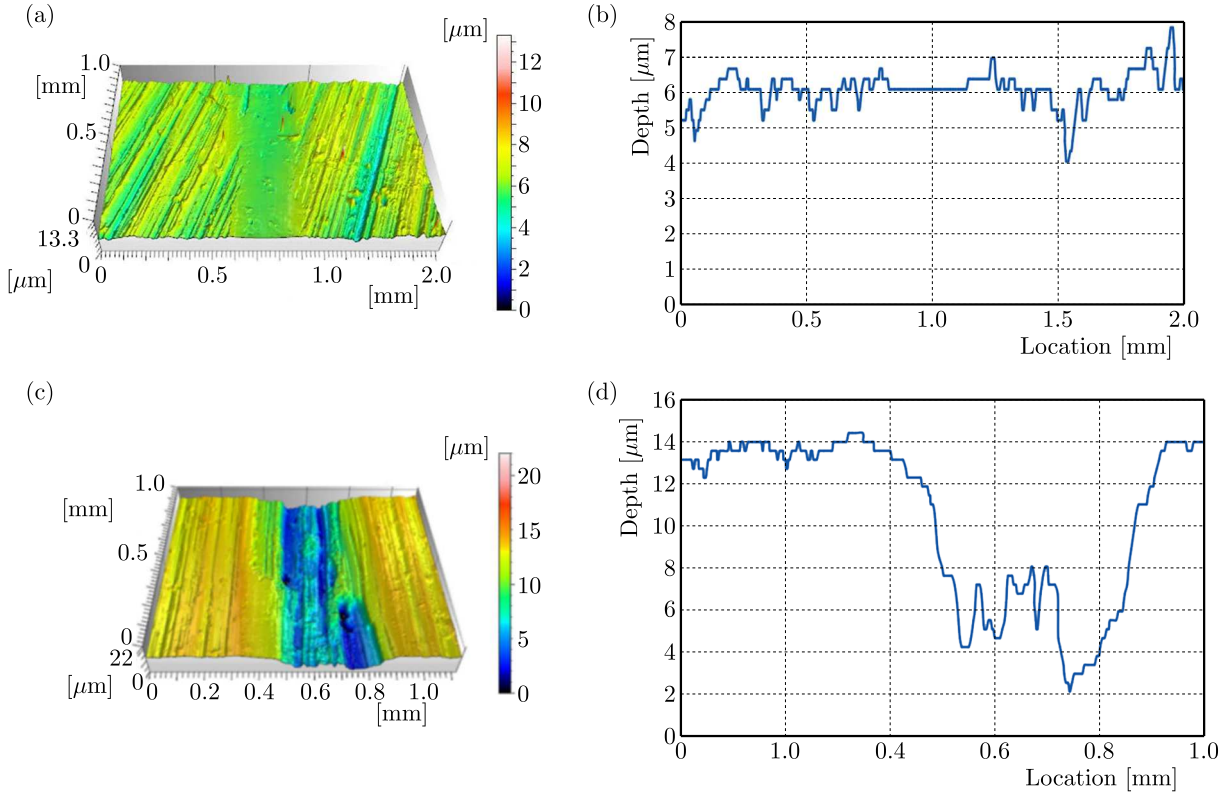

Fig. 6. The profiles of ISO 1083/JS/400-18 test discs under different condition: (a) 3D profile of the ISO 1083/JS/400-18 test disc tested with the ISO 1083/JS/600-3 test pin with DLC coating, (b) 2D profile in depth of the ISO 1083/JS/400-18 test disc tested with the ISO 1083/JS/600-3 test pin with DLC coating, (c) 3D profile of the ISO 1083/JS/400-18 test disc tested with the ISO 1083/JS/600-3 test pin without DLC coating, (d) 2D profile of the ISO 1083/JS/400-18 test disc tested with the ISO 1083/JS/600-3 test pin without DLC coating

under the unlubricated condition and a test load of 30 N. Figure 5b shows the corresponding 2D profile curve, Fig. 5c shows the surface profile of an ISO 185/JL/250 test disc specimen tested with an ISO 1083/JS/600-3 test pin specimen under the condition of lubrication and a test load of 100 N, Fig. 5d shows the corresponding 2D profile curve. As can be seen from the 2D profile curve (Fig. 5b), the wear depth in the x-coordinate direction is approximately 23 μm for unlubricated conditions. Comparing the 2D profile curves ((b) and (d)) under the two working conditions, it can be seen that the surface profile of the test area of the ISO 185/JL/250 test disc is relatively flat under lubrication conditions despite the increased test load, which indicates that the introduction of lubrication has a significant impact on roughness of the ISO 185/JL/250 test disc. Figures 6a-6d show the surface profile of ISO 1083/JS/400-18 test disc specimens tested using two types of ISO 1083/JS/600-3 test pin specimens (with and without DLC coating) with lubrication and a test load of 100 N. As can be seen from the 2D profile curve (Fig. 6b), the wear depth in the x-coordinate direction is approximately 11 μm. The surface of the ISO 1083/JS/400-18 test disc tested with ISO 1083/JS/600-3 test pin specimens with DLC coating shows good wear resistance.

3.3. Wear surface morphology analysis

Figure 7 shows SEM photographs of the wear scar of test disc specimens tested with the ISO 1083/JS/600-3 test pin under different conditions. It can be seen from Fig. 7a that severe

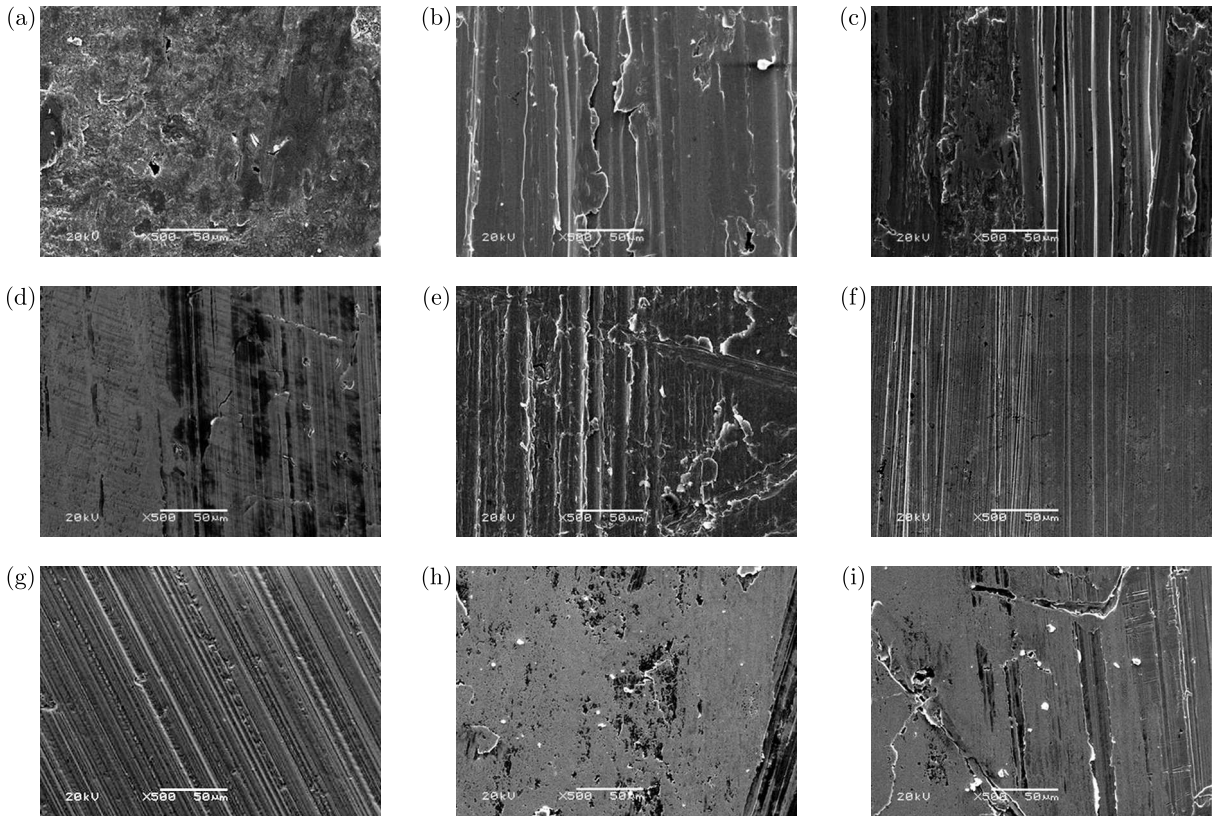

Fig. 7. SEM morphology of test disc specimens: (a) ISO 1083/JS/400-18 test disc, (b) ISO 1083/JS/400-18 test disc, (c) ISO 1083/JS/500-10 test disc, (d) ISO 185/JL/250 test disc, (e) L161 test disc, (f) tin-bronze test disc, (g) zirconia test disc, (h) ISO 1083/JS/400-18 test disc tested with test pin specimens with DLC coating, (i) ISO 185/JL/250 test disc tested with test pin specimens with DLC coating

adhesive wear occurs on the ISO 1083/JS/400-18 test disc under dry conditions. Compared with that, the wear degree of the ISO 1083/JS/400-18 test disc is alleviated due to the introduction of

lubrication, as shown in Fig. 7b. The wear behavior of the ISO 1083/JS/500-10 test disc under lubrication condition is shown in Fig. 7c. It can be seen from Fig. 7c that the delaminated areas are associated with the abrasive grooves and microcracks formed on the contoured surface of the ISO 1083/JS/500-10 test disc. In Fig. 7d, it is observed that the ISO 185/JL/250 test disc shows good wear resistance. Abrasive grooves can be clearly seen on L161 test disc in Fig. 7e, similar to the results shown in Fig. 7b,c. As shown in Fig. 7f,g, it is observed that there are shallow furrow scratches on the surface of the tin-bronze test disc, while the zirconia test disc has good wear resistance. Figures 7h,i show the effect of test pin specimens with DLC coating on the sliding wear performance of the ISO 1083/JS/400-18 and ISO 185/JL/250 test discs. It is found that for the ISO 1083/JS/400-18 test discs, the wear resistance can be improved by using DLC coating on the end face of the test pin. However, the introduction of DLC coating on the back of the test pin has no significant effect on the ISO 185/JL/250 test disc.

Figure 7 shows SEM photographs of the test disc specimens tested with the ISO 185/JL/250 test pin, and SEM photographs of the test disc specimens made of various materials under the test load of 100 N and lubrication conditions. Similar to the results shown in Fig. 7i, the ISO 185/JL/250 test disc has good wear resistance as shown in Fig. 8a. It can be seen form Fig. 8b, the wear degree of L161 test disc is relatively weak compared with the wear results of the test disc tested with the ISO 1083/JS/600-3 test pin (Fig. 7e). The wear behavior of the tin bronze and zirconia test discs is consistent with the wear results of the wear test using the ISO 1083/JS/600-3 test pin, as shown in Fig. 7d.

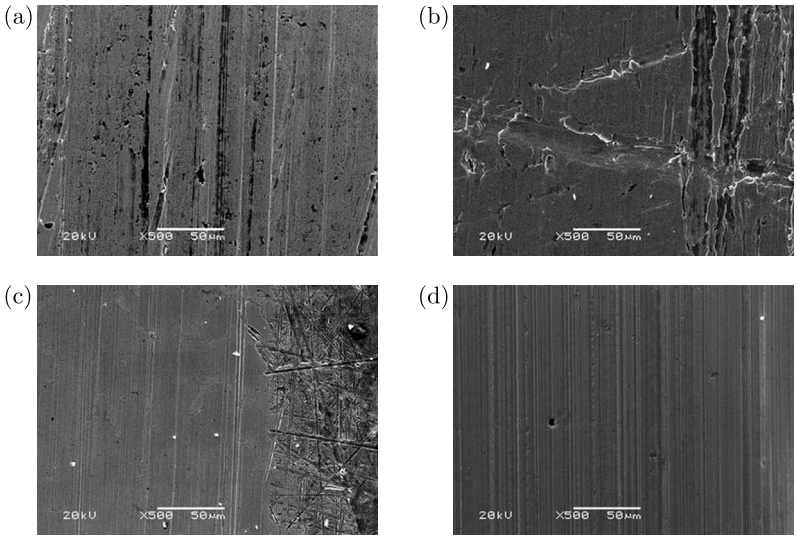

Fig. 8. SEM morphology of test disc specimens: (a) ISO 185/JL/250 disc, (b) L161 disc, (c) tin-bronze, (d) zirconia disc

4. Discussion

4.1. Influence of lubrication

The friction coefficient of tribo-pairs of the ISO 1083/JS/600-3 test pin and ISO 185/JL/250 test disc and the ISO 1083/JS/600-3 test pin and ISO 1083/JS/400-18 test disc under unlubricated conditions (test load of 30 N) is approximately 5 times higher than that under lubrication conditions (test load of 100 N).

The well-know adhesive wear model proposed by Archard is shown as

$$V_c = K\frac{LS}{H} \tag{B.1}$$

where V_c is the volume wear per unit sliding stroke, L is the load, H is the hardness, S is the sliding stroke, and K is the abrasive wear coefficient. The abrasive wear coefficient of a cast iron/cast iron pair under dry conditions is approximately $9.9 \cdot 10^{-4}$ (Rajkumar and Aravindan, 2013).

The hardness H and density ρ of the ISO 185/JL/250 test disc are 180 HV and 7.0 g/cm^3, respectively. Therefore, the wear weight of the ISO 185/JL/250 test disc can be calculated as the product of the volume wear per unit sliding stroke V_c, frequency f, test duration t and density ρ, which is in a value of 208 mg. The result obtained based on the Archard model overpredicts the adhesive wear, which may be due to the estimation of the abrasive wear coefficient K of the tribo-pairs of the 1083/JS/600-3 test pin and ISO 185/JL/250 test disc.

4.2. Material selection of crosshead liners

It is very important to select appropriate materials for crosshead liners, which can minimize wear caused by reciprocating motion of the crosshead in a reciprocating pump. As shown in Section 3, for ISO 1083/JS/600-3 and ISO 185/JL/250 test pin specimens, test disc specimens made of ISO 185/JL/250, tin-bronze, zirconia materials have good wear resistance. The test results suggest that the ISO 185/JL/250, tin-bronze, zirconia discs may be more suitable considering raw materials of the crosshead liner in a reciprocating pump.

4.3. Influence of DLC coating and plateau honing

Under the test load of 100 N and lubrication conditions, the friction coefficient between the ISO 1083/JS/500-10 and ISO 185/JL/250 test disc and the ISO 1083/JS/600-3 test pin end face is very similar to that between the ISO 1083/JS/500-10 and ISO 185/JL/250 test disc and test pin without DLC coating. Under dry conditions, the DLC coating method using the test load of 100 N shows good wear resistance in terms of the friction coefficient and wear weight compared with the results of the ISO 1083/JS/600-3 test pin without DLC coating using the test load of 30 N. The effect of the plateau honing method on wear resistance is not significant. For L161 test disc, the surface should be matched to ISO 1083/JS/600-3 and ISO 185/JL/250 test pins. Zhang *et al.* (2015) reported that the plateau honing method resulted in higher steady-state friction levels compared to other surface finish methods, which might relate to the intersection angle, surface roughness and lubrication conditions.

5. Conclusions

In this study, in order to explore wear behavior of tribo-pairs in a reciprocating pump, pin-on-disc wear tests under dry, lubrication conditions and DLC coating were carried out. The conclusions are as follows:

- The presence of a lubricant has a significant effect on wear behavior of tested specimens. The friction coefficients under a normal load of 30 N under dry conditions are approximately 5 times higher than those under a normal load of 100 N in VG 220 lubricated conditions.
- The tribo-pairs consisting of spheroidal graphite cast iron materials are most likely to cause abrasive wear. Test disc specimens made of ISO 185/JL/250, tin-bronze and zirconia show good wear resistance against two cast iron test pin specimens, which indicates the capability to be used as the linear raw material for crossheads.
- The DLC coating can improve tribological behavior of test pin substrate materials under lubricated sliding conditions. However, the plateau honing approach has little effect on the wear resistance of the tested disc specimens.

Acknowledgment

This research was funded by National Key Research and Development Program of China (2017YFC0804300, 2017YFC0804304) and CCTEG Project of China (2020-TD-ZD015).

References

1. ASTM D., 2010, 6425: Standard test method for measuring friction and wear properties of extreme pressure (EP) lubricating oils using SRV test machine, ASTM International
2. Ausserer F., Klien S., Velkavrh I., Forêt P., Diem A., 2016, Investigations of the sliding and wear behaviour in various gaseous atmospheres using a SRV testing apparatus, *Tribologie und Schmierungstechnik*, **63**, 1, 22-28
3. Ayyagari A., Barthelemy C., Gwalani B., Banerjee R., Scharf T.W., Mukherjee S., 2018, Reciprocating sliding wear behavior of high entropy alloys in dry and marine environments, *Materials Chemistry and Physics*, **210**, 162-169
4. Balarini R., Diniz G.A.S., Profito F.J., Souza R.M.D., 2020, Comparison of unidirectional and reciprocating tribometers in tests with MoDTC-containing oils under boundary lubrication, *Tribology International*, **149**, 105686
5. Cabanettes F., Dimkovski Z., Rosén B.G., 2015, Roughness variations in cylinder liners induced by honing tools' wear, *Precision Engineering*, **41**, 40-46
6. Carrera-Espinoza R., Figueroa-López U., Martínez-Trinidad J., Campos-Silva I., Hernández-Sánchez E., Motallebzadeh A., 2016, Tribological behavior of borided AISI 1018 steel under linear reciprocating sliding conditions, *Wear*, **362-363**, 1-7
7. Dang G., Tieu A.K., Su L., Wang P., Wang L., Lan X., Cui S., Zhu H., 2020, Investigation into reciprocating dry sliding friction and wear properties of bulk CoCrFeNiMo high entropy alloys fabricated by spark plasma sintering and subsequent cold rolling processes: Role of Mo element concentration, *Wear*, **460-461**,15, 203440
8. Gore M., Perera M., Styles G., King P.D., Rahnejat H., 2011, Wear characteristics of advanced honed and cross-hatched coated cylinder liners, *Proceedings of the 66th annual meeting and exhibition of the STLE*, **73**, 1-6
9. ISO-14242-2, 2016, Implants for surgery-wear of total hip-joint prostheses – Part 2: Methods of measurement
10. Jocsak J., Tomanik E., Wong V.W., Tian T., 2005, The characterization and simulation of cylinder liner surface finishes, *ASME Internal Combustion Engine Division Spring Technical Conference*, **41847**, 457-467
11. Khanlari K., Ramezani M., Kelly P., Cao P., Neitzert T., 2018, Comparison of the reciprocating sliding wear of 58Ni39Ti-3Hf alloy and baseline 60NiTi, *Wear*, **408-409**, 15, 120-130
12. Kim E.-S, Kim S.-M., Lee Y.-Z., 2018, The effect of plateau honing on the friction and wear of cylinder liners, *Wear*, **400**, 15, 207-212
13. Kim E.-S., Lee Y.-Z., 2021, Investigation of the effects of uneven plateau grinding on friction, wear rate, and localized surface damage on internal combustion engine cylinder liners, *International Journal of Automotive Technology*, **22**, 3, 561-567
14. Li R., Wang D.L., Wei, W., Li, S., 2021, Analysis of the movement characteristics of the pump valve of the mine emulsion pump based on the internet of things and cellular automata, *Mobile Information Systems*, **2021**
15. Liu K., Kang J.J., Zhang G.A., Lu Z.B., Yue W., 2021, Effect of temperature and mating pair on tribological properties of DLC and GLC coatings under high pressure lubricated by MoDTC and ZDDP, *Friction*, **9**, 6, 1390-1405

16. Malburg M.C., Raja J., Whitehouse D.J., 1993, Characterization of surface texture generated by plateau honing process, *CIRP Annals*, **42**, 1, 637-639

17. Miller J.E, 1987, *The Reciprocating Pump: Theory, Design, and Use*, Wiley-Interscience

18. Mohamadzadeh H., Saghafiany H., Kheirandish S., 2009, Sliding wear behavior of a grey cast iron surface remelted by TIG, *Journal of Materials Science and Technology*, **25**, 5, 622

19. Okubo H., Watanabe S., Sasaki S., Tokuta Y., Moriguchi H., Iba D., Moriwaki I., 2021, Tribological properties of a Mesh-Like nanostructured Diamond-Like Carbon (DLC) lubricated with a fully formulated oil at DLC/Steel contacts under boundary lubrication, *Coatings*, **11**, 7, 746

20. Onuoha C., Jin C., Farhat Z.N., Kipouros G.J., Plucknett K., 2016, The effects of TiC grain size and steel binder content on the reciprocating wear behaviour of TiC-316L stainless steel cermets, *Wear*, **350-351**, 15, 116-129

21. Rajkumar K., Aravindan S., 2013, Tribological behavior of microwave processed copper-nanographite composites, *Tribology International*, **57**, 282-296

22. Saeidi F., Meylan B., Hoffmann P., Wasmer K., 2016, Effect of surface texturing on cast iron reciprocating against steel under starved lubrication conditions: A parametric study, *Wear*, **348-349**, 17-26

23. Woydt M., Ebrecht J., 2003, Influence of test parameters on tribological measurements – results from international round robin tests, *Tribotest*, **10**, 1, 59-76

24. Yin F.L., Wang Y., Ji H., Ma Z.H., Nie S.L., 2021, Impact of sliding speed on the tribological behaviors of cermet and steel balls sliding against SiC lubricated with seawater, *Tribology Letters*, **69**, 2, 1-16

25. Zhang Z., Nie S., Yuan S., Liao W., 2015, Comparative evaluation of tribological characteristics of CF/PEEK and CF/PTFE/graphite filled PEEK sliding against AISI630 steel for seawater hydraulic piston pumps/motors, *Tribology Transactions*, **58**, 6, 1096-1104

Manuscript received April 4, 2022; accepted for print October 14, 2022

JOURNAL OF THEORETICAL AND APPLIED MECHANICS
61, 1, pp. 89-102, Warsaw 2023
https://doi.org/10.15632/jtam-pl/157570

A TOOL ORIENTATION SMOOTHING METHOD FOR FIVE-AXIS MACHINING TO AVOID SINGULARITY PROBLEMS

Chuanhui Cui
School of Mechanical Engineering and Automation, Beihang University, Beijing, China, and Collaborative Innovation Center for Advanced Aero-Engine, Beihang University, Beijing, China, and Dongchang College of Liaocheng University, Liaocheng, China

Zhengqing Zhu
School of Mechanical Engineering and Automation, Beihang University, Beijing, China, and Collaborative Innovation Center for Advanced Aero-Engine, Beihang University, Beijing, China
e-mail: by1807104@buaa.edu.cn

Shuai Chen
School of Mechanical Engineering and Automation, Beihang University, Beijing, China

Qiang Zheng, Jinfeng Chai, Xiancai Li
AECC South Industry Company Limited, ZhuZhou, China

In numerically controlled grinding of aeroengine blades, a sharp change in a rotating shaft caused by a singular zone greatly reduces grinding precision and quality. This paper proposes an algorithm to optimize the tool-path that combines optimization of the C-axis rotation angle, a modification to the tool orientation and adjustments to the tool position by taking a four-array machine tool with two rotational axes (B-axis and C-axis) as an example. The algorithm was verified using VERICUT software, furthermore, in machining experiments, the rotation amplitudes of the rotary axis in singular areas was effectively reduced, which ensured grinding quality of blades.

Keywords: aeroengine blade, smoothness of tool orientation, five-axis machine tool, singular area

1. Introduction

As blades play an important role in aeroengines, their surface accuracy and integrity greatly influence their fatigue life and aerodynamic performance under service environments. Therefore, blades are generally ground and polished to ensure surface integrity and accuracy in their final shape (Huang *et al.*, 2016; Chen and Zhao, 2015). The fixed-track grinding of blades with a super--abrasive elastic grinding wheel can solve grinding problems for hard-to-manufacture features, such as the leading edge, exhaust edge and the filet to realize complete blade grinding. However, it is important to avoid the interference between the tool axis and edge plates and to realize blade-body grinding without tool markings while machining blades with upper- and lower-edge plates. Therefore, tool orientation without the interference is generally specified at the upper- and lower-edge plates of blades based on shape parameters of the tool, whetras the planning of tool orientation is performed by the computer-aided machining (CAM) system through an interpolation vector (Ma *et al.*, 2015). As shown in Fig. 1a, due to the upper-edge plate, the tool orientation v_u is inclined to the right relative to the blade axis when the grinding tool is near the upper-edge plate of the blade in the blade grinding process. As shown in Fig. 1d, due to the lower-edge plate, the tool orientation v_l is inclined to the left relative to the blade axis when the grinding tool is near the lower-edge plate of the blade. As shown in Figs. 1b and 1c, due to

the opposite inclination direction of the tool position at the upper- and lower-edge plates, the tool orientation will be approximately parallel to the axis of the blade when the grinding tool is machining the middle part of the blade. If the blade axis is parallel to the axis of the machine tool turntable during the five-axis grinding process, singular areas from the five-axis computerized numerical control (CNC) machine tool inevitably occur during processing (Pal, 2005). In singular areas, the tool orientation is approximately parallel to the axis of the machine tool turntable for the five-axis tool, which causes small fluctuations in the tool orientation leading to large variations in the rotation shaft of the machine tool. This significantly increases the non-linear errors of the machine tools, worsens the processing state in these areas, and can even cause machining scrap (Chen *et al.*, 2020). Therefore, optimizing the five-axis tool-path in singular areas is essential to improve the machining precision and surface quality.

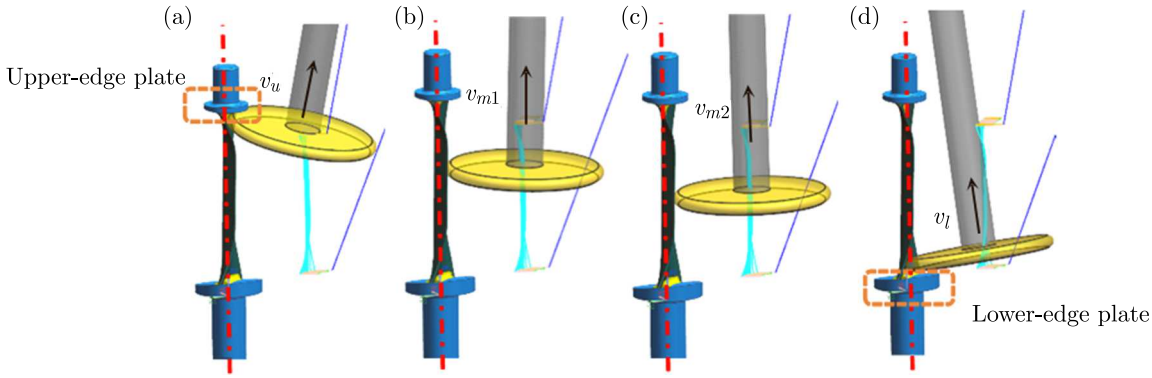

Fig. 1. The grinding process of the blade with the upper- and lower-edge plates: (a) attitude of tool orientation relative to the blade when machining the upper-edge plate, (b) attitude of the tool relative to the blade when machining the middle of the blade, (c) attitude of the tool relative to the blade when machining the middle of the blade, (d) attitude of tool orientation relative to the blade when machining the lower-edge plate

The existing five-axis machining singularity-avoidance method can be performed in two stages tool-path planning and post-processing without changing the workpiece clamping form (Cripps *et al.*, 2017; Wang, 2007) or rotating shaft configuration (Anotaipaiboon *et al.*, 2006). In the tool-path planning stage, singular regions can be avoided by optimizing the tool orientation. Affouard *et al.* (2004), Yang and Altintas (2013) and Wan *et al.* (2018) fitted the tool orientation for each tool position into spline curves and fine-tuned the control points to ensure that the tool orientation avoided the singular region of the five-axis machine tool, which improved the smoothness of the tool orientation. Castagnetti *et al.* (2008) and Lin *et al.* (2014, 2016) defined the feasible region of the tool orientation and optimized it within the feasible region to avoid singular regions and obtain better machining quality. Wang (2012) optimized the tool position in the singular region by monitoring the angle between the tool orientation and the rotation axis. Tajima and Sencer (2020) avoided singular regions through real-time path planning. Lartigue *et al.* (2004) and Lu *et al.* (2016) modified the tool-path by adjusting the control points for side milling, which improved the smoothness of the rotating shaft near the singular points and ensured machining accuracy. In the post-processing stage, Sørby (2007) modeled kinematics of a non-orthogonal machine tool and fine-tuned motion of the rotating axis near the singular point in post-processing to improve the robustness of the tool-path in the singular regions. It is noted that such a method inevitably introduces machining errors when adjusting motion of the rotating shaft. Munlin *et al.* (2004) reduced motion errors near singular points through the shortest-path planning during post-processing. Wang *et al.* (2008) and Chen *et al.* (2020) improved the machining accuracy of singular regions through linear interpolation.

In the planning stage of tool-path, the singular problem of tool-path can be realized by combining the structure of the machine tool. However, at present, the universal CAM system does not have this function, so it needs to carry on a secondary development based on the development interface provided by CAM, which is difficult to realize and is characterized by poor versatility. In the post-processing stage, the smoothness of the tool-path in singular regions is improved, and the non-linear errors in these areas are reduced by fine-tuning of motion of the rotating shaft, shortest-path planning and interpolation. However, the problem of an excessive rotation amplitude for the rotating shaft in singular regions is not fundamentally solved, and fine-tuning of motion introduces new machining errors. Interpolation causes machine-tool feed fluctuations due to tool points that are too dense, and this affects the machining efficiency and quality.

In this study, an algorithm to optimize the tool-path that combines optimization of the C-axis rotation angle, a modification of the tool orientation and adjustment to the points is proposed by taking a four-array machine tool with two rotational axes (B and C) as an example based on the previous research. This method improves the smoothness of the tool-path in the singular region, and the effectiveness of this method is proved by experiments.

2. Algorithm research

2.1. Overall algorithm flow

A flow chart of the overall algorithm is shown in Fig. 2, and it shows the following steps. Step 1: post-process the original tool-path data. Step 2: obtain tool-path segments located in the singular region based on the normal Z component of the tool position and fluctuations of the C-axis. Step 3: adjust the swing angles of the B-axis and C-axis corresponding to the tool position in the singular area based on the angular travel of the C-axis at the beginning and end of the tool rail section in the singular area so that these axes rotate uniformly. Step 4: smooth the B-axis and C-axis swing angles of the tool positions before and after the beginning and end points of the singular tool rail section to ensure connection between the singular section and the front and rear sections. Step 5: adjust tool orientation corresponding to the tool position according to the adjusted B-axis and C-axis swing angles. Step 6: calculate the tool position based on the adjusted tool orientation combined with the contact position, normal vector of the contact and cutter parameters. Step 7: reprocess the adjusted tool-path data after processing its position data in all singular areas to complete the tool-axis smoothing.

2.2. Kinematic analysis of the machine tool

The machine tool used in this study is a four-spindle rectangular array five-axis machine tool to achieve blade grinding and grinding, whose one rotary axis (C-axis) is on the table and the other one (B-axis) on the spindle, as shown in Fig. 3a. The tool is a drum-shaped tool, as shown in Fig. 3b. The coordinate system of the five-axis machine tool with a swing head and turntable is shown in Fig. 3c. The $O_W X_W Y_W Z_W$, $O_M X_M Y_M Z_M$, and $O_T X_T Y_T Z_T$ sets of axes are the coordinate systems of the workpiece, machine, and tool, respectively, and point$_B$ is the rotation center of the B-axis. The rotation center of the C-axis coincides with the origin of the workpiece coordinate system. The vector$_B$ is the tool coordinate origin O_T in the machine coordinate system relative to the coordinates of point B. The initial coordinates of the tool in the coordinate system are $P_t^{\mathrm{T}}(0,0,0,0,0,1)$. The coordinate of point P_t^{T} in the workpiece coordinate system should be consistent with the corresponding tool position $P_n^W(x_n, y_n, z_n, i_n, j_n, k_n)$ after coordinated movements for each machine tool axis (Geng *et al.*, 2018). If $(mx_n, my_n, mz_n, mb_n, mc_n)$

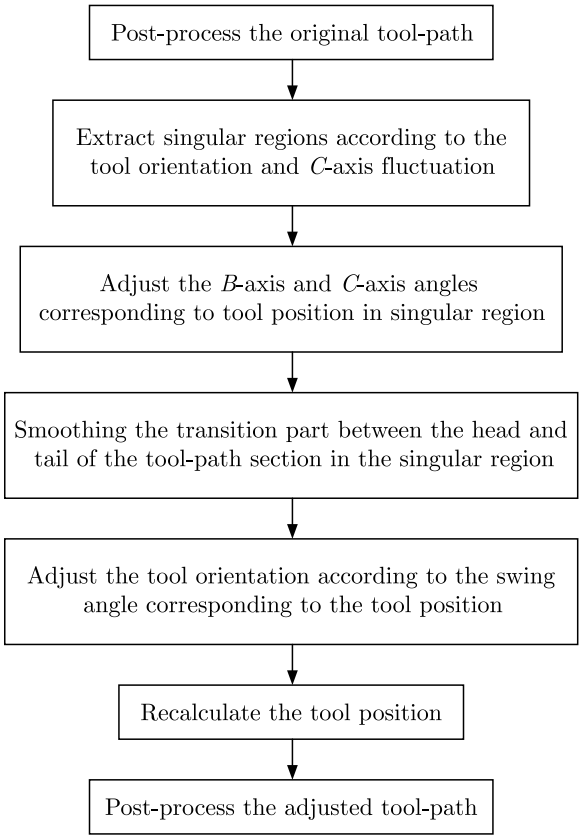

Fig. 2. Overall flow of the proposed algorithm

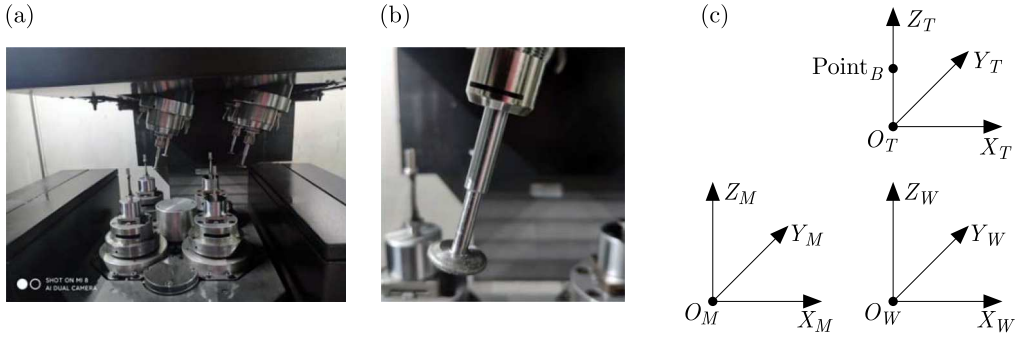

Fig. 3. (a) Four-spindle rectangular array five-axis machine tool, (b) drum-shaped tool, (c) coordinate system of the five-axis machine tool with a swing head and turntable: $O_W X_W Y_W Z_W$, $O_M X_M Y_M Z_M$, and $O_T X_T Y_T Z_T$ sets of axes are the coordinate systems of the workpiece, machine and tool, respectively, and point$_B$ is the rotation center of the B-axis

are the coordinates of the corresponding axes of the machine tool in the component coordinate system, there is a transformation relation as shown as

$$P_n^W = P_t^{\mathrm{T}} \mathrm{Trans}(\mathrm{vector}_B) \mathrm{Rot}(B, mb_n) \mathrm{Trans}(m_x, m_y, m_z) \mathrm{Rot}(C, mc_n) \tag{B.1}$$

When solving motion for each axis of the machine tool in reverse, the expansion of Eq. (2.1) gives two cases for motion of the B-axis and C-axis of the machine tool as

$$\begin{aligned} mb_{n1} &= \arccos(k_n) \\ mc_{n2} &= \begin{cases} \arctan(j_n/i_n) & i_n \geqslant 0 \\ 90^\circ \operatorname{sgn}(j_n) - \arctan(j_n/i_n) & i_n < 0 \end{cases} \end{aligned} \tag{B.2}$$

or

$$mb_{n2} = -\arccos(k_n)$$
$$mc_{n2} = \begin{cases} \arctan(j_n/i_n) & i_n \leqslant 0 \\ \arctan(j_n/i_n) - 90^\circ \operatorname{sgn}(j_n) & i_n > 0 \end{cases} \tag{B.3}$$

Equation (2.4) is used to calculate the total rotations Δ_1 and Δ_2 of the B and C axes corresponding to the two solutions, and the smaller value is selected as the current solution

$$\begin{aligned} \Delta_1 &= |mb_{n1} - mb_{n-1}| + |mc_{n1} - mc_{n-1}| \\ \Delta_2 &= |mb_{n2} - mb_{n-1}| + |mc_{n2} - mc_{n-1}| \end{aligned} \tag{B.4}$$

2.3. Determination of the singular area

Because the singularity problem is only related to the direction of the tool axis and not to the position of the tool, only the relationship between the rotation axis and the direction of the tool axis needs to be solved. The tool orientation $v_n(i_n, j_n, k_n)$ is a unit vector which satisfies $i_n^2 + j_n^2 + k_n^2 = 1$, therefore, a unit sphere (radius of the sphere has unit length, and it is commonly referred to as a Gaussian sphere in which each point corresponds to a blade-axis direction) is taken as an example. As shown in Fig. 4a, the tool orientation is expressed by v, the center point of the axis is located at the center of the sphere, and the end points are distributed on the sphere. Figure 4b shows a top-down view, which indicates that the initial position of v is parallel to the Z-axis, i.e., $v = (0, 0, 1)$, based on the analysis in Section 2.2. The included angle between any two tool orientations v_1 and v_2 on the unit circle is set as φv_1 and can reach v_2 in two simultaneous steps: firstly, rotation by α degrees around the Y-axis to v_m, and then rotation by β degrees around the Z-axis to v_2.

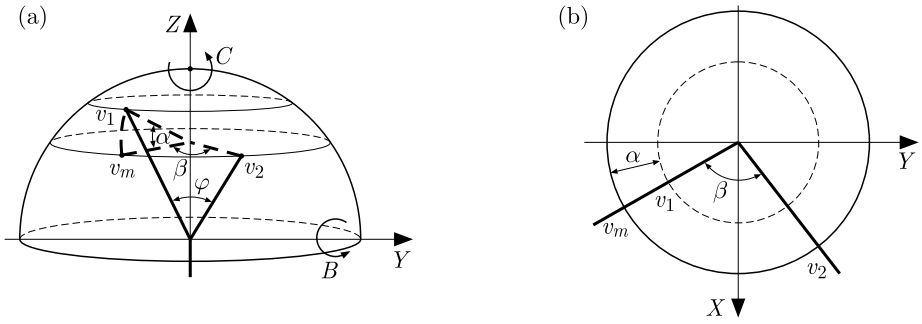

Fig. 4. (a) Gaussian sphere, (b) its top view

According to Eqs. (2.2) and (2.3), when k_n is equal to 1, b_n is 0 and c_n can be any value; this is called a singular point of the tool-path. At this time, the C-axis rotation angle corresponding to the previous tool position is taken as c_n to avoid the singular-point problem. When k_n approaches but is not equal to 1, small changes of i_n and j_n result in large changes in the C-axis rotation angle. Therefore, the singular area discrimination threshold is set as ε, while the corresponding $k_n, k_{n+1}, \ldots, k_{n+m}$ for each tool position and the size of ε are determined successively. The track segment of the tool that is continuously less than ε is the track segment in the singular area. Through a large number of experiments and analysis, ε is set from 0.9848 to 0.9962 (3°-5° corresponding to the swing angle of the B-axis).

To explain the machine-tool singularity phenomenon more intuitively, Fig. 5a shows the tool pose at two adjacent positions of the tool in the grinding process of the middle part of the blade body of the example blade. The tool orientations at the two adjacent tool positions are v_1 and v_2, respectively. As shown in Fig. 4b, the tool orientations are represented on the Gaussian

sphere O (O is the center of the Gaussian sphere), the circle O_s is a small-diameter circle with the Z-axis near the north pole on the surface of the Gaussian sphere O, which corresponds to a smaller conical angle φ ($\leqslant 10°$). The tool orientations v_1 and v_2 are on the circle O_s, and the angle φ between v_1 and v_2 is less than φ, which meets the maximum in the five-axis machining path-planning stage. However, as shown in Fig. 5c, in the top view of the Gaussian sphere O, $\dot{v}_1$ is the projection of v_1 onto the XOY plane, $\dot{v}_2$ is the projection of v_2 onto the XOY plane, $\angle\dot{v}_1O\dot{v}_2$ is the projection of $\angle v_1Ov_2$ onto the XOY plane, the $\angle\dot{v}_1O\dot{v}_2$ is obviously larger than the $\angle v_1Ov_2$, which produces a singularity phenomenon when the tool-path is from v_1 to v_2. The maximum angle of the C-axis can reach 90° in one cycle, which is much larger than the maximum allowable angle in a single cycle. For a five-axis machine tool with two rotational axes (B and C), singularity problems may occur only when the tool orientation appears in a circle with a smaller radius at the north pole for the Gaussian sphere, which is usually called a singular area.

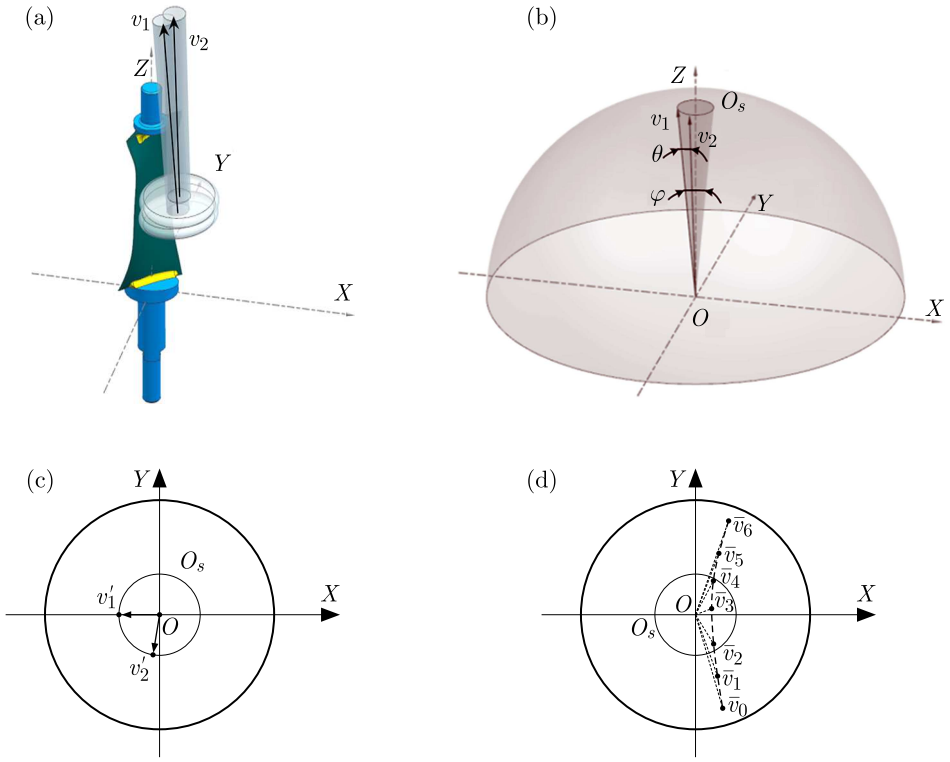

Fig. 5. Generation mechanism of a singular cone: (a) relationship between the tool and workpiece pose, (b) singular cone and tool orientations in the singular cone, (c) top view of the Gaussian sphere and C-axis rotation angle corresponding to the tool orientation in the singular area, (d) singularity of the machine tool in the C-axis

To further illustrate the singularity of the machine tool, the top view of the Gaussian sphere O (O is the center of the Gaussian sphere) is shown in Fig. 5d, where the circle O_s is the singular cone, and $\overline{v_0}, \overline{v_1}, \ldots, \overline{v_6}$ are continuous tool orientations, connecting the lines between O and each of the tool orientations. The angle between two adjacent lines is the angle of C-axis of the machine tool between two adjacent tool points when the machine tool is running. It can be seen from the figure that during transformation of the tool orientation from $\overline{v}_1$ to $\overline{v_5}$, the C-axis changes greatly. In this case, the tool-path segment from $\overline{v}_1$ to $\overline{v_5}$ is a singular tool-path segment. Here $\overline{v}_1$ is the first tool point corresponding to the tool orientation before the tool-path enters the singular region, $\overline{v_5}$ is the first tool point corresponding to the tool orientation after the tool-path leaves the singular region. In order to better describe the algorithm in this paper,

$\overline{v}_1$ is defined as the tool head orientation of the singular tool-path segment, and $\overline{v_5}$ is the tail of the tool orientation of the singular tool-path segment.

2.4. Normal vector adjustment principle of tool position

According to distribution of the head and tail of the singular tool-path segment, the tool orientations in the singular region are adjusted in two cases. In the first case, the projection angle of the tool orientation corresponding to the head and tail points in the singular area is less than 90° in the top view of the Gaussian sphere. As shown in Fig. 6a, v_1^1, v_2^1, v_3^1 and v_4^1 are tool orientations corresponding to the tool position points in the singular area, v_0^1 is the tool orientation corresponding to the tool position before the tool-path enters the singular area, and v_5^1 is the tool orientation corresponding to the first tool position after the tool-path leaves the singular area, with $\angle v_0^1 O v_5^1$ being less than 90°. During the movement of the cutter shaft from v_0^1 to v_5^1, the C-axis of the machine tool rotates significantly, which causes a singularity problem. The shortest line connection is between points v_0^1 and v_5^1 on the Gaussian sphere surface. From v_0^1, v_1^1, v_2^1, v_3^1, v_4^1 and v_5^1 the distance relationship between the corresponding tool positions of v_1^1, v_2^1, v_3^1 and v_4^1 will correspond to the adjustments in the connection of v_0^1 and v_5^1 on the connecting line. As shown in Fig. 6b, the amplitudes of motion for the B-axis and C-axis of the machine tool are remarkably small and uniform as the tool position is changed from v_0^1 to v_5^1, which avoids singular problems in the machining process.

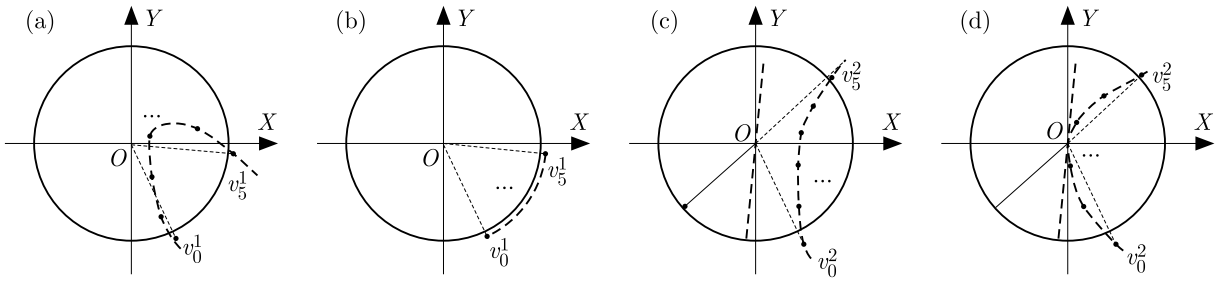

Fig. 6. According to the projection angle, different strategies are adopted to adjust tool orientation in the singular region: (a) projection angle less than 90° of tool orientation before the adjustment, (b) projection angle less than 90° of tool orientation after the adjustment, (c) projection angle greater than 90° of tool orientation before the adjustment, (d) projection angle greater than 90° of tool orientation after the adjustment

In the second case, the projection angle of the tool orientation corresponding to the head and tail points in the singular area is more than 90° based on the Gaussian sphere. As shown in Fig. 6c, the circle O_s is a top view of the singular cone, and v_1^2, v_2^2, v_3^2 and v_4^2 are the tool orientations corresponding to the tool positions in the singular area. v_0^2 is the tool orientation corresponding to the tool position before the tool-path enters the singular area, and v_5^2 is the tool orientation corresponding to the first tool position after the tool-path leaves the singular area. The graph shows that the C-axis of the machine tool rotates significantly as the tool position changes from v_0^2 to v_5^2, which causes singularity problems. The shortest line connection is made between point v_0^2, the north pole of the Gaussian sphere, and point v_5^2 on the surface of the Gaussian sphere. From v_0^2, v_1^2, v_2^2, v_3^2, v_4^2 and v_5^2, the distance relationships between the corresponding tool positions are v_1^2, v_2^2, v_3^2 and v_4^2, which corresponds to the adjustments in the connecting line from v_0^2 to v_5^2. As shown in Fig. 5d, the amplitudes of motion for the B-axis and C-axis are remarkably small and uniform as the tool position is changed from v_0^2 to v_5^2, which avoids singularity problems in the machining process.

2.5. Adjustment algorithm of swing angle corresponding to tool position in a singular region

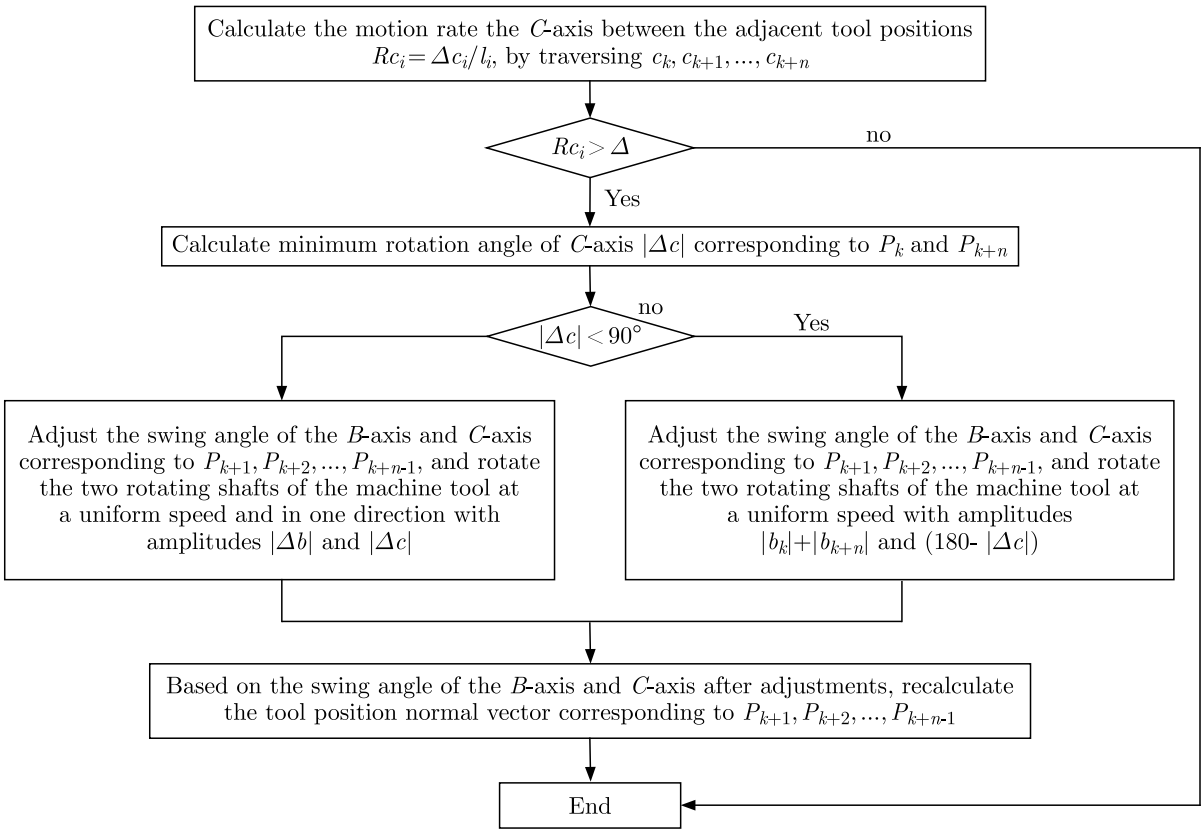

Fig. 7. Adjustment process of the tool orientation in a singular region

Figure 7 shows a flow chart of the tool-position normal-vector adjustment algorithm in a singular region. P_k is the starting point of the tool-path segment in the singular region, P_{k+n} is the end point, and the rotation angles of the axis are $b_k, b_{k+1}, \ldots, b_{k+n}$ and $c_k, c_{k+1}, \ldots, c_{k+n}$. The tool-path length l_i corresponding to each tool point is calculated in turn with P_k as the starting point. Then, P_{k+i} is calculated for each tool position corresponding to $t_i = l_i / \sum l_i$. Therefore, the procedure to adjust the tool orientation is as follows.

1. Calculate the rotation angle of the C-axis between the adjacent tool positions $\Delta c_i = c_{k+i} - c_{k+i-1}$, and then calculate the motion rate of the C-axis between the adjacent tool positions $Rc_i = \Delta c_i / l_i$ by traversing $c_k, c_{k+1}, \ldots, c_{k+n}$, where $i = 1, 2, \ldots, n$. If the value of Rc_i $(i = 1, 2, \ldots, n)$ is too large to indicate that there is a large fluctuation in the C-axis in this singular region, the threshold value θ of the C-axis is preset when the program is executed, θ is set to 1-3 in a lot of experimental analysis, judge whether $Rc_i > \theta$ $(i = 1, 2, \ldots, n)$ is established. If yes, perform Step 2; otherwise, the singular region is not necessary for optimization, and the program is stopped.
2. Set $i = 1$; calculate the effective motion stroke of the C-axis and B-axis during the machining stage from P_k to P_{k+n}. The effective travel of the C-axis is then $\Delta c = c_{k+n} - c_k$, and that of the B-axis is $\Delta b = b_{k+n} - b_k$ when $|\Delta c| > 180°$. Step 3 is performed by adding or subtracting $m \times 360$ so that Δc is in the range $-180°$ to $180°$.
3. Judge whether $|\Delta c| \leqslant 90°$ is valid. If $|\Delta c|$ remains unchanged, carry out Step 4; otherwise, implement Step 5.
4. If $\Delta b_{k+i} = \Delta b \times t_i$, $\Delta c_{k+i} = \Delta c \times t_i$; perform Step 11.
5. If $\Delta c > 90°$, $\Delta c = -(180 - \Delta c)$, e.g., $\Delta c < -90°$, $\Delta c = 180 + \Delta c$; perform Step 6.

6. If $\Delta c_h = |\Delta c|/2$, $\Delta c_{k+i} = \Delta c \times t_i$; perform Step 7.
7. Judge whether $|\Delta c_{k+i}| \leqslant \Delta c_h$ is true. If true, execute Step 8; otherwise, skip to Step 9.
8. $\Delta b_{k+i} = 2 \times b_k \times t_i$; perform Step 11.
9. $\Delta b_{k+i} = b_k + 2 \times b_{k+n} \times (t_i - 0.5)$; perform Step 10.
10. If $\Delta c_{k+i} \geqslant 0$ is true, then $\Delta c_{k+i} = \Delta c_{k+i} + 180°$; otherwise $\Delta c_{k+i} = \Delta c_{k+i} - 180°$, perform Step 11.
11. Determine whether $i = n$ is true. If true, the adjustment process is over; otherwise, $i = i+1$ and move to Step 3.

2.6. The change of head and tail normal vectors for the tool-path in singular regions by smoothing

After adjusting the tool orientation in a singular region, the relationship that describes the original normal vector variations for the tool position is changed so that the swing angles of the B-axis and C-axis mutations occur at the boundary transition of the singular region. Figures 8a and 8b, respectively, show changes in the tool orientation corresponding to the tool position before and after tool-orientation adjustments along the cutter track section in the singular region. There is a sudden change in the normal vector of the tool axis at tool positions v_2 and v_7, which correspond to the head and tail of the tool-path section in the adjusted singular region. If this is left untreated, speed fluctuations will appear when the machine tool operates here, which will affect the machining quality.

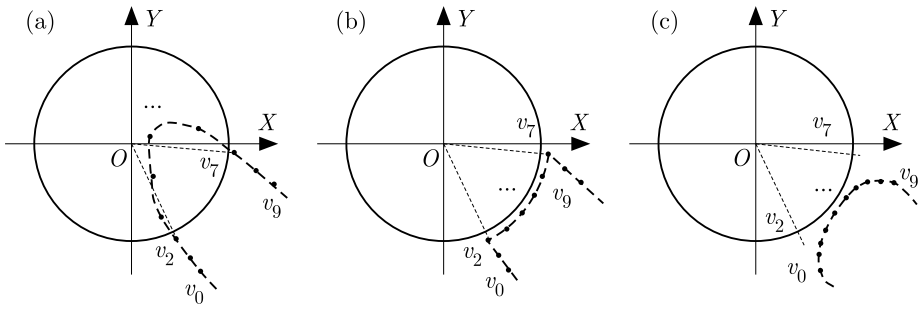

Fig. 8. Smoothing of the head and tail normal vectors for the tool-path in singular regions: (a) normal projection of tool orientation before the adjustment, (b) normal projection of tool orientation after the adjustment, (c) normal vector projection of tool orientation after the smoothing

As shown in Fig. 8b, there are two front tool positions P_0 and P_1, and two rear tool positions P_3 and P_4 corresponding to the tool position P_2, which takes the length of the tool-path section as a parameter. Then, the swing angles of the B-axis and C-axis corresponding to the five tool sites are fitted to quadratic Bezier curves using the least-squares method, which is then inversely calculated based on the corresponding parameters of each tool site for P_1, P_2 and P_3. The tool--axis smoothing at the head of the tool-path section in the singular region is then completed based on the corresponding swing angle of the B-axis and C-axis.

Taking the swing angle of the B-axis as an example, the specific processing approach is explained starting from P_0. The corner of b_i $(i = 0, 1, \ldots, 4)$, which corresponds to the normal vector of each tool-position contact is calculated, and the tool-path length l_i corresponding to each tool position is calculated with P_0 as the starting point

$$l_i = \begin{cases} 0 & i = 0 \\ l_{i-1} + \mathrm{dis}(P_i - P_{i-1}) & i = 1, 2, \ldots, 4 \end{cases} \tag{B.5}$$

where $\mathrm{dis}(P_i - P_{i-1})$ is the distance between P_{i-1} and P_i.

The value $t_i = l_i/l_4$ $(i = 0, 1, \ldots, 4)$ is taken as the corresponding b_i parameters. Refer to the description of quadratic B-spline in reference (Riesenfeld, 1975), the planning node vector $\mathbf{U}(0, 0, 0.5, 1, 1)$ is combined with t_i $(i = 0, \ldots, 4)$ to calculate the basis function corresponding to $N_{j,i}$ $(i = 0, \ldots, 4)$, where $j = 0, 1, 2, 3$ as

$$\begin{aligned} N_{j,0} &= \begin{cases} 1 & u_j \leqslant t_i < u_{j+1} \\ 0 & \text{otherwise} \end{cases} \\ N_{j,p}(t_i) &= \frac{t_i - u_i}{u_{i+p} - u_i} N_{j,p-1}(t_i) + \frac{u_{i+p+1} - t_i}{u_{i+p+1} - u_{i+1}} N_{j+1,p-1}(t_i) \\ \mathbf{E} &= \begin{bmatrix} N_{0,2}t_0 & \cdots & N_{2,2}(t_0) \\ \vdots & \ddots & \vdots \\ N_{0,2}(t_4) & \cdots & N_{2,2}(t_4) \end{bmatrix} \end{aligned} \tag{B.6}$$

where b_i $(i = 0, \ldots, 4)$ is written in the form of the column vector $\mathbf{B} = [b_0, \ldots, b_4]^{\mathrm{T}}$. Equation (2.7) is used to solve each control point of the fitted B-spline, where $\mathbf{X} = [x_0, x_1, x_2]^{\mathrm{T}}$, $\mathbf{X}$ is a 3×1 matrix, x_0, x_1 and x_2 are the values of B-spline control points

$$\mathbf{X} = (\mathbf{E}^{\mathrm{T}}\mathbf{E})^{-1}\mathbf{E}^{\mathrm{T}}\mathbf{B} \tag{B.7}$$

Finally, b_i $(i = 0, \ldots, 4)$ is fitted to a B-spline curve, which can be inversely calculated through the fitted spline curve of b_i $(i = 1, 2, 3)$ to obtain smooth B-axis motion data.

2.7. Recalculation of tool position

The tool and workpiece surfaces have common normal vectors at the cutter contact point during machining. Therefore, the coordinates of the tool position (Xu and Chen, 2014) can be solved by combining the tool orientation and parameter information of the cutter when the normal vectors of the contact point are known. Commonly used tools for blade grinding and grinding are drum-shaped, as shown in Fig. 9. Given the tool diameter D, fillet radius R, contact point P_c, contact normal vector v_c, and normal vector of tool orientation v_0, the tool position P_0 can be obtained from

$$\begin{aligned} P_1 &= P_c + Rv_c & v_1 &= v_0 \times (v_c \times v_0) \\ P_2 &= P_1 + \Big(\frac{D}{2} - R\Big)v_1 & P_0 &= P_2 - Rv_0 \end{aligned} \tag{B.8}$$

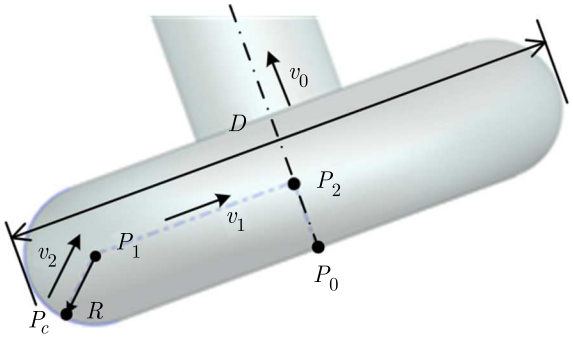

Fig. 9. Calculation of the normal vector for contact in a drum cutter

Similarly, for the commonly used ball cutters in milling, the radius R of the cutter, contact point P_c, contact normal vector v_c and tool orientation v_0 can be used to obtain the tool position P_0 from Eq. (2.8). The round-corner cutters commonly used in milling are similar

to drum cutters in that given the tool diameter D, radius R, contact point P_c, contact normal vector v_c and tool orientation v_0, the tool position P_0 can be obtained from

$$P_0 = P_c + Rv_c - Rv_0 \tag{B.9}$$

Other commonly used tools can be derived in turn.

3. Verification example

As shown in Fig. 1, to realize full profile grinding of concave or convex surfaces with upper- and lower-edge plates in a certain model, the cutter shaft of the upper- (lower-) edge plate needs to tilt to the right (left) to avoid interfering with the cutter shaft. The cutter shaft in the middle is determined from the CAM system based on the interpolation of the built-in rules. Therefore, the blade-axis normal is nearly parallel to the blade axis when machining the middle part of the blade body. The blade axes are installed parallel to the C-axis of the rotating axles when a four-array machine tool has two rotational axes (B and C). Figure 10 shows the swing values

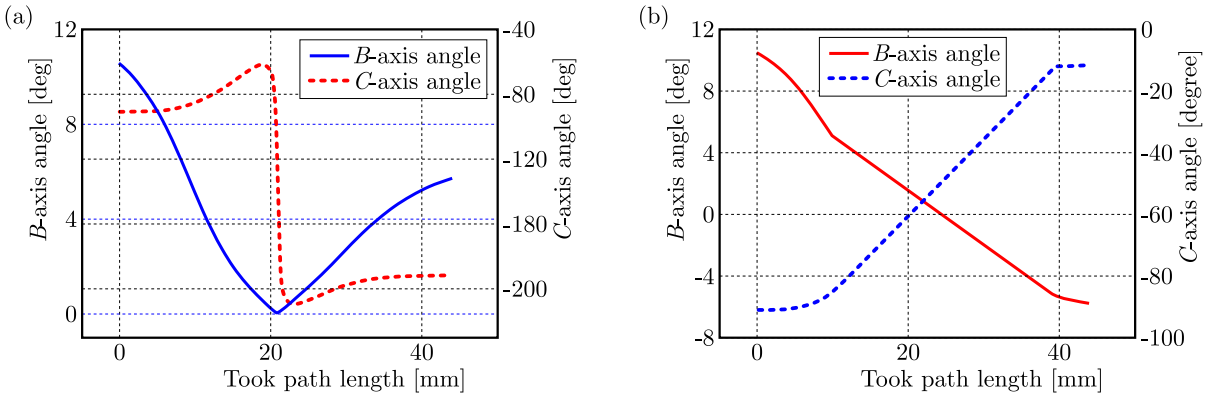

Fig. 10. Comparison of the B-axis and C-axis rotation angles (a) before and (b) after optimization

of the B-axis and C-axis corresponding to the fifth row of the tool-path in the program before and after optimization. Figure 10a indicates that the entire swing amplitude of the C-axis in the original tool-path is large with a sharp change. Meanwhile, there is a sudden change in the B-axis direction, which causes sharp acceleration and deceleration of the machine tool to produce large non-linear errors. Figure 10b shows the corresponding swings in the B-axis and C-axis after tool-path optimization. The total rotation angle of the C-axis is reduced significantly and the overall operation is smooth, while there is no sudden change in the direction of the B-axis. This can ensure smooth operation of the machine tool and plays a positive role in improving the processing quality.

It should be emphasized that because of the particularity of the structure of the array machine tool, the 840D numerical control system can not realize the RTCP function, so the machine tool is sensitive to the nonlinear error caused by the singular problem, and so the cutting simulation of the tool path before formal machining is particularly important. Cutting simulations were performed using the VERICUT software package, as illustrated in Fig. 11. In the simulation results, the light-yellow part of the blade is the surface of the workpiece, and the purple part is the surface of the workpiece after processing. From the simulation results shown in Fig. 11b, it can be clearly seen that when the tool-path is not optimized, large nonlinear errors are generated due to the singular region of the tool-path, which leads to a serious over-cutting problem, leading to the scrap of the processed workpiece. The simulation results in Fig. 11c show that there is no obvious over-cutting after optimization.

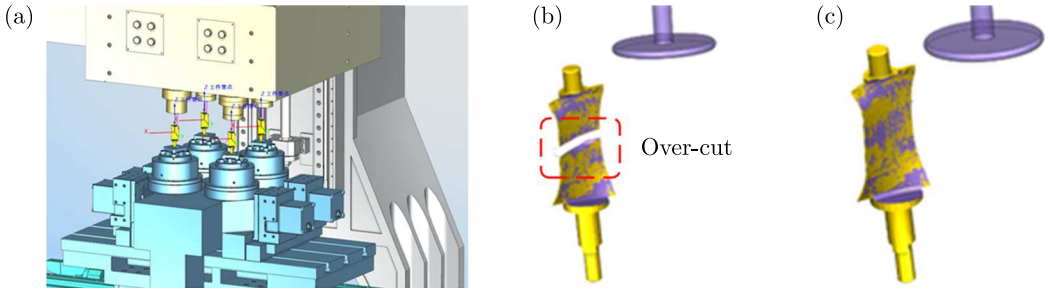

Fig. 11. VERICUT simulation model and its results, showing: (a) simulation model, (b) tool-path cutting simulation before optimization, (c) tool-path cutting simulation after optimization

In the grinding process, grinding process parameters directly affect quality of the surface processing of blades. Considering the surface profile and roughness requirements of titanium alloy fan blades, and combined with the experimental experience of grinding process parameter optimization in the early stage of our research group, the grinding processing parameters are shown in Table 1. A blade is machined using the optimized tool-path, as illustrated in Figs. 12a and 12b, and there is no undercut on the surface of the blade after machining. In the vertical section curve shown in Figs. 12a and 12b, 40 equidistant points are accurately detected with a coordinate-measuring machine which is equipped with a Renishaw SP25M contact scanning probe (Beijing, Hangruisiwei PONY866, Metrolog XG13 contact measuring system, MPE=(2.5+4L/1000)um and the diameter of the probe is 1.5 mm). The results are shown in Fig. 12c, where the maximum surface error is less than 0.02 mm, which meets the design requirements (profile tolerance −0.03 mm-+0.05 mm). Therefore, it can be said that the proposed optimization method can meet the actual processing requirements.

Table 1. Grinding process parameters

	Convex	Concave	Leading-edge and trail-edge
Tool	D38r1.5 (Drum wheel)	D38r1.5 (Drum wheel)	D26r1.5 (Drum wheel)
Parameters	Speed 5000 r/min Feed 1200 mm/min Preloading 0.2 mm Single tool-path	Speed 5000 r/min Feed 1200 mm/min Preloading 0.2 mm Single tool-path	Speed 7000 r/min Feed 1000 mm/min Preloading 0.2 mm Single tool-path

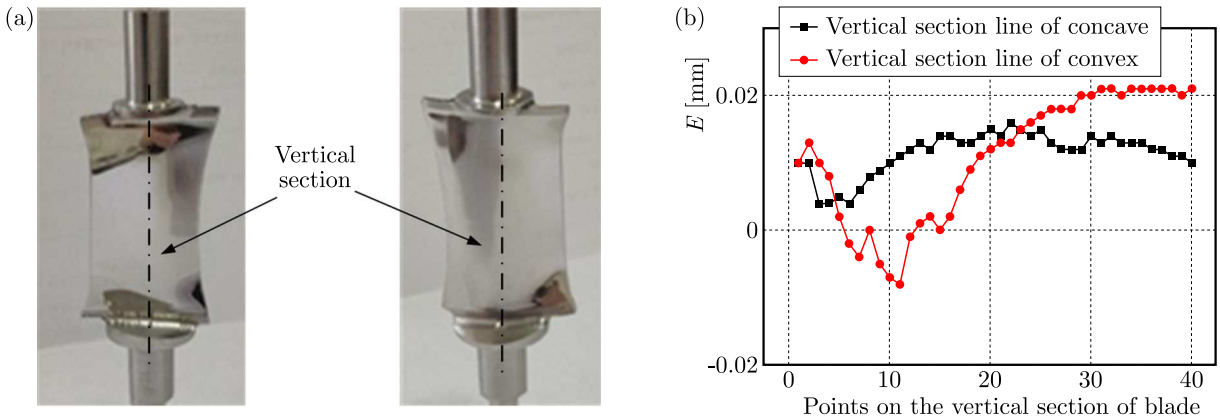

Fig. 12. Grinding effect on the back/basin surface of a double-ended blade model: (a) concave, (b) convex, (c) data for accuracy detection

4. Summary

To solve the problem of singular regions in the tool-path for five-axis grinding and grinding of full-profile aircraft-engine blades, a tool-path optimization algorithm that combines optimization of the B-axis and C-axis rotation angles, modifications of the tool-axis vectors and adjustments to the tool position is proposed in the post-processing stage of the tool-path. This method is easier to implement the tool orientation smoothing than the secondary development of CAM software.

The smoothness of the tool-path in singular regions is improved without interpolating or encrypting the original path. Problems such as rapid rotations of the rotating shaft in the singular regions and excessive non-linear errors are avoided. VERICUT simulation and actual processing verification can meet the actual machining requirements.

Funding

This work was supported by the National Science and Technology Major Project of the Ministry of Science and Technology of China (grant No. 2018ZX04004001).

References

1. Affouard A., Duc E., Lartigue C., Langeron J.M., Bourdet P., 2004, Avoiding 5-axis singularities using tool-path deformation, *International Journal of Machine Tools and Manufacture*, **44**, 4, 415-425
2. Anotaipaiboon W., Makhanov S.S., Bohez E.L.J., 2006, Optimal setup for five-axis machining, *International Journal of Machine Tools and Manufacture*, **46**, 9, 964-977
3. Castagnetti C., Duc E., Ray P., 2008, The domain of admissible orientation concept: A new method for five-axis tool-path optimization, *Computer-Aided Design*, **40**, 9, 938-950
4. Chen G.L., Zhao C.R., 2015, Digital production line of precision forging aeroengine blade (in Chinese), *Aeronautical Manufacturing Technology*, **22**, 78-83
5. Chen L.J., Wei G.X., Sui Y.Z., Wang Z.Z., 2020, Non-linear error control method for five-axis machining singular zone, *Modular Machine Tool and Automatic Manufacturing Technique*, **3**, 111-113, 118
6. Cripps R.J., Cross B., Hunt M., Mullineux G., 2017, Singularities in five-axis machining: Cause, effect and avoidance, *International Journal of Machine Tools and Manufacture*, **116**, 40-51
7. Geng C., Wu Y., Qiu J., 2018, Analysis of nonlinear error caused by motions of rotation axes for five-axis machine tools with orthogonal configuration, *Mathematical Problems in Engineering*, **2018**, 8, 1-16
8. Huang Y., Xiao G.J., Zou L., 2016, Current situation and development trend of grinding technology for blisk (in Chinese), *Acta Aeronautica et Astronautica Sinica*, **37**, 2045-2064
9. Lartigue C., Tournier C., Ritou M., Dumur D., 2004, High-performance NC for HSM by means of polynomial trajectories, *CIRP Annals*, **53**, 1, 317-320
10. Lin Z.W., Fu J.Z., Shen H.Y., Gan W.F., 2014, Non-singular tool-path planning by translating tool orientations in C-space, *International Journal of Advanced Manufacturing Technology*, **71**, 9-12, 1835-1848
11. Lin Z.W., Fu J.Z., Shen H.Y., Xu G.H., Sun Y.F., 2016, Improving machined surface texture in avoiding five-axis singularity with the acceptable-texture orientation region concept, *International Journal of Machine Tools and Manufacture*, **108**, 1-12
12. Lu Y.A., Bi Q.Z., Zhu L.M., 2016, Five-axis flank milling tool-path generation with smooth rotary motions, *Procedia CIRP*, **56**, 161-166

13. Ma L., Wang H.X., Zhang Y., 2015, Grinding parameters optimization for leading and trailing edge of aero-engine blade (in Chinese), *Modular Machine Tool and Automatic Manufacturing Technique*, **22**, 78-83

14. Munlin M., Makhanov S.S., Bohez E.L.J., 2004, Optimization of rotations of a five-axis milling machine near stationary points, *Computer-Aided Design*, **36**, 12, 1117-1128

15. Pal M., 2005, Random forest classifier for remote sensing classification, *International Journal of Remote Sensing*, **26**, 1, 217-222

16. Riesenfeld R.F., 1975, *Nonuniform B-Spline Curves*, 2nd ed. USA-JAPAN Conference Proceedings, 551-555

17. Sørby K., 2007, Inverse kinematics of five-axis machines near singular configurations, *International Journal of Machine Tools and Manufacture*, **47**, 2, 299-306

18. Tajima S., Sencer B., 2020, Real-time trajectory generation for 5-axis machine tools with singularity avoidance, *CIRP Annals*, **69**, 1, 349-352

19. Wan M., Liu Y., Xing W.J., Zhang W.H., 2018, Singularity avoidance for five-axis machine tools through introducing geometrical constraints, *International Journal of Machine Tools and Manufacture*, **127**, 1-13

20. Wang D., Chen Z.T., Chen W.Y., 2008, Detection and control of non-1inear errors in 5-axis machining (in Chinese), *J. Beijing Univ. Aeronaut. Astronaut.*, **34**, 9, 1003-1006, 1091

21. Wang L.N., 2012, Study on singular point problem in 5-axis NC machining (in Chinese), *Journal of Mechanical Engineering and Automation*, **5**, 122-124, 129

22. Wang R.Q., 2007, *Theoretical Research on Wide-Stripe NC Machining and its Application in Blade Machining* (in Chinese), Beijing: Beihang University, 156-189

23. Xu R., Chen Z., 2014, Method of five-axis tool radius compensation based on post-processor, *Journal of Mechanical Engineering*, **50**, 13, 157-164

24. Yang J.X., Altintas Y., 2013, Generalized kinematics of five-axis serial machines with non-singular tool path generation, *International Journal of Machine Tools and Manufacture*, **75**, 119-132

Manuscript received May 29, 2022; accepted for print October 17, 2022

JOURNAL OF THEORETICAL AND APPLIED MECHANICS
61, 1, pp. 103-117, Warsaw 2023
https://doi.org/10.15632/jtam-pl/157311

ANALYSIS OF PROGRESSIVE COLLAPSE OF A SUPER-LONG SPAN LATTICED STEEL ARCH STRUCTURE

Shuangchao Guo, Delin Xu, Kaiguang Shang, Shuo Yang, Di Wang, Gen Li
Beijing Construction Engineering Group Co., Ltd, Beijing, China

Bing Zheng
Department of Civil Engineering, China Agricultural University, Beijing, China

Yong Jiao
Beijing Construction Engineering Group Co., Ltd, Beijing, China
e-mail: jy701210@sina.com

The progressive collapse of a space grid structure which has a large number of members and a large span is the focus of current research. Before the progressive collapse of the structure, there is a problem of instability of the members. In this paper, dynamic nonlinear analysis of a super-long span latticed steel arch structure is carried out to study its progressive collapse process using a Kinematic Hardening Plasticity constitutive model compiled by Vumat material subprogram in Abaqus, which takes into account instability of the members. Differences in the dynamic response process of the structure at the collapse moment and the failure sequence of the members using the member stability model and the material failure constitutive model are compared. Compared with the material failure constitutive model, when the member stability constitutive model is used, the proportion of compressive buckling members in the structural failure is higher, and the bearing capacity of the structure is lower when the initial failure occurs. The structure suffers from localized member compressive failure rather than material yielding, which leads to the progressive collapse of the structure.

Keywords: progressive collapse, steel arch truss structure, compression instability

1. Introduction

The steel arch truss structure, as one of the common forms of space grid structures, combines the advantages of arch and truss, light self-weight, large span, good force performance and short construction period, which make it to be widely used in large-span public buildings such as stadiums, terminals and industrial plants (Zhu *et al.*, 2013; Cai *et al.*, 2010; Zhao and Wu, 2016). The progressive collapse of such large public buildings will pose a great threat to people's life safety and public property once it occurs. The traditional concept believes that the spatial grid structure itself has a high degree of redundancy, thus not collapsing on a large scale. In 1978, the overall collapse and damage of a stadium with a quadrangular pyramid grid system in the center of Hartford City in the United States occurred in a heavy snowstorm, which aroused the attention of domestic and foreign scholars to the progressive collapse of space grid structures (Jiang and Chen, 2012).

Progressive collapse is a process of overall collapse or disproportionate large-scale collapse caused by local failure of the structure (GB50068, 2018). The research on the progressive collapse resistance of structures has been going on for more than 40 years. At present, the research on the progressive collapse resistance of frame structures (Song and Sezen, 2013; Zhang, 2013; Koh and Krauthammer, 2019; Wang and Wang, 2021) and truss structures (Zhao *et al.*, 2019; Miyachi *et al.*, 2012) is relatively mature, and the research focus is shifting to large-span space structures.

For space grid structures, the occurrence of progressive collapse is mainly caused by stability failure of compression members and strength failure of the node zone (Tian *et al.*, 2019). The failure of members is the key to structural design, which can be divided into two types: strength failure and instability failure. The ultimate bearing capacity of the instability failure, generally occurring in compression members, is far less than the yield strength of the strength failure, generally occurring in tension members. Before the overall failure of the space grid structure, there will be a problem of instability of the members, hence finding the key members is an important problem in analysis of the progressive collapse of the structure. The transformed load path method is the most commonly used analysis method to study the progressive collapse of space structures. Tian *et al.* (2019) proposed a dynamic analysis method to simulate the progressive collapse of large-span spatial lattice structures, and analyzed the progressive collapse resistance mechanism of large-span single-story spatial lattice structures. By assuming failure of some key members, the structure is analyzed to determine whether a new load transfer path can be formed and thus whether the progressive collapse of the structure will occur. For the purpose of considering the instability of the member, some scholars use the Vumat subprogram provided by Abaqus to compile the constitutive model of the member, and use the self-defined failure criterion of the member to find the key member (Ding *et al.*, 2011; Ge, 2012). Wilkes and Krauthammer (2019) proposed a method based on energy flow to analyze failure members in a structure. Han *et al.* (2018) identified two forms of collapse of the grid structure through the displacement criterion and found the key members based on the sensitivity method. Han *et al.* (2021) used a transformed load path method to analyze the progressive collapse performance of a single layer latticed shell structure and determined the effect of key members and member groups on the progressive collapse resistance of the structure.

At present, the research on progressive collapse performance of space grid structures is mainly focused on single-layer or double-layer latticed shell structures, and the analysis on truss structures is mainly focused on a plane truss, relatively less than a spatial truss. It should be highlighted that most of Vumat subprograms are only available for pipe section members, while the constitutive model compiled by the Vumat subprogram used in this paper can be applied to arbitrary sections, taking into account instability of the member. The force status of the member is monitored by the subprogram and the failure member is removed in real time, making it easier to find the location of key members. In this paper, an explicit dynamic calculation method for a super-long span space steel arch truss structure is conducted to study the difference between the material failure constitutive model and the member stability constitutive model compiled by the Vumat subprogram in progressive collapse analysis of the structure, verifying the feasibility of the Kinematic Hardening Plasticity constitutive model compiled by the Vumat subprogram in practical engineering applications.

2. Materials and methods

2.1. Model information

The model is based on a super-long span latticed steel arch structure divided into two parts and arranged symmetrically. Its plane size is 211 m×460 m and the height is about 60 m. A total of 32 main trusses are arranged longitudinally with a distance of 15 m, and each part has 16 trusses. The main spatial arch truss has an inverted triangle section, width of 4 m and variable height from 5.5 m to 7 m. Seven connecting trusses and a number of spaced cross struts are arranged between the main trusses to ensure the out-of-plane stability of the main truss. The arch curve is a three-center circular arch with height of about 60 m, forming an inverted quadrangular pyramid space arch truss structure system with a rise-to-span ratio of 0.28. Figure 1 plots the top view of half of the arch truss model that has been established in Abaqus. In order

to describe the instability of the members during progressive collapse of the model more clearly, the key positions of the first truss on both sides have been marked with I-IV in the structure top view.

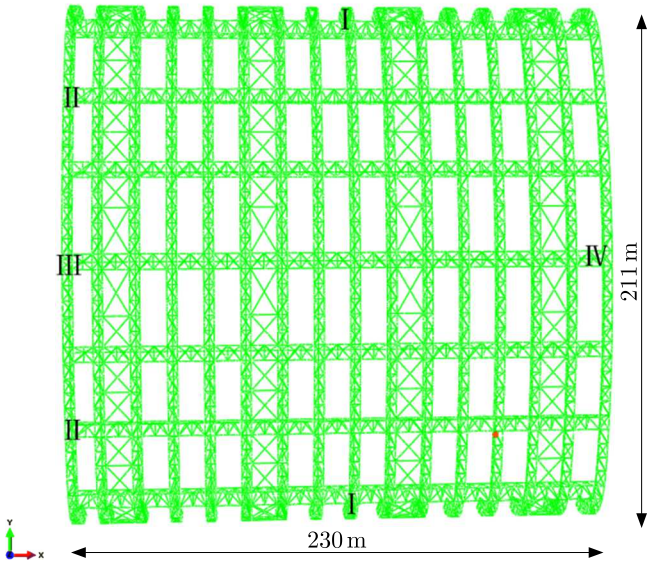

Fig. 1. Top view of the model

2.2. Material performance and section type

Section types of the simplified model members are all steel pipe, and the section materials are all Q345 steel whose main material parameters are shown in Table 1.

Table 1. Material parameter

Yield stress f_y	Elastic modulus E	Density ρ	Poisson's ratio ν	Breaking strain
345 MPa	206 GPa	7850 kg/m^3	0.3	0.02

The members are mainly divided into the upper chord, lower chord and web member according to their positions in the truss. Table 2 is a summary of the member section types used in different parts of the structure, where $\emptyset$ represents pipe section, the former number and the latter one represent the outer radius and thickness of the pipe section, respectively.

Table 2. Section types of the members

Member parts	Section type
Upper and lower chord	$\emptyset560 \times 25$, $\emptyset500 \times 24$, $\emptyset450 \times 24$, $\emptyset400 \times 24$, $\emptyset377 \times 20$, $\emptyset351 \times 18$, $\emptyset351 \times 16$, $\emptyset325 \times 16$, $\emptyset299 \times 14$, $\emptyset273 \times 14$, $\emptyset273 \times 10$, $\emptyset245 \times 12$
Web members	$\emptyset245 \times 12$, $\emptyset219 \times 10$, $\emptyset219 \times 8$, $\emptyset194 \times 8$, $\emptyset180 \times 8$, $\emptyset159 \times 6$, $\emptyset140 \times 5$, $\emptyset114 \times 4$, $\emptyset89 \times 4$

2.3. The constitutive model

In this paper, two constitutive models are employed to study progressive collapse performance of the arch truss structure considering compression instability of the members. The first one is the material failure constitutive model which applies material failure as the failure criterion for

element members. As Q345 steel is adopted, the stress-strain curve of Q345 steel is simplified to a two-stage folding line for simplified model calculation. When the compressive and tensile stresses of the members reach the yield stress, the modulus of elasticity of the member is reduced by 0.01 times of the original value. The ultimate strain of Q345 steel is 0.025, and when the material strain is close to the ultimate strain, the maximum stress and strain fluctuate less and have less influence on the calculation results. The member is determined to fail when strain of the member exceeds the failure strain of the material which is set to 0.02 in this paper. The stiffness change of the material at different stress stages is described by multiplying the elastic modulus by different coefficients k, that is, $E' = kE$. The stress-strain equations of the material failure constitutive model is given in Eq. (2.1), where ε_y represents the strain at which the member stress reaches the yield strength f_y. In the process on progressive collapse of the space grid structure, slender compression members are peculiarly prone to buckling and tend to fail before reaching the yield load, making the actual bearing capacity of the member lower

$$k = \begin{cases} 1 & \text{for} \quad -\varepsilon_y \leqslant \varepsilon \leqslant \varepsilon_y \\ 0.01 & \text{for} \quad |\varepsilon| > \varepsilon_y \end{cases} \tag{B.1}$$

Vumat is a program interface provided by Abaqus finite element software for users to compile self-defined materials. The second one is based on the Vumat subprogram in Abaqus to develop a Kinematic Hardening Plasticity constitutive model considering compression instability of members. This model introduces the Marshall model and the stability coefficient of the compressed member. The Marshall model (Marshall *et al.*, 1977) is based on the hysteresis curve obtained from a steel circular tube test, which describes the hysteresis performance of an inelastic member containing initial defects and a decrease of axial stiffness after compression instability. The model is optimized on the basis of the Marshall model, and the stress-strain curve of the optimized model is shown in Fig. 2. The optimized model consists of several straight lines, indicating that the elastic modulus of the member differs at different stages. When the axial strain of the member, represented by the X-axis, is greater than 0, the member is in tension. The stiffness change of the material at different stress stages is described by multiplying the elastic modulus of the material by different coefficients k, that is $E' = kE$

$$k = \begin{cases} 0.01 & \text{for} \quad \varepsilon > \varepsilon_y \\ 1 & \text{for} \quad \varepsilon_{cr} \leqslant \varepsilon \leqslant \varepsilon_y \\ \alpha & \text{for} \quad \varepsilon' \leqslant \varepsilon < \varepsilon_{cr} \\ \beta & \text{for} \quad \varepsilon < \varepsilon' \end{cases} \tag{B.2}$$

where ε_{cr} represents the strain at which the stress reaches the yield strength P_{cr}. P_{cr} represents the critical stress when instability of the compression member occurs, calculated by the stability coefficient φ of the compression member in the Standard for Design of Steel Structures (GB50017-2017), that is $P_{cr} = \varphi f_y$. φ is calculated according to parameters such as section type, length, elastic modulus and radius of gyration of the member, and the physical meaning of critical control point φ is the same as the stability coefficient of pressure brace in the Standard for Design of Steel Structures. When the compressive stress of the member exceeds the compressive instability critical stress P_{cr} of the member, the axial stiffness will decrease. α and β represent the initial weakening coefficient of the elastic modulus and the deep weakening coefficient of stiffness after instability of the compression member occurs, respectively. ε' represents the critical strain at the initial weakening and deep weakening of the elastic modulus of the member. The calculation formula is as follows

$$\varepsilon' = \varepsilon_{cr} - \frac{(1-\gamma)\sigma_{cr}}{-\alpha E} \tag{B.3}$$

where α, β, γ are coefficients summed up from the hysteresis curve of the steel round tube test, and the values in this model are as follows

$$\alpha = 0.13 \qquad \beta = 0.02 \qquad \gamma = 0.28$$

σ_u, ε_u are the stress and strain when the member is unloaded under compression, and the calculation formula for k is as follows

$$k = \frac{\sigma_y - \sigma_u}{\varepsilon_y - \varepsilon_u} \tag{B.4}$$

When strain of the member reaches point D, which is the failure strain of the member, it indicates that the member has completely lost its bearing capacity. At this time, it is determined that the member is failed and then deleted.

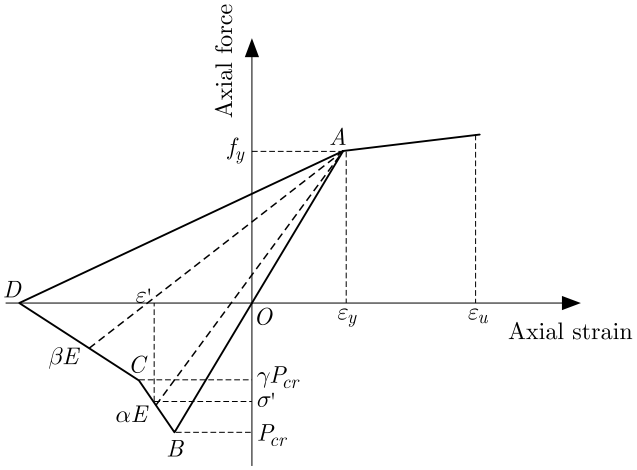

Fig. 2. Member-stabilized constitutive model

In order to introduce this model into the subprogram, some important material parameters need to be defined. Table 3 shows description of the main material parameters in the Vumat subprogram, and these nine parameters need to be added in the Abaqus user-defined material. With the input material parameters, the subprogram will automatically calculate the compression instability critical pressure P_{cr} and other related parameters of each member. The Vumat subprogram monitors the stress state of the members and updates parameters like the elastic modulus in real time by using the feature of transferring specific variables with the main program at the beginning and end of each incremental step, which simulates member stiffness degradation. The strain of the member is also used as an indicator to determine failure of the member. When the member is in compression, the failure is judged when the strain is greater than the D point, and when the member is in tension, the failure is judged when the strain is greater than the ultimate strain.

When using the Vumat subprogram, Abaqus cannot automatically calculate the transverse shear stiffness of the section, and the user needs to define and input the transverse shear stiffness K_{23} and K_{13} of the section. The calculation formula for the shear stiffness of the beam section is as follows

$$K_{13} = K_{23} = mGA \qquad G = \frac{E}{2(1+\nu)}$$

where G is the shear modulus, A is the cross-sectional area and m is the shear non-uniformity coefficient of the section, which is selected according to the section category (parameter 9) in Table 1. When the section type is circular, take 0.89.

Table 3. Vumat main parameters

Material parameters	Illustrate
1	Elastic modulus
2	Poisson's ratio
3	Yield strength
4	Weak axis radius of inertia
5	Hardening factor (0.01)
6	Marshall simplified model parameter $\alpha(-0.13)$
7	Marshall simplified model parameter $\beta(-0.02)$
8	Marshall simplified model parameter $\gamma(0.28)$
9	Section category (1)

2.4. Load

The explicit module of Abaqus is employed to simulate the progressive collapse process of the calculation structure, and only a dynamic display analysis step with a time length of 4 s is added. To simulate the load condition of the upper part of the steel arch truss structure, 5 times gravity load (49 m/s^2) is added along the z-direction, which increases linearly to the maximum value in the first 2 s, and remains constant in the last 2 s so as to avoid oscillations in the results. The load amplitude curve is shown in Table 4.

Table 4. Load amplitude

Time/frequency	Amplitude
0	0
2	1
4	1

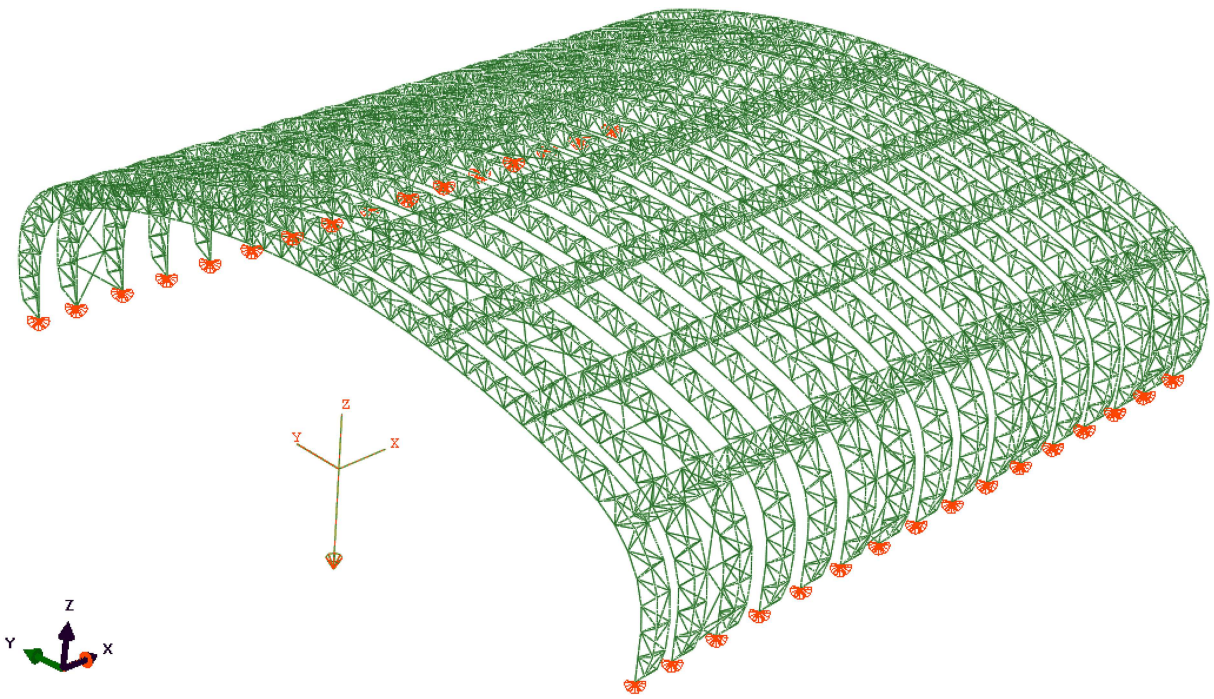

Fig. 3. Constraints and loads

The supports on both sides of the structure are all hinged. The displacement of nodes in x, y and z directions are constrained. Figure 3 shows the constraint position and load application direction of the structure.

2.5. Structural failure criterion

At present, there are many failure criteria for determining structure collapse. Displacement criteria are applied in this paper to determine whether progressive collapse occurs. When the vertical displacement of the structural node exceeds 1/50 of the span, it is considered that the structure has collapsed. The maximum span of this structure is 211 m, hence when the maximum vertical displacement of the structure exceeds 4.2 m, the collapse of the structure is judged.

3. Analyses and results

3.1. The material failure constitutive model

3.1.1. Vertical displacement of the structure

Figures 4-8 are displacement diagrams at different times when the material failure constitutive model is used for progressive collapse analysis. In Figs. 5-11, positions of failed members at different times are marked with red circles. Figure 4 shows the displacement diagram of the structure at $t = 2.0$ s, which is the moment when all loads are applied to the structure. It can be seen that the vertical displacement is basically symmetrically distributed along the central axis of the main truss. The vertical displacement of the middle zone of the truss is larger than that of the two sides. Figure 5 shows the displacement at $t = 2.9$ s, when the first failure member appears, the maximum vertical displacement of the structure reaches 3.891 m, which does not exceed 1/50 of the span. Figure 6 shows the displacement at $t = 3.0$ s, after the member failure, the vertical displacement increases rapidly, the maximum node displacement is 6.34 m, which exceeds 1/50 of the span, and the collapse of the structure is judged. Figures 7 and 8 display displacement diagrams of the structure at different angles at $t = 4.0$ s. It can be found that during the whole process from the beginning of loading to the end, the vertical displacement of zone III is larger than that of other positions. The maximum displacement point appears at the mid-span position of the first truss, on the left in Fig. 8. When $t = 4.0$ s, the maximum nodal displacement of the structure reaches 57.43 m, leading to serious overall deformation of the structure. In Fig. 7, zone I and III are the most severely damaged, and the structure failure occurs basically.

3.1.2. Member failure order

At $t = 2.0$ s, the structural load reaches the maximum value, and there is no failure member in the structure. At $t = 2.9$ s, the first failure member appears at the marked position of zone III in Fig. 5, which is the upper chord of the truss, and the failure form is compression failure. It can be seen from Fig. 6 that during the time from 2.880 s to 3.000 s, with the position of the first failure member as the center, spreading along the direction of the connecting truss, more failure members appear in the adjacent positions. Meanwhile, a part of the trusses in zone I has failure members, all of which are the upper chords of the truss, and the failure mode is tensile failure. It can be seen from Fig. 7 that during the time from 3.0 s to 4.0 s, due to influence of the internal force redistribution of the structure, the load originally borne by the failure member is transferred to the surrounding members, and a large number of failure members appear, thus resulting in further structural damage. It is worth noting that the locations of failure members are mainly concentrated in zone I and III. Most of the failure members in zone I are the upper

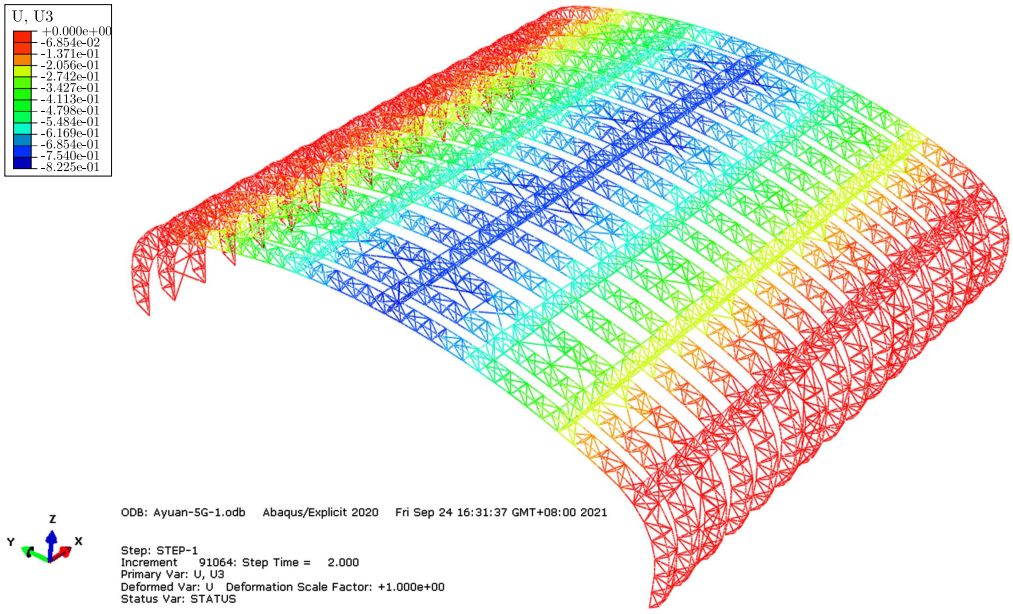

Fig. 4. Structure displacement diagram, $t = 2.0\,\mathrm{s}$

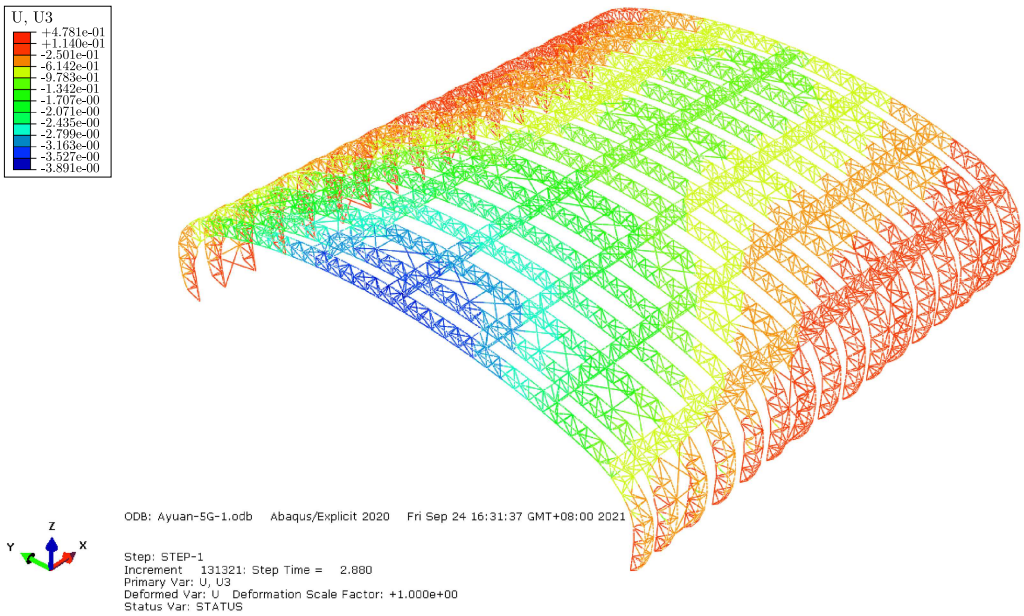

Fig. 5. Structure displacement diagram, $t = 2.9\,\mathrm{s}$

chord members of the truss, and a small part contains diagonal web members. At first, only a few upper chords of the trusses are damaged by tension, and finally the upper chords of all trusses in the same position are damaged. Zone III is the one where the failure member occurs first, with the largest vertical displacement of the structure. After the first failure member appears, other failure members spread from zone III to zone IV. In general, the largest number of failure members and the most serious structural damage lie in zone III.

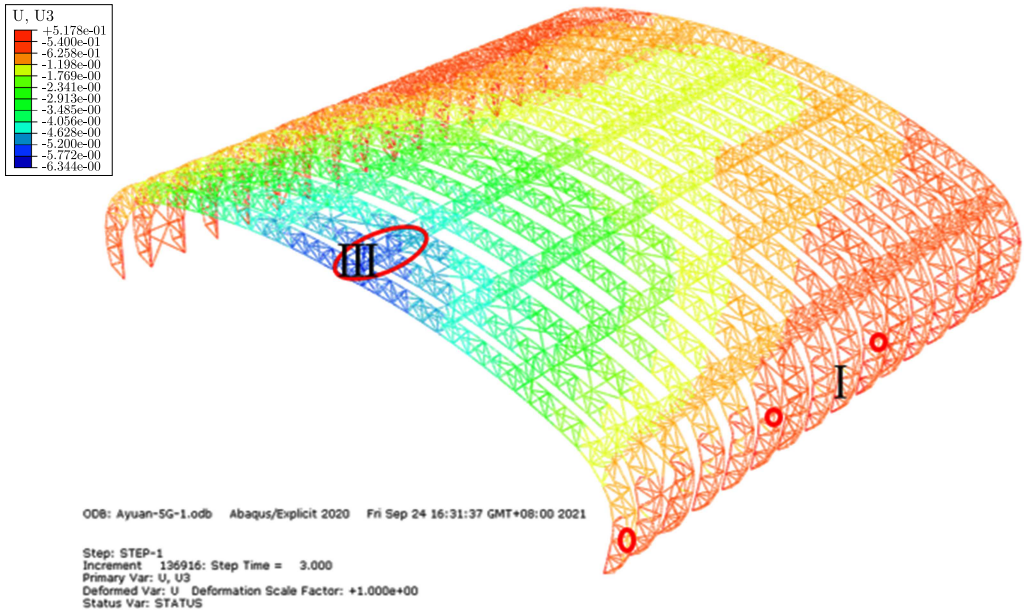

Fig. 6. Structure displacement diagram, $t = 3.0\,\mathrm{s}$

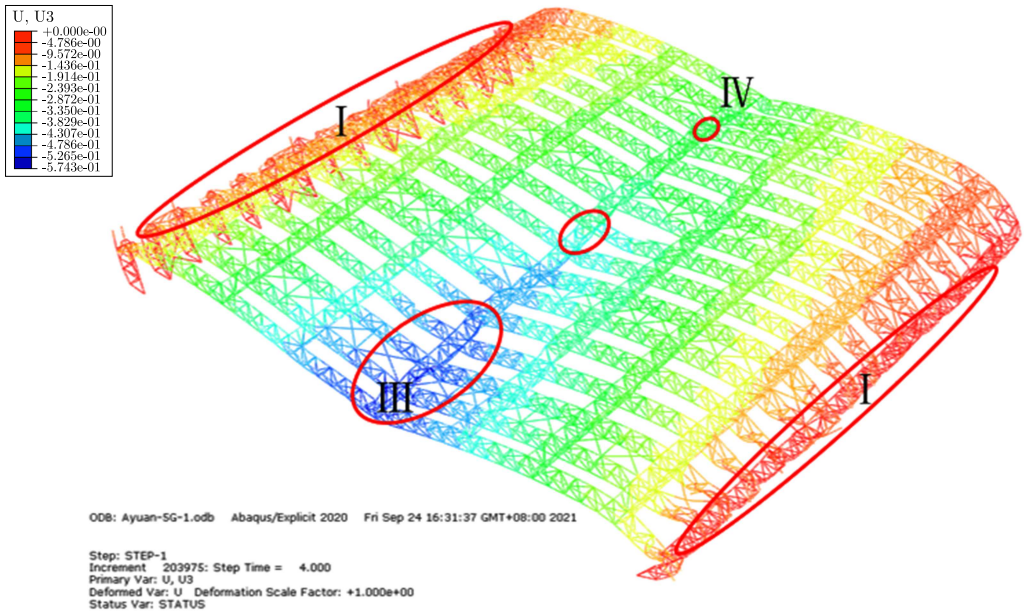

Fig. 7. Structure displacement diagram, $t = 4.0\,\mathrm{s}$

3.2. Member-stabilized constitutive model

3.2.1. Vertical displacement of the structure

The displacement process at different times with the member stability constitutive model is shown in Figs. 9-12. Figure 9 depicts the displacement of the structure at $t = 1.32\,\mathrm{s}$, which is the moment when the first instable member appears in the structure. It can be seen from the figure that the overall vertical displacement distribution of the structure at the moment of initial loading is basically consistent with Fig. 4, with the vertical displacement in the middle of the truss being larger and gradually decreasing to both sides. As can be seen from Fig. 10, the maximum nodal vertical displacement of the structure is 4.52 m, which exceeds 1/50 of the span of the structure at $t = 1.76\,\mathrm{s}$, at this time the structure has collapsed. The displacement diagram

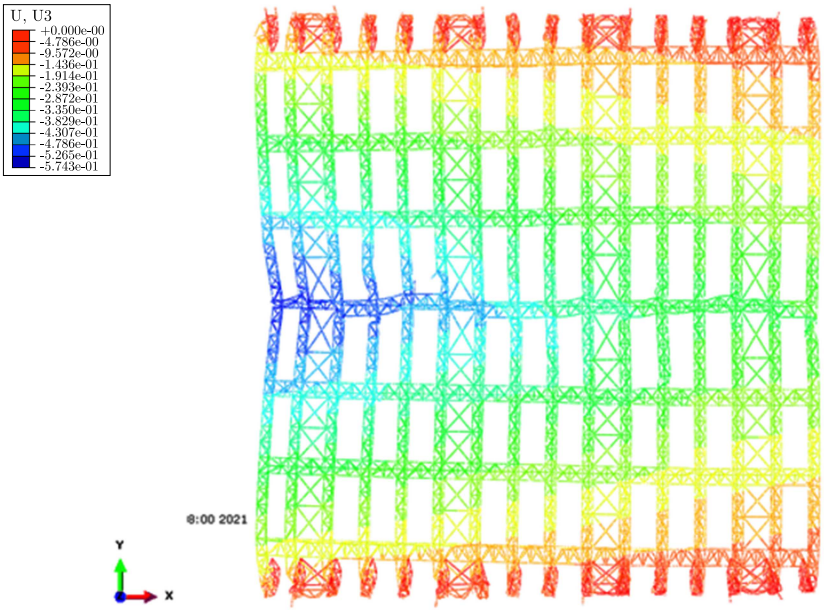

Fig. 8. Top view of structure, $t = 4.0\,\mathrm{s}$

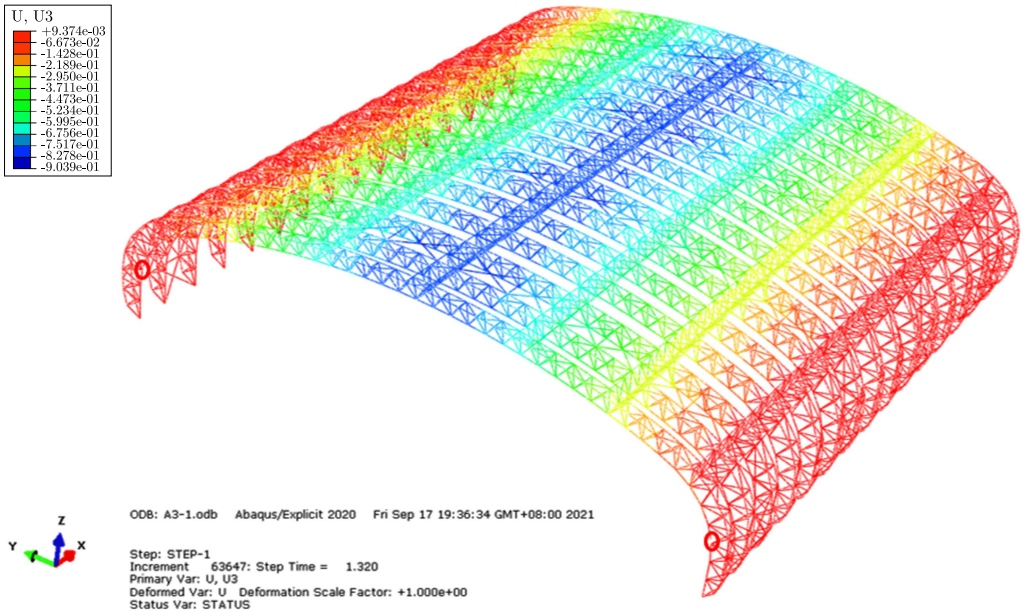

Fig. 9. Structure displacement diagram, $t = 1.32\,\mathrm{s}$

of the structure at $t = 2.48\,\mathrm{s}$, shown in Fig. 11, illustrates that the maximum nodal vertical displacement is 30.5 m. At this moment the superstructure collapses as a whole and severe outward deformation occurs at the arch shoulder. When $t = 3.291\,\mathrm{s}$, the support is basically destroyed and the structure completely failed. Zone III is the zone with the largest vertical displacement of the structure, where the vertical displacement is larger than that in zone IV and basically the same as that in zone II. Compared with the material failure constitutive model, the collapse of the structure occurs earlier when considering compression instability of the members. When the load does not reach the maximum value, the structure has collapsed. Furthermore, the collapse of the structure occurs faster and the bearing capacity of the structure is lower.

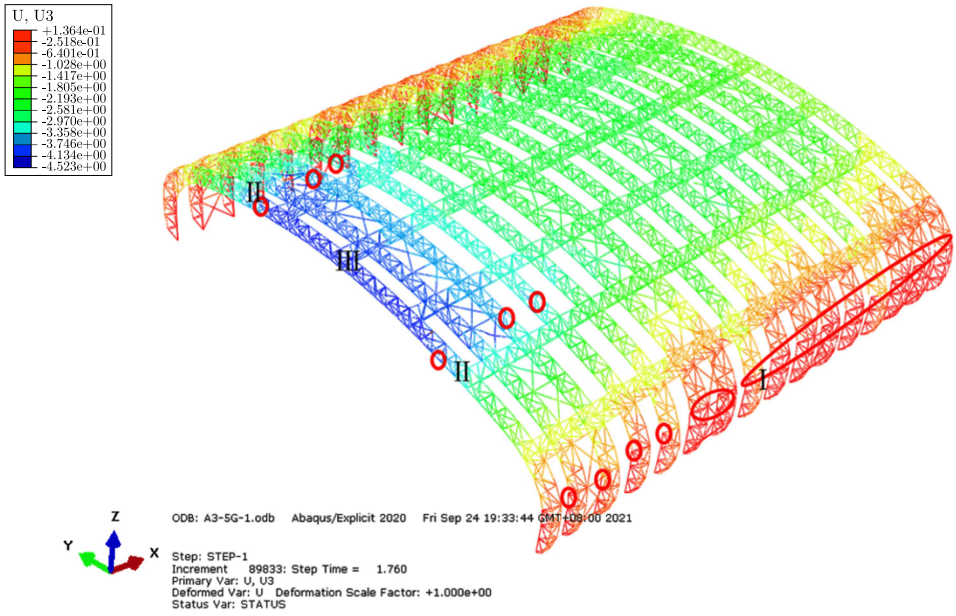

Fig. 10. Structure displacement diagram, $t = 1.76$ s

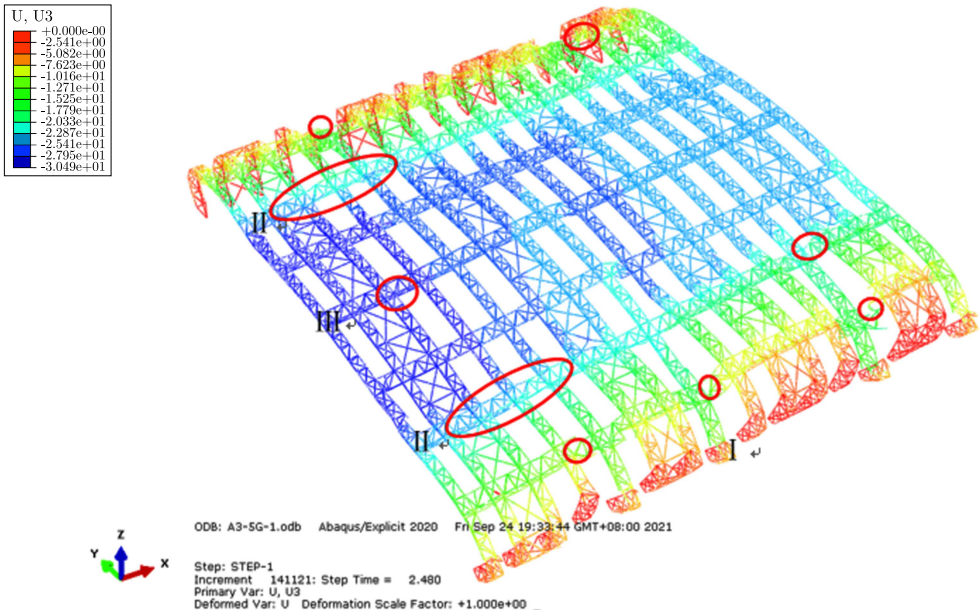

Fig. 11. Structure displacement diagram, $t = 2.48$ s

3.2.2. Member failure sequence

At $t = 1.320$ s, the earliest failure members of the structure appear in the first truss on the left, located in zone I on both sides of the truss. They belong to the lower chords of the truss, and their failure type is compression failure. During the time from 1.320 s to 1.760 s, the lower chords with compression failure appear in zone I of all trusses (the failure members in zone I on the other side are not marked in Fig. 10). In addition, there are diagonal web members that fail under compression near zone I and II, and the failure members of the superstructure are mainly concentrated in left trusses. From 1.76 s to 2.48 s, the lower chord with compression failure begins to appear in zone III, and more failure members appear near zone II, expanded from the left truss to the right truss. It can be seen from the failure members marked in Fig. 11

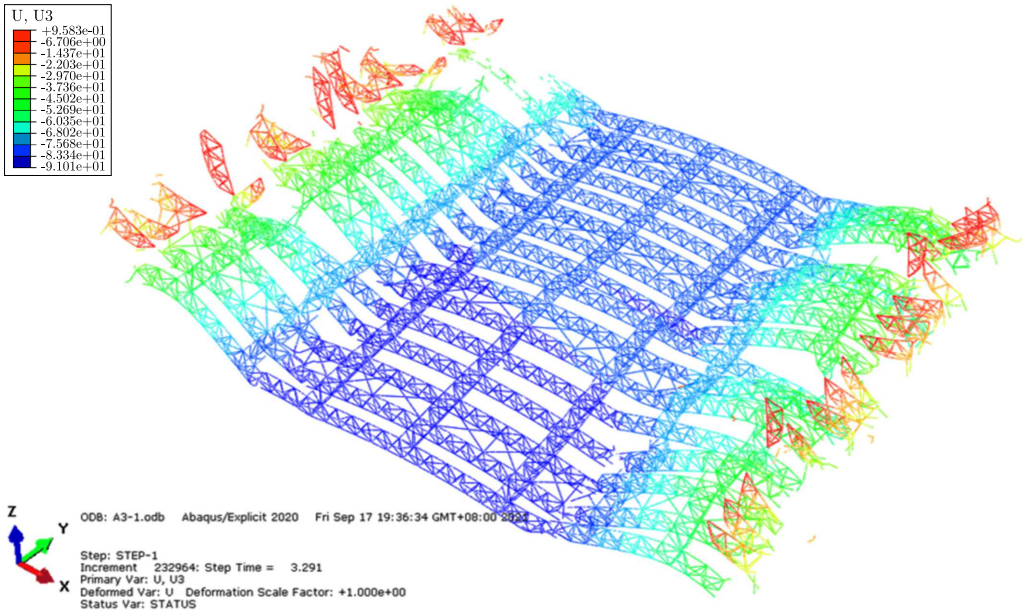

Fig. 12. Structure displacement diagram, $t = 3.29\,\mathrm{s}$

that at $t = 2.48\,\mathrm{s}$, a large number of failure members appear in the structure, most of which are compression failure members, mainly located in zone I and II. The connecting truss near zone II, with many compression failure members which are mainly lower chord and diagonal web members, is seriously damaged. A part of the connecting truss is broken, and the overall structure deformation is large. A large number of compression failure members in zone I leads to the collapse of the truss, which means that the truss has lost its bearing capacity and the vertical displacement of the structure increases rapidly. Figure 12 shows the vertical displacement diagram of the structure at 3.29 s, and the structure completely fails at this time.

3.3. The difference between calculation results of the two constitutive models

3.3.1. The first failure member

Figure 13 reveals the location of the first failure member and the node with the maximum vertical displacement for both constitutive models. The first failure members, which are all compression failure members, all appear on the lowermost truss (corresponding to the first truss on the far left in Fig. 1), whereas location and time are not the same. When adopting the double broken linear constitutive model, the structure firstly exhibits the compression failure at $t = 2.880\,\mathrm{s}$, located in the middle of the first truss on the left, which is the upper chord in member 1 in Fig. 13. When using the member stability constitutive model considering member instability, the first compression failure member appears at $t = 1.320\,\mathrm{s}$, much earlier than when adopting the double broken linear constitutive model. At this moment the structural load just reached about 3/5 of the maximum load. The failure member is the lower chord of the truss, as shown in member 2 in Fig. 13.

3.3.2. Type and location of failed members

The failure members of the structure using the material failure constitutive model are mainly concentrated in zone I and III. The failure members appear first in zone III, among which the number of tension failure members and compression failure members is similar. The failure members in zone I are mainly the upper chord members of the truss with tension failure, such as the position of member 3 in Fig. 13. The failure members of the structure using the material

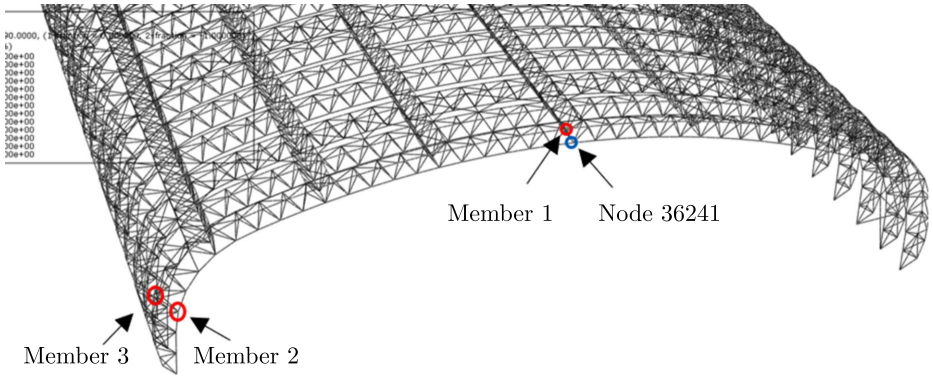

Fig. 13. The failure members and maximum displacement node

failure constitutive model compiled by Vumat and considering member instability are mainly concentrated in zone I and II, most of which are compression failure members. Zone I is the earliest location where the failure member occurs, which is mainly the lower chord of the truss with compression failure, such as the position of member 2 in Fig. 13. The failure members in zone II, more than those in zone III, are mainly diagonal web members and upper chords of the connecting trusses.

3.3.3. Maximum nodal vertical displacement

During the loading process using the two constitutive models, the maximum vertical displacement occurs in the middle of the first truss on the left in zone III. The displacement time history curve of selected node 36241 with the maximum displacement of the structure is depicted as Fig. 14, from which it can be observed that at the same moment, the vertical displacement of node 36241 when using the member stability constitutive model is larger than that when using the material failure constitutive model. Moreover, when using the member stability constitutive model, the structure progressive collapse occurs earlier and the vertical displacement increases faster, indicating that the structural failure process is more rapid.

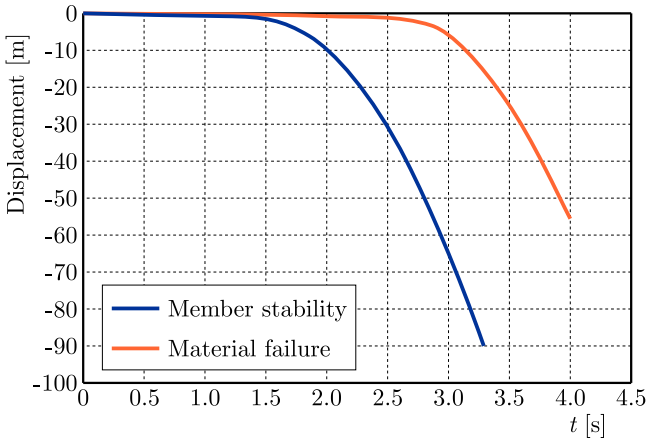

Fig. 14. Displacement time history curve of node 36241

4. Conclusions

In this paper, numerical simulation is used to analyze the progressive collapse process of a super-long span latticed steel arch structure using two constitutive models. The similarities and

differences of the collapse time of the structure and the failure sequence of the members are compared, and the conclusions are as follows:

- From the calculation results using the two constitutive models, the first failure member appears in the first truss on the left which is the weak point of the structure. In the structure using the constitutive model considering member compression instability, the first compression instability member appears earlier, before the load reaches the maximum value.
- Using the member stability constitutive model the failure of most members in the structure is compression failure. For example, the failure type of members in zone I of the truss is primarily compression failure of the lower chord members. However, the failure type of members in zone I is primarily tension failure of the upper chord members when using the material failure constitutive model.
- In the structure using the member stability constitutive model, the collapse of the structure occurs earlier and the collapse process is more rapid. Considering the member compression instability, the actual ultimate bearing capacity of the member is lower.

References

1. Cai J.G., Wang F.L., Feng J., Zhang J., Huang L., Sheng P., Zhen W., Chen Q., 2010, Progressive collapse analysis of cable-arch structures of the New Guangzhou Railway Station, *Journal of Building Structures*, **7**, 31, 103-109
2. Ding Y., Ge J.G., Li Z.X., 2011, Instantaneous component-removing method for analysis of regressive collapse of space grid structure, *Journal of Tianjin University*, **44**, 6, 471-476
3. GB50017, 2017, Code for design of steel structures, Ministry of Construction of the People's Republic of China, Beijing, China
4. GB50068, 2018, Unified standard for reliability design of building structures, Ministry of Construction of the People's Republic of China, Beijing, China
5. Ge J.G., 2012, Collapse mechanism and anti-collapse measures of single-layer reticulated shell structure under strong earthquake, Ph.D. Thesis, Tianjin University, Tianjin, China
6. Han Q.H., Deng D.D., Xu Y., Zhang X.Z., 2018, Study on progressive collapse failure mode and collapse limit displacement of 8 grid structure, *Spatial Structures*, **24**, 1, 9-16+61
7. Han R., Yin T.Y, Yang X.D, Zhang Y., Zhang Y.S., Ju J.S., 2021, Study on progressive collapse resistance of single-layer reticulated shells, *Journal of Physics: Conference Series*, **1777**, 012037
8. Jiang X., Chen Y., 2012, Progressive collapse analysis and safety assessment method for steel truss roof, *Journal of Performance of Constructed Facilities*, **26**, 3, 230-240
9. Koh Y.H., Krauthammer T., 2019, Exploring numerical approaches for pre-test progressive collapse assessment of RC frame structures, *Engineering Structures*, **201**, 109776
10. Marshall P., Gates W., Anagnostopoulos S., 1977, Inelastic dynamic analysis of tubular offshore structures, *Proceedings of Ninth Annual Offshore Technology Conference*, Houston, Texas
11. Miyachi K., Nakamura S., Manda A., 2012, Progressive collapse analysis of steel truss bridges and evaluation of ductility, *Journal of Constructional Steel Research*, **78**, 192-200
12. Song B.I., Sezen, H., 2013, Experimental and analytical progressive collapse assessment of a steel frame building, *Engineering Structures*, **56**, 664-672
13. Tian L.M., Wei J.P., Hao J.P., 2018, Anti-progressive collapse mechanism of long-span single--layer spatial grid structures, *Journal of Constructional Steel Research*, **144**, 270-282

14. Tian L.M., Wei J.P., Hao J.P., 2019, Optimisation of long-span single-layer spatial grid structures to resist progressive collapse, *Engineering Structures*, **188**, 394-405

15. Wang J.J., Wang W., 2021, Theoretical evaluation method for the progressive collapse resistance of steel frame buildings, *Journal of Constructional Steel Research*, **179**, 106576

16. Wilkes J., Krauthammer T., 2019, An energy flow approach for progressive collapse assessment, *Engineering Structures*, **190**, 333-344

17. Zhang J.X., 2013, Progressive collapse behaviour and design method of multi-story steel frames, Master Thesis, Tsinghua University, Beijing, China

18. Zhao X.F., Shen B., Ma K.J., Wang H., He Z., Zhang X.H., Wu B., 2019, Study on the dynamic analysis method of progressive collapse of plane truss structures, *Progress in Steel Building Structures*, **1**, 21, 15-22

19. Zhao X.H., Wu B., 2016, Application of cable arch trusses in large span dry coal shed structure, *Building Structure*, **S1**, 46, 519-522

20. Zhu Y.F., Feng J., Cai J.G., Zhuang L.P., 2013, Analysis on progressive collapse resistance of truss string structure of Meijiang Exhibition Center, *Journal of Building Structures*, **3**, 34, 45-53

Manuscript received February 23, 2022; accepted for print October 3, 2022

JOURNAL OF THEORETICAL AND APPLIED MECHANICS
61, 1, pp. 119-127, Warsaw 2023
https://doi.org/10.15632/jtam-pl/158008

RESEARCH ON TIME-VARYING RELIABILITY OF WIND POWER GEARBOX WITH FAILURE CORRELATION

Mingliang Zheng

Mechanical and Electrical Engineering of Wuxi Taihu University, Wuxi, China
e-mail: zhmlwxcstu@163.com

In the process of reliability modeling and design of a wind power gearbox, the influence of failure correlation of system components and random dynamic loads can not be ignored. In this paper, taking the output power of each shaft of the gearbox as the starting point, distribution parameters of stress and strength for critical failed components (gear and bearing) of the gearbox are solved. After normalization of these parameters, and when there is a linear correlation between the loads of each component, finally, the time-varying reliability related to failure correlation is calculated based on a full probability differential method by using the stress strength interference theory at the system level, and the results are verified by the Monte-Carlo simulation method. It is found that the failure correlation caused by the external dynamic loads between components can significantly reduce reliability of the gearbox system. The stronger the correlation, the lower the reliability of the gearbox system. Meanwhile, the time-varying reliability conforms to characteristics of the "failure bathtub curve" of typical mechanical products. This paper can lay a foundation for the time-varying reliability optimization design and structural robustness design of the wind power gearbox.

Keywords: wind power gearbox, failure correlation, stress-strength, time-varying reliability

1. Introduction

Wind power is a renewable energy with great resource potential and mature technology. The gearbox in the wind power transmission system is a necessary and high cost component in the whole wind turbine. Its main function is to realize transmission of energy from the impeller to the generator and change the transmission speed. Its reliability has always been a major problem in the wind power industry. Qin *et al.* (2012) deeply studied gearbox reliability considering the coupled action of gear and bearing under random dynamic loads. They used the test coefficient distribution method to deal with failure correlation, and reliability calculation depended on dynamical equations. Lewis (2001) proposed an approximate numerical method for estimating the static failure probability of a gearbox by using the stress-strength interference model. Considering the time-varying effect of loads, Wang *et al.* (2014) studied the dynamic reliability of a gear transmission system of a wind turbine. Giger and Armando (2011) revised the structure of a wind power gearbox for improving reliability, but this structure was difficult to manufacture and its life could not be calculated quantitatively. Zhou *et al.* (2013) only evaluated the dynamic reliability of a wind power gearbox according to correlation between two failure modes of a pair of gears. They only aimed at meshing of a pair of gears and did not study reliability of the system. Ditlevsen (1979) proposed a second-order reliability interval estimation method by considering the correlation between two failure modes of the whole gearbox, but calculation of the correlation coefficient was empirical. The latest research on the reliability of a wind power gearbox was made by Guo *et al.* (2020), Bhardwaj *et al.* (2019), Jiang *et al.* (2018), Liu *et al.* (2016), Bejger *et al.* (2021), Hosseinzadeh and Salmasi (2016), Röder *et al.* (2021) and so on. Although the above references adopted reliability analysis and structural optimization design of

a gearbox from different aspects, and achieved some corresponding theoretical results, but there are few studies considering component failure correlation and system time-varying reliability at the same time.

Due to complexity of the internal and external excitation and the correlation between the coupling effects of various components in the wind power gearbox system, stress of the gear and bearing is time-varying and has failure correlation. The data in the references (Jantara *et al.*, 2020; Mo *et al.*, 2018) show that the reliability of the gearbox is dynamic and has attenuation characteristics, and the data in the references (Inturi *et al.*, 2022; Srinivasan and Robert, 2021) show that the parts of the whole gearbox system are not independent, and there is a certain correlation between failure of gearbox parts. So the time-varying reliability of a wind power gearbox with failure correlation is more accurate and in line with the actual situation. In this paper, taking a MW type of a wind power gearbox as the research object, we establish a time-varying reliability evaluation model considering failure correlation. Specifically, using relevant standards of the mechanical design, the distribution of parameters determines the dynamic meshing force of each gear pair and the dynamic contact force of each support bearing. On this basis, according to the stress-strength interference model at the system level, and using a sequential statistical method in a random process, the law of change with time of the gearbox reliability considering multiple actions of a random load and failure correlation is solved. The accurate evaluation of the reliability of the wind power gearbox system considering failure correlation has great practical significance for safe operation and maintenance strategy of the whole wind turbine.

2. Model of the wind power gearbox

Because the planetary gear transmission adopts multiple planetary gears to share the load and realize power diversion, it has an advantage of small volume, light weight and strong bearing capacity. However, considering the relatively complex structure and difficult processing of a large internal gear ring, the transmission structure with one-stage planetary plus two-stage parallel shafts (NGW type) is usually adopted for a large wind power gearbox. Its transmission structure (Chen *et al.*, 2011) is shown in Fig. 1.

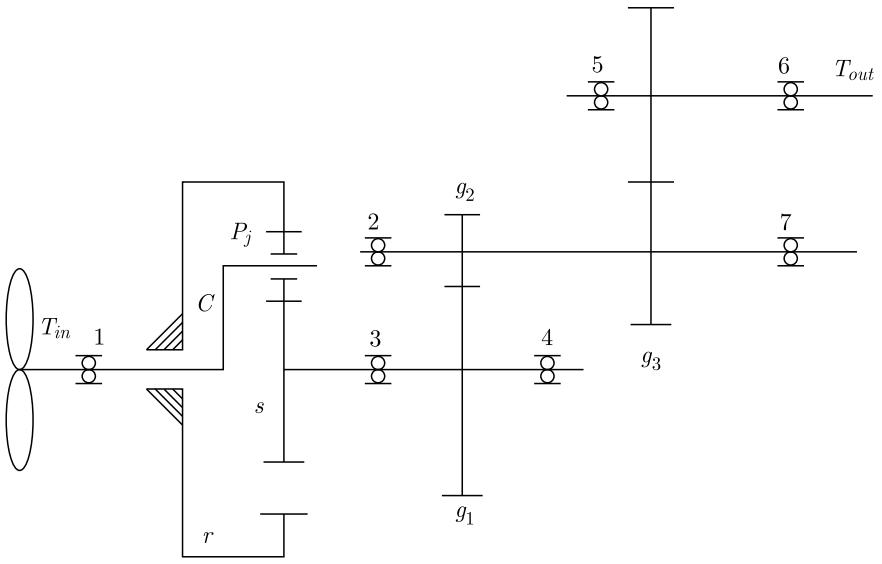

Fig. 1. A sketch of a wind power gear transmission system

Here, the planet carrier is the input and the inner gear ring is fixed, r, s, p, c, g, T_{in}, T_{out} represent the inner gear ring, solar gear, planetary gear, planetary frame, helical gear, input torque and output torque, respectively.

According to the main failure modes of gears and rolling bearings in the wind power gearbox, gears usually adopt a hard tooth surface, so wear and plastic deformation of the gear tooth surface are not the main causes of gearbox failure. In this paper, the reliability of the gear tooth root bending fatigue strength is evaluated. The reliability of the rolling bearing is calculated according to the pitting failure mode of the rolling element inner and outer ring raceway. According to current working conditions and empirical data of the wind turbine transmission system during operation, the reliability of the input and output shaft, planetary carrier, planetary shaft and spline connection in the system are generally very high, so calculation of the reliability of the transmission system mainly considers the influence of the gear and bearing. It is defined that as long as one of the three planetary gears in the row star drive fails, the row star drive cannot work normally. In this way, the failure mode of the whole wind power gearbox system is divided into sixteen failure unit events. Therefore, the reliability block diagram of the wind power gearbox is shown in Fig. 2.

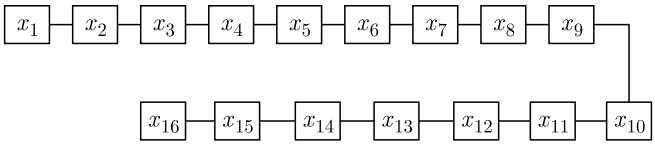

Fig. 2. Reliability block diagram of the gearbox

Here, 1-16 is internal gear 1, solar gear 2, planetary gears 3-5, helical gears 6-7, helical gears 8-9 and rolling bearings 10-16.

3. Stress and strength distribution of components

3.1. Fatigue reliability analysis of the gear root

For an involute spur gear, the tangential load is the circumferential force, which is a quotient of torque and radius. For the multiple gears split, according to equal division, the tangential loads of wind power gears in Fig. 1 are calculated according to GB/T3480-1997, as shown in Table 1.

Table 1. Tangential loads of gears in the wind power gearbox

Tangential load	s and p	p and r	1 and 2	3 and 4
F_τ	$2T_s/(n_w d_s)$	$\approx 2T_s/(n_w d_s)$	$2T_4/d_4$	T_6/d_6

Here, n_w is the number of planetary gears, d_i is the dividing circle diameter of gears, and T_i is the output torque of gears.

The diameter of the gear pitch circle and the tooth load distribution coefficient can be calculated, the service coefficient and dynamic load coefficient can borrow dynamic characteristics of the existing wind power gearbox, and the other coefficients can be found in the mechanical design manual. Each correction coefficient under known conditions is calculated according to the GB/T3480-1997. According to the ISO 6336 standard, the calculation formulas of contact fatigue stress and strength of the gear are

$$\begin{aligned} S_H &= \frac{K_A K_V K_{F\beta} K_{F\alpha} F_\tau}{b m_n} Y_{F\alpha} Y_{s\alpha} Y_\varepsilon Y_\beta = w F_\tau K_A \\ \sigma_H &= \sigma_{F\,lim} Y_N Y_S Y_{\delta rel} Y_{R\,rel} Y_X \end{aligned} \tag{B.1}$$

Here, S_H is the root bending stress, σ_H is the bending fatigue strength, w is a constant, K_A is the usage coefficient, K_V is the dynamic load factor, b is the working tooth width, m_n is the normal modulus, $K_{F\beta}$ is the load distribution coefficient along the tooth direction, $K_{F\alpha}$ is the load distribution coefficient between teeth, F_τ is the tangential load, $Y_{F\alpha}$ is the tooth top coefficient, $Y_{s\alpha}$ is the top stress correction coefficient, Y_ε is the coincidence coefficient, Y_β is the helix angle coefficient, $\sigma_{F\,\mathrm{lim}}$ is the nominal bending fatigue limit stress of the test tooth root, Y_S is the correction coefficient of the tested gear, Y_N is the life coefficient, $Y_{\delta\,rel}$ is the sensitivity coefficient of the relative root fillet, $Y_{R\,rel}$ is the surface condition coefficient of the relative root, Y_X is the size coefficient.

Setting the standard deviation of the transmission power P according to the 3σ principle, the mean and standard deviation of the tangential load on the gear can also be calculated, and then the mean and standard deviation of each stress distribution of the gears can be found. In mechanical design, it is generally believed that the above relevant random parameters all obey the normal distribution, and then the stress and strength also obey the normal distribution.

3.2. Reliability analysis of the rolling bearing

Under the action of an external random wind load, the contact stress of the rolling bearing in the wind power gearbox is alternating, and the contact fatigue failure is the main failure form of the rolling bearing. A large number of tests show that the contact fatigue life of rolling bearing obeys the Weibull distribution (Wu and Li, 2002), so the corresponding time-varying reliability evaluation model is

$$R_{bp}(t) = \exp\Big[-0.10536\Big(\frac{t}{t_{90}}\Big)^q\Big] \qquad t_{90} = \frac{16670}{n_b}\Big(\frac{C_z}{f_b P}\Big)^\varepsilon \tag{B.2}$$

Here, $q = 3/2$, $\varepsilon = 10/3$, C_z is the rated dynamic load, n_b is the working speed of the bearing, P is the equivalent momentum load, f_b is the load bearing coefficient.

According to the modern mechanical design manual, the fatigue characteristics δ_{-1} of bearing steel can be found, so the fatigue strength of the bearing is

$$\delta_{bp} = \frac{\delta_{-1}\beta_q}{K_{\delta c}} \tag{B.3}$$

Here, δ_{-1} is the fatigue strength of standard specimens, β_q is the reinforcement coefficient, $K_{\delta c} = (K_\delta/\varepsilon_\delta) + (1/\beta) - 1$ is the comprehensive correction coefficient, K_δ, ε_δ, β are selected according to the conventional design.

4. Time-varying reliability of the gearbox with failure correlation

Due to the coupled action and load correlation between the components of the wind power gearbox system, it is impossible to directly multiply each component by using the independent series theory to calculate the reliability of the gearbox system, nor to solve its reliability by using the completely related weak link theory. At the same time, the load borne by the wind power gearbox system is random and repeated for many times, and the influence of load action times on the system reliability must be considered. According to the method in (Wang *et al.*, 2010), the random variable of maximum stress S_{max} as the equivalent load of the dynamic stress stochastic process $S(t)$ in the design reference period T is calculated by sequential statistical theory. So, we can obtain the probability distribution function, the mean and the variance of S_{max}.

We assume that there is a linear correlation between different load stresses borne by each gear. Not considering strength degradation, the strength of each component is independent. For the load and strength are non-normal distributions, they are transformed into approximate

normal distributions and normalized. The reliability model (Xie *et al.*, 2009) of a wind power gearbox system considering failure correlation when different structural components bear the same external load is obtained, and the reliability expression is

$$R^n = \int_0^{+\infty} f_0(S) \prod_{i=1}^{n} \left(\int_{u_i+\sigma_i S}^{+\infty} g_{min}(\delta)\, d\delta \right) dS \tag{B.1}$$

Here, $g_{min}(\delta) = PDF(\min(\delta_1, \delta_2, \delta_n))$ is the probability density function of minimum order--strength statistics, $f_0(S)$ is the standard normal probability density function, u_i, σ_i are the mean and standard deviation of stress distribution.

So, the time-varying reliability and failure rate of the wind power gearbox system in Fig. 1 are

$$\begin{aligned} R(m) &= \left[\int_0^{+\infty} m[F_0(S)]^{m-1} f_0(s) \prod_{i=1}^{16} \left(\int_{\mu_i+\sigma_i S}^{+\infty} g_{min}(\delta)\, d\delta \right) dS \right] \\ &= \left(\int_0^{+\infty} m[F_0(S)]^{m-1} f_0(S)[1 - G_{min}(\mu_1 + \sigma_1 S, \mu_2 + \sigma_2 S, \ldots, \mu_{16} + \sigma_{16} S)] \right) \end{aligned} \tag{B.2}$$

and

$$\begin{aligned} G_{min}(\delta_1, \delta_2, \ldots, \delta_n) &= 1 - \prod_{i=1}^{n} [1 - G_i(\delta_i)] \\ \lambda(m) &= \frac{-R'(m)}{R(m)} \end{aligned} \tag{B.3}$$

Here, $R(m)$ is the reliability function, $\lambda(m)$ is the failure rate function, m is the number of peak occurrences in T, in this paper $m = t$, $G_{min}(\delta)$ is the probability distribution function of minimum order-statistical strength, $F_0(S)$ is the standard normal probability distribution function of stress.

For comparison, assuming that all loads and strengths are independent of each other, the time-varying reliability of the wind power gearbox under random wind loads is as follows

$$R'(t) = \prod_{i=1}^{9} \left(\int_0^{+\infty} f_{s_{max\,i}}(s) \int_s^{+\infty} g_i(\sigma)\, d\delta \right) \prod_{i=1}^{7} R_{bpi}(t) \tag{B.4}$$

5. Example analysis

For convenience, the seven rolling bearings are selected to be of the same type 23076CC/W33. Specific physical and geometric design parameters of a MW type of the wind power gearbox are given in reference (An *et al.*, 2013). According to the method in this paper and the mechanical design manual, the calculation results of dynamic parameters of the wind power gearbox are brought into Table 2.

Considering the repeated action of loads and the failure correlation of gears, the results of Table 2 are brought into Eqs. (4.2) and $(4.3)_2$ according to the method presented in this paper. Through numerical integration, the first-second moment method and the perturbation method (Wang *et al.*, 2013; Liu *et al.*, 2016; Hu *et al.*, 2014), the change laws of the time-varying reliability and failure rate of the wind power gearbox during the working life are calculated, as shown in Fig. 3.

Table 2. Distribution parameters of the wind power gearbox

Name	Sun gear	Planet gear	Inner gear	Helical gear 1	Helical gear 2	Helical gear 3	Helical gear 4
Mean stress u_{s_H}	450.7	505.7	604.3	644.3	704.4	506.9	501.2
Standard deviation stress σ_{s_H}	2.3	2.6	3.2	3.3	3.6	1.3	1.3
Fatigue strength u_{σ_H}	754.5	754.5	627.4	754.5	754.5	754.5	754.5
Standard deviation strength σ_{σ_H}	25.7	20.6	25.7	25.7	25.7	25.7	25.7
Rolling bearing	Contact stress				$N(454, 342)$		
	Fatigue strength				$N(875, 502)$		
	Reliability function				$R(t) \approx \exp[-10^5(t/87)^{3/2}]$		

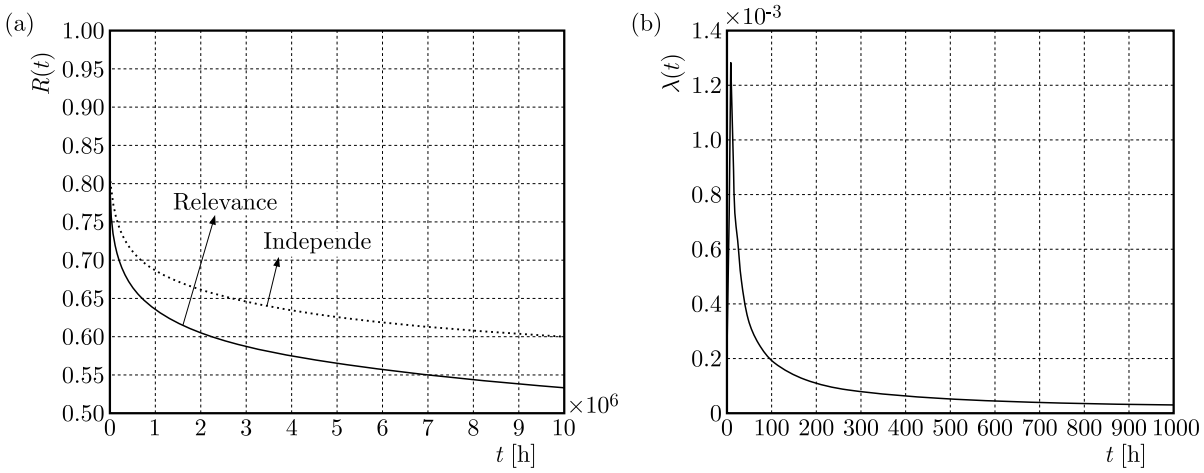

Fig. 3. (a) The time-varying reliability of system, (b) failure rate of the system

As can be seen from Fig. 3a, the reliability of the wind power gearbox gradually decreases with time, and the decreasing slope first grows and then diminishes. Comparing with the independent failure of components, the reliability of the wind power gearbox has a positive correlation with the correlation of components, that is, the better correlation, the lower reliability. With an increase of time, the impact of correlation is more obvious. As can be seen from Fig. 3b, the failure rate curve of the wind power gearbox shows characteristics of an early failure period and accidental failure period in the "bathtub" curve, that is, it gradually decreases and tends to be stable with an increase of time, so the failure is in line with life characteristics of typical mechanical products.

In order to verify the accuracy of calculation results, the Monte-Carlo method is used to determine the reliability of the gear and bearing respectively, and according to the reliability formula of a series system (Xie *et al.*, 2016, 2017), the reliability of the gearbox system is presented in Table 3.

Table 3. The result of Monte-Carlo simulation

Number of times	Reliability
One hundred thousand	0.865442
Two hundred thousands	0.865421
Five hundred thousands	0.865386
One million	0.865342
Two millions	0.865321
Five millions	0.865321

As can be seen from Table 3, with an increase of number of times, the reliability tends to be stable numerically, and the larger the number of simulation time is, the closer is the result of reliability to reality. When the number of times reaches two millions, that is, the time t is 56 h, the reliability value is close to the calculation result of Eq. $(4.3)_1$ (when the time t is 56 h, the value of the integral formula is 0.8653), so the above calculation model is effective.

6. Conclusion

Under the action of an external random wind load, gear meshing forces and rolling bearing contact forces of a wind power gearbox change with time, and its reliability index should be time--varying. Moreover, there is a statistical correlation between failure modes of various components of the system. An estimation method for time-varying reliability of the wind power gearbox with failure correlation is proposed. The main contents are: (1) Taking the output power of the wind power gearbox as the starting point, the transmission power of various components in the gearbox is calculated according to the mechanical design manual. Then through the relationship between power and load, stress distribution parameters of the failed components are found. (2) According to the stress-strength interference theory at the system level and the sequential statistical method in a random process, a reliability model of the wind power gearbox considering both failure correlation and time-varying is established. The function curves of reliability and failure rate are solved by numerical integration. (3) Comparing with the system reliability of the independent failure of components, it can be seen that the correlation between components greatly reduces reliability of the system, that is, the failure of one unit in the gearbox will accelerate the failure of another unit. (4) The reliability of the wind power gearbox working continuously for 56 hours is 86.53%, and characteristics of the failure rate conform to the life "bathtub curve" of typical mechanical products.

By making use of modern manual for mechanical design, a practical method for evaluation the reliability without complex calculation is presented in this paper. Further, we can continue to study the reliability of the wind power gearbox assuming that there is correlation between strength degradation of the components.

Acknowledgement

This research received a grant from the Natural Science Foundation of Universities in Jiangsu Province (20KJD460001) and was sponsored by Qing Lan Project of Universities in Jiangsu Province (2022-29).

References

1. An Z.W., Liu B., Xu J., 2013, Dynamic reliability analysis of wind power gearbox component, *Proceedings of 2013 International Conference on Quality, Reliability, Risk, Maintenance and Safety Engineering*, 215-219

2. Bejger A., Frank E., Bartoszko P., 2021, Failure analysis of wind turbine planetary gear, *Energies*, **14**, 20, 6768-6776

3. Bhardwaj U., Teixeira A.P., Guedes Soares C., 2019, Reliability prediction of an offshore wind turbine gearbox, *Renewable Energy*, **41**, 693-706

4. Chen T., Sun W., Zhang X., 2011, Stochastic reliability optimization of wind power gears under variable wind speed, *Journal of Shenyang University of Technology*, **33**, 5, 497-505

5. Ditlevsen O., 1979, Narrow reliability bounds for structural system, *Journal of Structural Mechanics*, **7**, 4, 453-472

6. Giger U., Armando K., 2011, Redesign of a gearbox for SMW wind turbines, *Proceedings of ASME 2011 International Design Engineering Technical Conferences and Computers and Information in Engineering Conference*, 635-641

7. Guo Y., Sheng S.W., Phillips C., Keller J., Veers P., Williams L., 2020, A methodology for reliability assessment and prognosis of bearing axial cracking in wind turbine gearboxes, *Renewable and Sustainable Energy Review*, **127**, 109-124

8. Hosseinzadeh M., Salmasi F.R., 2016, Analysis and detection of a wind system failure in a micro-grid, *Journal of Renewable and Sustainable Energy*, **8**, 43-50

9. Hu P., Lu J.C., Zhang Y.M., 2014, Analysis of dynamic response and sensitivity of gear systems based on stochastic perturbation theory, *Journal of Northeastern University (Natural Science)*, **32**, 5, 257-262

10. Inturi V., Penumakala P.K., Sabareesh, G.R., 2022, Effect of multiple defects and multi--component failure on the dynamic behaviour of a wind turbine gearbox, *Arabian Journal for Science and Engineering*, **47**, 7, 8967-89931

11. Jantara Jr V.L., Basoalto H. B., Papaelias M., 2020, A damage mechanics approach for lifetime estimation of wind turbine gearbox materials, *International Journal of Fatigue*, **137**, 3, 105671-105680

12. Jiang L., Xiang D., Tan Y.F., Nie Y.H., Cao H.J., Wei Y.Z., Zeng D., Shen Y.H., Shen G., 2018, Analysis of wind turbine gearbox's environmental impact considering its reliability, *Journal of Cleaner Production*, **180**, 846-857

13. Lewis E.E., 2001, A load-capability interference model for common-mode failures in 1-out-of-2 G systems, *IEEE Transactions on Reliability*, **50**, 1, 47-51

14. Liu B., An Z.W., Kou H.K., 2016, Wind turbine gearbox reliability analysis based on the system level stress-strength model, *Journal of Shanghai Jiaotong University (Science)*, **21**, 4, 484-488

15. Liu Y., Li T.X., Liu K., 2016, Chatter reliability of turning processing system based on fourth moment method, *Journal of Mechanical Engineering*, **52**, 20, 193-200

16. Mo S., Zhang T., Jin G.G., Feng Z.Y., Gong J., Zhu S.P., 2018, Dynamic characteristics and load sharing of herringbone wind power gearbox, *Mathematical Problems in Engineering*, **1**, 1-24

17. Qin D.T., Zhou Z.G., Yang J., 2012, Dynamic reliability analysis of gear drive system of wind turbine under random wind load, *Journal of Mechanical Engineering*, **48**, 3, 1-8

18. Röder J.L., Jacobs G., Duda T., Bosse D., Herzog F., Tobias D.D., 2021, Simulative investigation of wind turbine gearbox loads during power converter fault, *Forschung im Ingenieurwesen*, **85**, 251-256

19. Srinivasan R., Robert T.P., 2021, Remaining useful life prediction on wind turbine gearbox, *International Journal of Recent Technology and Engineering*, **9**, 5, 57-65

20. Wang L., Shen T., Chen C., Chen H.T., 2014, Dynamic reliability analysis of gear transmission system of wind turbine in consideration of randomness of loadings and parameters, *Mathematical Problems in Engineering*, **1**, 1-10

21. Wang Q.Q., Zhang Y.M., Wang Y.B., Lu H., 2013, Dynamic reliability analysis of double random vibration system, *Journal of Vibration, Measurement and Diagnosis*, **33**, 4, 670-675

22. Wang X.G., Zhang Y.M., Wang B.Y., 2010, Dynamic reliability sensitivity analysis of mechanical components, *Journal of Mechanical Engineering*, **46**, 10, 188-193

23. Wu B., Li M.F., 2002, *Reliability Model of Mechanical Parts and Systems*, Beijing, Chemical Industry Press

24. Xie L.Y., Bai E.J., Qian W.X., 2017, Time-dependent series system reliability analysis method and application to gear transmission systems, *International Journal of Reliability, Quality and Safety Engineering*, **24**, 3, 12-20

25. Xie L.Y., Wang Z., Zhou J.Y., 2009, *Basic Theory and Method of Mechanical Reliability*, Beijing, Science Press

26. Xie L.Y., Wu N.X., Qian W.X., Wu N.X., 2016, Time domain series system definition and gear set reliability modeling, *Reliability Engineering and System Safety*, **155**, 97-104

27. Zhou Z.G., Qin D.T., Yang J., 2013, Dynamic reliability analysis of wind turbine gear transmission system considering failure correlation, *Acta Energiae Solaris Sinica*, **34**, 7, 1-8

Manuscript received September 26, 2022; accepted for print November 8, 2022

JOURNAL OF THEORETICAL AND APPLIED MECHANICS
61, 1, pp. 129-146, Warsaw 2023
https://doi.org/10.15632/jtam-pl/157462

RESEARCH ON VIBRATION EVOLUTION OF A BALL BEARING WITHOUT THE CAGE UNDER LOCAL VARIABLE-DIAMETER RACEWAY DAMAGE

Enwen Zhou, Yanling Zhao, Huanqing Zhang

Key Laboratory of Advanced Manufacturing Intelligent Technology Ministry of Education, Harbin University of Science and Technology, Harbin, China

Corresponding author Yanling Zhao, e-mail: ztgsci1118@163.com

This article presents an analysis of vibration evolution of a ball bearing without the cage. A vibration model in which time-varying displacement, time-varying stiffness, contact force and collision force are comprehensively considered, is proposed. On this basis, the law of motion of the bearing is studied. It is shown that a variable-diameter raceway affects the radius of curvature, which effects the dispersion of rolling elements. The damaged variable--diameter raceway leads to discrete failure, contact force and collision force of rolling elements, which are main reasons that cause vibration mutation. The bearing motion changes from quasi-periodic to chaotic motion.

Keywords: ball bearing, vibration evolution, variable-diameter raceway, damage

1. Introduction

Rolling bearings are one of the essential supporting parts in rotating machinery. Severe friction and collision between the cage and the rolling element will make the bearing significantly warm up in a short time. Therefore, a ball bearing without the cage plays an important role in the field of high precision machinery instead of a traditional bearing. However, the designed local variable-diameter raceway of a ball bearing without the cage can realize automatic discretization of rolling elements. It can reduce wear and vibration caused by random collisions. High frequency contact between a rolling element and the variable-diameter raceway is the main reason for an increase of vibration. The damaged variable-diameter raceway leads to collision and discrete failure of rolling elements (Zhao *et al.*, 2021, 20221).

Although a large number of scholars studied the influence of the bearing damage model on vibration characteristics, vibration behavior caused by different damage forming factors is far from being well understood. McFadden and Smith (1984) considered the influence of geometric shape, rotational speed, contact load, acceleration sensor sensitivity, vibration attenuation and other factors. The local damage induced by a pulse excitation is simplified. The influence of damage on vibration characteristics of bearings was studied. Fan *et al.* (2017) considered additional contact deformation caused by the inner and outer ring damage combined with bearing damage and bearing seat in the horizontal direction under an unbalanced force. Eight degrees of freedom vibration differential equation was established. Behzad *et al.* (2011) believed that the form of bearing damage was a random variation of the roughness amplitude in a particular range. Khanam *et al.* (2015) proposed that a periodic pulse generated by bearing damage seriously affects vibration characteristics of the bearing.

Vibration characteristics of bearings are affected by the impact force generated by rolling over the damaged raceway. According to the principle of engineering mechanics, the function

expression of an impact force is established to simulate the response of the bearing seat. A relative importance of variable stiffness and ball mass to the raceway impact was further studied. The elastic deformation of bearing members under a centrifugal force and external load was considered by Liu *et al.* (2019). They analyzed the influence of roll deformation, flange deformation, external load and rotational speed on flexible and rigid vibration. Yang *et al.* (2019) investigated bending-torsional coupling vibration of an aeroengine blade shell tribological dynamic model, which was caused by thermal load. Zheng *et al.* (2021) proposed a dynamic model of a rolling bearing based in an impact system. Considering the collision between the rolling element and damage, they regarded contact between the rolling element and the raceway as a nonlinear spring.

Cui *et al.* (2019) established a dynamic model considering geometrical characteristics and deformation of the rolling element. Vibration response characteristics under different damage sizes were studied. They further deduced a functional relationship between vibration characteristics and damage size. Liu *et al.* (2018) proposed a new bearing vibration model with a notch, which gave a time-varying contact force between the notch and the shoulder. Parmar *et al.* (2021) verified the vibration response law of rolling bearings with local defects and dynamic misalignment by numerical simulation and experiment. Shah and Patel (2019) established mechanical vibration models of deep groove ball bearings under healthy and damaged conditions. A dynamic model of an angular contact ball bearing and floating displacement bearing system was reformulated by Xi *et al.* (2019). They studied the dynamic-frequency response function of a spindle bearing system at different speeds and the time-history response of the spindle bearing system under different cutting forces. Yang *et al.* (2018) analyzed vibration signals of bearings and casings, and established a dynamic model of a nonlinear rolling bearing rotor-bearing-casing system. Liu *et al.* (2022) used Hertz's contact theory and the relative relationship between rolling element and damage to determine the additional contact area. Liu *et al.* (2022) adopted the locomotive--track space coupling dynamic model with traction power transmission to obtain the dynamic vibration response of the system.

There are many studies on damage vibration of bearings. The study of bearing damage is limited to single damage geometry, and most of the papers establish specific dynamic models of bearing damage. At present, few scholars studied vibration characteristics of ball bearings wihout the cage. The vibration effects caused by rolling body collisions are also rarely considered.

In this paper, the vibration evolution model of a ball bearing without the cage under local variable-diameter raceway damage is established. By analyzing dynamic characteristics of rolling elements of a ball bearing without the cage under the condition of local variable-diameter raceway damage, a relationship equation between damage width and discrete spacing of rolling elements is established. This paper analyzes the impact force of the element rolling along a variable--diameter raceway when damage of the variable-diameter raceway occurs. A rolling element impact model is established. Combined with time-varying contact stiffness of the rolling element in the collision model, the bearing vibration equation was established. The vibration law and displacement velocity phase diagram of the bearing inner ring in the time domain and frequency domain are researched. Finally, this paper discusses the vibration evolution law of bearings under different damage degrees of local variable-diameter raceways.

2. Motion analysis of the rolling element under damage

In order to realize automatic discretization of the rolling element, we changed the radius of curvature of the local outer ring, which is defined as the variable-diameter raceway. The change of curvature radius affects rotational speed of the rolling body. The rotational speed of the rolling element decreases when it enters the variable-diameter raceway and increases when it

leaves. This keeps a certain distance between the rolling elements until the variable-diameter raceway is damaged and fails. Figure 1 shows a schematic diagram of a cage free bearing with a local variable-diameter raceway. Periodic motion of the rolling element is the cause of damage of the variable-diameter raceway, which varies in the contact point between the rolling element and the variable-diameter raceway. Contact points e_1 and e_2 expand outwards to e_1' and e_2', respectively. The inner ring extrudes the rolling body outwards, which causes that the junction points p_1 and p_2 between the variable-diameter raceway and the conventional raceway expand to p_1' and p_2'. When the radius of curvature decreases to a certain value with the expansion of damage, the distance between adjacent rolling elements decreases continuously and a collision occurs. This is defined as a discrete failure.

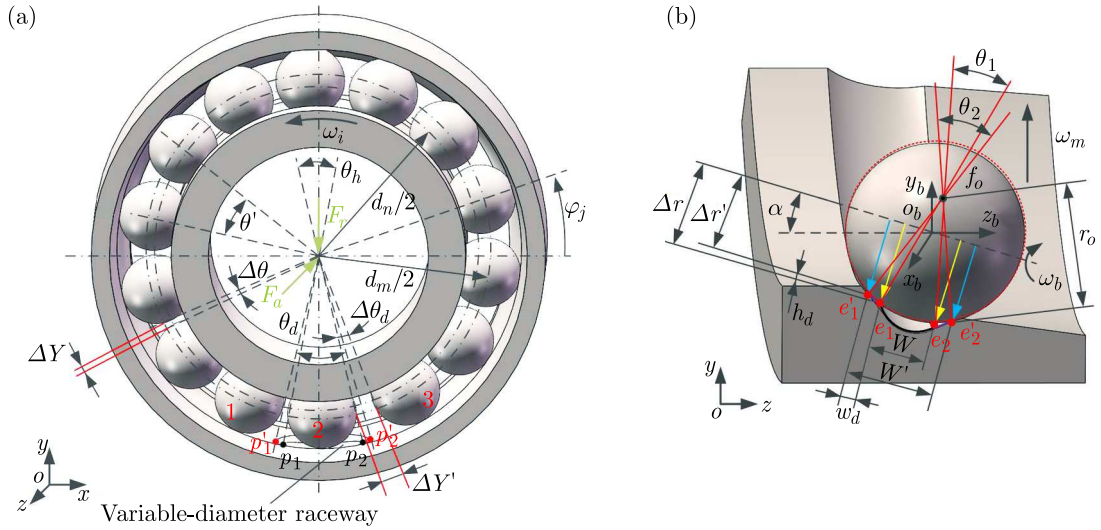

Fig. 1. Diagram of a ball bearing without the cage: (a) variable-diameter raceway structure; (b) rolling element contact

According to geometrical characteristics of the variable-diameter raceway, the circumferential span angle and the discrete spacing of the damaged variable-diameter raceway are obtained

$$\begin{aligned} \theta_d &= \theta_h + 4\arcsin\frac{w_d}{d_m + D_w\cos\alpha} \\ \Delta Y' &= \frac{\pi d_n}{180}\Big(\theta_h + 4\arcsin\frac{w_d}{d_m + D_w\cos\alpha}\Big)\Big(\frac{D_w}{2(\Delta r - h_d)}\Big) \end{aligned} \tag{B.1}$$

where θ_d and θ_h denote circumferential span angle corresponding to the undamaged and damaged variable-diameter raceway, respectively. $\Delta Y'$ is the discrete distance between two rolling element after damage. It can be used as a condition to judge the discrete failure. Damaged width and length of the variable-diameter raceway are respectively expressed as w_d and h_d. D_w is diameter of the rolling element, d_m is diameter of the bearing pitch circle and α is the rolling element contact angle. The radius of rotation is expressed by Δr.

Based on equation $(2.1)_2$, when the variable-diameter raceway is damaged, the discrete spacing parameter that affects the rolling element is mainly the effective radius of gyration. Conventional raceway rolling speed can be expressed as $V_1 = \omega_m d_m/2$, V_2 is the rolling speed of the variable-diameter raceway. Therefore, the velocity difference between adjacent rolling elements ΔV can be calculated from

$$\begin{aligned} V_2 &= \omega_m'\Big(\frac{d_m}{2} + (D_w - \Delta r')\cos\alpha\Big) \\ \Delta V &= \frac{\omega_i d_m}{4}\Big(1 - \frac{D_w}{d_m}\cos\alpha\Big) - \frac{\omega_b \Delta r'\Big((D_w - \Delta r')\cos\alpha + \frac{dm}{2}\Big)}{D_w\cos\alpha + \frac{d_m}{2}} \end{aligned} \tag{B.2}$$

where ω_m and ω'_m are angular velocities in revolution of the conventional and local variable--diameter raceway, respectively. When the variable-diameter raceway is damaged, the corresponding radius of rotation is expressed as $\Delta r'$. ω_i and ω_b are rotational angular velocities of the inner ring and rolling element, respectively.

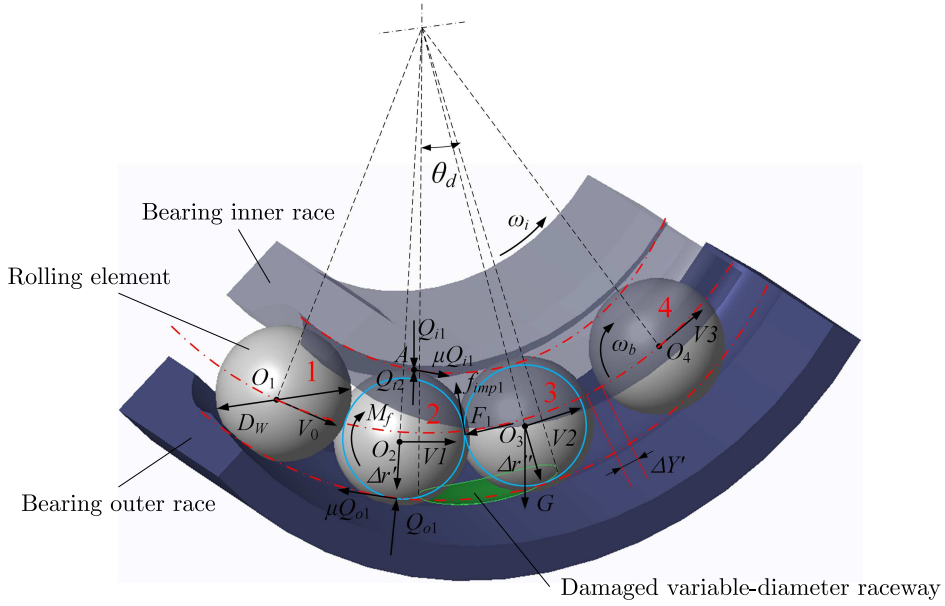

Fig. 2. Collision diagram for discrete failures

The rolling elements with the increasing velocity difference collide when $\Delta Y'$, and $\Delta Y' \geqslant 2\Delta Y$. Then the variable-diameter raceway undergoes a discrete failure, which is illustrated in Fig. 2. The radius of curvature $\Delta r'$ is

$$\Delta r' \leqslant \frac{D_w}{\Delta r \theta_d} 2(D_w - 2\Delta r)\theta_h + 2\Delta r \theta_d \tag{B.3}$$

Due to the short collision action time of the rolling element, there is no residual deformation after the collision, the collision deformation between the rolling element is regarded as elastic deformation. When the two rolling bodies collide at the speed V_1 and V_2, respectively, the relationship between deformation and velocity can be expressed as

$$\Delta V = \frac{d\delta_{imp}}{dt} = V_1 - V_2 \tag{B.4}$$

The force normal to the collision between the rolling bodies at any instant is

$$F_1 = m\frac{dV_1}{dt} = -m\frac{dV_2}{dt} = K_{bb}\delta_{imp}^{3/2} \tag{B.5}$$

The maximum collision deformation $d\delta_{imp}/dt$ is zero. Combined with Eq. (2.5), the integral and quadratic integral are solved to obtain the dynamic expression t^* of the deformation time in collision

$$t^* = \frac{\delta^*_{imp}}{\Delta V} \int \frac{d(\delta_{imp}/\delta^*_{imp})}{\sqrt{1 - (\delta_{imp}/\delta^*_{imp})^{5/2}}} \tag{B.6}$$

where δ^*_{imp} is the maximum deformation caused by collision of the rolling body.

After the moment of maximum compression t^* has been reached, deformation at the time of the rolling element collision can be fully recovered, and we obtain the total collision time T_c

$$T_c = 2t^* = 2\frac{\delta^*_{imp}}{\Delta V}\int_0^1 \frac{d(\delta_{imp}/\delta^*_{imp})}{\sqrt{1-(\delta_{imp}/\delta^*_{imp})^{5/2}}} = 2.94\frac{\delta^*_{imp}}{\Delta V} \tag{B.7}$$

The contact deformation of the rolling element affects the friction force at the collision point. The instantaneous force of rolling element 1 on the bearing inner ring is calculated by using the angular momentum conservation law

$$\Big(\frac{f_{imp}D_w}{2} - \mu Q_{t2}\frac{D_w}{2}\Big)(\omega_b - \omega'_b)T_c = \frac{1}{2}I\omega_b^2 - \frac{1}{2}I\omega_b'^2 \tag{B.8}$$

Rolling element 2 disconnects from the inner ring at the variable-diameter raceway, when rolling element 2 hits rolling element 1. We believe that the speed of rolling element 1 does not change at this time, and rotational speed $\omega'_b = \omega_b$, so we obtain

$$Q_{t2} = \frac{f_{imp}}{\mu} - \frac{2I\omega'_b\Delta V}{2.94\delta^*_{imp}\mu D_w} \tag{B.9}$$

where Q_{t2} is the load on the inner ring when the rolling body collides, μ is the coefficient of sliding friction, I is the moment of inertia of rolling elements.

3. Establishment of the vibration model under damage

In order to establish the proposed vibration model when the variable-diameter raceway is damaged, the time-varying stiffness, time-varying displacement and contact force of the rolling element rolling over the variable-diameter raceway are analyzed.

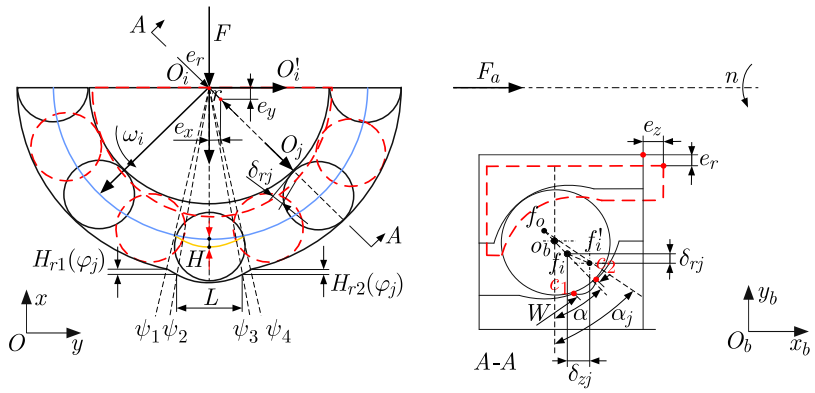

Fig. 3. Diagram of displacement change between the rolling element and inner ring

As shown in Fig. 3, when the rolling element passes along the variable-diameter raceway, the inner ring is detached. The rolling element position changes to produce the time-varying displacement H. The distance between the rolling element and the two contact points of the local variable-diameter raceway is $W(\varphi_j)$. The distance from the contact point of the rolling body to the beginning of the reducer raceway is $L(\varphi_j)$. The time-varying displacement of the rolling element in the variable-diameter raceway can be calculated from

$$\begin{aligned} L(\varphi_j) &= \frac{L}{2} - \Big(\frac{D_w}{2}\cos\alpha + \frac{d_m}{2}\Big)\tan\Big(\frac{3\pi}{2} - \mathrm{mod}(vp_j)\Big) \\ W(vp_j) &= W\sqrt{1 - \frac{[L(vp_j) - L/2]^2}{L^2/4}} \end{aligned} \tag{B.1}$$

and

$$
\begin{aligned}
H(\varphi_j) &= \sqrt{r_o^2 - W^2(\varphi_j)} - \sqrt{\Big(\frac{D_w}{2}\Big)^2 - W^2(\varphi_j)} + \frac{D_w}{2} - r_o \\
H_1(\varphi_j) &= \sqrt{r_o^2 - [W^2(\varphi_j) + w_d]^2} - \sqrt{\Big(\frac{D_w}{2}\Big)^2 - [W(\varphi_j) + w_d]^2} + \frac{D_w}{2} - r_o \\
&\qquad \psi_1 \leqslant \operatorname{mod}(\varphi_j 2\pi) < \psi_2 \\
H_{r1}(\varphi_j) &= H_r \frac{\operatorname{mod}\Big(\Big(\varphi_j - \frac{3\pi}{2} + \frac{\theta_d}{2}\Big), 2pi\Big)}{\psi_2 - \psi_1} \qquad \psi_2 \leqslant \operatorname{mod}(\varphi_j 2\pi) < \psi_3 \\
H_{r2}(\varphi_j) &= H_r \frac{\operatorname{mod}\Big(\Big(\frac{3\pi}{2} + \frac{\theta_d}{2} - \varphi_j\Big), 2pi\Big)}{\psi_4 - \psi_3} \qquad \psi_3 \leqslant \operatorname{mod}(\varphi_j 2\pi) < \psi_4
\end{aligned}
\tag{B.2}
$$

where $H(\varphi_j)$ is the time-varying displacement of the elliptical variable-diameter raceway without damage, see Fig. 3, the damage variable-diameter raceway is divided into three regions. $H_1(\varphi_j)$ caused by the damage width w_d and the damage depth h_d of the variable-diameter raceway is time-varying displacement of the element rolling on the damaged elliptical variable--diameter raceway in the $\psi_2 - \psi_3$ region. $H_{r1}(\varphi j)$ and $H_{r2}(\varphi_j)$ are the time-varying displacements of the rolling element in two sections of $\psi_1 - \psi_2$ and $\psi_3 - \psi_4$. The reason of time-varying displacement is that the contact point of the raceway with the conventional raceway extends outward after the damage of the raceway.

The damage of the variable-diameter raceway is related to the position of the contact point of the conventional raceway and the annular span angle. Thus the location of the two ends of damage can be expressed as

$$
\begin{aligned}
\psi_1 &= \frac{3\pi}{2} - \frac{1}{2}\Big(\theta_h + 4\arcsin\frac{w_d}{d_m + D_w\cos\alpha}\Big) \\
\psi_4 &= \frac{3\pi}{2} + \frac{1}{2}\Big(\theta_h + 4\arcsin\frac{w_d}{d_m + D_w\cos\alpha}\Big)
\end{aligned}
\tag{B.3}
$$

The total deformation of the rolling element and the collar is divided into two parts. It is the deformation amount of the rolling element when it rolls along the conventional raceway and the damaged variable raceway. The rolling element enters the $\psi_1 - \psi_4$ region and extrudes radially towards the outer ring. At this time, the reason for the decrease of time-varying displacement H is the contact deformation between the rolling element and the inner ring. Therefore, the total deformation δ_j for the time-varying displacement H segmentation function is given by the following formula

$$
\delta_j = \begin{cases}
\sqrt{(e_x\cos\varphi_j + e_y\cos\varphi_j - H\cos\alpha)^2 + (e_z - H\sin\alpha)^2} & \psi_1 \leqslant \varphi_j \leqslant \psi 4 \\
\sqrt{(e_x\cos\varphi_j + e_y\cos\varphi_j)^2 + e_z^2} & \text{other}
\end{cases}
\tag{B.4}
$$

The contact force Q_j between the rolling element and the raceway is related to the elastic contact displacement δ_j, which can be analyzed and calculated by the Hertz contact theory

$$
Q_j = K\sqrt{\delta_j^3} \tag{B.5}
$$

where K is time-varying contact stiffness of the rolling element in the bearing.

The contact force of the inner ring is the combined force of each rolling element and the contact force of the inner ring when the rolling element is in the bearing region. The contact

force generated by deformation of the inner ring is decomposed along the coordinate axis xyz in the three directions, respectively. Its components $F = [F_{ix}, F_{iy}, F_{iz}]$ are

$$\begin{aligned} F_{ix} &= -\sum_{j=1}^{N} Q_j \cos\varphi_j \cos\alpha_j \qquad F_{iy} = -\sum_{j=1}^{N} Q_j \sin\varphi_j \cos\alpha_j \\ F_{iz} &= -\sum_{j=1}^{N} Q_j \sin\alpha_j \end{aligned} \tag{B.6}$$

The time-varying displacement of the damaged variable-diameter raceway is not enough to offset the contact deformation of the ring due to circumferential expansion. Therefore, we need to solve the contact stiffness K_{edge} and equivalent contact stiffness K_{edge} between the rolling element and the damaged variable-diameter raceway

$$\begin{aligned} K_{edge} &= \frac{4}{3}\frac{E_2(1-v_1^2)+E_1(1-v_2^2)}{E_1E_2}\sqrt[4]{\frac{D_w^2 r_o r}{(D_w+2r)(2f_o-D_w)}} \\ K'_{edge} &= 2\Big(K_{edge}\cos^2\frac{\beta_d}{2} + \frac{2T\sin[\rho\sin(\beta_d/2)\mp D_w/2]}{\rho D_w}\Big) \end{aligned} \tag{B.7}$$

where E_1 and E_2 are moduli of elasticity of the materials, ρ denotes the curvature radius of the trajectory of mass center of the rolling element, β_d is the support force angle and T is the rolling element support force.

After the equivalent contact stiffness of the rolling element and the damaged variable--diameter raceway is obtained, the time-varying contact stiffness K of the rolling element around the revolution can be obtained

$$K = \begin{cases} \left[K_i^{-2/3} + {K'_{edge}}^{-2/3}\right]^{-3/2} & \psi_1 < \mathrm{mod}(\varphi_j, 2\pi) < \psi_4 \\ \left[K_i^{-2/3} + K_o^{-2/3}\right]^{-3/2} & \text{other} \end{cases} \tag{B.8}$$

where K_i is the contact stiffness between the rolling element and the bearing inner ring, K_o is the contact stiffness between the rolling element and the outer ring in the conventional raceway.

Vibration characteristics of the bearing inner ring are caused by the contact collision between discrete failure of the rolling element and bearing. This collision occurs only in the radial plane of the bearing, without considering vibration caused by the extrusion of the bearing inner ring. Therefore, this paper establishes the vibration equation of the bearing inner ring, which simplifies calculation on the following assumptions.

- The contact deformation between the rolling element and raceway is considered, the plastic deformation caused by the contacting materials is ignored. We do not take into account microscopic slip friction in the contact region.
- The rolling element performs pure rolling motion on the raceway, the influence of gyro motion and sliding of the rolling body is ignored.
- We ignore the effect of lubricant film between the rolling element and raceway on motion and contact characteristics.
- The load and inner ring speed are stable without fluctuation during operation of the bearing.

From what has been discussed above, the time-varying stiffness, time-varying displacement and contact force of the rolling element rolling along the raceway with variable diameter are obtained. In order to establish the vibration model of the damaged raceway, the bearing is simplified as a spring-damping system. The vibration model of variable-diameter raceway damage is established.

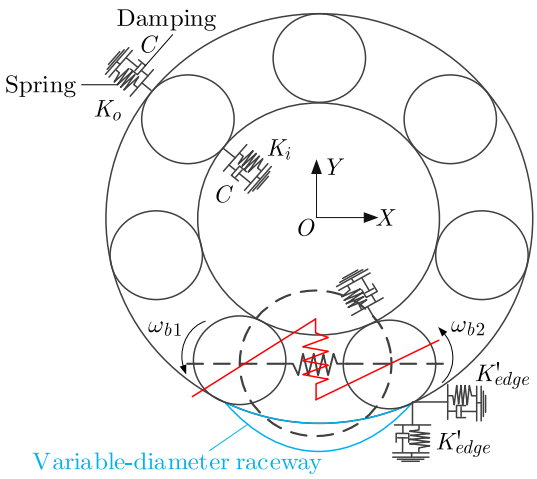

Fig. 4. Bearing vibration model

The vibration model of the ball bearing without the cage under the damage condition is shown in Fig. 4.

According to Newton's second law, based on variable-diameter raceway damage caused by time-varying displacement and time-varying stiffness excitation, a differential equation of vibration of the inner ring with the damaged variable-diameter raceway is established

$$\begin{aligned}
m_i\ddot{x}_i + c\dot{x}_i &= \lambda_j\Big(-\sum_{j=1}^{N} Q_j\cos(\phi_j\alpha)\cos\alpha_j\Big) + \Big(\frac{f_{imp}}{\mu} - \frac{2I\omega'\Delta V}{2.94\delta^*_{imp}\mu D_w}\Big)\cos\alpha\sin\psi_1\\
m_i\ddot{y}_i + c\dot{y}_i &= \lambda_j\Big(-\sum_{j=1}^{N} Q_j\sin(\phi_j\alpha)\cos\alpha_j\Big) + \Big(\frac{f_{imp}}{\mu} - \frac{2I\omega'\Delta V}{2.94\delta^*_{imp}\mu D_w}\Big)\cos\alpha\sin\psi_1 - F_r\\
m_i\ddot{z}_i + c\dot{z}_i &= \lambda_j\Big(-\sum_{j=1}^{N} Q_j\sin\alpha_j\Big)\Big) + \Big(\frac{f_{imp}}{\mu} - \frac{2I\omega'\Delta V}{2.94\delta^*_{imp}\mu D_w}\Big)\sin\alpha - F_a
\end{aligned} \tag{B.9}$$

where m_i are masses of the bearing inner ring and spindle, $\dot{x}_i$, $\dot{y}_i$ and $\dot{z}_i$ are velocities in the x, y and z directions of the inner circle, $\ddot{x}_i$, $\ddot{y}_i$ and $\ddot{z}_i$ are vibration accelerations in the x, y and z directions of the inner circle, F_a and F_r are the axial and radial loads borne by the bearing, λ_j denotes the control coefficient of contact deformation between the rolling elements.

4. Simulation research

Taking the angular contact ball bearing without the cage as an example, the radial load of the bearing is set to 500 N. Vibration characteristics of damaged variable-diameter raceway are found. The basic parameters of the damaged variable-diameter raceway bearing are shown in Table 1, and the material parameters of the bearing without the cage are shown in Table 2.

According to the discrete failure conditions obtained by Eq. $(2.1)_2$, the critical value of w_d is calculated. Figure 5 presents a relationship between the discrete distance of rolling elements and damage width of the variable-diameter raceway. Equation $(2.2)_2$ shows that the discrete spacing of the rolling element is 1.361 mm when the discrete failure occurs. In this paper, w_d is selected as 0.1 mm and 0.59 mm, MATLAB is used for programming, and the vibration equation is numerically solved by using the four-order Runge-Kutta algorithm with a fixed step.

Table 1. Basic parameters of damaged variable-diameter raceway bearings

Bearing parameters	Numerical values
Bearing inner diameter d_i [mm]	30
Bearing outer diameter d_o [mm]	62
Bearing width B [mm]	16
Section circle diameter d_m [mm]	46
Rolling element diameter D_w [mm]	9.525
Variable-diameter raceway length L [mm]	11.5
Variable-diameter raceway width W [mm]	3.5
Damage width w_d [mm]	0.1 (0.59)
Bearing contact angle α	15
Number of scrolling bodies N	10

Table 2. Bearing material parameters without the cage

Inner and outer rings	Values	Rolling element	Values
Modulus of elasticity of bearing steel [MPa]	$2.08 \cdot 10^5$	Modulus of elasticity of bearing steel [MPa]	$2.08 \cdot 10^5$
Poisson's ratio of bearing steel	0.3	Poisson's ratio of bearing steel	0.3
Bearing steel density [kg/mm^3]	$7.85 \cdot 10^{-6}$	Bearing steel density [kg/mm^3]	$7.85 \cdot 10^{-6}$

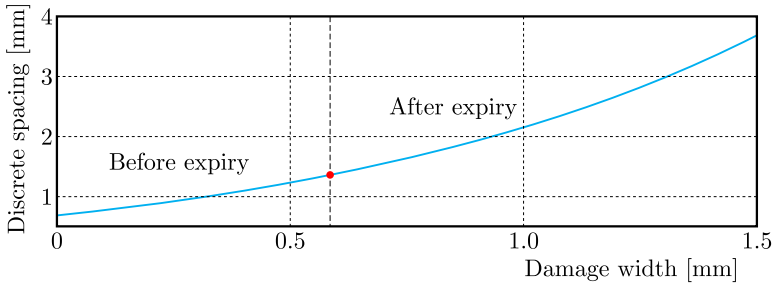

Fig. 5. Plot of bearing damage width versus discrete spacing

4.1. Simulation results and analysis of motion models

According to the differential equation of bearing vibration, the relation between the velocity and displacement of the inner ring and the damaged variable-diameter raceway is obtained. In Figs. 6 and 7, the bearing inner ring along the x-axis and y-axis direction displacement – velocity phase diagram is shown.

At three operating speeds, the inner ring of the bearing presents multiple closed rings along the x and y axes, and the bearing exhibits quasi-periodic motion, see Fig. 6.

As can be seen in Fig. 7, the phase diagram of the inner circle along the x- and y-axis directions does not repeat and fills a certain part of the phase space. Therefore, the inner circle motion is chaotic.

The displacement-velocity phase diagram of the inner ring at different rotational speeds is analyzed. When the damage width of the variable-diameter raceway is 0.1 mm, the inner ring motion is quasi-periodic under three rotational speeds. When the damage width of the variable--diameter raceway is 0.59 mm, the inner ring motion is chaotic at three speeds. With an increase of the damage width of the variable-diameter raceway, when the damage width is greater than or equal to 0.59 mm, the discrete failure of the rolling element occurs. The rolling element squeezes the inner ring to produce an instantaneous force, so motion of the inner ring changes from quasi-periodic to chaotic motion.

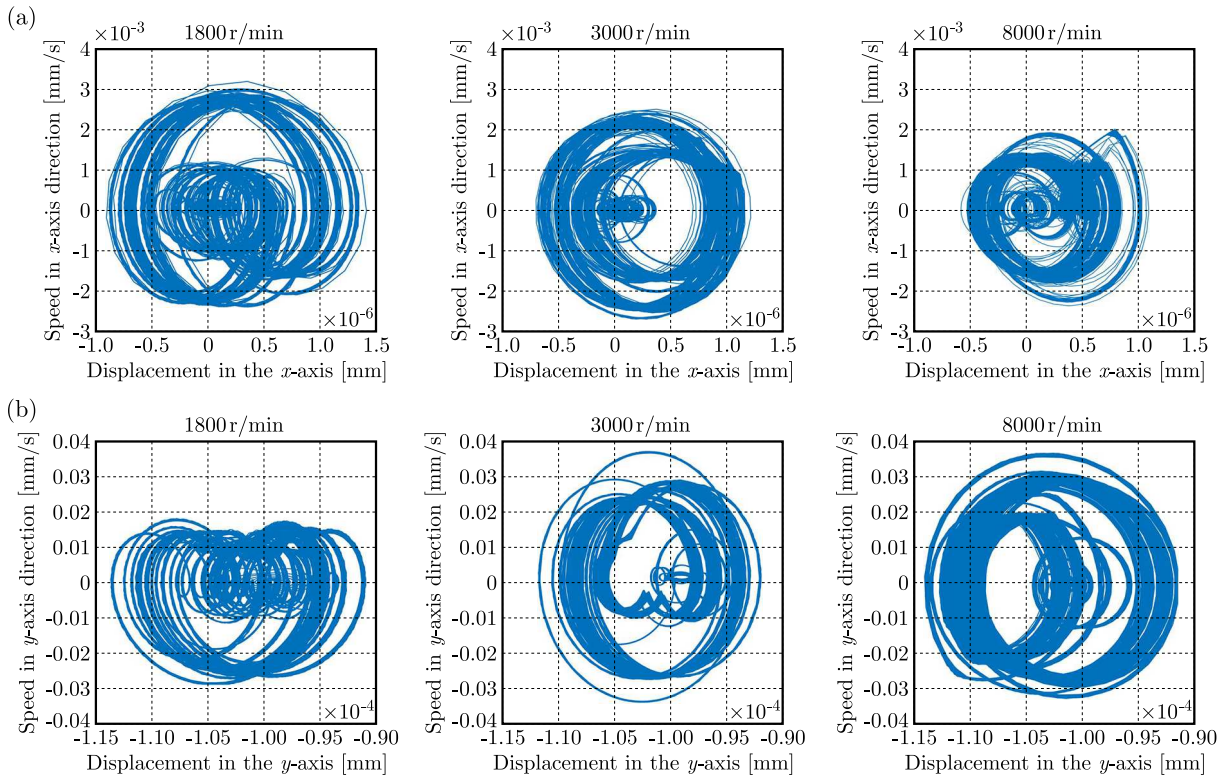

Fig. 6. Displacement-velocity phase diagram at 0.1 mm damage width of the variable-diameter raceway: (a) in x-axis direction, (b) phase in y-axis direction

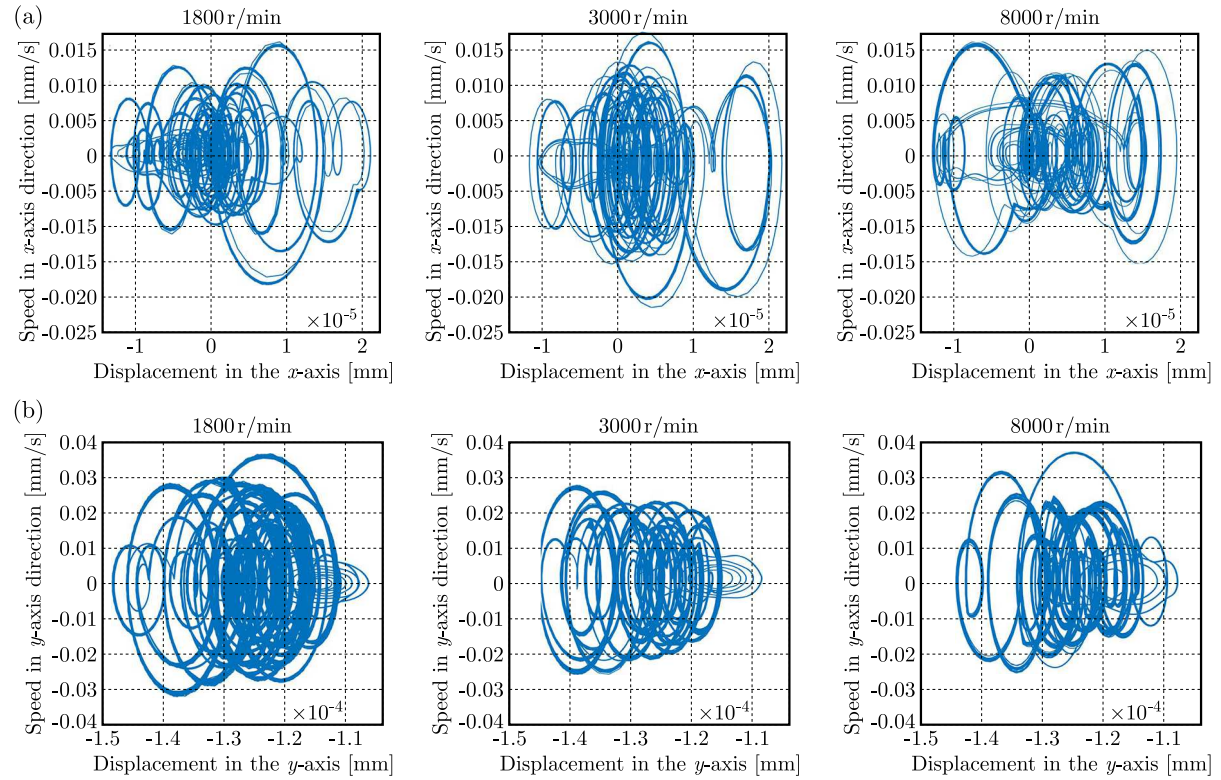

Fig. 7. Displacement-velocity phase diagram at 0.59 mm damage width of the variable-diameter raceway: (a) in x-axis direction, (b) phase in y-axis direction

After the law of motion of the rolling element is obtained, velocity changes of the two adjacent rolling elements passing along the variable-diameter raceway are simulated. Figure shows the velocity simulation result curve of the selected adjacent rolling elements.

It can be seen in Fig. 8a, the velocity change of the adjacent rolling elements in the conventional raceway is not obvious. The speed of roll 1 and 2 is kept at 1750-1780 mm/s. The radius of curvature of the damaged raceway changes and the velocity of two rolling elements fluctuates obviously. Figures 9 and 10 display the local magnification of motion within the range of 0.45-0.47 s, and the spacing curves of the adjacent rolling elements respectively.

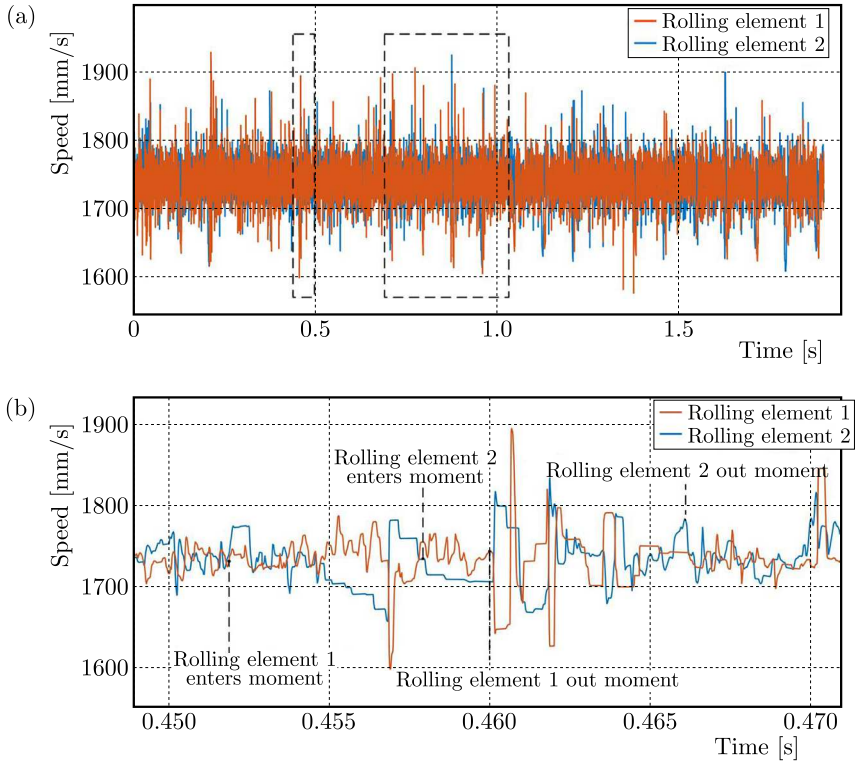

Fig. 8. Velocity curve: (a) damage to the adjacent rolling elements on the variable-diameter raceway, (b) local magnification curve of the adjacent rolling elements velocity

As shown in Fig. 8b, rolling element 1 enters the damaged variable-diameter raceway. Rolling element 1 is not detached from the damaged variable-diameter raceway. At this point, element 2 enters the damaged deceleration raceway. The time during which the rolling element passes along the damaged variable-diameter raceway is about 0.007 s. The damage width of the variable--diameter raceway increases. Although the acceleration between rolling elements decreases, there is still a time when the common acceleration is positive. When the acceleration difference between rolling element 3 and 2 is greater than that between rolling element 2 and 1, the distance between rolling element 1 and 2 and the distance between rolling element 2 and 3 both increase. As the acceleration becomes negative, the velocity starts to decrease. The velocity difference between rolling element 2 and 1 is getting smaller and smaller, which eventually leads the adjacent rolling element to the discrete failure.

The discrete spacing of adjacent rolling bodies reflects the degree of damage to the variable--diameter raceway and is represented by the ball spacing of three adjacent rolling elements. The effect of variable-diameter raceway damage on rolling element dispersion is studied, as shown in Fig. 9

The acceleration difference between rolling element 2 and 3 is larger than that between rolling element 2 and 1. The ball spacing between rolling element 2 and 3 varies greatly from Fig. 9a.

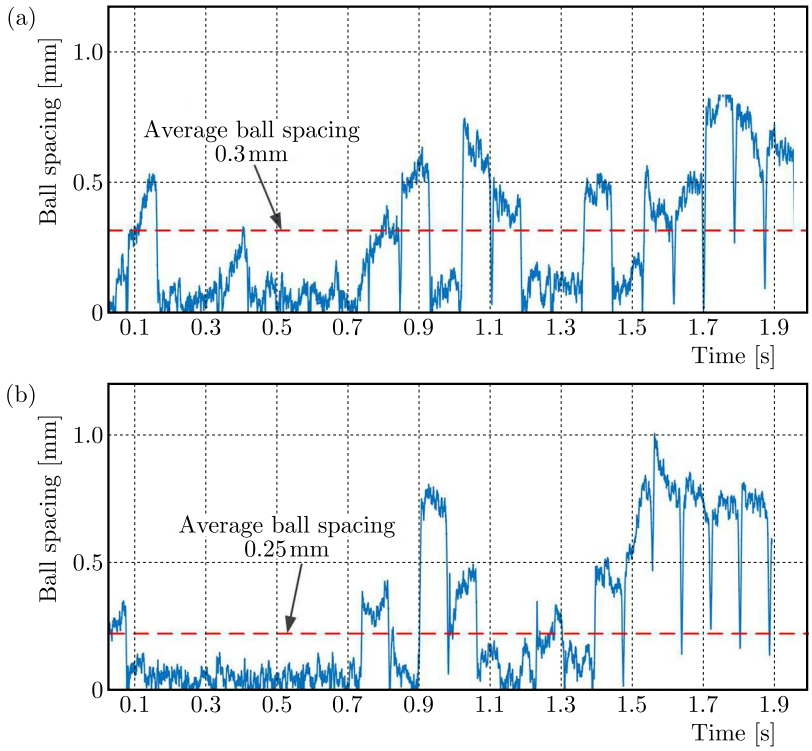

Fig. 9. Ball spacing between adjacent rolling bodies: (a) ball distance between rolling element 2 and 3, (b) ball distance between rolling element 1 and 2

The average pitch is about 0.3 mm. When the ball spacing of the rolling element is 0, adjacent rolling elements 3 and 2 collide. It can be seen from Fig. 9b that the ball spacing between rolling element 1 and 2 remains unstable. The average ball distance between the two rolling elements is about 0.25 mm, which is less than that of rolling elements 1 and 2. In the time range of 0.1 s-0.7 s, the ball spacing between rolling element 1 and 2 is always about 0. Adjacent rolling elements 1 and 2 collide.

4.2. Simulation results and analysis of vibration models

According to equations (3.9), the vibration acceleration of the inner ring is calculated. This time, the bearing speed is 1800 r/min. The damaged width of the variable-diameter raceway is 0.1 mm, 0.3 mm and 0.59 mm, respectively. The width of 0.1 mm, 0.3 mm and 0.59 mm represent the degree of mild, moderate and severe damage of the variable-diameter raceway, respectively.

Figure 10 shows the vibration acceleration curve with a damaged width of 0.1. The amplitude of acceleration has obvious periodic characteristics in Fig. 10a. It shows that the amplitude is stable and the rolling elements are loaded uniformly. It can be seen from Fig. 10b that the maximum amplitude of the acceleration curve is about 70 m/s^2, and the interval between the two peaks is about 0.006 s.

The amplitude of vibration acceleration of the bearing increases with an increase of the damage width, but changes periodically in Fig. 11a. The amplitude change is small. In the local enlargement of Fig. 11b, the maximum value of acceleration curve change caused by the damaged raceway is about 100 m/s^2. At this time, the rolling element remains discrete in the movement process. A_1 and B_1 respectively represent vibration values of the rolling element when it enters and leaves the variable-diameter raceway. The interval between the two peaks is about 0.006 s, which is the same as monopulse vibration with mild damage. With an increase

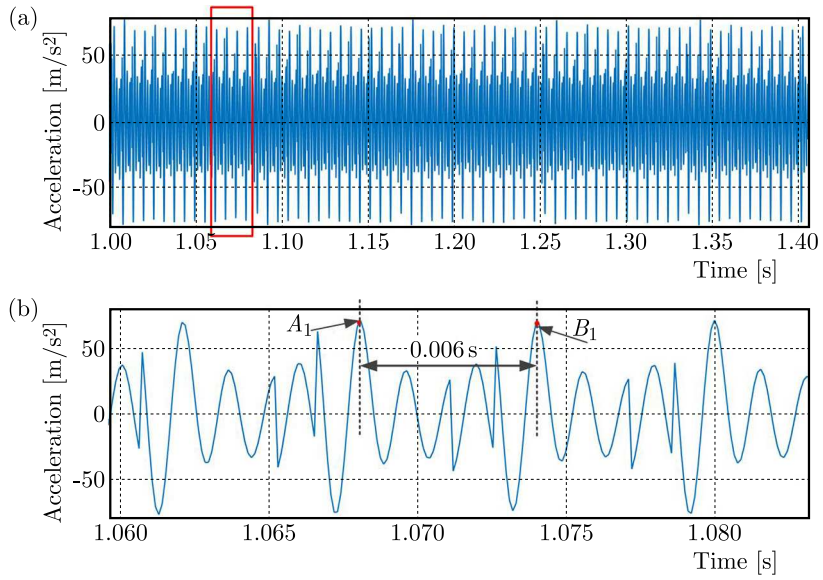

Fig. 10. $w_d = 0.1$ mm: (a) vibration acceleration curve, (b) partial enlarged drawing

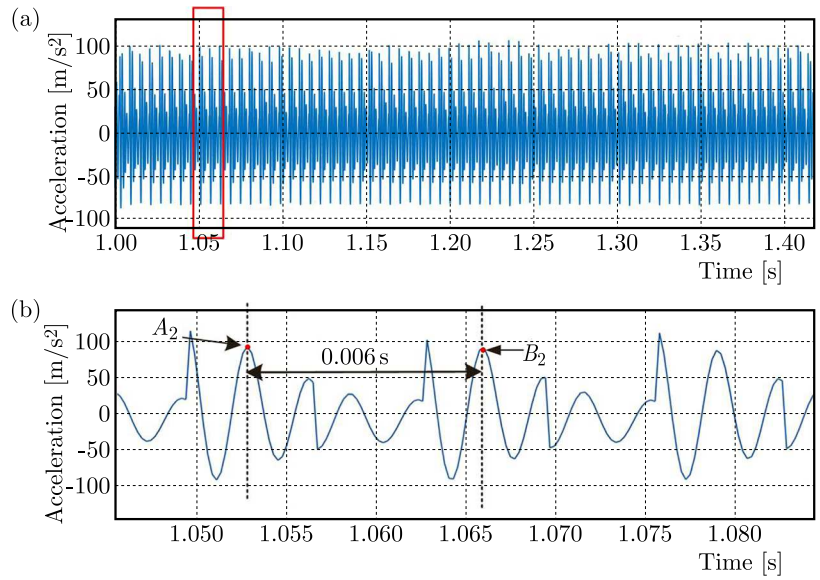

Fig. 11. $w_d = 0.3$ mm: (a) vibration acceleration curve, (b) partial enlarged drawing

of damage, the rolling element generates an impact excitation at the variable-diameter raceway and the vibration amplitude increases.

As shown in Fig. 12a, the maximum change in the acceleration curve due to damage to the reducer raceway is approximately 100 m/s^2. There are several locations in the diagram where the peak acceleration is approximately zero, indicating that 14 rolling elements are packed together at this time. Figure 12b shows that when the damage width is 0.59 mm and the circumferential span angle of the damaged variable-diameter raceway is 26.28°, p_1' and p_2' are at the moment when the rolling element enters and leaves the damaged variable-diameter raceway. Due to the increase of the damage width of the variable-diameter raceway, the number of rollers changes, and the collision force between the rollers causes an instantaneous force act on the roller on the bearing inner ring. Therefore, the acceleration amplitude of the inner ring increases significantly when the damage width of the variable diameter raceway is 0.59.

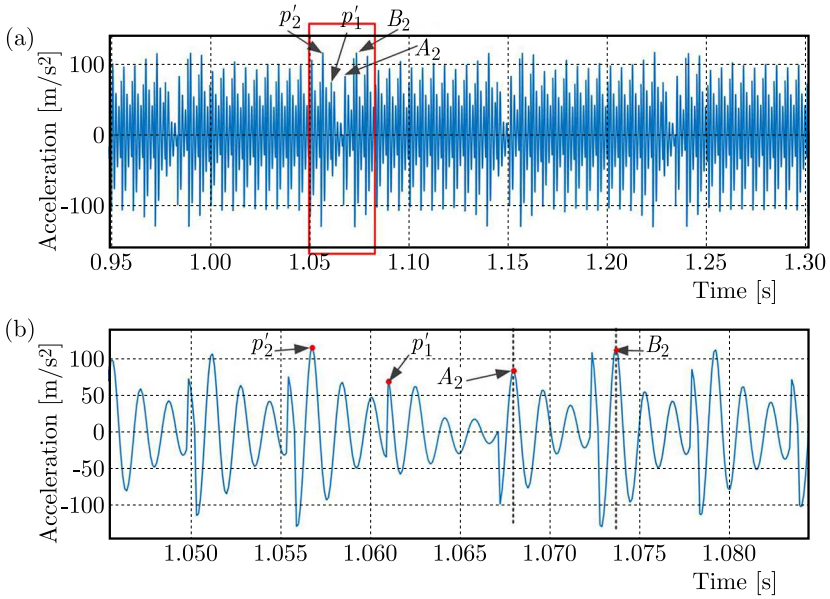

Fig. 12. $w_d = 0.59$ mm: (a) vibration acceleration curve, (b) partial enlarged drawing

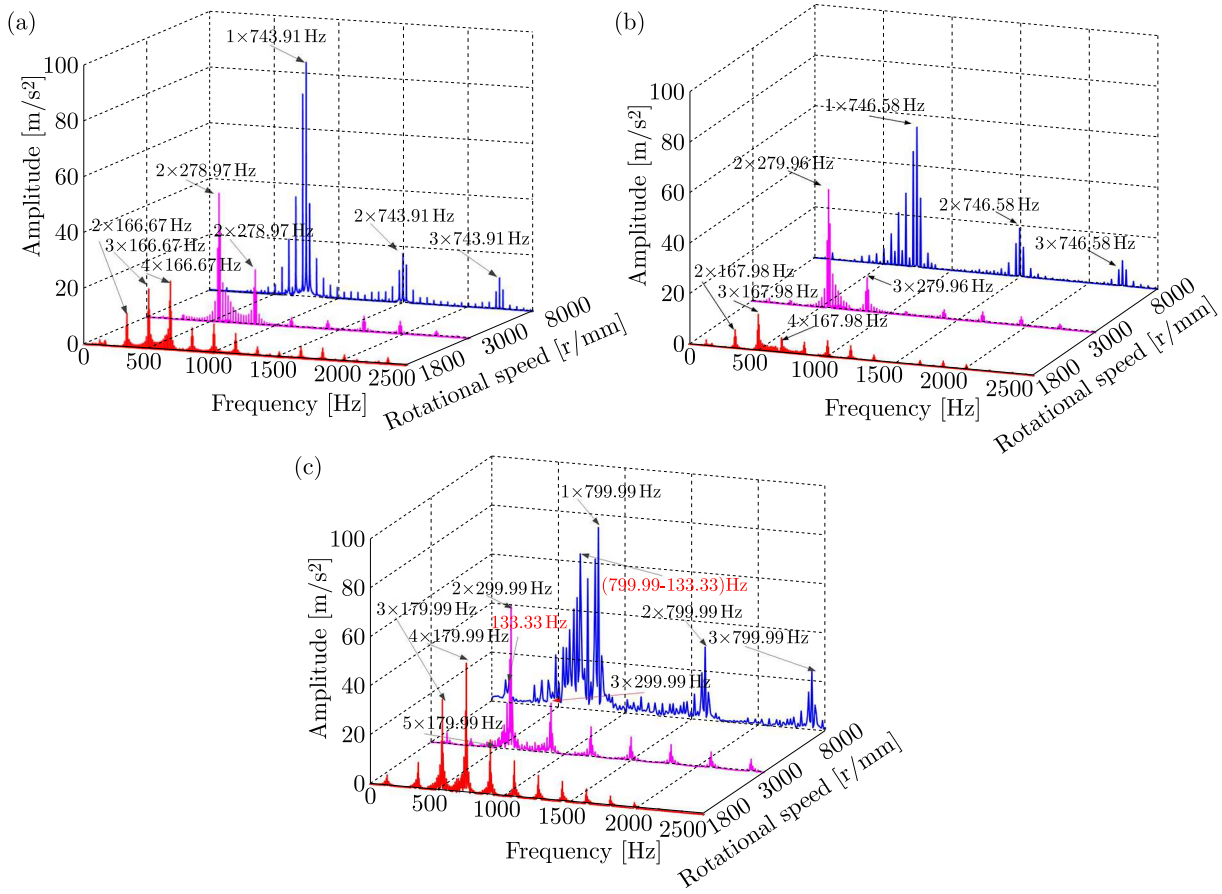

Fig. 13. Frequency-domain waterfall diagram: (a) $w_d = 0.1$, (b) $w_d = 0.30$, (c) $w_d = 0.59$

In order to further investigate the effect of different speeds on vibration in the frequency domain, three speeds of 1800 r/min, 3000 r/min, and 8000r/min are selected for numerical simulation in this paper.

Figure 13 shows that the amplitude of vibration acceleration of the bearing inner ring increases significantly with an increase of rotational speed. However, the vibration amplitude of mild damage is higher than that of moderate damage under the condition of low and high speed. Although most of the rolling elements are dispersed at this time, there is still a small part of the rolling elements in contact, which does not affect motion of the bearing. Although most of the rolling elements have been dispersed under the influence of rotational speed, there is still a small part of the rolling bodies in contact with each other, which does not affect motion of the rolling bodies. The corresponding frequency peak of each rotational speed is approximately a multiple relationship of its theoretical frequency, and the bearing rollers can be dispersed at three rotational speeds at $w_d = 0.1$ and $w_d = 0.3$. The corresponding frequency amplitudes at each speed are greater than the theoretical values of $w_d = 0.59$. Moreover, asymmetry of the inner ring rotation center intensifies with an increase of rotational speed. It results in a larger frequency characteristic peak of bearing vibration, which leads to the aggravation of bearing vibration.

The analysis of the time and frequency domain shows that vibration of the inner ring of the ball bearing without the cage becomes more complex, and the vibration amplitude increases with an increase of damage width.

5. Experimental research

The outer ring with a variable-diameter raceway machined by EDM is installed on the ball bearing without the cage. The experiment is carried out on a T10-60 machine. Vibration data of the ball bearing without the cage under different working conditions are measured. The T10-60 machine is shown in Fig. 14a. The outer ring of the ball bearing without the cage is shown in Fig. 14b. The experimental scheme is shown in Table 3.

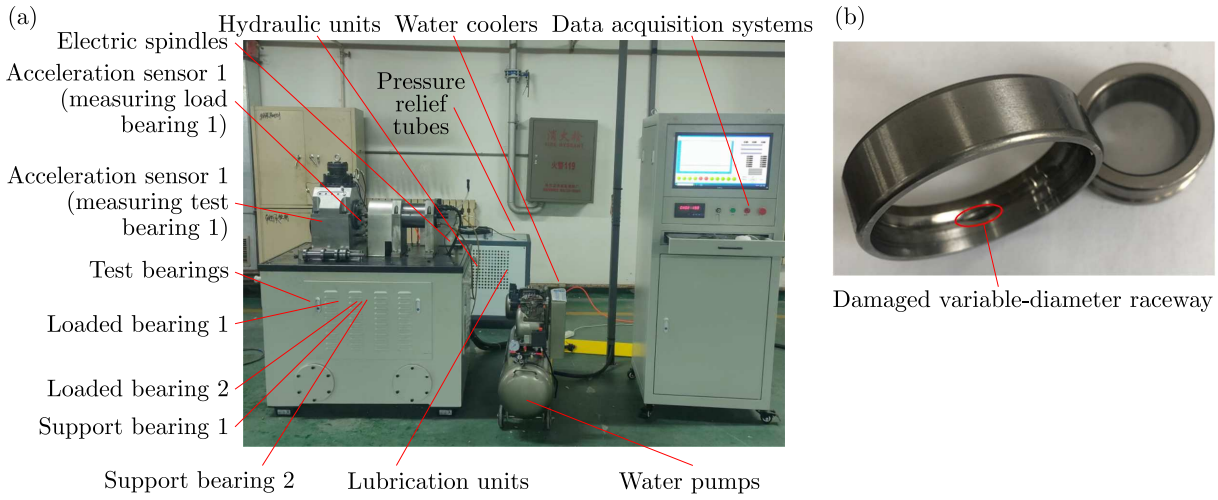

Fig. 14. Experiment equipment: (a) model T10-60 bearing vibration tester, (b) diagram of the damaged variable-diameter raceway

The vibration data was collected after the bearings entered steady operation. The vibration curves of the bearings were given for radial forces of 300 N, 500 N and 800 N at a speed of 1800 r/min without the ball bearings cage, as shown in Fig. 15.

As shown in Fig. 15, the amplitude range of the vibration curve of the damaged variable--diameter raceway bearing under the action of a 300 N radial force is about (1.2-1.5) mm/s^2. The amplitude range of the vibration curve under the action of a 500 N radial force is (1.25-1.45) mm/s^2. There is almost no change compared with the bearing vibration under the

Table 3. Experimental scheme

Rotational speed [r/min]	1800			3000	8000
Radial load [N]	300	500	800	500	500
Lubrication method	Oil lubrication				
Mounting method	Reducing raceway at lowest point of load area				
Damage to variable-diameter raceway position	Outer ring				

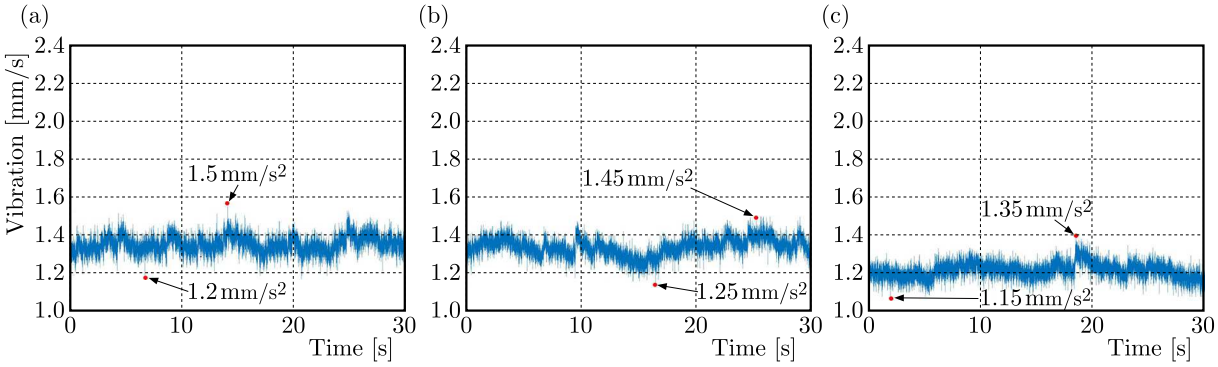

Fig. 15. Vibration acceleration test curve for bearings at 1800 r/min: (a) $F_r = 300$ N, (b) $F_r = 500$ N, (c) $F_r = 800$ N

radial force of 300 N. For a 800 N radial force, the amplitude is (1.15-1.35) mm/s^2. Compared with 300 N and 500 N radial forces, the bearing vibration is slightly reduced. The load has little influence on the vibration amplitude, which can be seen from the vibration curves of bearings under three loads.

In order to further verify the influence of speed of the damaged variable-diameter raceway bearing on vibration, the operating speeds of 3000 r/min and 8000 r/min were selected, and the vibration data of the damaged variable-diameter raceway were measured under the same radial load of 500 N, as shown in Fig. 16.

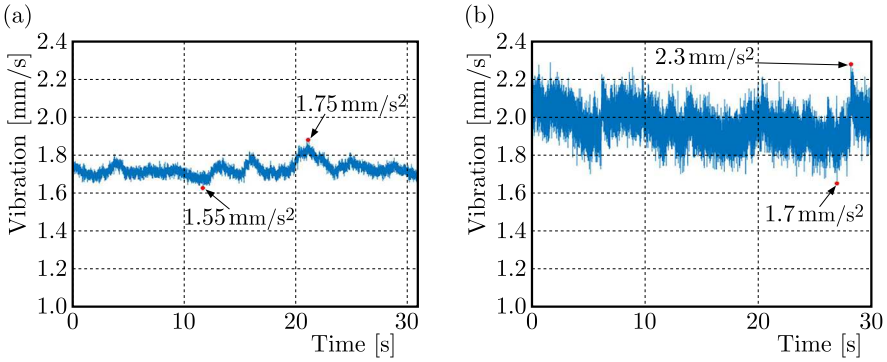

Fig. 16. Vibration acceleration experiment curve of the bearing: (a) speed is 3000 r/min, (b) speed is 8000 r/min

It can be seen from Fig. 16 that the vibration acceleration range of the bearing at 3000 r/min is (1.55-1.75) mm/s^2. The vibration acceleration range of the bearing at 8000 r/min is (1.7--2.3) mm/s^2. Obviously, with the increase of rotational speed, vibration of the damaged variable--diameter raceway intensifies. Compared with Fig. 15b, the radial load is the main factor affecting the vibration amplitude. This shows that the operational speed has a significant correlation with vibration of the damaged variable-diameter raceway.

The precision electronic analytical balance BSM220.4 is used in this paper, and the measurement accuracy is 0.1 mg. In order to ensure the weighing accuracy, the experimental samples are cleaned by ultrasonic waves for 10 minutes. Then they are blown dry and weighed. According to the literature (Zhao *et al.*, 2021), it can run for 300 hours under dry friction. Table 4 shows the amount wear extent of the damaged variable-diameter raceway at the same time and different speed.

Table 4. Wear extent at different speeds

Bearing number	Rotate speed [r/min]	Initial mass [g]	Damaged mass [g]	Wear extent [mg]
1	1800	90.1779	90.1727	2.2
2	3000	89.7026	89.6995	3.1
3	8000	89.8427	89.8303	12.4

The wear degree of the raceway becomes worse with an increase of rotational speed. The wear extent at high speed is much higher than that at middle and low speed, which may be due to the violent collision force of the rolling element at high speed. Wear occurs on the surface of rolling elements.

The experimental results for three rotational speeds show that the vibration amplitude of the bearing without the cage in the damaged variable-diameter raceway does not change significantly with the load. But vibration intensifies with an increase of rotational speed. This is consistent with the comparison results of the damaged frequency-domain waterfall diagram in the simulation.

6. Conclusions

The damage of the variable-diameter raceway leads to an increase of bearing vibration, which will accelerate the failure of the machine. This paper analyzes the influence of the damaged variable--diameter raceway on dynamic characteristics of the rolling element. The vibration equation of the ball bearing without the cage is established. Vibration of the damaged variable-diameter raceway is studied by numerical solution, simulation analysis and experiment. The specific conclusions are as follows:

- With deterioration of the variable-diameter raceway, the vibration amplitude of the bearing increases obviously. Vibration fluctuation caused by the discrete failure of the rolling element indicates that the collision force between rolling elements is the main factor resulting in violent vibration.
- The vibration acceleration of the bearing in the conventional raceway is less than that in the variable raceway. The contact point changes from point 1 to point 2 when the rolling element enters the variable-diameter raceway. This leads to time variation of displacement and contact stiffness.
- The velocity-displacement phase diagram is analyzed. Damage visibility of the local variable-diameter raceway increases. Due to the discrete failure of the rolling element, an instantaneous force is generated in the rolling element extrusion inner ring. Therefore, the inner-loop motion is transformed from quasi-periodic to chaotic motion.
- The local variable-diameter raceway is slighty damaged and does not affect the dispersion effect. Vibration occurs only at the theoretical frequency or its multiple. However, when damage of the local variable-diameter raceway is large, the dispersion effect is affected. Vibration is greater than that of the theoretical frequency value or its multiple.

The frequency variation of damage can be used as the basis for monitoring the state of the machine system in the future.

Acknowledgments
This work was supported by the National Natural Science Foundation of China(51875142), China.

References

1. Behzad M., Bastami A.R., Mba D., 2011, A new model for estimating vibrations generated in the defective rolling element bearings, *Journal of Vibration and Acoustics – Transactions of the ASME*, **133**, 4, 041011
2. Cui L.L., Jin Z., Huang J.F., Wang H.Q., 2019, Fault severity classification and size estimation for ball bearings based on vibration mechanism, *IEEE Access*, **7**, 56107-56116
3. Fan J., Cui W., Han Q.K., 2017, Vibration signal modeling of a localized defective rolling bearing under unbalanced force excitations, *Journal of Vibroengineering*, **19**, 7, 5009-5019
4. Khanam S., Dutt J.K., Tandon N., 2015, Impact force based model for bearing local fault identification, *Journal of Vibration and Acoustics – Transactions of the ASME*, **137**, 5, 051002
5. Liu J., Tang C.K., Shao Y.M., 2019, An innovative dynamic model for vibration analysis of a flexible rolling element bearing, *Mechanism and Machine Theory*, **135**, 27-39
6. Liu J., Wu H., Shao Y.M., 2018, A theoretical study on vibrations of a ball bearing caused by a dent on the races, *Engineering Failure Analysis*, **83**, 220-229
7. Liu Y.Q., Chen Z.G., Wang K.Y., Zhai W.M., 2022, Surface wear evolution of traction motor bearings in vibration environment of a locomotive during operation, *Science China – Technological Sciences*, **65**, 4, 920-931
8. McFadden P.D., Smith J.D., 1984, Model for the vibration produced by a single point-defect in a rolling element, *Journal of Sound and Vibration*, **96**, 1, 69-82
9. Parmar V., Saran V.H., Harsha S.P., 2021, Effect of dynamic misalignment on the vibration response, trajectory followed and defect-depth achieved by the rolling-elements in a double-row spherical rolling-element bearing, *Mechanism and Machine Theory*, **162**, 104366
10. Shah D.S., Patel V.N., 2019, A dynamic model for vibration studies of dry and lubricated deep groove ball bearings considering local defects on races, *Measurement*, **137**, 535-555
11. Xi S.T., Cao H.R., Chen X.F., 2019, Dynamic modeling of spindle bearing system and vibration response investigation, *Mechanical Systems and Signal Processing*, **114**, 486-511
12. Yang Y., Ouyang J., Wu X.L., Jin Y.L., Yang Y.R., Cao D.Q., 2019, Bending-torsional coupled vibration of a rotor-bearing-system due to blade-casing rub in presence of non-uniform initial gap, *Mechanism and Machine Theory*, **140**, 170-193
13. Yang Y.Z., Yang W.G., Jiang D.X., 2018, Simulation and experimental analysis of rolling element bearing fault in rotor-bearing-casing system, *Engineering Failure Analysis*, **92**, 205-221
14. Zhao Y.L., Wang Q.Y., Wang M.Z., Pan C.Y., Bao Y.D., 2022, Discrete theory of rolling elements for a cageless ball bearing, *Journal of Mechanical Science and Technology*, **36**, 4, 1921-1933
15. Zhao Y.L., Zhang J.W., Zhou E.W., 2021, Automatic discrete failure study of cage free ball bearings based on variable-diameter contact, *Journal of Mechanical Science and Technology*, **35**, 11, 4943-4952
16. Zheng L.K., Xiang Y., Sheng C.X., 2021, Nonlinear dynamic modeling and vibration analysis of faulty rolling bearing based on collision impact, *Journal of Computational and Nonlinear Dynamics*, **16**, 6, 061001

Manuscript received May 28, 2022; accepted for print October 3, 2022

JOURNAL OF THEORETICAL AND APPLIED MECHANICS
61, 1, pp. 147-162, Warsaw 2023
https://doi.org/10.15632/jtam-pl/158823

PREDICTIONS OF FRACTURE RESISTANCE OF SPRUCE WOOD UNDER MIXED-MODE LOADING USING NON-LOCAL FRACTURE THEORY AND NUMERICAL MODELLING

Marek Romanowicz

Bialystok University of Technology, Department of Mechanical Engineering, Bialystok, Poland

e-mail: m.romanowicz@pb.edu.pl

A novel analytical model to predict fracture resistance of a quasi-brittle material, like wood, is presented. The model is based on a scaling parameter introduced into the non-local fracture theory to take into account the specimen size effect on the development of the damage zone. An expression for length of the critical process zone, which can be used in damage tolerant design of wooden structures is derived from this theory. The model is validated with mixed-mode bending tests. A numerical analysis using cohesive elements is performed to understand the role of specimen size in the development of the damage zone. The analytical predictions of the fracture resistance and the critical process zone length for wood are compared with numerical results and experimental data available in the literature.

Keywords: mixed-mode bending test, process zone length, resistance curve, fracture criteria, cohesive zone model

1. Introduction

Two approaches have been reported in the literature to consider damage processes occurring ahead of the crack tip in quasi-brittle materials: the concept of cohesive fracture models originated by Barenblatt (1962) and Dugdale (1960) and the concept of non-local fracture models introduced by Novozhilov (1969). The first approach is through decohesion of the upper and lower surfaces of the process zone ahead of the crack tip. The second approach involves averaging of the stresses over this zone. It can be seen in Fig. 1 that the averaged stress over the length L_{cz} cannot exceed the strength of the material in the non-local model, whereas the cohesive model assumes a gradual loss of stiffness over the length L_{cz}.

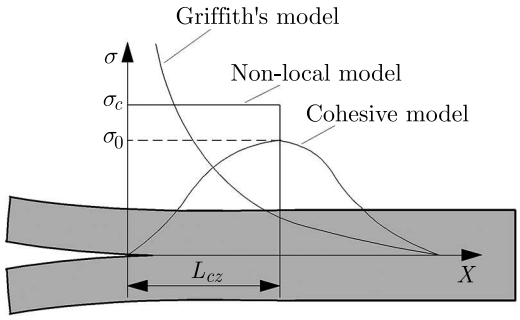

Fig. 1. Stress distribution ahead of the crack tip

Development of the fracture process zone (FPZ) in a quasi-brittle material like wood leads to a stable crack growth before the complete fracture (Morel *et al.*, 2005). The ability to predict the stable growth of a pre-existing crack under a mixed-mode loading is a key requirement in damage tolerant design of wooden structures. In recent studies (de Moura *et al.*, 2010; Phan *et*

al., 2016), the initiation and propagation fracture toughnesses of wood under the mixed-mode loading have been typically described by an empirical power law combining energy release rates in mode I and II with their critical values, i.e. $(G_I/G_{Ic})^m + (G_{II}/G_{IIc})^n = 1$, where m, n are constants.

Originally developed by Reeder and Crews (1990) to study the mixed-mode interlaminar fracture toughness of composite laminates, the mixed-mode bending test (MMB) was also used to investigate the resistance to crack growth in wood (de Moura *et al.*, 2010; Phan *et al.*, 2016). The use of this test is justified by the fact that it is capable of keeping a constant mixed-mode ratio during crack growth. In the framework of equivalent linear elastic fracture mechanics (LEFM) proposed by Bazant and Kazemi (1990), the secant compliance estimated from any point of the load-displacement curve corresponds to the initial elastic compliance of the cracked specimen, in which the crack length is given by the actual one plus a correction due to the FPZ development, i.e. $a_{eq} = a_0 + \Delta a$. Using this approach, it has been found that variations of mode I and mode II energy release rates with crack length (R-curves) for wood follow an initially increasing trend before reaching a plateau, which indicates the appearance of self-similar propagation of the main crack with its critical FPZ.

Numerous analytical and numerical models have been proposed to calculate the variation of the energy release rate directly from the MMB test data. Within the framework of simple beam theory, the cracked specimen is considered as an assemblage of three rigidly connected sublaminates (Reeder and Crews, 1990). In order to take into account the effects of deflections and rotations at the crack tip, crack length corrections are introduced into the simple beam theory (Williams, 1989; Wang and Williams, 1992). According to enhanced beam theory, the two sublaminates are partially connected by a deformable interface to take into account the crack propagation. Splitting of the two sublaminates is modeled by applying elastic brittle (Bennati *et al.*, 2013a,b) or elastic damaging constitutive laws (Xie *et al.*, 2016a,b). Compared to the simple beam theory, the enhanced beam theory is capable of capturing the pre-peak nonlinearity of load--displacement response. However, due to the assumptions of the beam theory, it over-predicts the pre-peak stiffness and process zone length. Numerical simulations of the MMB test are typically performed in the framework of the finite element method by using the virtual crack closure technique (Xie and Biggers, 2006; Oliveira *et al.*, 2007) or the cohesive zone model (Alfano and Crisfield, 2001; Camanho and Dávila, 2002). The main difference between them is that the latter has the capability to model damage mechanisms, whereas the former does not. However, since numerical predictions are mesh-dependent, care must be taken to ensure that element sizes are capable of capturing strain and stress gradients near the crack tip.

The objective of this paper is to show that the non-local fracture theory proposed by Seweryn and Mróz (1998) is capable of predicting the propagation fracture toughness of wood under mixed-mode loading conditions. To date, only the initiation fracture toughness of wood has been analyzed by using this fracture theory (e.g. Romanowicz, 2019). In previous papers, it has been assumed that the compliance within the damage zone and the process zone length are material properties. Extension of the non-local fracture theory to the study of the crack propagation resistance requires redefining these concepts. In this paper, the quasi-brittle fracture characteristics predicted from the extended non-local theory are verified against MMB test data available in the literature and numerical simulations accounting for cohesive properties of wood.

2. Non-local theory of quasi-brittle fracture

In this Section, a novel analytical approach for estimating the critical process zone length L_{cz} based on the non-local fracture theory is presented. According to the non-local fracture theory

proposed by Seweryn and Mróz (1998), a crack starts to grow when a stress function $R(\sigma_\theta, \tau_{r\theta})$ averaged over the process zone length l_{cz} reaches the maximum value

$$\max\left(\frac{1}{l}\int_0^{l_{cz}} R(\sigma_\theta, \tau_{r\theta})\, dr\right) = 1 \tag{B.1}$$

where σ_θ, $\tau_{r\theta}$ are the stress components in a polar coordinate system (r, θ) originated at the crack tip. This fracture theory is motivated by the fact that the stress distribution within the process zone is difficult to estimate precisely. For this reason, it is convenient to use the average value of stress. For a damage zone weakened by microcracks, Seweryn and Mróz (1998) proposed the following elliptic function for calculating the fracture toughness

$$R(\sigma_\theta, \tau_{r\theta}) = \sqrt{\Big(\frac{\sigma_\theta}{\sigma_c}\Big)^2 + \rho\Big(\frac{\tau_{r\theta}}{\sigma_c}\Big)^2} \tag{B.2}$$

where σ_c is the tensile strength representing the ratio of the sliding and extensional compliance of the material within the damage zone. Maximizing the average value of $R(\sigma_\theta, \tau_{r\theta})$ with respect to θ, the location of the critical plane is determined. The non-local model of crack propagation is formulated by assuming that the process zone length is much less than the crack length. On this assumption, the stress distribution associated with damage mechanisms occurring ahead of the crack tip is dominated by a singular crack tip solution of the type $r^{-0.5}$. It was reported by Romanowicz (2019) that the stress function (2.2) has for orthotropic materials its maximum at $\theta = 0^\circ$ if the reinforcement direction coincided with the crack axis. Thus, in the case of self-similar crack growth, stress function (2.2) can be expressed as

$$R(\sigma_\theta, \tau_{r\theta}) = \frac{1}{\sigma_c}\sqrt{\frac{K_I^2}{2\pi r} + \rho\frac{K_{II}^2}{2\pi r}} \tag{B.3}$$

where K_I, K_{II} are stress intensity factors for pure opening and pure sliding modes, respectively. Substituting (2.3) into (2.1) and integrating from $r = 0$ to $r = l_{cz}$ the non-local criterion of crack propagation is given in terms of stress intensity factors as

$$K_I^2 + \rho K_{II}^2 = \frac{l_{cz}\sigma_c^2\pi}{2} \tag{B.4}$$

On the assumptions of LEFM, the stress intensity factors for orthotropic materials are related to strain energy release rates by the relationship proposed by Sih *et al.* (1965)

$$G = G_I + G_{II} = \frac{K_I^2}{E_I} + \frac{K_{II}^2}{E_{II}} \tag{B.5}$$

where: G, G_I, G_{II} are total, mode I and II energy release rates, respectively, E_I, E_{II} are generalized elastic moduli. The procedure for calculating E_I, E_{II} is provided in Appendix A. One potential limitation in application of Eq. (2.4) is that the compliance ratio is, in general, an unknown parameter. In order to overcome this limitation, the ratio can be calibrated by fitting theoretical predictions to experimental data. In this paper, the compliance ratio is thus defined as some multiple of the ratio between E_I and E_{II}

$$\rho = \frac{E_I}{nE_{II}} \tag{B.6}$$

where n is an empirical parameter. In the previous papers on the initiation fracture toughness of wood (Romanowicz, 2019), the compliance ratio was assumed to be $\rho = (K_{Ic}/K_{IIc})^2$, where

K_{Ic} and K_{IIc} are mode I and II critical stress intensity factors. By using Eqs. (2.5) and (2.6), the non-local criterion of crack propagation (2.4) can be now expressed in terms of mode I and II energy release rates as

$$nG_I + G_{II} = \frac{l_{cz}\sigma_c^2 \pi n}{2E_I} \tag{B.7}$$

When the process zone is fully developed $l_{cz} = L_{cz}$, the fracture resistance can be estimated from the strain energy release rate as $G = G_R$. Formally, substituting $l_{cz} = L_{cz}$ into (2.7) means that the non-local criterion predicts the moment of complete fracture. In this paper, the value of L_{cz} is chosen so as to make non-local criterion (2.7) equivalent to the semi-empirical mixed-mode propagation criterion proposed by Benzeggagh and Kenane (1996). According to this criterion, the total fracture resistance is a power function of the mixed-mode ratio G_{II}/G

$$G_R = G_{IR} + (G_{IIR} - G_{IR})\Big(\frac{G_{II}}{G}\Big)^m \tag{B.8}$$

where: G_R, G_{IR} , G_{IIR} are total, mode I and II fracture resistances, m is an empirical parameter. Since the strength σ_c and modulus E_I are constants, it is reasonable to assume that the length L_{cz} occurring in non-local criterion (2.7) should follow the same trend as the fracture resistance G_R predicted by the Benzeggagh and Kenane criterion. It should be noted that it is possible to rewrite the Benzeggagh and Kenane criterion so that the left hand sides of Eqs. (2.7) and (2.8) are equal when $l_{cz} = L_{cz}$

$$nG_{IR} + G_{IIR} = nG_{IR} + (G_{IIR} - G_{IR})\Big(\frac{G_{II}}{G}\Big)^m \tag{B.9}$$

Finally, by equating the right hand sides of Eqs. (2.7) and (2.9), the length of the fully developed process zone can be written as a power function of the mixed-mode ratio G_{II}/G

$$L_{cz} = \frac{2E_I}{\sigma_c^2 \pi n}\Big[nG_{IR} + (G_{IIR} - G_{IR})\Big(\frac{G_{II}}{G}\Big)^m\Big] \tag{B.10}$$

Substituting (2.10) into (2.7), the non-local criterion takes the form of the Benzeggagh and Kenane criterion. Mode I and II process zone lengths are calculated by setting $G_{II}/G = 0$ and $G_{II}/G = 1$ in (2.10), as follows

$$L_{Icz} = \frac{2E_I G_{IR}}{\sigma_c^2 \pi} \qquad L_{IIcz} = \frac{2E_I}{\sigma_c^2 \pi n}[G_{IIR} + (n-1)G_{IR}] \tag{B.11}$$

Figure 2 shows solutions of the dimensionless characteristic length L_{cz} for a fixed value of m and various values of n. It is interesting to note that the variation of process zone length with ratio G_{II}/G becomes smaller as n increases and for large values of n, a constant process zone length equal to L_{Icz} is observed. From Eqs. (2.11), mode I process zone length is not influenced by the parameter n and when $n = 1$, mode II process zone length can be written in terms of G_{IIR} only. Based on these findings, the parameter n controls the value of mode II process zone length and the steepness of the curve describing the relationship between the process zone length and the mixed-mode ratio. It can be interpreted as a scaling parameter for the ratio of the sliding and extensional compliance of the material within the damage zone.

3. Finite element simulations of quasi-brittle fracture

In this Section, the finite element implementation of a bilinear cohesive zone model proposed by Alfano and Crisfield (2001) and Camanho and Dávila (2002) is presented to predict damage

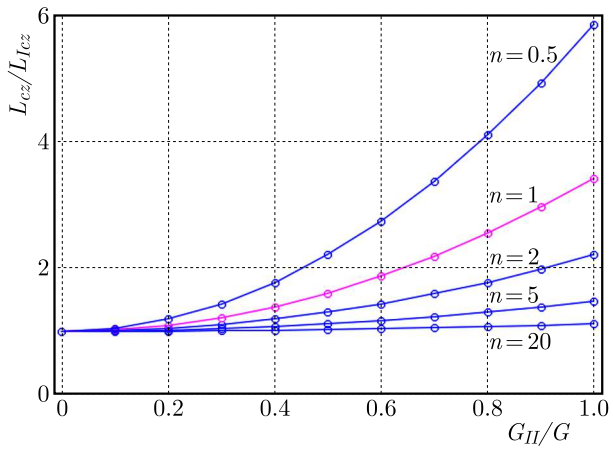

Fig. 2. Effect of the parameter n on the variation of dimensionless process zone length with the mixed-mode ratio

evolution in wood. Finite element analyses have been conducted under mode I, mode II and mixed-mode loading using the double cantilever beam (DCB), end notched flexure (ENF) and mixed-mode bending (MMB) specimens, respectively. The deformed finite element meshes and boundary conditions corresponding to these cases are shown in Fig. 3. The MMB test uses a lever to simultaneously apply the loads which are similar to those applied to the DCB and ENF tests. Mixed-mode ratios are controlled by the lever length c. Five different lever lengths $c = 160$, 200, 235, 335, 435 mm are studied. The length $2L$, width B and thickness $2h$ of the specimens are 750 mm, 30 mm and 30 mm, respectively. The length of the support span $2l$ is fixed in all tests at 650 mm. The length of the pre-crack a_0 measured from the beam support point is 227 mm. These specimens correspond to those used in experiments performed by Phan *et al.* (2016) on Norway spruce in the TL crack system. The specimen material is assumed to be linearly elastic and orthotropic (Table 1). The specimen geometry is meshed with two-dimensional plane strain 4 node elements in Ansys (PLANE182). The mesh is refined along a predefined crack path located at the midplane of the specimen. The elements ahead of the crack tip have the length 0.6 mm. Frictionless contact is assigned between the crack surfaces. The MMB test apparatus is modeled explicitly using beam elements (BEAM188) with material properties much stiffer than those of the specimen. In order to connect the rigid beam elements with the plane elements and to enforce the appropriate boundary conditions, multi-point constraints (MPC184) are used.

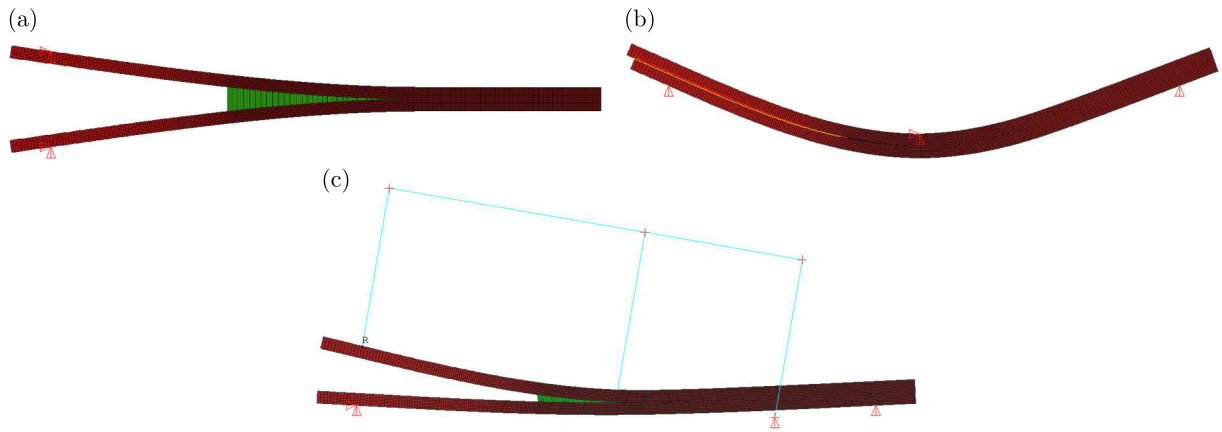

Fig. 3. Finite element meshes and boundary conditions used in the simulations: (a) DCB test, (b) ENF test, (c) MMB test

Table 1. Elastic properties of Norway spruce (Dourado *et al.*, 2008) and its tensile strength in the tangential direction (Pedersen *et al.*, 2003)

E_L [MPa]	E_R [MPa]	E_T [MPa]	ν_{TL} [–]	ν_{RL} [–]	ν_{TR} [–]	G_{TL} [MPa]	G_{RT} [MPa]	G_{RL} [MPa]	σ_c^{T} [MPa]
9900	730	410	0.018	0.032	0.306	610	22	500	2.7

Crack propagation is modeled by using zero-thickness cohesive elements (INTER202) based on a bilinear traction-separation constitutive relationship, $\sigma_i = \sigma_i(\delta_i)$, with $i = I, II$. The response of cohesive elements is linear-elastic up to the onset of damage. After the damage onset, the interface elements start losing their stiffness linearly. When the stiffness of the cohesive elements reduces to zero, crack growth occurs. Mode I and mode II energy release rates are calculated in Ansys as

$$G_I = \int_0^{\delta_I} \sigma_I \, d\delta_I \qquad G_{II} = \int_0^{\delta_{II}} \sigma_{II} \, d\delta_{II} \tag{B.1}$$

The mixed-mode cohesive zone model implemented here requires two cohesive strengths σ_I^0 and σ_{II}^0, two separations at the onset of damage δ_I^0 and δ_{II}^0, and two separations at the moment of fracture δ_I^c and δ_{II}^c to predict the evolution of damage. In order to ensure that both tractions vanish simultaneously at complete separation, the ratios δ_I^0/δ_I^c and $\delta_{II}^0/\delta_{II}^c$ are assumed to be equal in the present study. For more information about the bilinear cohesive zone model, see Appendix B.

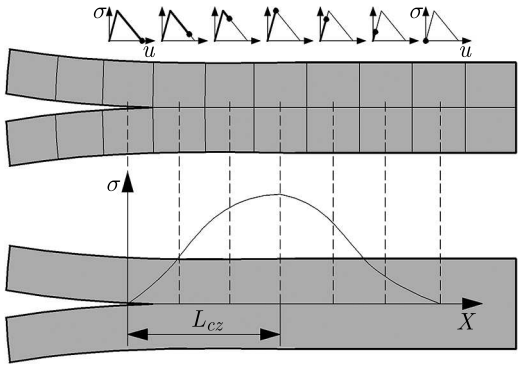

Fig. 4. Development of the fracture process zone

A model of the fracture process zone and its finite element implementation is shown in Fig. 4. The fracture process zone is a region ahead of the crack tip where the finite elements experience irreversible deformation. The numerical process zone length L_{cz} is calculated by adding the lengths of cohesive elements that are currently damaged $L_{cz} = \sum l_i$. In order to investigate the influence of cohesive strength on the load-deflection response and the process zone length of Norway spruce, parametric studies under mode I and mode II conditions have been conducted for experimentally established values of mode I and II fracture resistances $G_{IR} = 0.286\,\mathrm{N/mm}$, $G_{IIR} = 0.979\,\mathrm{N/mm}$ (Phan *et al.*, 2016). It can be seen in Figs. 5a and 5b that as the cohesive strength increases, the peak load increases and the load-deflection response gets closer to the linear elastic solution obtained by using the simple beam theory. Details of the analytical solutions for the load-deflection response of the beam specimens can be found by Xie *et al.* (2016a). It should be noted that the analytical solutions are for the case of infinitely stiff interface with brittle failure (δ_I^0 and $\delta_{II}^0 \to 0$, σ_I^0 and $\sigma_{II}^0 \to \infty$) and the observed deviation of

the initial stiffness from the linear elastic solution is typical for numerical simulations that use the bilinear cohesive zone model (e.g. Xie *et al.*, 2016b).

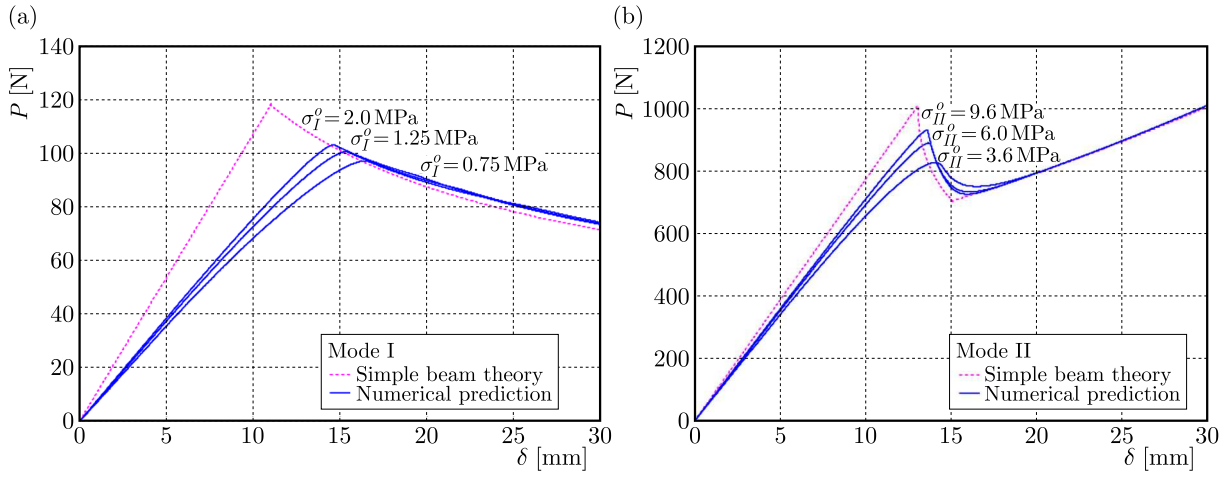

Fig. 5. Effect of cohesive strength on the load-displacement response for (a) mode I and (b) mode II loading

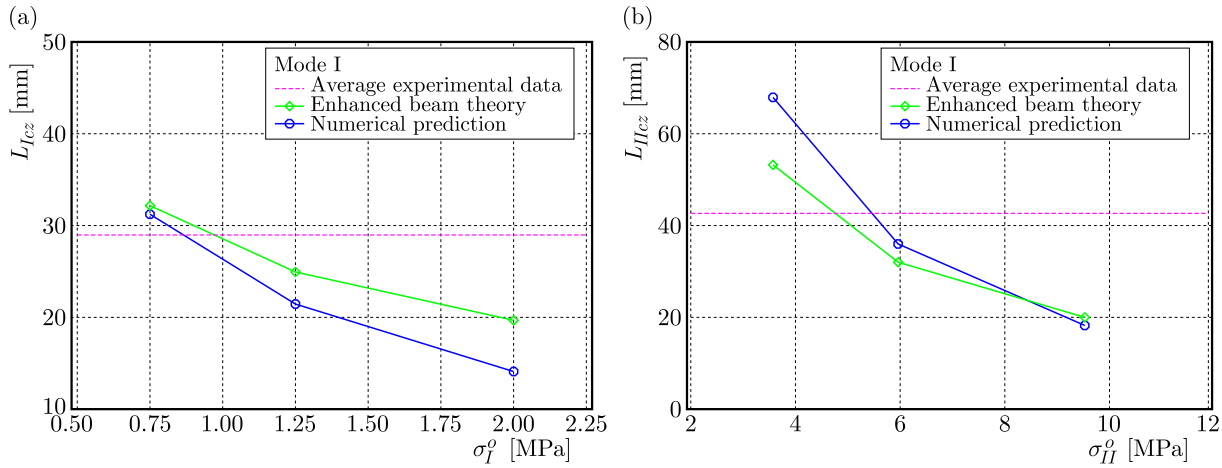

Fig. 6. Variation of the process zone length with cohesive strength for (a) mode I and (b) mode II loading (experimental data from Phan *et al.* (2016))

As shown in Figs. 6a and 6b, the process zone length, on the contrary, decreases with the increasing cohesive strength. This trend is found to agree with the analytical solution based on the enhanced beam theory (Xie *et al.*, 2016b)

$$L_{Icz} = \frac{1}{2}\sqrt[4]{\frac{E_{eff} G_{IR} h^3}{(\sigma_I^0)^2}} \qquad L_{IIcz} = \frac{1}{2}\sqrt{\frac{E_{eff} G_{IR} h}{(\sigma_{II}^0)^2}} \tag{B.2}$$

where $E_{eff} = E_L(1 - \nu_{LR}\nu_{RL})$ is found using the elastic constants (Table 1). Since the experimental load-deflection curves for Norway spruce are not available in Phan *et al.* (2018), the cohesive properties are calibrated in such a way that they satisfy equations

$$G_{IR} = \frac{1}{2}\sigma_I^0 \delta_I^c \qquad G_{IIR} = \frac{1}{2}\sigma_{II}^0 \delta_{II}^c \tag{B.3}$$

and simultaneously the fracture process zone lengths predicted from the finite element models correspond closely to the reference values obtained from the experiments $L_{Icz} = 29$ mm, and $L_{IIcz} = 42.8$ mm (Phan *et al.*, 2016). Taking the above into account, the interface with

$\sigma_I^0 = 1.25\,\text{MPa}$ and $\sigma_{II}^0 = 6\,\text{MPa}$ is chosen for the rest of the study. It is interesting to note that the adjusted value for the cohesive strength σ_I^0 of Norway spruce is in good agreement with the literature data $\sigma_I^0 = 1.66\,\text{MPa}$ (Dourado *et al.*, 2008) obtained for different specimen types. All cohesive properties used in the present study are summarized in Table 2.

Table 2. Cohesive properties of Norway spruce

σ_I^0 [MPa]	δ_I^0 [mm]	δ_I^c [mm]	σ_{II}^0 [MPa]	δ_{II}^0 [mm]	δ_{II}^c [mm]
1.25	0.04576	0.4576	6	0.03263	0.3263

Loads and deflections obtained from numerical simulations are processed with the compliance based beam method (CBBM) proposed by de Moura *et al.* (2010) to achieve mode I and II fracture resistances. CBBM is an example of the data reduction method which enables the determination of strain energy release rates on the assumptions of equivalent LEFM based on the theoretical specimen compliances

$$G_I = \frac{P_I^2}{2B}\frac{dC_I}{da} \qquad G_{II} = \frac{P_{II}^2}{2B}\frac{dC_{II}}{da} \tag{B.4}$$

where P_I, P_{II} are mode I and II components of the applied load, C_I, C_{II} are mode I and II compliances, B is the specimen width. For more information about this method, see Appendix C.

4. Results and discussion

In this Section, the theoretical and numerical predictions of the fracture resistance and the process zone length of Norway spruce under combined mode I and mode II loadings are compared with the experimental results reported by Phan *et al.* (2016). The key difference between experimental and numerical techniques for analyzing the crack growth resistance lies in the way of determining the crack length. In the experimental study performed by Phan *et al.* (2016), the crack length is calculated by setting the experimental specimen compliance to the relationship $C(a) = \delta/P$ between the compliance and crack length obtained from a linear-elastic finite element analysis. In the present study, the crack length required by CBBM is estimated by setting the numerical specimen compliance to the compliance function $C(a)$ derived from the beam theory (Appendix C).

Figures 7a and 7c show numerical predictions of the load-deflection and crack evolution curves by the cohesive zone model for different loading conditions. It is interesting to note that the crack starts to grow long before the peak load is reached. The observed pre-peak behavior is associated with the formation of the fracture process zone. The location of the transition point from stable to self-similar crack propagation on the crack evolution curve is found to appear just behind the peak load on the load-deflection curve. The critical loads are depicted by arrows in Figs. 7a-7c. It can be seen from these figures that the post-peak behavior under pure mode I loading differs from those under pure mode II and mixed-mode loading. In the case of pure mode I loading, the post-peak slope of both curves is almost constant, which is attributed to the self-similar crack growth regime. In the cases of pure mode II and mixed-mode loading, the post-peak slope of both curves changes because the specimens exhibit a load recovery when the crack approaches the central loading point, $a = 325\,\text{mm}$.

In the framework of equivalent LEFM, the crack stability is characterized by a resistance curve (R-curve) which indicates changes in the energy release rate as a function of crack length. Evolutions of the resistance to crack growth in Norway spruce obtained from CBBM for different loading conditions are shown in Figs. 8a-8c. They start from initial nonzero values of

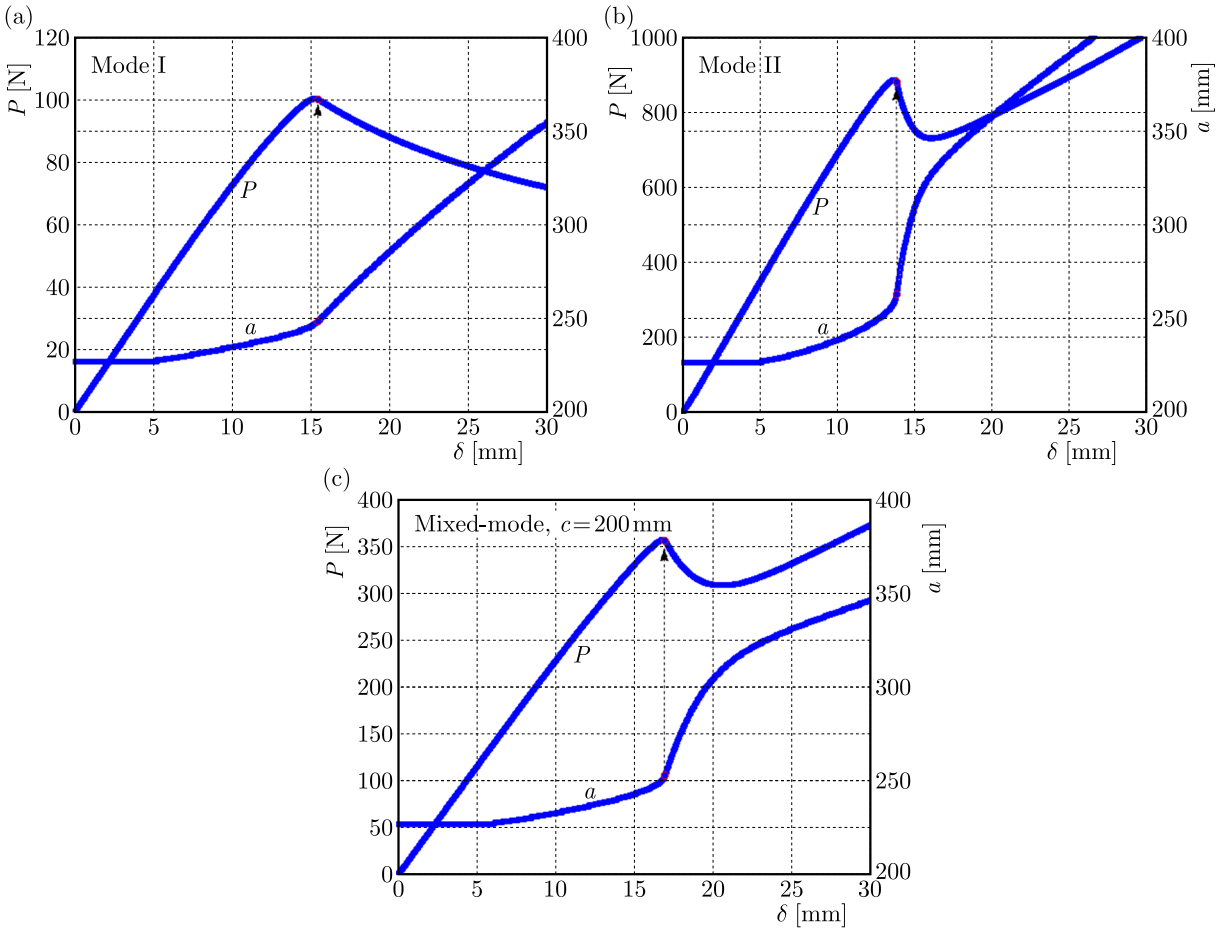

Fig. 7. The load-displacement and crack evolution curves from (a) DCB test, (b) ENF test and (c) MMB test

the energy release rate and consist of three distinct phases: the initial ascending phase followed by a plateau, and then another ascending phase. The numerical results are compared with the available experimental data (Phan *et al.*, 2016) to assess the performance of CBBM for the prediction of fracture resistance. Figure 9 compares the numerical predictions of R-curves obtained for the lever length $c = 160\,\text{mm}$ using average material properties with the test data obtained from one specimen. It can be seen from this figure that CBBM fits the shape and magnitude of the experimental data reasonably well.

As discussed in the previous Section, fracture simulations using the cohesive zone model are capable of analyzing the development of the fracture process zone. The length of the process zone is calculated as the maximum distance between the centers of two cohesive elements located to the right of the current crack tip which have experienced damage. Numerical modeling of the process zone length in Norway spruce as a function of the crack length for different mixed-mode loading conditions is shown in Figs. 8a-8c. It can be seen that after the initial increase, the process zone length reaches for each loading case its maximum value and then remains constant over some increment of the crack length. The maximum value of the process zone length allows us to estimate the onset of self-similar crack propagation and, in this way, to clearly identify the point on the resistance curve where the fracture resistance is established. The fracture resistances are depicted by arrows in Figs. 8a-8c. The total fracture resistances G_R and the fully developed cohesive zone lengths L_{cz} calculated in this way for seven different mixed-mode ratios G_{II}/G are shown in Figs. 10 and 11, respectively.

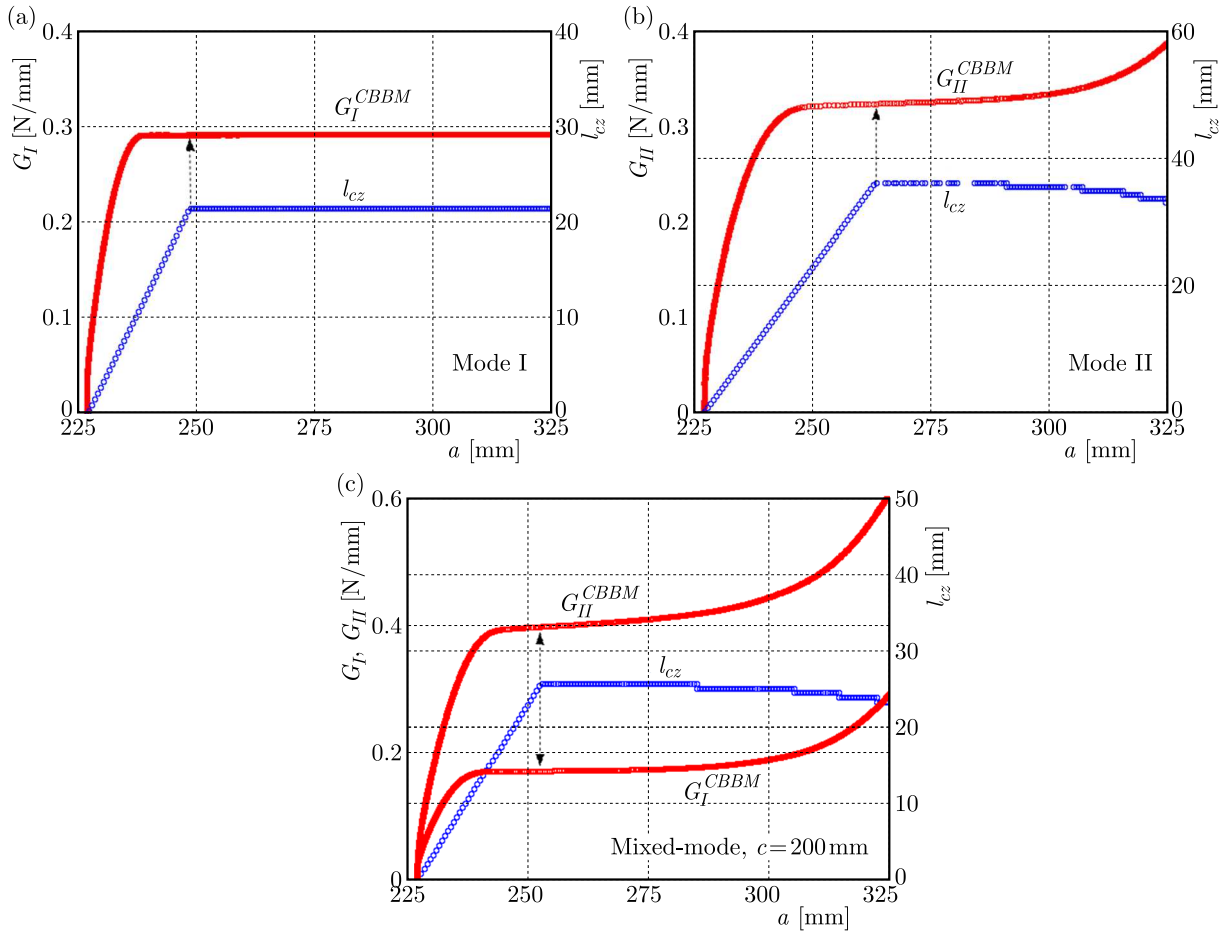

Fig. 8. The resistance curves and variations in the process zone length during crack propagation for (a) mode I, (b) mode II and (c) mixed-mode loading

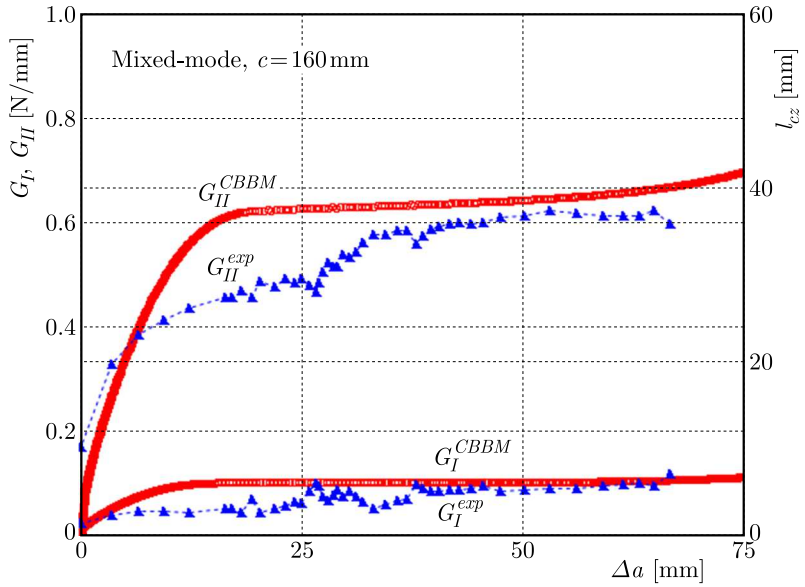

Fig. 9. Comparison between the predicted and measured resistance curves for $c = 160$ mm (experimental data from Phan *et al.* (2016))

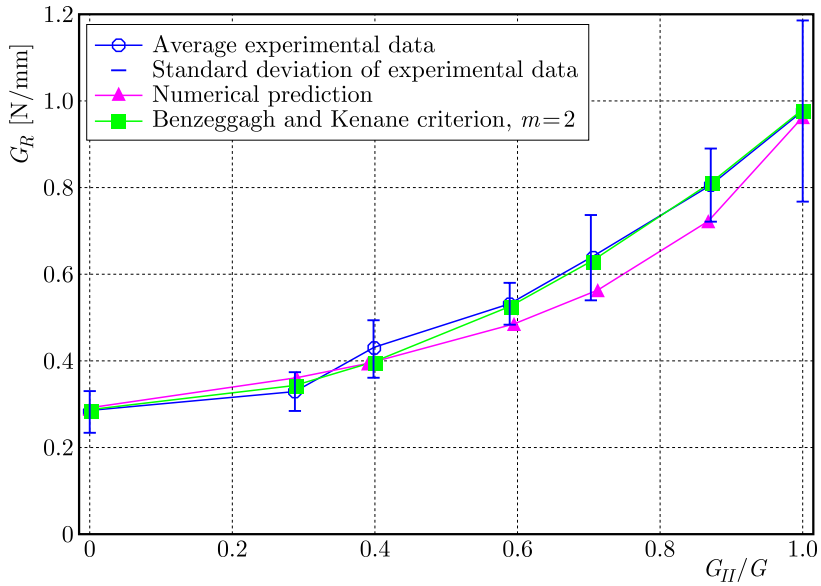

Fig. 10. Comparison between the predicted and measured fracture resistance of Norway spruce (experimental data from Phan *et al.* (2016))

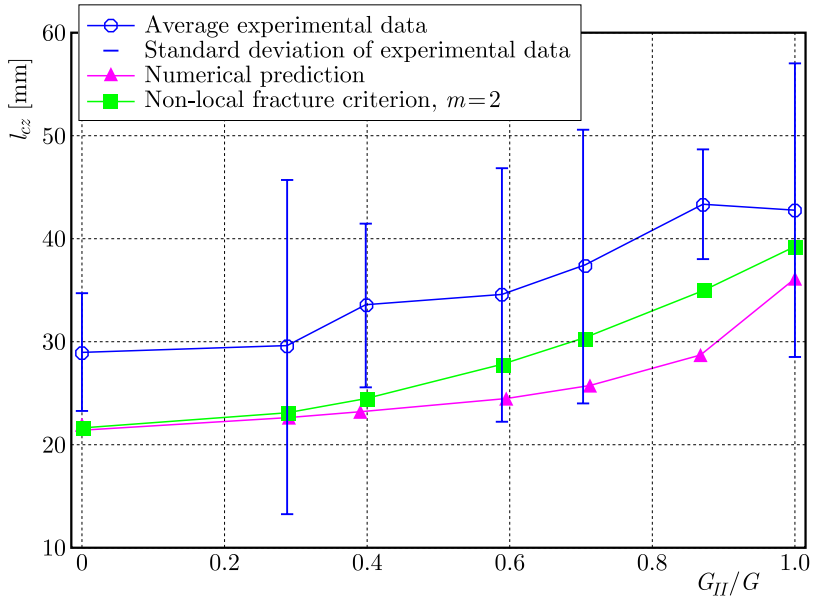

Fig. 11. Comparison between the predicted and measured process zone length of Norway spruce (experimental data from Phan *et al.* (2016))

Furthermore, Figs. 8a-8c show that it is only in the case of pure mode I loading that the specimen is capable of keeping the maximum value of the process zone length during the entire crack growth process. In the cases of pure mode II and mixed-mode loading, the process zone length beyond the maximum value decreases with the increasing crack length. This is because when the crack approaches the central loading point, the compressive stress zone at the center of the specimen disturbs the development of the fracture process zone. Thus, the development of the damage zone is influenced not only by the mixed-mode ratio but also by the specimen size. This finding sheds new light on the role of the scaling parameter n in the theoretical solution of the L_{cz} given by Eq. (2.10). It should be noted that there is a similarity between the theoretical and numerical solutions of the process zone length for pure mode I loading, namely that the

theoretical solution of the L_{Icz} is not influenced by the parameter n, whereas the numerical solution of L_{Icz} is free from the specimen size effect.

Figures 10 and 11 compare the theoretical and numerical predictions of the fracture resistance and critical process zone length of Norway spruce with the experimental data reported by Phan *et al.* (2016). The measured fracture resistance and critical process zone length of wood increase with an increase in the mixed-mode ratio. It can be seen from these figures that both the numerical prediction as well the analytical solution follow the trend of experimental points. In the case of the fracture resistance, the Benzeggagh and Kenane criterion with the parameter m taking the value of 2 is in a better agreement with the experimental data than the numerical prediction. In the case of the critical process zone length, the non-local fracture criterion with the parameter n taking the value of 3 provides a slightly better fit to the experimental data than the numerical prediction. The deviation of numerical predictions from experimental points is caused by the approximation of the true cohesive behavior of wood by the bilinear traction--separation law. The discrepancy between the theoretical predictions and experimental points is due to the fact that the fracture behavior is dependent not only on the specimen geometry and loading conditions but is also affected by the cohesion between the crack surfaces, which is not explicitly taken into account in the fracture criteria.

It should be noted that, similar to the parameter m, the parameter n is experimentally calibrated. Since the value of L_{Icz} is independent of n, only the value of L_{IIcz} is fitted in the calibration such that the shape of the theoretical curve describing the relationship between the process zone length and mixed-mode ratio matches the shape obtained experimentally. The value of mode II critical process zone length calculated for $n = 3$ is $L_{IIcz} = 39.2\,\text{mm}$, whereas the same length obtained without scaling the compliance of the damage zone, for $n = 1$, has the value $L_{IIcz} = 74.3\,\text{mm}$, which is far from the measured value. This finding shows that the introduction of the parameter n into the non-local fracture model can be regarded as an advantage. The physical explanation of the parameter n is as follows. Since geometry of the body affects the development of the damage zone, it is reasonable to assume that the coalescence of microcracks in infinite bodies differs from that in slender bodies, such as beams. This means that the compliance of the damage zone depends on the specimen size and needs to be calibrated. Furthermore, it should be noted that a similar calibration procedure, as described above, is applied to the numerical model to estimate cohesive properties.

5. Conclusions

The applicability of non-local fracture theory to characterize fracture behavior of wood has been verified by comparing theoretical predictions with experimental data available in the literature and with numerical simulations accounting for cohesive properties of wood. The theoretical, numerical and experimental results presented in this paper have shown that not only the fracture resistance but also the process zone length depends nonlinearly on the mixed-mode ratio. The non-local fracture theory offers the ability to model the quasi-brittle fracture in wood without the need for using cohesive parameters which are difficult to estimate in practice. The concept of introduction of a scaling parameter into the non-local fracture theory has been proposed to take into account the specimen size effect on the development of the damage zone. The use of this scaling parameter has significantly improved the accuracy of the prediction of the critical process zone length. The ratio of the sliding and extensional compliance of the material within the damage zone has been defined as the ratio between the generalized elastic moduli, which has made it possible to achieve equivalence between the non-local and Benzeggagh and Kenane predictions of the fracture resistance. In this way, for the first time, the non-local theory has provided a physical explanation for the Benzeggagh and Kenane empirical criterion. The

comparison has shown that with much lower computational complexity, the proposed non-local model achieves a better efficiency than the numerical simulations.

Acknowledgement

The research described here was financially supported by the Ministry of Science and Higher Education of Poland under the grant No. WZ/WM-IIM/3/2020.

Appendix A. Calculation of generalized elastic moduli

Following Sih *et al.* (1965), energy release rates can be related to stress intensity factors through generalized elastic moduli. Under plane strain conditions, the generalized elastic moduli E_I and E_{II} in the global coordinate system (x_1, x_2, x_3) aligned with the principal axes of orthotropy (L, T, R) are given by

$$E_I = \left[\frac{S'_{11}S'_{22}}{2}\left(\sqrt{\frac{S'_{22}}{S'_{11}}}+\frac{2S'_{12}+S'_{66}}{2S'_{11}}\right)\right]^{-0.5} \qquad E_{II} = \left[\frac{(S'_{11})^2}{2}\left(\sqrt{\frac{S'_{22}}{S'_{11}}}+\frac{2S'_{12}+S'_{66}}{2S'_{11}}\right)\right]^{-0.5} \tag{A.1}$$

where the constants S'_{11}, S'_{12}, S'_{22} and S'_{66} are related to components of the compliance matrix $\{S_{ij}\}$ by

$$S'_{ij} = S_{ij} - \frac{S_{i3}S_{j3}}{S_{33}} \qquad i,j = 1,2,6 \tag{A.2}$$

where the compliance matrix $\{S_{ij}\}$ relates the stress and strain components in the principal material directions according to generalized Hooke's law

$$\varepsilon_i = S_{ij}\sigma_i \qquad i,j = 1,2,\ldots,6 \tag{A.3}$$

Appendix B. Bilinear mixed-mode cohesive zone model

The behavior of the material in the cohesive zone is assumed to be linear-elastic up to the onset of damage, and after that, elastic damaging with linear softening is observed (Alfano and Crisfield, 2001; Camanho and Dávila, 2002). The constitutive relationships between stresses σ_i on the crack plane and the corresponding relative displacements δ_i are as follows

$$\sigma_i = k_i(1-d_i)\delta_i \qquad i = I, II \tag{B.1}$$

where k_i are the initial stiffness values and d_i are damage variables which satisfy the following conditions

$$d_i = \begin{cases} 0 & \text{when} \quad \delta_i \leqslant \delta_i^0 \\ 1 & \text{when} \quad \delta_i = \delta_i^c \end{cases} \tag{B.2}$$

where δ_i^0, δ_i^c are separations at the onset of damage and at the moment of fracture, respectively. When the material is under mixed-mode loading, the separation at damage onset is calculated based on the quadratic stress criterion

$$\left(\frac{\sigma_I}{\sigma_I^0}\right)^2 + \left(\frac{\sigma_{II}}{\sigma_{II}^0}\right)^2 = 1 \tag{B.3}$$

where σ_I^0 and σ_{II}^0 are cohesive strengths. Using (B.3), the mixed-mode relative displacement corresponding to the onset of softening is given by

$$\delta_m^0 = \sqrt{(\delta_I^0)^2(\delta_{II}^0)^2\frac{1+\beta^2}{(\delta_{II}^0)^2+\beta^2(\delta_I^0)^2}} \tag{B.4}$$

where $\beta = \delta_{II}/\delta_I$ is the mixed-mode ratio. The separation at fracture is calculated based on the linear energetic criterion

$$\frac{G_I}{G_I^c} + \frac{G_{II}}{G_{II}^c} = 1 \tag{B.5}$$

where G_I^c and G_{II}^c are the critical strain energy release rates. Using (B.5), the mixed-mode relative displacement corresponding to total decohesion is given by

$$\delta_m^c = \frac{2(1+\beta^2)}{\delta_m^0}\Big(\frac{k_I}{G_I^c} + \frac{\beta^2 k_{II}}{G_{II}^c}\Big)^{-1} \tag{B.6}$$

Appendix C. Equations of the compliance based beam method

In this paper, the strain energy release rates G_I and G_{II} are calculated using the Compliance Based Beam Method proposed by de Moura *et al.* (2010). Since the MMB test combines the DCB and ENF tests, equations for the strain energy release rate from these tests are used to calculate individual components of G for the MMB test. Mode I component is given by

$$G_I = \frac{6P_I^2}{B^2h}\Big(\frac{2a_{eqI}^2}{E_{fI}h^2} + \frac{1}{5G_{LT}}\Big) \tag{C.1}$$

where a_{eqI} is the equivalent crack length in mode I estimated from the current specimen compliance

$$C_I = \frac{8a_{eqI}^2}{E_{fI}Bh^2} + \frac{12a_{eqI}}{5BhG_{LR}} \tag{C.2}$$

and E_{fI} is the flexural modulus in mode I estimated from the initial specimen compliance C_{0I}

$$E_{fI} = \frac{8(a_0+\Delta)^3}{Bh^3}\Big(C_{0I} - \frac{12(a_0+\Delta)}{5BhG_{LT}}\Big)^{-1} \tag{C.3}$$

where a_0 is the initial crack length, B and h are width and half-thickness of the specimen, respectively, constants Δ and Γ are given by

$$\Delta = h\sqrt{\frac{E_{fI}}{11G_{LT}}\Big[3 - 2\Big(\frac{\Gamma}{1+\Gamma}\Big)^2\Big]} \qquad \Gamma = 1.18\frac{\sqrt{E_{fI}E_T}}{G_{LT}} \tag{C.4}$$

where E_L, E_T and G_{LT} are the longitudinal, tangential and shear moduli, respectively. Mode II component is given by

$$G_{II} = \frac{(9P_{II}^2a_{eqII}^2}{16E_{fII}B^2h^3} \tag{C.5}$$

where E_{fII} is the flexural modulus in mode II estimated from the initial specimen compliance C_{0II}

$$E_{fII} = \frac{3a_0^3 + 2l^3}{8Bh^3}\Big(C_{0II} - \frac{3l}{10G_{LT}Bh}\Big)^{-1} \tag{C.6}$$

and a_{eqII} is the equivalent crack length in mode II estimated from the current specimen compliance C_{II}

$$a_{eqII} = \Big[\frac{C_{corrII}}{C_{0corrII}}a_0^3 + \frac{2}{3}\Big(\frac{C_{corrII}}{C_{0corrII}} - 1\Big)l^3\Big]^{1/3} \tag{C.7}$$

where

$$C_{corrII} = C_{II} - \frac{3l}{10G_{LT}Bh} \qquad C_{0corrII} = C_{0II} - \frac{3l}{10G_{LT}Bh} \tag{C.8}$$

The load P applied to the MMB test can be separated into mode I and mode II loading components as follows

$$P_I = \frac{3c-l}{4l}P \qquad P_{II} = \frac{c+l}{l}P \tag{C.9}$$

where l is the half span length of the beam, c is the lever length.

References

1. Alfano G., Crisfield M.A., 2001, Finite element interface models for the delamination anaylsis of laminated composites: Mechanical and computational issues, *International Journal for Numerical Methods in Engineering*, **50**, 1701-1736
2. Barenblatt G.I., 1962, The mathematical theory of equilibrium cracks in brittle fracture, *Advances in Applied Mechanics*, **7**, 55-129
3. Bazant Z.P., Kazemi M.T., 1990, Size effect in fracture of ceramics and its use to determine fracture energy and effective process zone length, *Journal of the American Ceramic Society*, **73**, 1841-1853
4. Bennati S., Fisicaro P., Valvo P.S., 2013a, An enhanced beam-theory model of the mixed-mode bending (MMB) test. Part I: Literature review and mechanical model, *Meccanica*, **48**, 443-462
5. Bennati S., Fisicaro P., Valvo P.S., 2013b, An enhanced beam-theory model of the mixed-mode bending (MMB) test. Part II: Applications and results, *Meccanica*, **48**, 465-484
6. Benzeggagh M.L., Kenane M., 1996, Measurement of mixed-mode delamination fracture toughness of unidirectional glass/epoxy composites with mixed-mode bending apparatus, *Composites Science and Technology*, **56**, 439-449
7. Camanho P.P., Dávila C.G., 2002, Mixed-mode decohesion finite elements for the simulation of delamination in composite materials, *Technical Report NASA/TM-2002-211737*, National Aeronautics and Space Administration, USA
8. de Moura M.F.S.F., Oliveira J.M.Q., Morais J.J.L., Xavier J., 2010, Mixed-mode I/II wood fracture characterization using the mixed-mode bending test, *Engineering Fracture Mechanics*, **77**, 144-152
9. Dourado N., Morel S., de Moura M.F.S.F., Valentin G., Morais J., 2008, Comparison of fracture properties of two wood species through cohesive crack simulations, *Composites Part A*, **39**, 415-427
10. Dugdale D.S., 1960, Yielding of steel sheets containing slits, *Journal of the Mechanics and Physics of Solids*, **8**, 100-104
11. Morel S., Dourado N., Valentin G., 2005, Wood: a quasibrittle material. *R*-curve behavior and peak load evaluation, *International Journal of Fracture*, **131**, 385-400
12. Mróz Z., Seweryn A., 1998, Non-local failure and damage evolution rule: Application to a dilatant crack model, *Journal of Physics IV*, **8**, 257-268

13. Novozhilov V.V., 1969, On the necessary and sufficient criteria for brittle strength, *Prikladnaja Matematika i Mekhanika*, **33**, 212-222

14. Oliveira J.M.Q., de Moura M.F.S.F., Silva M.A.L., Morais J.J.L., 2007, Numerical analysis of the MMB test for mixed-mode I/II wood fracture, *Composites Science and Technology*, **67**, 1764-1771

15. Pedersen M.U., Clorius C.O., Damkilde L., Hoffmeyer P., 2003, A simple size effect model for tension perpendicular to the grain, *Wood Science and Technology*, **37**, 125-140

16. Phan N.A., Morel S., Chaplain M., 2016, Mixed-mode fracture in a quasi-brittle material: *R*-curve and fracture criterion: Application to wood, *Engineering Fracture Mechanics*, **156**, 96-113

17. Reeder J.R., Crews J.H., 1990, Mixed-mode bending method for delamination testing, *AIAA Journal*, **28**, 1270-1276

18. Romanowicz M., 2019, A non-local stress fracture criterion accounting for the anisotropy of the fracture toughness, *Engineering Fracture Mechanics*, **214**, 544-557

19. Seweryn A., Mróz Z., 1998, On the criterion of damage evolution for variable multiaxial stress states, *International Journal of Solids and Structures*, **35**, 1589-1616

20. Sih G.C., Paris P.C., Irwin G.R., 1965, On cracks in rectilinearly anisotropic bodies, *International Journal of Fracture Mechanics*, **1**, 189-203

21. Wang Y., Williams J.G., 1992, Corrections for mode II fracture toughness specimens of composites materials, *Composites Science and Technology*, **43**, 251-256

22. Williams J.G., 1989, End corrections for orthotropic DCB specimens, *Composites Science and Technology*, **35**, 367-376

23. Xie D., Biggers S.B., 2006, Progressive crack growth analysis using interface element based on the virtual crack closure technique, *Finite Elements in Analysis and Design*, **42**, 977-984

24. Xie J., Waas A.M., Rassaian M., 2016a, Closed-form solutions for cohesive zone modeling of delamination toughness tests, *International Journal of Solids and Structures*, **88-89**, 379-400

25. Xie J., Waas A.M., Rassaian M., 2016b, Estimating the process zone length of fracture tests used in characterizing composites, *International Journal of Solids and Structures*, **100-101**, 111-126

Manuscript received October 30, 2022; accepted for print November 29, 2022

JOURNAL OF THEORETICAL AND APPLIED MECHANICS
61, 1, pp. 163-173, Warsaw 2023
https://doi.org/10.15632/jtam-pl/157510

RESEARCH ON CREEP-FATIGUE MODEL OF ANCHORED JOINTED ROCK MASS

Yang Song
Department of Architecture and Transportation, Liaoning Technical University, Fuxin, Liaoning Province, China
Bo Fan
Department of Civil Engineering, Liaoning Technical University, Fuxin, Liaoning Province, China
e-mail: 3577566424@qq.com
Yong-Qi Li
School of Civil and Transportation Engineering, Hebei University of Technology, Tianjin, China
He-Ping Wang
Department of Civil Engineering, Liaoning Technical University, Fuxin, Liaoning Province, China

To explore the mechanical response of anchored rock mass with an interaction of fatigue and creep, this paper selects the fatigue amplitude and fatigue frequency as influencing factors to carry out a fatigue-creep experiment of the anchored rock mass. Based on fractional order theory and binary perturbation theory, a new fractional order creep model is constructed. The results show that compared with the Burgers model, the newly proposed creep model can better describe the whole process of creep deformation of the anchored jointed rock mass under fatigue loading.

Keywords: shear creep, anchored jointed rock mass, fractional order, fatigue load, damage

1. Introduction

With in large-scale strategic engineering of deep rock mass in China, ensuring stability of a deep rock mass structure and preventing catastrophes have become the first priority. The existing research shows: Deep rock mass has obvious rheological characteristics, and it is very easy to aggravate its rheological state due to blasting, earthquake and other disturbances, thus causing instability and failure of deep rock mass (Feng *et al.*, 2022; Wiatowski *et al.*, 2021). Therefore, the influence of load on deep rock masses cannot be ignored.

In the recent years, many scholars have conducted a series of studies on rheological properties of rock mass: Chen *et al.* (2014) used acoustic emission testing (AE) to record creep behavior of granite at different temperatures, and proposed a creep model based on a damage mechanism. Fu *et al.* (2008) used CT testing technology to study microdamage evolution characteristics of mudstone under an impact disturbance load. Hu *et al.* (2019) carried out long-term compressive creep tests and numerical simulation tests on single-fractured sandstone by means of a single--stage loading, and established a creep model considering rock damage. Huang *et al.* (2017) established a disturbance factor function based on plastic deformation, and further established the evolution equation of the creep disturbance factor through change characteristics of plastic deformation with time. Liu and Zhang (2020) established a creep equation, considering dual effects of stress and time, by analyzing the deterioration law of creep parameters under the action of time. Nadimi and Shahriar (2014) attempted to predict a long-term creep parameter using triaxial creep tests and to define time-dependent characteristics of the bounding material. It was observed that the creep rate of a grouting material specimen directly depends on the

deviator of stress. Wu *et al.* (2020) proposed a variable-parameter fractional derivative element based on fractional theory, and developed a mathematical model describing rock shear creep.

The above research mainly analyzed the damage evolution law of rock under creep load (Chen *et al.*, 2013; Güneyisi *et al.*, 2016; Luo *et al.*, 2020). However, in the deep rock mass, creep deformation of rock will be aggravated under a fatigue load disturbance such as blasting and earthquake. At present, there are few reports on the research of this engineering phenomenon. Therefore, this paper studies the mechanical response of anchored jointed rock mass under creep--fatigue interaction, analyzes shear creep characteristics, and establishes a shear creep model by introducing fractional order theory and a binary disturbance principle.

2. Test overview

2.1. Experimental design

Marble is selected as a raw material for this test. First, marble is cut into a 100 mm×100 mm×50 mm rectangular block as the hanging wall and footwall of the joint test piece. Secondly, cement mortar (cement: river sand: water = 1:1.5:0.8) is selected for the joint part; it is used to bond the hanging wall and footwall. Third, the bolt adopts HRB335 steel with a yield strength of 335 MPa, and the grouting part adopts cement mortar. The test piece is shown in Fig. 1a.

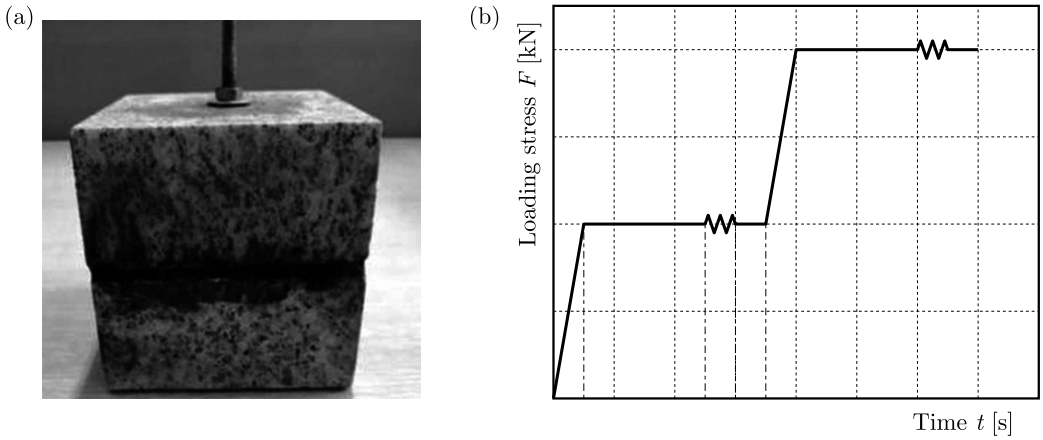

Fig. 1. Specimen and loading path: (a) specimen and (b) loading path

This experiment adopts the method of controlling variables. Creep fatigue tests were carried out for four fatigue frequencies of 0.02 Hz, 0.04 Hz, 0.06 Hz and 0.08 Hz and four fatigue amplitudes of 2 kN, 4 kN, 6 kN and 8 kN. The test grouping is shown in Table 1.

Table 1. Trial grouping

Influencing factors	Group	Fatigue amplitude [kN]	Fatigue frequency [Hz]
Fatigue amplitude	1-1	2	0.02
	1-2	4	0.02
	1-3	6	0.02
	1-4	8	0.02
Fatigue frequency	2-1	2	0.02
	2-2	2	0.04
	2-3	2	0.06
	2-4	2	0.08

2.2. Loading scheme

The shear device of a TAW2000 triaxial tester is utilized in this test. As a step-by-step loading can avoid the discrete phenomenon of the test results, the shear creep test of the anchored jointed rock mass is carried out by a step loading in this test. The loading path is shown in Fig. 1b. The specific loading steps are listed as follows:

(1) Normal load: Apply the normal stress to the test piece at a loading rate of 0.05 MPa/s and keep the normal load unchanged when the normal stress reaches the established stress level of 0.2 MPa.
(2) Creep load: Based on the direct shear test, the primary shear stress is determined to be 0.1 MPa. When the creep load reaches the predetermined value of 0.1 MPa, the load remains constant for a certain period. Afterward, the creep shear stress of each stage increases by 0.1 MPa.
(3) Fatigue load: According to the experimental groups shown in Table 1, the fatigue load is applied after the creep of each load level in the test piece. The loading path is shown in Fig. 1b.

3. Test overview

3.1. Test curve analysis

Through sorting and analyzing the test data, the data with typical curve characteristics are selected and plotted as shown in Figs. 2 and 3. In this study, the stress threshold of creep failure refers to the stress value at the time of failure in the process of creep. The following results can be obtained from the figures.

When the fatigue amplitude is increased from 2 kN to 8 kN, the creep failure stress thresholds of the specimen are 0.56 MPa, 0.50 MPa, 0.45 MPa and 0.40 MPa in turn, and the degrees of decline were 9.28%, 18.73% and 28.19%. When the fatigue frequency is increased from 0.02 Hz to 0.08 Hz, the creep failure stress thresholds of the specimen are 0.56 MPa, 0.50 MPa, 0.46 MPa and 0.40 MPa in turn, and the degrees of decline of the creep failure stress threshold are 9.60%, 18.17% and 28.14%, respectively, as shown in Fig. 2. The creep failure stress thresholds for the two groups of specimens show a linear decreasing trend, and the degree of decline is similar. This finding shows that the sensitivities of the fatigue amplitude and fatigue frequency to the creep failure stress threshold of the anchored jointed rock mass are equivalent.

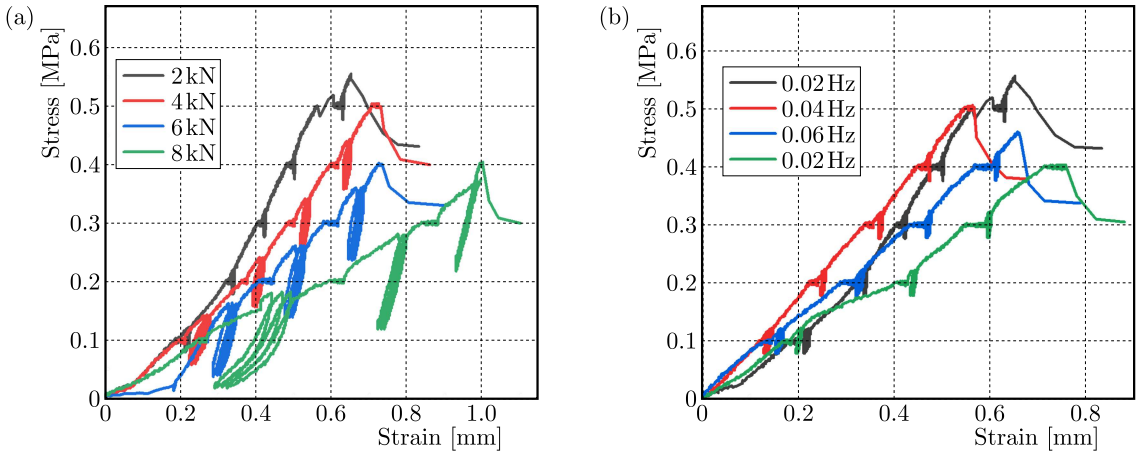

Fig. 2. Stress-strain curve: (a) fatigue amplitude and (b) fatigue frequency

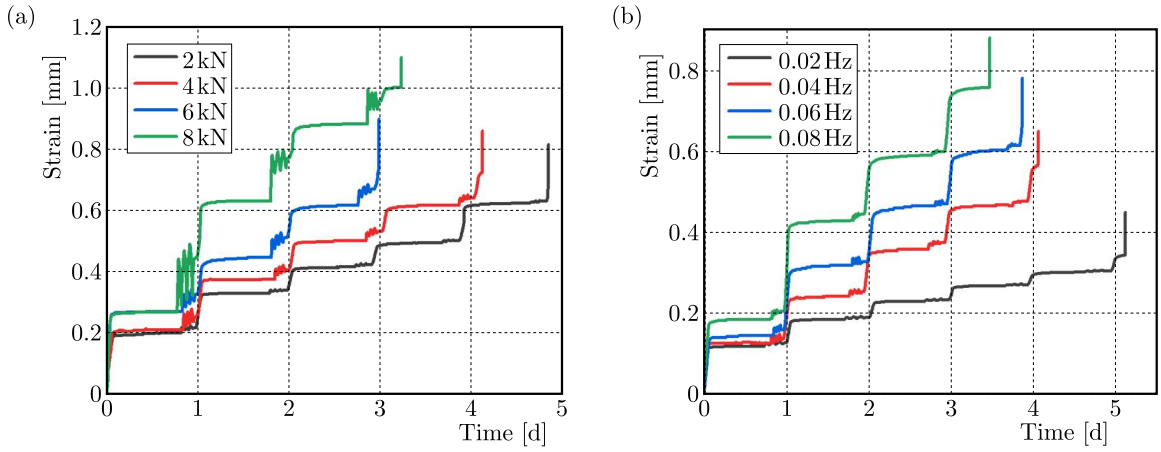

Fig. 3. Strain time history curve: (a) fatigue amplitude and (b) fatigue frequency

According to Fig. 3, the change trend of the shear creep fatigue curve with different fatigue factors, which is similar, can be divided into four stages: attenuation creep stage, stable creep stage, fatigue creep stage and accelerated creep stage. When the fatigue amplitude is increased from 2 kN to 8 kN, and the fatigue frequency is increased from 0.02 Hz to 0.08 Hz, the speed of the specimen entering the accelerated creep stage is obviously accelerated. Specifically, when the influence factor is the fatigue amplitude, the failure time of the specimen decreases from 4.83d to 2.98d, with a decrease of 38.30%. When the influence factor is the fatigue frequency, the failure time of the specimen decreases from 5.12d to 3.47d, with a decrease of 32.22%.

3.2. Isochronal shear stress-strain curves

According to the stress-strain curve, the strain-time history curve and the Boltzmann superposition principle, isochronous curve clusters of shear stress-strain of the specimen are drawn. The time intervals of the curves are 0.0d, 0.2d, 0.4d and 0.6d. Thus, the long-term strength for accelerated creep deformation of the specimen with different fatigue amplitudes is determined, where 0d is the relative starting time when each level of shear stress is applied. Due to the limited scope of the article, only isochronous curve clusters with a fatigue amplitude of 4 kN and a fatigue frequency of 0.04 Hz are given, as shown in Fig. 4.

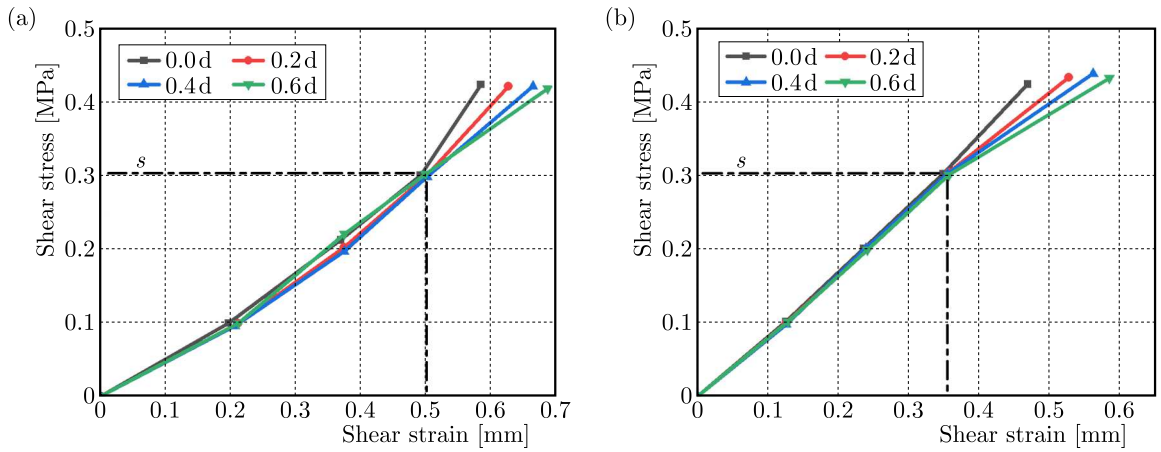

Fig. 4. Stress-strain isochronous curve cluster: (a) 4 kN and (b) 0.04 Hz

When the fatigue amplitudes are 2 kN, 4 kN, 6 kN and 8 kN, the corresponding long-term strengths of the test piece are 0.403 MPa, 0.300 MPa, 0.199 MPa and 0.202 MPa. When the

fatigue frequency is increased from 0.02 Hz to 0.08 Hz, the corresponding long-term strengths of the specimen are 0.403 MPa, 0.302 MPa, 0.298 MPa and 0.300 MPa. These results conclude that the long-term strength of the specimen shows an initially decreasing and then stabilizing trend. The main reason is that when the fatigue load is at a low level, it can promote rapid development of internal cracks of the specimen, thereby reducing the long-term strength of the specimen. When the fatigue amplitude is large, the specimen can quickly form through cracks and, simultaneously, the strength of the joint part is weakened to a great extent so that the shear strength of the specimen is mainly provided by the anchor bolt. Therefore, the long-term strength of the specimen will be stabilized.

3.3. Equivalent Shear Modulus

To further evaluate creep mechanical properties of the anchored jointed rock mass under fatigue loading, the concept of Equivalent Shear Modulus is proposed in this paper. Namely, the equivalent shear modulus is the ratio of shear stress to shear strain corresponding to the long-term strength of the specimen. Equivalent Shear Modulus can be obtained by sorting and analysing the stress-strain isochronous cluster curve data. To quantitatively evaluate the change law of Equivalent Shear Modulus, the author uses the Origin software to fit the data; the fitting curve is shown in Fig. 5. Under the action of different fatigue amplitudes and fatigue frequencies, the change law of Equivalent Shear Modulus of the specimen shows a downward quadratic curve. When the influence factor is the fatigue amplitude, Equivalent Shear Modulus of the specimen decreases from 0.827 MPa to 0.321 MPa, with a decrease of 61.18%. When the influence factor is the fatigue frequency, the long-term shear modulus of the specimen decreased from 0.827 MPa to 0.519 MPa, with a decrease of 37.24%. Under the effect of fatigue amplitude, Equivalent Shear Modulus decreases more sharply. Therefore, the fatigue amplitude is more sensitive to Equivalent Shear Modulus of the specimen.

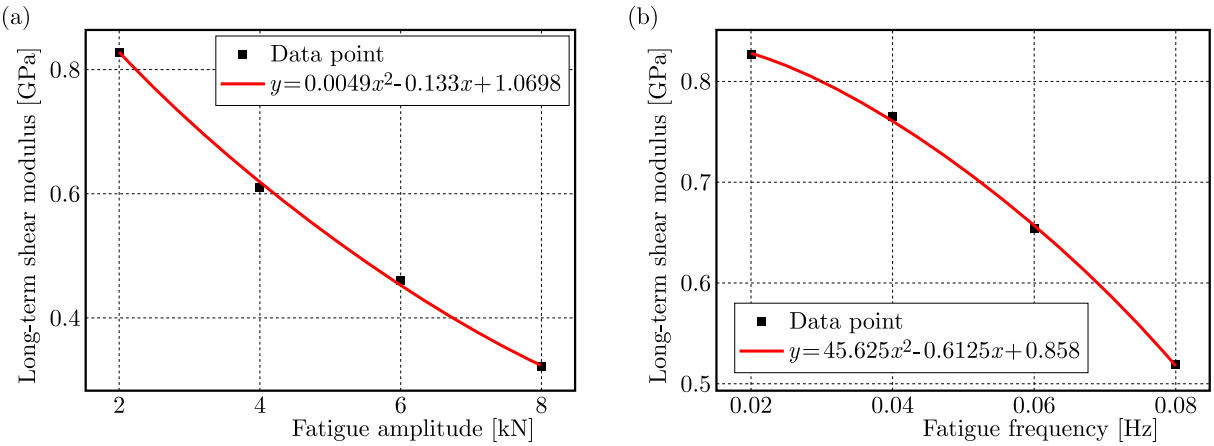

Fig. 5. Fitting curve: (a) fatigue amplitude, (b) fatigue frequency

3.4. Failure mode of joint surface

Figure 6 is the typical failure mode of the joint surface during the test. It can be seen from the figure that, with an increase of fatigue load, the influence of shear stress on the joint surface gradually increases, which makes the crack gradually expand from one end to both ends, specifically, the crack shape of the joint surface changes from V to X.

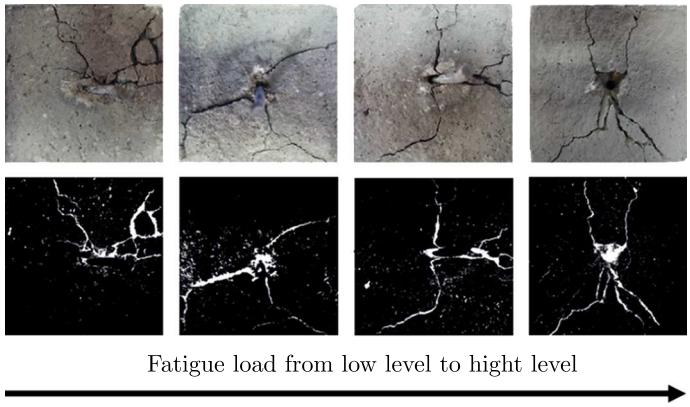

Fig. 6. Failure diagram of joint surface

4. Establishment of the shear creep model

4.1. Abel element

As fractional order theory can solve complex mechanical models, an increasing number of scholars worldwide have tried to apply fractional calculus theory to research of rock rheological models in recent years. The most commonly utilized definition of fractional calculus is the definition method of Riemann-Liouville (R-L) fractional calculus (Chen *et al.*, 2010), which is defined as follows: the function f is piecewise continuous in the interval $(0,+\infty)$, and it is integrable in any subinterval of $(0,+\infty)$

$$\frac{d^{-\gamma}f(t)}{dt^{-\gamma}} = \frac{1}{\Gamma}\int_0^t (t-\xi)^{\gamma-1} f(\xi)\, d\xi \tag{C.1}$$

It is known that the ideal elastic body satisfies Hooke's law, while the Newtonian fluid satisfies Newton's law. Based on the above theory, we can estimate the rheological element

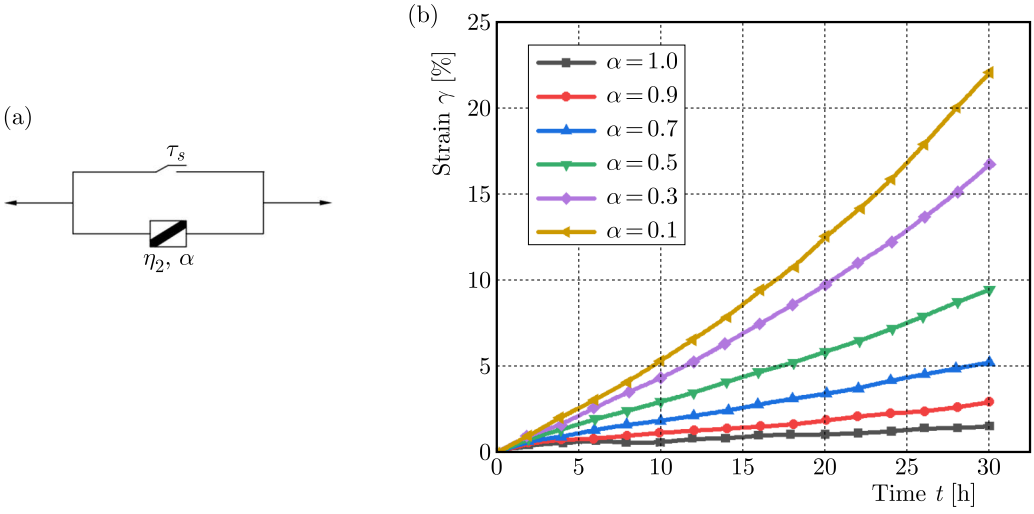

Fig. 7. Abel element: (a) Abel element, (b) creep curve

(Abel element) between the ideal elastomer and the Newtonian fluid, as shown in Fig. 7a. The constitutive relation may satisfy

$$\tau(t) = \eta\frac{d^{\alpha}\gamma(t)}{dt^{\alpha}} \qquad \gamma(t) = \frac{\tau}{\eta}\frac{t^{\alpha}}{\Gamma(\alpha+1)} \qquad 0<\alpha<1 \tag{C.2}$$

where $\gamma(t)$ is the shear strain, $\tau(t)$ is the shear stress, η is the viscosity coefficient, and α is the derivative order.

As is apparent from Fig. 7b, when the derivative order decreases, the slope of the curve gradually increases. This phenomenon is consistent with the characteristics of the accelerated creep stage of soft rock, which shows that the smaller the derivative order is, the easier it is for the Abel element to characterize the accelerated creep stage of soft rock.

4.2. Damage function

Desai and Zhang (1998) proposed a concept of the relative disturbance state. This theory can provide a unified theoretical basis for elastic, plastic and creep deformation, microcracks, damage and softening, hardening and cyclic fatigue. Based on this theory, Desai proposed theory of duality disturbance (TDD). He suggests that engineering materials gradually change from a relatively undisturbed dynamic state to a relatively completely disturbed dynamic state through self-regulation of microcrack structures, producing a mixed response. This approach is not considered by classical damage theory. Therefore, the theory of duality disturbance can be applied to better describe the damage of rock mass under a complex stress state. The basic equation is

$$\sigma^0 = (1-D)\sigma^n + D\sigma^c \qquad d\sigma^0 = (1-D)d\sigma^n + dD\sigma^c - dD(\sigma^n - \sigma^c) \tag{C.3}$$

where 0, n, and c represent the apparent state, relatively undamaged state and relatively completely damaged state, respectively. D is the disturbance function and it is a measure of the degree of disturbance. Since the internal mechanism of the disturbance is not clear, for the sake of simplification and application, it is assumed that it is only related to a certain internal variable f. For typical elastoplastic materials, it is assumed to be related to the equivalent shear modulus. And it is usually represented by Weibull curves

$$D = D(f) = D_u\sigma^c[1 - \exp(-Af^B)] \tag{C.4}$$

where D_u is the ultimate fatigue damage variable, usually taken as 1, A and B are material related constants, f is the equivalent shear modulus.

From Section 3.3, under the action of different fatigue amplitudes and fatigue frequencies, the long-term shear modulus of the anchor body changes in a quadratic curve, as shown in Fig. 5. The specific expression of the equivalent shear modulus is

$$f = ax^2 + bx + c \tag{C.5}$$

where a, b, c are correlation coefficients.

4.3. Fractional damage creep model

The anchored jointed rock mass is a composite material body, and its internal stress distribution is extremely complex and changeable. To simplify the stress calculation process, the bolt, joint and rock mass are regarded as a unified whole, and we only consider the macroscopic mechanical response of the jointed rock mass with anchors. As we know, the classical rheological model can better characterize decay creep and stable creep, but it lacks a quantitative description of the accelerated creep stage of soft rock. This problem is also an urgent problem to be solved.

According to the investigation, the generalized Kelvin model has characteristics of instantaneous deformation, attenuation creep and elastic aftereffect, and it can better characterize viscoelastic rock with attenuation creep and stable creep properties. As described in Section 3.1, the Abel element is a rheological element between the elastic element and the Newtonian element. The rheological rate of the Abel element gradually increases with the decreasing derivative

order. Therefore, the Abel element can effectively represent the accelerated creep stage of the rock mass. To establish a creep model capable of characterizing the acceleration stage of soft rock, the author concatenates the generalized Kelvin style with Abel elements to establish a new fractional shear creep model. In this model, the long-term strength serves as the accelerated creep stress threshold. When the shear stress is less than the long-term strength, the new model degenerates into the generalized Kelvin one. A schematic of the model is shown in Fig. 8. The creep equation of the fractional order creep model is expressed as follows

$$\gamma = \begin{cases} \dfrac{\tau}{G_1} + \dfrac{\tau}{G_2}\Big[1 - \exp\Big(-\dfrac{G_2}{\eta_1}t\Big)\Big] & 0 < \tau < \tau_s \\ \dfrac{\tau}{G_1} + \dfrac{\tau}{G_2}\Big[1 - \exp\Big(-\dfrac{G_2}{\eta_1}t\Big)\Big] + \dfrac{\tau - \tau_s}{\eta_2}\dfrac{t^\alpha}{\Gamma(\alpha+1)} & \tau \geqslant \tau_s \end{cases} \tag{C.6}$$

With the interaction of fatigue and creep, the shear modulus of the anchored jointed rock mass is bound to decay with the continuous expansion of cracks. As previously mentioned, the long-term shear modulus of the specimen shows a quadratic curve decay trend with the increasing fatigue load. Therefore, the author establishes a damage factor by combining binary disturbance theory and damage theory to characterize the process of the specimen gradually changing from a relatively undisturbed dynamic state to a relatively completely disturbed dynamic state. The fractional creep constitutive equation considering damage is expressed as follows

$$\gamma = \begin{cases} (1-D)\Big\{\dfrac{\tau}{G_1} + \dfrac{\tau}{G_2}\Big[1 - \exp\Big(-\dfrac{G_2}{\eta_1}t\Big)\Big]\Big\} & 0 < \tau < \tau_s \\ (1-D)\Big\{\dfrac{\tau}{G_1} + \dfrac{\tau}{G_2}\Big[1 - \exp\Big(-\dfrac{G_2}{\eta_1}t\Big)\Big]\Big\} + D\dfrac{\tau - \tau_s}{\eta_2}\dfrac{t^\alpha}{\Gamma(\alpha+1)} & \tau \geqslant \tau_s \end{cases} \tag{C.7}$$

where there are shear moduli of the elastic body and viscosity coefficients.

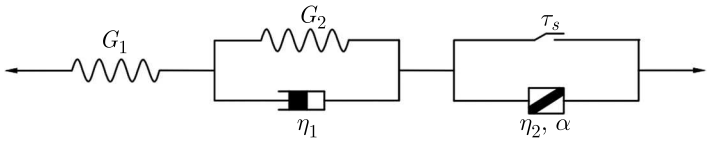

Fig. 8. Schematic of the nonlinear fractional Burgers model

4.4. Parameter identification

To solve the relevant parameters of the fractional damage creep model, this paper mainly adopts the segmented solution method to process the experimental data. Now, the solution method of the model at different shear stress levels is given:

(1) The first step is to judge the long-term strength of the specimen under different fatigue loads. The long-term strength can be determined according to the isochronous stress-strain curve cluster, as shown in Section 3.2.

(2) The second step is to determine the damage function. First, we can fit and determine the value of damage functions $f = ax^2 + bx + c$, as shown in Section 3.3. Then, according to the research results of Deng *et al.* (2017), we determine the damage variable parameters A and B.

(3) The mathematical expression of the nonlinear fractional model, Eqs. (4.7), is programmed into the Origin software, and the Levenberg-Marquardt method is used to fit the rheological parameters of the nonlinear fractional model for the test data of each stress level, so as to determine values of G_1, G_2, η_1, η_2, α.

To verify the accuracy of the model, the author selects a group of experimental data from the two variables of the fatigue amplitude and fatigue frequency and solves the relevant parameters according to the above steps. The fitting results are shown in Fig. 9 and Table 2. The results show that the fractional damage model proposed in this paper can fit the accelerated creep stage of the anchored jointed rock mass better than the Burgers model, which indicates that the model can better reflect the overall shear creep process of the anchored jointed rock mass under different fatigue loads.

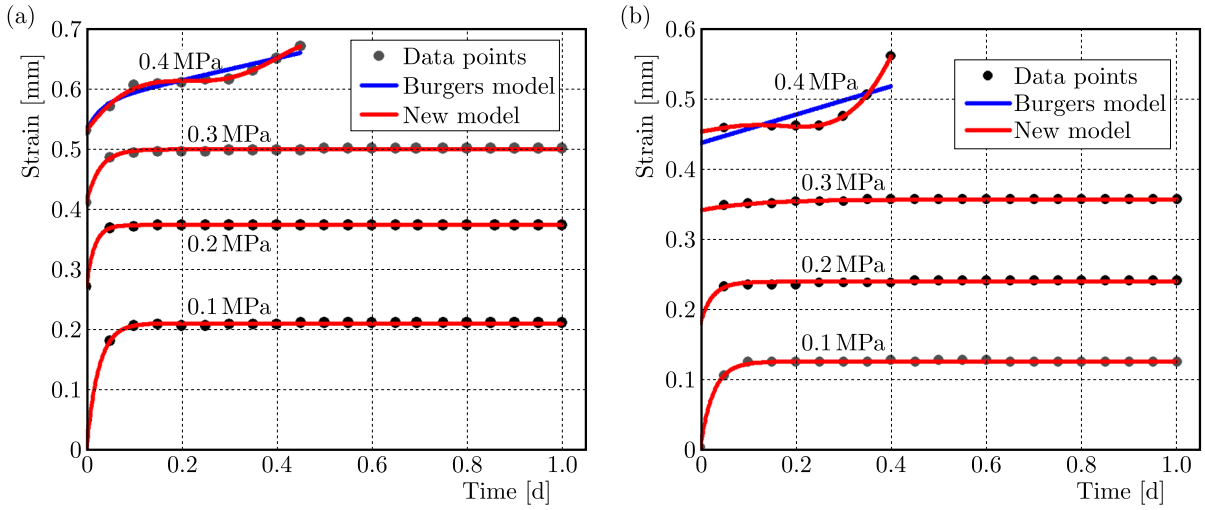

Fig. 9. Schematic of the fitting curve: (a) 4 kN and (b) 0.04 Hz

Table 2. Summary of model parameters

	Grading	G_1	G_2	η_1	A	B	a	b	c	η_2	α	R^2
4 kN	1	1.89	49.53	0.71	0.42	5.69	0.49	−0.13	1.07	–	–	0.99
	2	2.11	72.44	0.46	0.44	4.59	0.49	−0.13	1.07	–	–	0.97
	3	2.61	19.64	0.82	0.56	4.76	0.49	−0.13	1.07	–	–	0.97
	4	4.95	41.22	0.44	0.76	5.68	0.49	−0.13	1.07	1.27	0.29	0.92
0.04 Hz	1	1.98	13.56	0.72	0.56	1.26	0.46	−0.61	0.86	–	–	0.96
	2	2.66	49.55	0.29	0.36	1.34	0.46	−0.61	0.86	–	–	0.95
	3	3.14	14.03	0.46	0.34	4.23	0.46	−0.61	0.86	–	–	0.95
	4	5.21	47.59	0.39	0.12	1.35	0.46	−0.61	0.86	1.49	0.34	0.93

5. Conclusion

To reveal the accelerating effect of low cycle fatigue loads such as earthquakes and blasting on the shear creep instability of deep rock mass, we adopt the control variable method to investigate the effect of different fatigue amplitudes and fatigue frequencies on the creep characteristics of the rock mass with anchored joints. According to the experimental results, we use the Abel element to characterize the accelerated creep stage and simulate the transition process of the specimen from a relatively undisturbed dynamic state to a relatively fully disturbed dynamic state with the theory of duality disturbance. The conclusions are summarized as follows:

- A comparison of the shear creep stress-strain curves of the anchored jointed rock mass with different influence factors reveals that the creep failure stress threshold of the specimen linearly decreases with the increasing fatigue amplitude and fatigue frequency. The

sensitivity of the two to the creep failure stress threshold is equivalent, which indicates that the fatigue load has an obvious accelerating effect on the anchored jointed rock mass.

- To evaluate the macro performance of the anchored jointed rock mass, we propose a concept of the long-term shear modulus. Through the Origin software fitting, it is determined that the long-term shear modulus of the specimen decreases in a quadratic curve with the increasing fatigue amplitude and fatigue frequency. The difference between them is that the fatigue amplitude is more sensitive to the long-term shear modulus of the specimen, and the decrease is larger.
- In this paper, we connect the generalized Kelvin model and the Abel element in series. Combined with the theory of duality disturbance, a nonlinear fractional order creep model is constructed, which can describe the transition process of the anchored jointed rock mass from a relatively undisturbed to relatively fully disturbed state. Compared with the Burgers model, this model can well simulate the whole process of three stages of rock specimens: attenuation creep, stable creep and accelerated creep

Acknowledgments

The research described in this paper was financially supported by the National Natural Science Foundation (51974146, 52174078), Liaoning Natural Science Foundation (2019-ZD-0042) and Innovative Talents Support Program for Universities in Liaoning Province (21-1071).

References

1. Cao P., Wen Y., Wang Y., Yuan H., Yuan B., 2016, Study on nonlinear damage creep constitutive model for high-stress soft rock, *Environmental Earth Sciences*, **15**, 4, 75-90
2. Chen H.J., Xu W.Y., Wang W., Wang R., Shi C., 2013, A nonlinear viscoelastic-plastic rheological model for rocks based on fractional derivative theory, *International Journal of Modern Physics, B*, **27**, 25, 135-149
3. Chen L., Wang C.P., Liu J.F., Liu Y.M., Liu J., Su R., Wang J., 2014, A damage-mechanism-based creep model considering temperature effect in granite, *Mechanics Research Communications*, **56**, 2, 76-82
4. Chen W., Sun H.G., Li X.C., 2010, *Fractional Derivative Modeling of Mechanics and Engineering Problems*, Beijing: Science Press
5. Deng H.-F., Hu A.-L., Li J.-L., Zhang X.-J., Hu Y., Chang D.-L., Zhu M., 2017, Statistical constitutive model of sandstone degradation damage under water-rock action, *Rock and Soil Mechanics*, **38**, 3, 631-639
6. Desai C.S., Zhang W., 1998, Computational aspects of disturbed state constitutive models, *Computer Methods in Applied Mechanics and Engineering*, **151**, 3-4, 361-376
7. Feng F., Chen S., Zhao X., Li D., Wang X., Cui J., 2022, Effects of external dynamic disturbances and structural plane on rock fracturing around deep underground cavern, *International Journal of Coal Science and Technology*, **9**, 1, 15-27
8. Fu Z.L., Guo H., Gao Y.F., 2008, Creep damage characteristics of soft rock under disturbance loads, *Journal of Earth Science*, **19**, 3, 292-297
9. Güneyisi E., Gesoglu M., Naji N., Ipek S., 2016, Evaluation of the rheological behavior of fresh self-compacting rubberized concrete by using the Herschel-Bulkley and modified Bingham models, *Archives of Civil and Mechanical Engineering*, **16**, 1, 9-19
10. Hu B., Yang S., Xu P., Tian W., 2019, Time-scale effect of the creep model parameters and particle flow simulation of sandstone with a single crack, *Chinese Journal of Geotechnical Engineering*, **41**, 5, 864-873

11. Huang M., Jiang Y., Wang S., Deng T., 2017, Identification of the creep model and its parameters of soft rock on the basis of disturbed state concept, *Chinese Journal of Solid Mechanics*, **38**, 6, 570-578

12. Li S.H., Zhu W.C., Niu L.L., Yu M., Chen C.F., 2018, Dynamic characteristics of green sandstone subjected to repetitive impact loading: phenomena and mechanisms, *Rock Mechanics and Rock Engineering*, **51**, 1921-1936

13. Liu W., Zhang S., 2020, Research on rock creep model based on dual effects of stress and time, *Journal of Central South University*, **51**, 8, 2256-2265

14. Luo F., Zhang y., Zhu Z., 2020, Creep constitutive model for frozen sand of Qinghai-Tibet Plateau, *Journal of Harbin Institute of Technology*, **52**, 2, 26-32

15. Nadimi S., Shahriar K., 2014, Experimental creep tests and prediction of long-term creep behavior of grouting material, *Arabian Journal of Geosciences*, **7**, 8, 3251-3257

16. Song Y., Li Y.Q., Wang W.Y., *et al.*, 2020, Shear creep characteristics and constitutive model analysis of jointed rock mass, *Journal of China Coal Society*, **45**, 4, 1357-1366

17. Szkudlarek Z., Janas S., 2021, Active protection of work area against explosion of dust-gas mixture, *International Journal of Coal Science and Technology*, **8**, 4, 674-684

18. Wang C., Chen L., Liang J., Liu J., 2014, Creep constitutive model for full creep process of granite considering thermal effect, *Rock and Soil Mechanics*, **35**, 9, 2493-500+506

19. Wei L., Zhu Z., Meng Q., 2019, Dynamic characteristics of marble damaged by cyclic loading, *Explosion and Shock Waves*, **39**, 8, 63-73

20. Wiatowski M., Muzyka R., Kapusta K., Chrubasik M., 2021, Changes in properties of tar obtained during underground coal gasification process, *International Journal of Coal Science and Technology*, **8**, 5, 1054-1066

21. Wu L.Z., Luo X.H., Li S.H., 2020, A new model of shear creep and its experimental verification, *Mechanics of Time-Dependent Materials*, **25**, 429-446

Manuscript received September 12, 2022; accepted for print October 24, 2022

JOURNAL OF THEORETICAL AND APPLIED MECHANICS
61, 1, pp. 175-187, Warsaw 2023
https://doi.org/10.15632/jtam-pl/158574

ON THE YIELD SURFACE OF A TYPICAL BENDING-DOMINANT PERIODIC LATTICE METAMATERIAL

Yongjun Wang, Jinxing Liu

Faculty of Civil Engineering and Mechanics, Jiangsu University, Zhenjiang, China

Corresponding author Jinxing Liu, e-mail: jxliu@mails.ucas.ac.cn

A theoretical method for analyzing the initial yield of a typical bending-dominant periodic lattice (BDPL) is established. Based on the principle of strain energy equivalence, the macroscopic effective stiffnesses of lattices are calculated. An empirical formula is employed to consider the contributions of both the axial force and bending moment. The initial yield surface of BDPL can be figured out by comparing the effective stress of each strut to the yield strength of the matrix material. The method is applicable to various BDPLs, which we believe is a helpful extension to the method for lattices comprising axial-tension bars in the literature.

Keywords: bending-dominant periodic lattice (BDPL), yield, metamaterial, strain energy equivalence

1. Introduction

With recent developments of additive manufacturing technologies, lattice metamaterials have been attracting more and more attentions from both industry and academia. It is a promising option in designs of metamaterials to choose lattice-type microstructures. Lattice materials can be divided into two types: stretching-dominant lattice and bending-dominant lattice (Deshpande *et al.*, 2001). Stretching-dominant lattices are famous for lightweight, high specific strength and stiffness (Evans *et al.*, 2001; Evans, 2001) and have been applied in many areas. Unlike stretching--dominant lattices, the bending-dominant lattices are used to provide other extraordinary mechanical properties such as negative Poisson's ratio (Chen *et al.*, 2017), compression-induced twist (Frenzel *et al.*, 2017), negative effective swelling (Liu *et al.*, 2016) and so on.

The macroscopic effective yield strength of lattice materials is an important index to evaluate its mechanical performance. It is also considered that yield behavior is a failure precursor of lattice materials and it plays a significant role in engineering designs. Thus, a comprehensive understanding on the yield behavior is of great necessity. An analytical initial yield surface equation of the octet-truss lattice material, which is a typical stretching-dominant lattice, was established by Deshpande *et al.* (2001). Wang and McDowell (2004, 2005) made a detailed theoretical derivation of six kinds of two-dimensional beam lattice structures and gave corresponding initial yield surfaces under both biaxial and triaxial stresses. Yield behavior of a range of honeycombs under uniaxial loads have also been investigated so far (Gibson, 2003; Wang and McDowell, 2005). Xue *et al.* (2005) proposed a phenomenological elliptic yield surface criterion based on the yield strength of stressing in different directions. Fan and Yang (2006) deduced three-dimensional yield surfaces of several stretching-dominant lattice materials.

To date, unlike stretching-dominant lattices, yield properties of BDPLs have been rarely reported. It can be imagined that BDPLs can have a very different yield response when compared with the stretching-dominant lattices because of the coupling of axial deformation and bending

deformation. This is our present focus. We assume that the in-plane (xy plane) deformation can be taken as a plane strain problem.

This paper is structured as follows. In Section 2, a new method used to investigate the yield behavior of BDPL is briefly presented. In Section 3, based on the principle of strain energy equivalence (PSEE) and finite element simulation, we obtain the constitutive equation of BDPL. The geometry equation is derived in Section 4. In Section 5, the stiffness matrix of a unit cell is calculated. The initial yield surfaces of BDPL are obtained in Section 6. The paper ends with conclusions in Section 7.

2. Material and methods

2.1. Material

The schematic diagram of BDPL is shown in Fig. 1a. Based on the previous work (Wang *et al.*, 2020), we adopt a specimen with an enough number of cells to reduce the influence of boundary conditions. Geometric parameters T, H and W the thickness, height and width of BDPL, respectively. The unit cell is shown in Fig. 1b, which is composed of four curved bars with the same curvature radius r and central angle α. For each strut, its thickness is b and the spacing between two ends is L. The dimensions of BDPL are as follows: $H = W = 100\,\text{mm}$, $T = 10\,\text{mm}$, $b = 1\,\text{mm}$, $L = 4.762\,\text{mm}$ and the central angle $\alpha = 60°$. The adopted matrix material is Aluminum, with density $\rho = 2700\,\text{kg/m}^3$, Young's modulus E and Poisson's ratio ν 70 GPa and 0.33, respectively, and yield strength $\sigma_Y = 110\,\text{MPa}$.

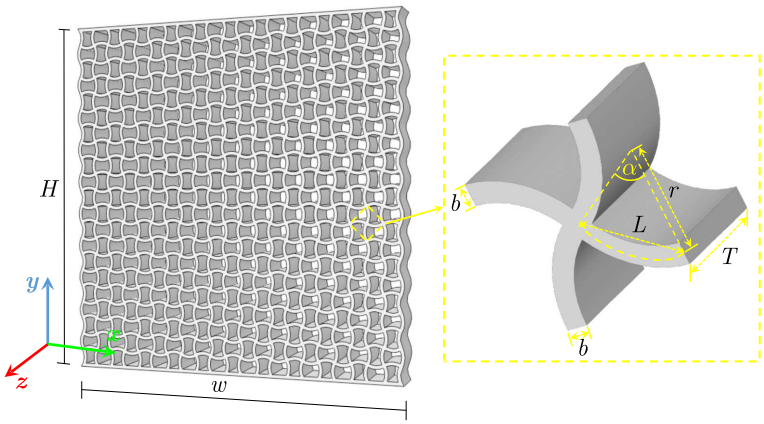

Fig. 1. Schematic of the lattice: (a) the whole structure and (b) the unit cell

2.2. Methods

The present research roadmap is shown in Fig. 2. Based on the principle of strain energy equivalence, the macroscopic effective stiffnesses of the lattice are calculated. The relation between the displacements of lattice joints and the macroscopic uniform strain prescribed can be obtained by combining a method of particular displacement fields (MPDF) and finite element analyses. Furthermore, by analyzing the relation between deformation and stress of a single periodic unit cell, forces on both ends of each curved strut can be expressed as a linear function of the macroscopic stresses. An empirical formula for calculating the effective stress is employed to consider the contributions of both the axial force and bending moment. Finally, the initial yield surface of BDPL can be figured out by comparing the effective stress of each curved strut to the yield strength of the matrix material.

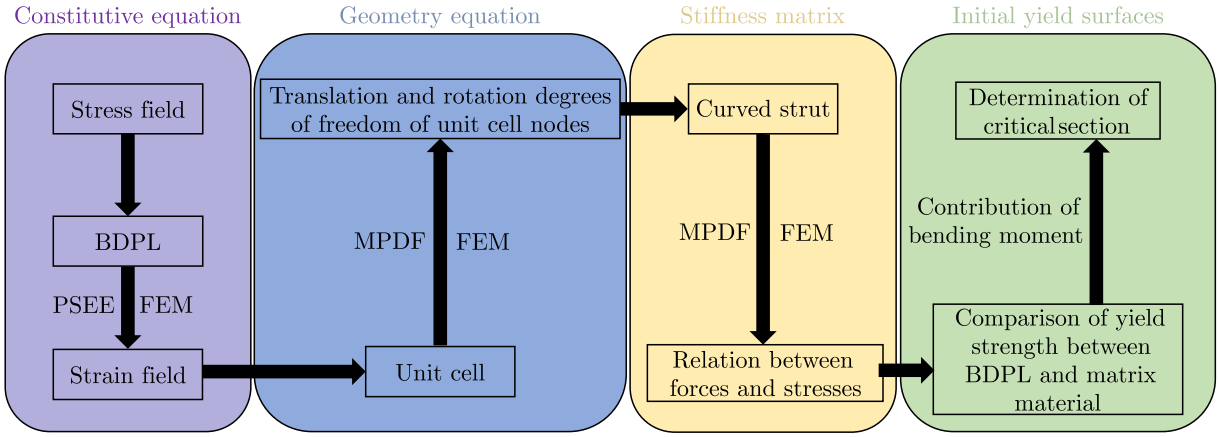

Fig. 2. The present research roadmap

3. Constitutive equation

A representative unit cell is used to replace BDPL, as shown in Fig. 3. The effective modulus of elasticity of BDPL is calculated by using an equivalent uniform medium with the same effective mechanical properties. This equivalence is established by equalizing the strain energies of two media (discrete and continuous) under the same loading and boundary conditions. Usually, a uniform strain field is prescribed for simplicity. According to the principle of strain energy equivalence, we have

$$U_{discrete} = U_{continuum} \tag{C.1}$$

The strain energy of the discrete unit cell is expressed as

$$U_{discrete} = \sum_{i=1}^{n} U^i \tag{C.2}$$

where U^i represents the energy stored in the i-th curved strut, n stands for the total number of struts in a single unit cell. The strain energy of the equivalent continuum is written as

$$U_{continuum} = \frac{1}{2} \int_V \sigma\varepsilon \, dV \tag{C.3}$$

It is notable that in Eq. (3.3), $V = At$ under the assumed plane strain condition, and the integral over V is actually over A. This meaning for volume V remains unchanged throughout this article.

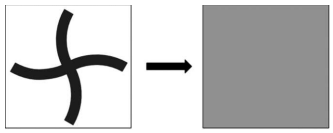

Fig. 3. Geometry of discrete and continuum unit cells

Under the plane stress conditions, the continuum constitutive equation is given in terms of the effective stiffness matrix C_{ij} by

$$\begin{Bmatrix} \sigma_{11} \\ \sigma_{22} \\ \sigma_{12} \end{Bmatrix} = \begin{bmatrix} C_{11} & C_{12} & 0 \\ C_{21} & C_{22} & 0 \\ 0 & 0 & C_{66} \end{bmatrix} \begin{Bmatrix} \varepsilon_{11} \\ \varepsilon_{22} \\ \varepsilon_{12} \end{Bmatrix} \tag{C.4}$$

where the elastic constants C_{11}, C_{22}, C_{12} and C_{21} in the matrix are calculated by finite element simulations one by one by prescribing proper uniform strain ε_{ij} fields. The designated displacements on the boundaries are given by

$$u_i = \varepsilon_{ij} X_j \qquad i,j = 1,2 \tag{C.5}$$

and X_i represents the coordinate of the boundary. Considering $C_{12} = C_{21}$, the strain energy of continuum is written as

$$U = \frac{V}{2}\sigma_{ij}\varepsilon_{ij} = [C_{11}(\varepsilon_{11})^2 + C_{22}(\varepsilon_{22})^2 + C_{66}(\varepsilon_{12})^2 + 2C_{12}(\varepsilon_{11})(\varepsilon_{22})] \tag{C.6}$$

Equation (3.6) can be numerically determined once the corresponding strain energy is obtained from finite element examples. For example, under the loading conditions shown in Fig. 4a, namely ε_{11} is specified and $\varepsilon_{22}, \varepsilon_{12} = 0$, the strain energy can be expressed as

$$U = \frac{V}{2}C_{11}(\varepsilon_{11})^2 \tag{C.7}$$

from which, the elastic constant C_{11} can be obtained. Similarly, the other elastic constants C_{22}, C_{12} and C_{66} can also be obtained by various specific finite element examples:
— for C_{22}: $\varepsilon_{11} = \varepsilon_{12} = 0$, $\varepsilon_{22} =$ const

$$U = \frac{V}{2}C_{22}(\varepsilon_{22})^2 \tag{C.8}$$

— for C_{12}: $\varepsilon_{11} =$ const , $\varepsilon_{12} = 0$, $\varepsilon_{22} =$ const

$$U = \frac{V}{2}[C_{11}(\varepsilon_{11})^2 + C_{22}(\varepsilon_{22})^2 + 2C_{12}(\varepsilon_{11})(\varepsilon_{22})] \tag{C.9}$$

— for C_{66}: $\varepsilon_{11} = \varepsilon_{22} = 0$, $\varepsilon_{12} =$ const

$$U = \frac{V}{2}C_{66}(\varepsilon_{12})^2 \tag{C.10}$$

Once the values of C_{11}, C_{22}, C_{12} and C_{66} are obtained, Young's modulus and Poisson's ratio of BDPL can be given as

$$\begin{aligned} E_1 &= \frac{C_{11}C_{22} - C_{12}^2}{C_{22}} \qquad E_2 = \frac{C_{11}C_{22} - C_{21}^2}{C_{11}} \\ \nu_{12} &= \frac{C_{12}}{C_{22}} \qquad \nu_{21} = \frac{C_{21}}{C_{11}} \end{aligned} \tag{C.11}$$

The finite element software Abaqus is used to simulate the response of lattice plates under above various boundary conditions. The BDPL plate has 21 curved struts along horizontal and vertical directions respectively. Element B21 with a mesh sweeping seed size of 0.1 mm was employed for simulations. Each strut between joints is divided into 10 beam elements to ensure the accuracy of simulation results, which is confirmed by comparing with the results under finer 15 elements per strut (error less than 1%). The parameter setting mentioned in Section 2.1 is employed. In the following, we list out the boundary conditions for calculating the effective moduli.

For calculating C_{11} (Fig. 4a and Eq. (3.7))

$$\begin{aligned} &u(0,y,z) = v(0,y,z) = 0 \qquad v(x,0,z) = v(x,H,z) = 0 \\ &u(W,y,z) = \text{const} \qquad w(x,y,0) = w(x,y,T) = 0 \end{aligned} \tag{C.12}$$

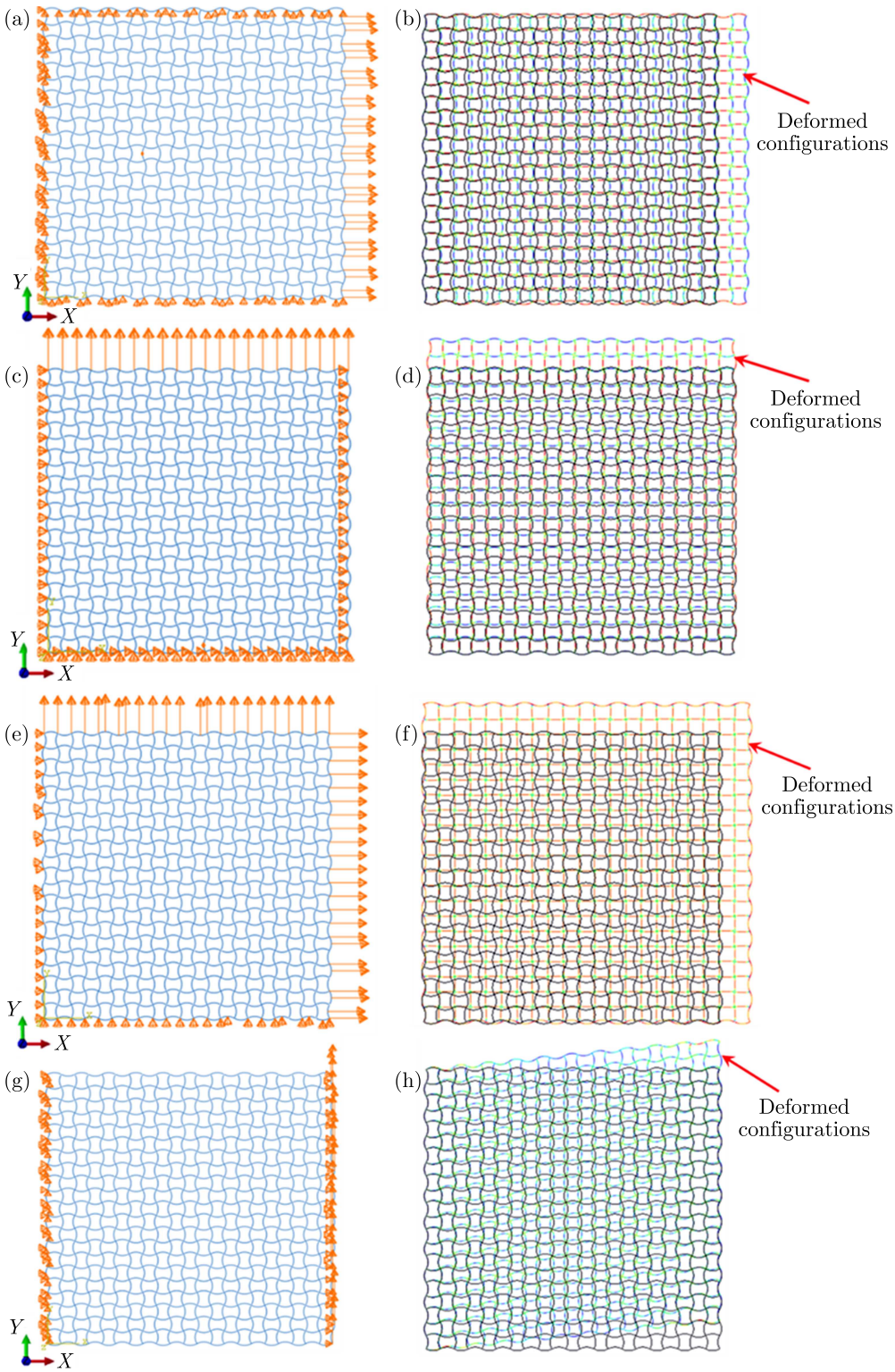

Fig. 4. (a), (c), (e) and (g) – Loading and boundary conditions for calculating C_{11}, C_{22}, C_{12} and C_{66}, respectively; (b), (d), (f), (h) – comparison between undeformed and deformed configurations

where, under the plane strain condition, three displacement components are functions of x and y, and are irrelated to z, i.e. $u(x, y, z) = u(x, y)$. The formula including z is simple for explicit prescribing the boundary conditions in FEM simulations.

For calculating C_{22} (Fig. 4c and Eq. (3.8))

$$\begin{aligned} &u(0,x,y,z) = u(W,y,z) = 0 \qquad u(x,0,z) = v(x,0,z) = 0 \\ &v(x,H,z) = \text{ const} \qquad w(x,y,0) = w(x,y,T) = 0 \end{aligned} \tag{C.13}$$

For calculating C_{12} (Fig. 4e and Eq. (3.9))

$$\begin{aligned} &u(0,y,z) = 0 \qquad v(x,0,z) = 0 \\ &u(W,y,z) = v(x,H,z) = \text{ const} \qquad w(x,y,0) = w(x,y,T) = 0 \end{aligned} \tag{C.14}$$

For calculating C_{66} (Fig. 4g and Eq. (3.10)

$$\begin{aligned} &u(0,y,z) = v(0,x,y,z) = 0 \qquad v(x,W,z) = \text{ const} \\ &u(x,W,z) = 0 \qquad w(x,y,0) = w(x,y,T) = 0 \end{aligned} \tag{C.15}$$

where u, v and w represent the displacements along the x, y and z direction, respectively.

Young's modulus and Poisson's ratio of BDPL in the x and y direction are obtained from Eq. (3.11)

$$E_1 = E_2 = 6.50\,\text{GPa} \qquad \nu_{12} = \nu_{21} = -0.32 \tag{C.16}$$

It can be seen that the studied BDPL has a negative Poisson's ratio.

The continuum constitutive equation under the plane stress condition is expressed by the stiffness matrix

$$\begin{Bmatrix} \sigma_{11} \\ \sigma_{22} \\ \sigma_{12} \end{Bmatrix} = \underbrace{\begin{bmatrix} C_{11} & C_{12} & 0 \\ C_{21} & C_{22} & 0 \\ 0 & 0 & C_{66} \end{bmatrix}}_{\text{Effective stiffness matrix}} \begin{Bmatrix} \varepsilon_{11} \\ \varepsilon_{22} \\ \varepsilon_{12} \end{Bmatrix} = 10^9 \begin{bmatrix} 7.24 & -2.31 & 0 \\ -2.31 & 7.24 & 0 \\ 0 & 0 & 1.00 \end{bmatrix} \begin{Bmatrix} \varepsilon_{11} \\ \varepsilon_{22} \\ \varepsilon_{12} \end{Bmatrix} \tag{C.17}$$

Then the compliance matrix $\mathbf{S}$ can be obtained by inverting the effective stiffness matrix shown in equation (3.17), i.e.

$$\begin{Bmatrix} \varepsilon_{11} \\ \varepsilon_{22} \\ \varepsilon_{12} \end{Bmatrix} = \underbrace{10^{-10} \begin{bmatrix} 1.54 & 0.49 & 0 \\ 0.49 & 1.54 & 0 \\ 0 & 0 & 10.00 \end{bmatrix}}_{\mathbf{S}} \begin{Bmatrix} \sigma_{11} \\ \sigma_{22} \\ \sigma_{12} \end{Bmatrix} \tag{C.18}$$

4. Geometry equation

The relation between the displacements of lattice joints and the macroscopic uniform strain prescribed can be obtained by combining the method of particular displacement fields and finite element analyses. As shown in Fig. 5, a unit cell comprises five joints and each joint has translational and rotational degrees of freedom. Symbols u_i, v_i and φ_i, represent horizontal, vertical displacement and rotation angle, respectively, and the subscript i is the joint number.

The specified uniform strain fields on the BDPL shown in Fig. 4a are $\varepsilon_{11} = 10^{-3}$, and $\varepsilon_{11} = \varepsilon_{22} = 0$. The displacements and rotation angle of each unit cell joint are extracted, as shown in the second column of Appendix A. Similarly, under the uniform strain fields like $\varepsilon_{22} = 10^{-3}$, $\varepsilon_{11} = \varepsilon_{12} = 0$ (Fig. 4c) and $\varepsilon_{12} = 5 \cdot 10^{-4}$, $\varepsilon_{11} = \varepsilon_{22} = 0$ (Fig. 4g), the displacements and rotation angle of each unit cell joint are also obtained in Appendix A. The relation between displacements of each joint in the unit cell and different macroscopic uniform strain fields can be derived from Appendix A. The geometry equation is simply written as

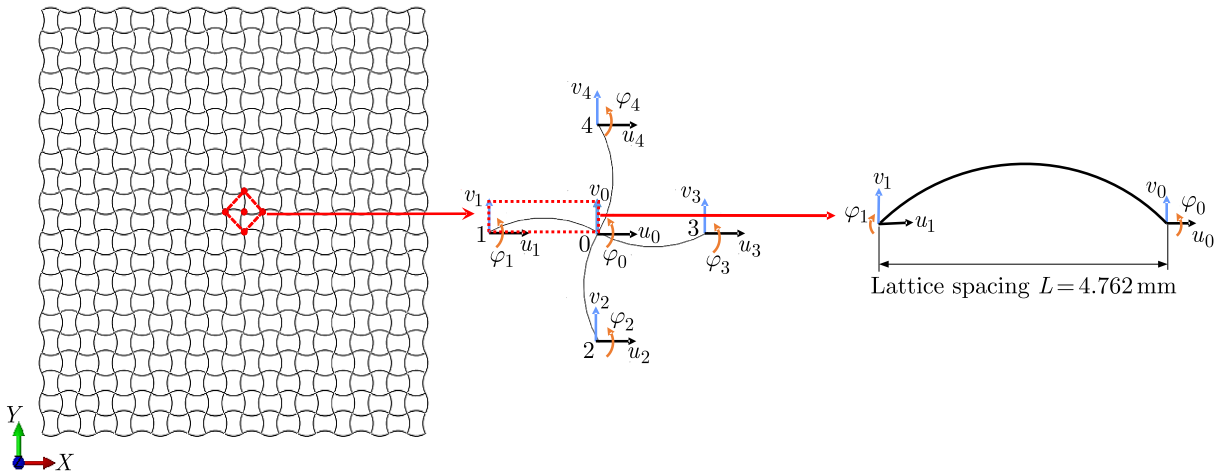

Fig. 5. (a) Schematic of the studied BDPL, (b) translational and rotational degrees of freedom and (c) the curved beam composing the unit cell

$$\left\{u_0 \quad v_0 \quad \varphi_0 \quad \cdots \quad u_4 \quad v_4 \quad \varphi_4\right\}^{\mathrm{T}} = \mathbf{B}_{15\times 3}\left\{\varepsilon_{11} \quad \varepsilon_{22} \quad \varepsilon_{12}\right\}^{\mathrm{T}} \tag{C.1}$$

The specific equation is found as given in Appendix B.

5. Stiffness matrix of unit cell

In order to obtain the stiffness matrix of a unit cell, it is needed to investigate the stiffness matrix of each curved strut in the unit cell firstly. We continue to use the method of particular displacement fields. We take out a curved strut from the unit cell, fix five degrees of freedom and give a prescribed value to the remaining one. The forces and bending moments of endpoints can be obtained from Abaqus. In this Section, the prescribed displacement and rotation angle are 10^{-4} mm and 10^{-4} rad, respectively.

Taking 1-0 strut as an example, the stiffness matrix of a single curved strut is obtained as

$$\begin{Bmatrix} F_{x_1} \\ F_{y_1} \\ M_1 \\ F_{x0}^{(1-0)} \\ F_{y0}^{(1-0)} \\ M_0^{(1-0)} \end{Bmatrix} = \mathbf{A}^{(1-0)} \begin{Bmatrix} u_1 \\ v_1 \\ \varphi_1 \\ u_0 \\ v_0 \\ \varphi_0 \end{Bmatrix} \tag{C.1}$$

The calculated parameters of $\mathbf{A}^{(1-0)}$ are given in Appendix B.

The incidence matrices in Eqs. (4.1) and (3.18) are denoted as $\mathbf{B}$ and $\mathbf{S}$, respectively. The displacement and strain incidence matrix $\mathbf{B}^{(1-0)}$ for the joint pair comprising 0 and 1 can be extracted from $\mathbf{B}$. Finally, the forces on both ends of each curved strut can be expressed as a linear function of the macroscopic stresses

$$\begin{Bmatrix} F_{x_i} \\ F_{y_i} \\ M_i \\ F_{x0}^{(i-0)} \\ F_{y0}^{(i-0)} \\ M_0^{(i-0)} \end{Bmatrix} = \mathbf{A}^{(i-0)}\mathbf{B}^{(i-0)}\mathbf{S} \begin{Bmatrix} \sigma_{11} \\ \sigma_{22} \\ \sigma_{12} \end{Bmatrix} \qquad i = 1,2,3,4 \tag{C.2}$$

6. Initial yield surfaces of BDPL

6.1. Empirical formula

An empirical formula (Liu *et al.*, 2008) for calculating the effective stress is employed to consider the contributions of both the axial force and bending moment. The effective stress in the curved strut is defined as

$$\sigma = \frac{N}{A} + a\frac{(|M_i|, |M_j|)_{max}}{W_z} \tag{C.1}$$

As shown in Fig. 6, where N is the normal force in the considered strut, M_i and M_j are the bending moments at the joint i and j of the strut, W_z is the section modulus. The coefficient a plays a role in regulating the contribution of the bending moment to the effective stress. Lilliu and van Mier (2003) set the coefficient to 0.005 (Karihaloo *et al.*, 2003; Liu *et al.*, 2007). In order to investigate the effects of this parameter, a is set to 0.005 and 0.0075.

For a particular stress status, it is necessary to find out the curved strut easiest to yield among the unit cells subjected to the prescribed macroscopic strain field.

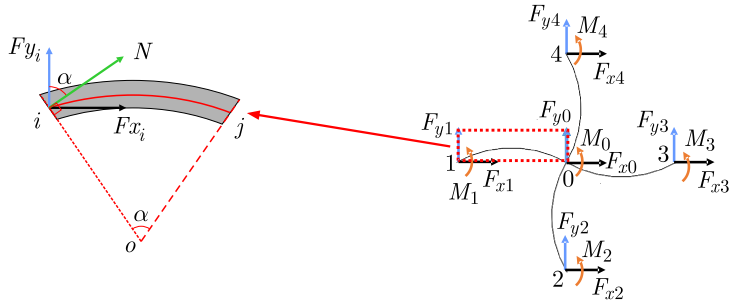

Fig. 6. (a) Curved strut, (b) schematic of end forces and moments of the unit cell

6.2. Yield surface calculations

According to the geometric parameters in Section 2.1, the section area A of the strut and section modulus W_z are $10^{-5}\,\mathrm{m}^2$, $(1/6)\cdot 10^{-3}\,\mathrm{m}^3$, respectively. The linear function between the effective stresses and forces in $(\varepsilon_{11}, \varepsilon_{22})$ space is easily obtained from Eq. (5.2).

For 1-0 strut, we have

$$N = F_{x_1}\cos 30^\circ + F_{y_1}\sin 30^\circ \tag{C.2}$$

From equation (6.1), the effective stress can be expressed in the form

$$|\sigma| = \left|\left(\frac{N}{A}\right)_{max}\right| + \left|a\frac{M_0}{W_z}\right|_{max} = |(-4.77\sigma_{11} + 0.36\sigma_{22})_{max}| + |(600aM_0)_{max}| \tag{C.3}$$

where, the operation of simply considering the maximum effective normal stress indicates that the source material has been assumed as isotropic.

The value of a is set to 0.005, the effective stress can be calculated as

$$|\sigma| = \left|\left(\frac{N}{A}\right)_{max}\right| + \left|\alpha\frac{M_0}{W_z}\right|_{max} = \begin{cases} 7.05\sigma_{11} + 2.73\sigma_{22} & \text{for} \quad \sigma_{11} > 0, \quad \sigma_{22} > 0 \\ 7.05\sigma_{11} - 2.73\sigma_{22} & \text{for} \quad \sigma_{11} > 0 \quad \sigma_{22} < 0 \\ -7.05\sigma_{11} + 2.73\sigma_{22} & \text{for} \quad \sigma_{11} < 0 \quad \sigma_{22} > 0 \\ -7.05\sigma_{11} - 2.73\sigma_{22} & \text{for} \quad \sigma_{11} < 0 \quad \sigma_{22} < 0 \end{cases}$$

(C.4)

the yield surface of 1-0 strut is given by

$$\frac{\sigma_{22}}{\sigma_Y}=\begin{cases}-2.58\dfrac{\sigma_{11}}{\sigma_Y}+0.37 & \text{for} \quad \sigma_{11}>0 \quad \sigma_{22}>0\\ 2.58\dfrac{\sigma_{11}}{\sigma_Y}-0.37 & \text{for} \quad \sigma_{11}>0 \quad \sigma_{22}<0\\ 2.58\dfrac{\sigma_{11}}{\sigma_Y}+0.37 & \text{for} \quad \sigma_{11}<0 \quad \sigma_{22}>0\\ -2.58\dfrac{\sigma_{11}}{\sigma_Y}-0.37 & \text{for} \quad \sigma_{11}<0 \quad \sigma_{22}<0\end{cases} \tag{C.5}$$

where σ_Y is the yield stress of the matrix material.

Similarly, for curved struts 2-0, 3-0 and 4-0, the yield surfaces are calculated as follows:

— 2-0

$$\frac{\sigma_{22}}{\sigma_Y}=\begin{cases}-0.39\dfrac{\sigma_{11}}{\sigma_Y}+0.14 & \text{for} \quad \sigma_{11}>0 \quad \sigma_{22}>0\\ 0.39\dfrac{\sigma_{11}}{\sigma_Y}-0.14 & \text{for} \quad \sigma_{11}>0 \quad \sigma_{22}<0\\ 0.39\dfrac{\sigma_{11}}{\sigma_Y}+0.14 & \text{for} \quad \sigma_{11}<0 \quad \sigma_{22}>0\\ 0.39\dfrac{\sigma_{11}}{\sigma_Y}-0.14 & \text{for} \quad \sigma_{11}<0 \quad \sigma_{22}<0\end{cases} \tag{C.6}$$

— 3-0

$$\frac{\sigma_{22}}{\sigma_Y}=\begin{cases}-2.58\dfrac{\sigma_{11}}{\sigma_Y}+0.37 & \text{for} \quad \sigma_{11}>0 \quad \sigma_{22}>0\\ 2.58\dfrac{\sigma_{11}}{\sigma_Y}-0.37 & \text{for} \quad \sigma_{11}>0 \quad \sigma_{22}<0\\ 2.58\dfrac{\sigma_{11}}{\sigma_Y}+0.37 & \text{for} \quad \sigma_{11}<0 \quad \sigma_{22}>0\\ -2.58\frac{\sigma_{11}}{\sigma_Y}-0.37 & \text{for} \quad \sigma_{11}<0 \quad \sigma_{22}<0\end{cases} \tag{C.7}$$

— 4-0:

$$\frac{\sigma_{22}}{\sigma_Y}=\begin{cases}-0.39\dfrac{\sigma_{11}}{\sigma_Y}+0.14 & \text{for} \quad \sigma_{11}>0 \quad \sigma_{22}>0\\ 0.39\dfrac{\sigma_{11}}{\sigma_Y}-0.14 & \text{for} \quad \sigma_{11}>0 \quad \sigma_{22}<0\\ 0.39\dfrac{\sigma_{11}}{\sigma_Y}+0.14 & \text{for} \quad \sigma_{11}<0 \quad \sigma_{22}>0\\ -0.39\dfrac{\sigma_{11}}{\sigma_Y}-0.14 & \text{for} \quad \sigma_{11}<0 \quad \sigma_{22}<0\end{cases} \tag{C.8}$$

From equations (6.5) to (6.8), we find that strut 1-0 has the same yield surface with strut 3-0, while strut 2-0 has the same yield surface with strut 4-0. The initial yield surface of BDPL in $(\sigma_{11},\sigma_{22})$ space is sketched in Fig. 7. The region beyond dashed lines represents the yield of each strut in the stress space. It can be considered that the area within the red solid lines keeps elastic without any strut yielding. In Fig. 8, the influence of parameter a is discussed. With an increase of a, the area surrounded by the yield surface decreases. The straight struts lattice can be considered as a special curved strut lattice with the central angle $\alpha=0^\circ$. In Fig. 9, the yield surface of the straight struts lattice is calculated, and it can be seen that the tensile and compressive strength of the straight struts lattice is better than the curved struts lattice.

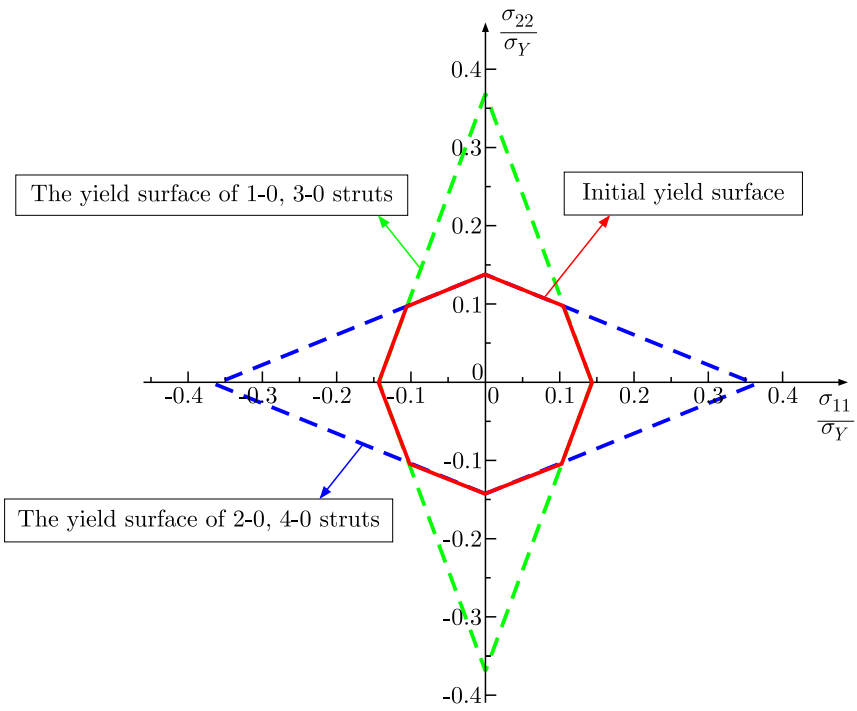

Fig. 7. The initial yield surface in $(\sigma_{11}, \sigma_{22})$ space of unit cell of BDPL

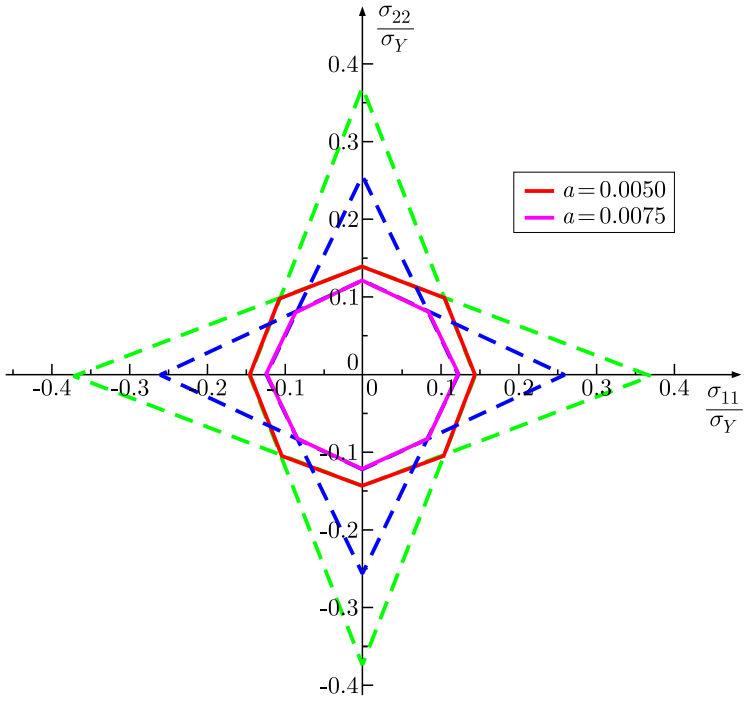

Fig. 8. The influence of a on initial yield surfaces of the unit cell of BDPL in $(\sigma_{11}, \sigma_{22})$ space

7. Conclusions

In this study, based on the principle of strain energy equivalence, the macroscopic effective stiffnesses of the corresponding equivalent continuum are calculated. The relation between the displacements of lattice joints and the macroscopic uniform strain prescribed have been obtained by combining the particular-displacement method and finite element analyses. By analyzing the

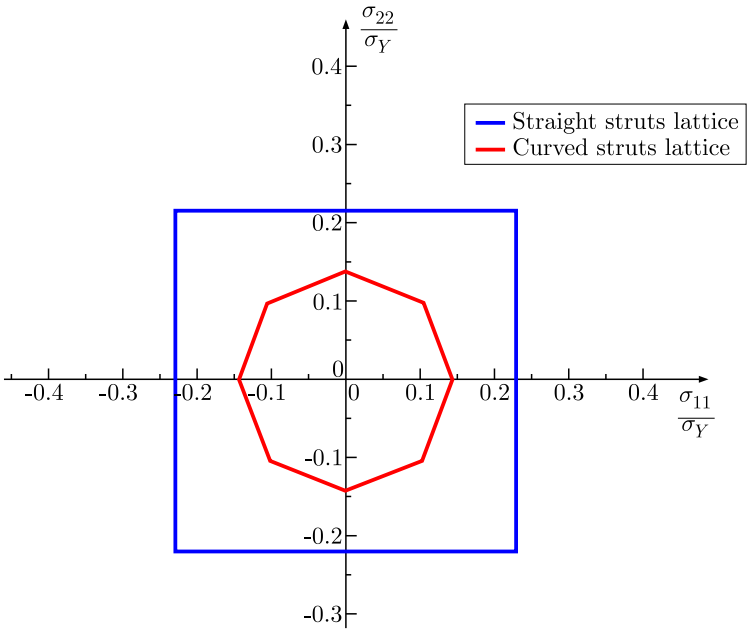

Fig. 9. The initial yield surface of the straight struts lattice ($\alpha = 0°$) and the curved struts lattice ($\alpha = 60°$) in $(\sigma_{11}, \sigma_{22})$ space

relation between deformation and stress of a single periodic unit cell, the forces on both ends of each curved strut can be expressed as a linear function of the macroscopic stresses. The yield surfaces are calculated successfully. Compared with the existing methods in the literature, the proposed method is convenient to deal with the yield problem of bending-dominant lattice metamaterials such as the curved strut lattice.

Particularly, an empirical formula for calculating the effective stress has been employed to consider the contributions of both the axial force and bending moment, by introducing a parameter a adjusting the relative contribution of bending to yield strength. It is found that a larger value of a leads to a lower yield strength.

Acknowledgements

The work was supported by the National Science Foundation of China (Grant No. 11972174 and Grant No. 11672119).

Appendix A

Table 1. Displacements and rotation angle of each unit cell joint

Displacement [mm] Rotation angle [rad]	Uniform strain fields		
	$\varepsilon_{11} = 10^{-3}$, $\varepsilon_{22} = \varepsilon_{12} = 0$	$\varepsilon_{22} = 10^{-3}$, $\varepsilon_{11} = \varepsilon_{12} = 0$	$\varepsilon_{12} = 5 \cdot 10^{-4}$, $\varepsilon_{11} = \varepsilon_{22} = 0$
u_0	$4.76 \cdot 10^{-2}$	$-3.39 \cdot 10^{-5}$	$7.42 \cdot 10^{-6}$
v_0	$-3.38 \cdot 10^{-5}$	$4.76 \cdot 10^{-2}$	$4.75 \cdot 10^{-2}$
φ_0	$1.65 \cdot 10^{-3}$	$1.65 \cdot 10^{-3}$	$5.33 \cdot 10^{-4}$
u_1	$4.28 \cdot 10^{-2}$	$-1.02 \cdot 10^{-4}$	$6.52 \cdot 10^{-6}$
v_1	$-3.38 \cdot 10^{-5}$	$4.76 \cdot 10^{-2}$	$4.24 \cdot 10^{-2}$

φ_1	$-1.65 \cdot 10^{-3}$	$-1.65 \cdot 10^{-3}$	$5.31 \cdot 10^{-4}$
u_2	$4.76 \cdot 10^{-2}$	$-3.38 \cdot 10^{-5}$	$2.59 \cdot 10^{-5}$
v_2	$-1.02 \cdot 10^{-4}$	$4.28 \cdot 10^{-2}$	$4.75 \cdot 10^{-2}$
φ_2	$-1.65 \cdot 10^{-3}$	$-1.65 \cdot 10^{-3}$	$5.33 \cdot 10^{-4}$
u_3	$5.24 \cdot 10^{-2}$	$3.38 \cdot 10^{-5}$	$7.42 \cdot 10^{-6}$
v_3	$-3.38 \cdot 10^{-4}$	$4.76 \cdot 10^{-2}$	$5.25 \cdot 10^{-2}$
φ_3	$-1.65 \cdot 10^{-3}$	$-1.65 \cdot 10^{-3}$	$5.33 \cdot 10^{-4}$
u_4	$4.76 \cdot 10^{-2}$	$-3.38 \cdot 10^{-5}$	$-7.42 \cdot 10^{-6}$
v_4	$3.38 \cdot 10^{-5}$	$5.24 \cdot 10^{-2}$	$4.75 \cdot 10^{-2}$
φ_4	$-1.65 \cdot 10^{-3}$	$-1.65 \cdot 10^{-3}$	$5.33 \cdot 10^{-4}$

Appendix B

The specific parameters of the matrices mentioned in the article are as follows

$$\mathbf{A}^{(1-0)} = 10^6 \begin{bmatrix} 1.19 \cdot 10^2 & 0 & -4.99 \cdot 10^{-2} & -1.19 \cdot 10^2 & 0 & 4.99 \cdot 10^{-2} \\ & 4.51 \cdot 10^1 & 1.07 \cdot 10^{-1} & 0 & -4.51 \cdot 10^1 & 1.07 \cdot 10^{-1} \\ & & 1.45 \cdot 10^{-3} & 4.99 \cdot 10^{-2} & -1.07 \cdot 10^{-1} & -9.36 \cdot 10^{-4} \\ & \text{Sym} & & 1.19 \cdot 10^2 & 0 & -4.99 \cdot 10^{-2} \\ & & & & 4.51 \cdot 10^1 & -1.07 \cdot 10^{-1} \\ & & & & & 1.45 \cdot 10^{-3} \end{bmatrix} \tag{B.1}$$

$$\begin{Bmatrix} u_0 \\ v_0 \\ \varphi_0 \\ u_1 \\ v_1 \\ \varphi_1 \\ u_2 \\ v_2 \\ \varphi_2 \\ u_3 \\ v_3 \\ \varphi_3 \\ u_4 \\ v_4 \\ \varphi_4 \end{Bmatrix} = 10^{-6} \underbrace{\begin{bmatrix} 4.76 \cdot 10^4 & -3.38 \cdot 10^1 & 1.49 \cdot 10^1 \\ -3.38 \cdot 10^1 & 4.76 \cdot 10^4 & 9.49 \cdot 10^4 \\ 1.65 \cdot 10^6 & 1.65 \cdot 10^6 & 1.07 \cdot 10^6 \\ 4.28 \cdot 10^4 & -1.02 \cdot 10^2 & 1.30 \cdot 10^1 \\ -3.38 \cdot 10^1 & 4.76 \cdot 10^4 & 8.48 \cdot 10^4 \\ -1.65 \cdot 10^6 & -1.65 \cdot 10^6 & 1.06 \cdot 10^6 \\ 4.76 \cdot 10^4 & -3.38 \cdot 10^1 & 5.19 \cdot 10^1 \\ -1.02 \cdot 10^2 & 4.28 \cdot 10^4 & 9.49 \cdot 10^4 \\ -1.65 \cdot 10^6 & -1.65 \cdot 10^6 & 1.07 \cdot 10^6 \\ 5.24 \cdot 10^4 & 3.38 \cdot 10^1 & 1.49 \cdot 10^1 \\ -3.38 \cdot 10^1 & 4.76 \cdot 10^4 & 1.05 \cdot 10^5 \\ -1.65 \cdot 10^6 & -1.65 \cdot 10^6 & 1.07 \cdot 10^6 \\ 4.76 \cdot 10^4 & -3.38 \cdot 10^1 & -1.49 \cdot 10^1 \\ 3.38 \cdot 10^1 & 5.24 \cdot 10^4 & 9.49 \cdot 10^4 \\ -1.65 \cdot 10^6 & -1.65 \cdot 10^6 & 1.07 \cdot 10^6 \end{bmatrix}}_{\mathbf{B}_{(15\times 3)}} \begin{Bmatrix} \varepsilon_{11} \\ \varepsilon_{22} \\ \varepsilon_{12} \end{Bmatrix} \tag{B.2}$$

References

1. Chen Y., Li T., Scarpa F., Wang L., 2017, Lattice metamaterials with mechanically tunable Poisson's ratio for vibration control, *Physical Review Applied*, **7**, 024012
2. Deshpande V., Ashby M., Fleck N., 2001, Foam topology: bending versus stretching dominated architectures, *Acta Materialia*, **49**, 1035-1040

3. Deshpande V.S., Fleck N.A., Ashby M.F., 2001, Effective properties of the octet-truss lattice material, *Journal of the Mechanics and Physics of Solids*, **49**, 1747-1769

4. Evans A., 2001, Lightweight materials and structures, *MRS Bulletin*, **26**, 790-797

5. Evans A.G., Hutchinson J.W., Fleck N.A., Ashby M.F., Wadley H.N.G., 2001, The topological design of multifunctional cellular metals, *Progress in Materials Science*, **46**, 309-327

6. Fan H., Yang W., 2006, An equivalent continuum method of lattice structures, *Acta Mechanica Solida Sinica*, **19**, 103-113

7. Frenzel T., Kadic M., Wegener M., 2017, Three-dimensional mechanical metamaterials with a twist, *Science*, *358*, 1072-1074

8. Gibson L.J., 2003, Cellular solids, *MRS Bulletin*, **28**, 270-274

9. Karihaloo B.L., Shao P.F., Xiao Q.Z., 2003, Lattice modelling of the failure of particle composites, *Engineering Fracture Mechanics*, **70**, 2385-2406

10. Lilliu G., van Mier J.G., 2003, 3D lattice type fracture model for concrete, *Engineering Fracture Mechanics*, **70**, 927-941

11. Liu J., Gu T., Shan S., Sung H.K., Weaver J.C., Bertoldi K., 2016, Harnessing buckling to design architected materials that exhibit effective negative swelling, *Advanced Materials*, **28**, 6619-6624

12. Liu J.X., Deng S.C., Zhang J., Liang N.G., 2007, Lattice type of fracture model for concrete, *Theoretical and Applied Fracture Mechanics*, **48**, 269-284

13. Liu J.X., Zhao Z.Y., Deng S.C., Liang N.G., 2008, A simple method to simulate shrinkage-induced cracking in cement-based composites by lattice-type modeling, *Computational Mechanics*, **43**, 477-492

14. Wang A., McDowell D., 2004, The in-plane mechanical properties of various periodic honeycombs, *Journal of Engineering of Material and Technology*, **126**, 137-156

15. Wang A., McDowell D., 2005, Yield surfaces of various periodic metal honeycombs at intermediate relative density, *International Journal of Plasticity*, **21**, 285-320

16. Wang Y., Chi Z., Liu J., 2020, On buckling behaviors of a typical bending-dominated periodic lattice, *Composite Structures*, **258**, 113204

17. Xue Z., Vaziri A., Hutchinson J.W., 2005, Non-uniform hardening constitutive model for compressible orthotropic materials with application to sandwich plate cores, *Computer Modeling in Engineering and Sciences*, **10**, 79

Manuscript received July 27, 2022; accepted for print November 18, 2022

JOURNAL OF THEORETICAL AND APPLIED MECHANICS
61, 1, pp. 189-201, Warsaw 2023
https://doi.org/10.15632/jtam-pl/158842

RESEARCH ON OPTIMAL DESIGN OF VIBRATION REDUCTION OF CENTRIFUGAL AIR CONDITIONING CHILLER BASED ON PARTICLE DAMPING

Wangqiang Xiao, Jinsong Shi, Hui Chen

Xiamen University, China

e-mail: wqxiao@xmu.edu.cn; 1479953400@qq.com; 752310376@qq.com

Hua Liu

State Key Laboratory of Air-Conditioning Equipment and System Energy Conservation, China

Correspnding author, e-mail: shi09052021@126.com

Considering vibration of centrifugal air-conditioning chillers at working conditions of 300 Hz and 386 Hz, a vibration reduction method for centrifugal air-conditioning chillers based on particle damping is proposed. Firstly, the vibration transfer path of the chillers is determined based on dynamic characteristics analysis of the chillers. Secondly, the vibration sensitive area of the compressor is determined by finite element analysis. Then the energy dissipation is calculated by the discrete element method (DEM) to determine the optimal installation scheme of the damper. Finally, the vibration reduction effect of the chillers after arranging the damper is verified by experiments.

Keywords: centrifugal air-conditioning chiller, particle damping, DEM, optimal scheme, vibration reduction

1. Introduction

As a new type of high-efficiency air-conditioning technology, centrifugal air-conditioning chillers have attracted a lot of attention in recent years due to their high energy-saving efficiency and excellent load performance (Hassan *et al.*, 2020; Deng and Yang, 2020). As the core equipment of air-conditioning, chillers are widely used in all walks of life. During operation of centrifugal air--conditioning chillers, vibrations will directly affect their safety. After the vibration intensity of the chillers exceeds a certain value, it will affect the precision of related equipment, extremely easy to cause deterioration of structural stress and thus affecting the service life of the chillers. Moreover, because structural vibration of the chillers is transmitted to the installation foundation, it will cause vibration damage to the installation and reduce comfort of the working environment (Geng *et al.*, 2021; Jiang, 2015). Therefore, it is particularly necessary to conduct vibration reduction research on centrifugal air-conditioning chillers.

At present, the commonly used method to reduce vibration for chillers is to arrange rubber shock isolation pads, spring vibration isolators and additional vibration damping supports between the chillers support and the foundation, or to change the resonance frequency of the chillers through structural design (Mo and Ding, 2019). Wang (2004) distributed rubber damping pads and low-frequency large-load damping spring shock absorbers evenly between the chillers support and the foundation, and used multi-layer damping pads in series to improve the damping effect. The vibration reduction measures adopted for the chillers are to install vibration damping rubber pads at the foundation, and to use expansion joints as a flexible connection between the compressor and the pipeline to absorb the vibration displacement of the chillers (Xing, 2016).

According to the test results of the electric motor balance, Fang *et al.* (2019) modified the motor by adding counterweight to adjust the electric motor balance, which solved the problem of excessive vibration of the chillers. However, whether it is to improve dynamic balance of the compressor or to install rubber and spring shock absorbers on the chillers, there are defects. Dynamic balancing will change the original structure of chillers, making it difficult to ensure balance accuracy, making the assembly process more complicated and bringing difficulties to the design process of the chillers. In the installation of rubber and spring shock absorbers, due to defects of rubber and springs such as oil resistance and deformation, the chillers require frequent replacement of the installed materials during use. Over time, vibration isolation performance will be significantly reduced.

Particle damping is a type of passive control technology (Lu *et al.*, 2018). Based on theory of energy dissipation mechanism, the technology fills particles inside a structure or a specific cavity container. It consumes vibration energy of the system through the damping effect formed by friction and collision between particles and the container wall as well as between particles, so as to achieve the purpose of suppressing vibration of the system. (Xiao and Xu, 2021; Nallusamy *et al.*, 2020; Zhang *et al.*, 2020). Particle dampers are arranged flexibly and insensitive to temperature and environmental changes (Lei *et al.*, 2018). They are suitable for use in harsh environments with high reliability (Wang and Li, 2011). At the same time, particle dampers introduce minor changes to the original structure and are suitable for use in narrow spaces such as chillers (Severson *et al.*, 2008; Cheng and Yang, 2014; Romdhane *et al.*, 2013). Due to the above advantages, particle dampers are widely used in aerospace, mechanical vibration control, civil engineering and other fields (Lu *et al.*, 2020).

In this paper, considering advantages and disadvantages of the traditional air conditioning damping method and design requirements of the centrifugal chiller, particle dampers is introduced into the centrifugal air-conditioning chillers. Dynamic characteristics of the chiller are analyzed and the vibration transfer path is obtained. Through modal analysis of the compressor, the vibration sensitive region of the compressor is found, and the installation position of dampers is preliminarily determined and designed. The effects of different particle sizes and excitation on energy dissipation of particles of the chiller and the optimal installation scheme of dampers on the chiller were studied by DEM. Finally, experimental results show that particle dampers can effectively reduce vibration of the chiller.

2. Dynamic characteristics of a centrifugal chiller

A centrifugal air-conditioning chiller is excited by special equipment to cause vibration during the actual working process. The compressor is the main vibration source in the chiller. In order to better design a particle damper, it is necessary to analyze vibration characteristics of the compressor to find the root cause of the vibration and optimize and improve the structure according to the principle of particle damping.

2.1. Analysis of vibration characteristics of the centrifugal chiller

A centrifugal chiller is mainly composed of a compressor, pipeline, condenser, evaporator, support frame and raft frame. Regular frequency multiplication in the dynamic response curve of the compressor indicates that the main source of vibration is the fixed frequency excitation of the compressor rotor. When the compressor is running at a frequency of 386 Hz, acceleration sensors are arranged at a total of 6 measuring points from the compressor to the raft frame. According to the vibration test standard, the sensors are all arranged vertically. The positions of measuring points 1-6 are shown in Fig. 1. The root mean square of vibration acceleration is measured, and the vibration transmission path is analyzed and identified.

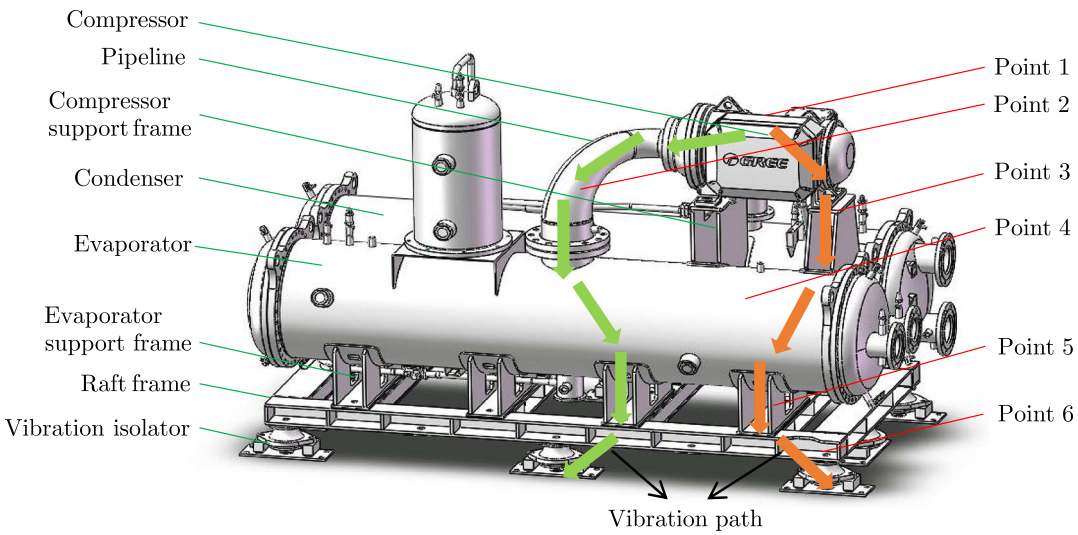

Fig. 1. Composition and location of the measurement point of the chiller

There are two main paths for vibration transmission in the chiller. One is compressor → compressor support frame → condenser → condenser support frame → raft frame → vibration isolator → platform. The second is compressor → pipeline → condenser → condenser support frame → raft frame → vibration isolator → platform. According to the actual test, the dynamic response of the whole chiller decreases gradually from top to bottom. The response of the compressor top and pipeline is the largest, followed by the response of the compressor foot, and the bottom of the raft has the smallest response.

2.2. Finite element analysis of the chiller

Modal parameters are the basis for the optimal design of structural dynamic characteristics of the chiller. Through modal analysis, the vibration mode of the chiller is obtained when it is subjected to external excitation, especially the vibration mode with greater vibration, which lays a foundation for design of particle dampers and optimization of the chiller in the next step.

As a continuous structure, the chiller can be discretized into a system with n degrees of freedom during finite element analysis. Since finite element analysis is only applicable to linear steady systems, assuming that the chiller has linear dynamic characteristics at a certain stage and does not change with time, a multi-degree of freedom dynamic differential equation belonging to the linear system is established considering damping characteristics of the structure, as follows

$$\mathbf{M}\ddot{\mathbf{u}}(t) + \mathbf{C}\dot{\mathbf{u}}(t) + \mathbf{K}\mathbf{u}(t) = \mathbf{F}(t) \tag{B.1}$$

Among them, $\mathbf{M}$, $\mathbf{C}$, $\mathbf{K}$ are the mass, damping and stiffness matrices of the chiller system. $\ddot{\mathbf{u}}(t)$, $\dot{\mathbf{u}}(t)$ and $\mathbf{u}(t)$ are the acceleration, speed and displacement response vectors of the system. $\mathbf{F}(t)$ are the external stable excitations that the chiller bears.

The characteristic equation of the system can be obtained as

$$(\mathbf{K} - \omega^2\mathbf{M})\boldsymbol{\varphi} = \mathbf{0} \tag{B.2}$$

where ω^2 is the eigenvalue corresponding to the characteristic equation, and $\boldsymbol{\varphi}$ is the eigenvector. In order to make the equation easy to solve, Eq. (2.2) needs to be decoupled. Introduce the coordinate transformation

$$\mathbf{u}(t) = \boldsymbol{\varphi}\mathbf{q}(\omega)\mathrm{e}^{\mathrm{j}\omega t} \tag{B.3}$$

Decouple Equation (2.3)

$$-\omega^2\mathbf{M}\boldsymbol{\varphi}\mathbf{q}(\omega)+\mathbf{K}\boldsymbol{\varphi}\mathbf{q}(\omega)=\mathbf{f}(\omega) \tag{B.4}$$

Solving the above formula, the i-th natural frequency ω_i and the i-th displacement u_i, that is, the modal vibration shapes of the chiller system can be obtained.

2.3. Modal analysis of the chiller compressor

There are many parts in the actual compressor model. In order to improve calculation efficiency, the compressor model is simplified under the premise of satisfying the real performance. The material of the compressor is steel. Its material parameters are elastic modulus of 200 GPa, Poisson's ratio of 0.3, and density of 7850 kg/m^3. The boundary condition is that the lower end of the support frame connected to the compressor is set to a fixed constraint, and the compressor foot and the upper end of the support frame are constrained by bolts. Too large mesh size can lead to insufficient accuracy, and mesh size that is too small consumes computer resources. To ensure precision and accuracy of meshing and to avoid excessive calculations, the mesh element size is set to 5 mm to divide the model into tetrahedral elements. Extracting the first 6 modes of the compressor, the frequency distribution is shown in Table 1, and the mode shape cloud diagram is shown in Fig. 2.

Table 1. Compressor mode

Mode order	1	2	3	4	5	6
Frequency [Hz]	51.35	173.87	334.36	479.18	509.54	525.34

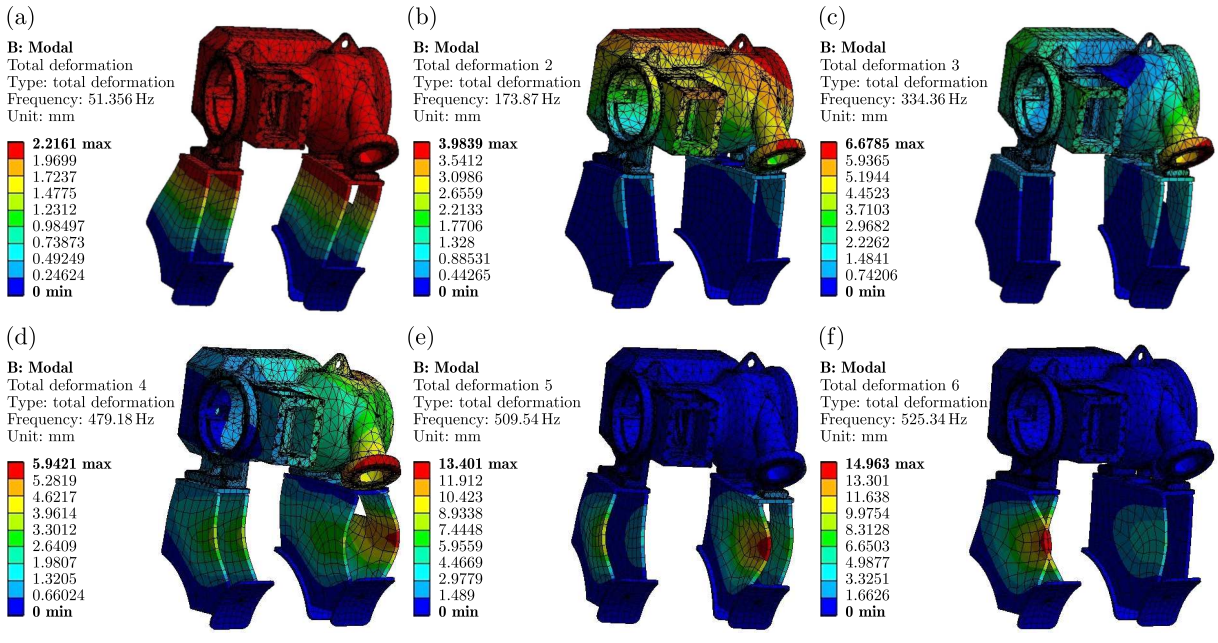

Fig. 2. Compressor modal vibration shape diagram: (a) first-order mode, (b) second-order mode, (c) third-order mode, (d) fourth-order mode, (e) fifth-order mode, (f) sixth-order mode

According to Table 1 and Fig. 2, it can be seen that the first and second modes are mainly bending and deformation of the upper part of the support frame and the compressor. The third and fourth modes are bending and deformation of the compressor foot and the support frame. The fifth and sixth modes are bending and deformation of the support frame.

The modal analysis shows that the top, middle and the support frame of the compressor are vibration sensitive areas, and the installation area of the particle damper is preliminarily determined. For the compressor, the particle damper is mounted on the top of the compressor and installed in parallel at the position of the supporting plate and rigidly installed in series between the compressor and the supporting plate.

3. Discrete element model of the particle damper

3.1. Design of the particle damper for the compressor

In order to better suppress generation and propagation of vibration from the source, considering actual characteristics of a relatively uneven structure of the compressor, a particle damper was rigidly installed between the compressor and the support frame in this paper. The installation scheme of the particle dampers is shown in Fig. 3. J1 and J2 are two types of particle dampers glued to the compressor top. J3 and J4 are two types of particle dampers bolted to the compressor foot. J5 is a type of particle damper bolted to the compressor support frame. The damper housing is made of steel.

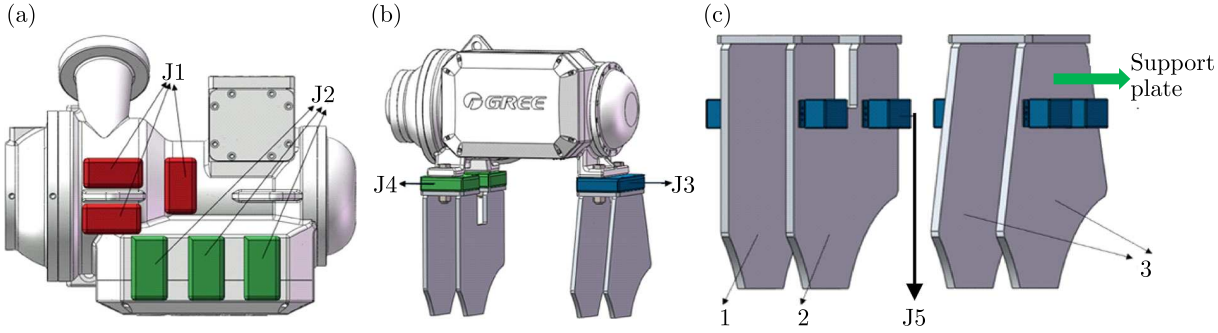

Fig. 3. The installation scheme of particle dampers: (a) on top, (b) on foot, (c) on support frame

The size of J1 is 120 mm×60 mm×50 mm and the size of J2 is 110 mm×60 mm×50 mm. The sizes of J3, J4 and J5 are 250 mm×150 mm×50 mm,165 mm×150 mm×50 mm and 127 mm×50 mm×40 mm, respectively. Two types of particle dampers J1 and J2 are glued on top of the compressor. The damperd raised the compressor vertically by 50 mm. Several through-holes with a diameter of 6 mm were opened on the support frame, and particle damper J5 was bolted to the support frame.

3.2. Mechanical model of the compressor particle dampers

When the compressor runs at the excitation frequency, it sets the particle dampers in motion, causing collision and friction between particles in the dampers and between the particles and the damper wall. In this process, a force between the particles must be generated. Based on the Hertz-Mindlin contact theory, the mechanical contact model of particle damping is shown in Fig. 4.

When the compressor is running under rated conditions, the equation of motion of the particles at a certain moment is

$$m_i \frac{d^2 X_i}{dt^2} - m_i g = \sum_{j=1}^{S_i} (F_{nij} + F_{tij}) + F_{ij}(t) \qquad I_i \frac{d^2 \varphi_i}{dt^2} = \sum_{j=1}^{S_i} T_{ij} \tag{B.1}$$

where F_{nij} is the normal contact force between the particle i and j, F_{tij} is the tangential contact force between the particle i and j, $F_{ij}(t)$ is the external excitation of the particle system. T_{ij} is

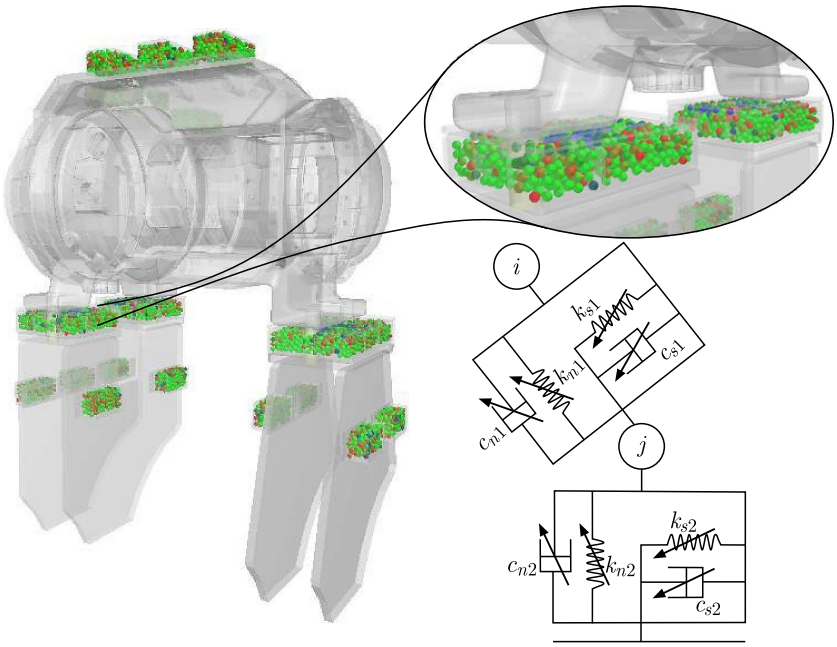

Fig. 4. Particle contact model of the compressor

the torque generated by the tangential contact force. m_i is mass of the particle i. I_i is the moment of inertia of the particle i. g is the acceleration of gravity. X_i is the displacement vector of the particle i. φ_i is the angular displacement vector of the particle i. s_i is the number of particles in contact with the particle i at a given moment.

The normal contact force between the particles is

$$F_{nij} = F_{kn} + F_{cn} \tag{B.2}$$

and

$$F_{kn} = \frac{4}{3}E^*\sqrt{R^*\alpha^3} \qquad F_{cn} = -2\sqrt{\frac{5}{6}}\beta\sqrt{S_n m^*}v_n^{rel} \tag{B.3}$$

where E^* is the equivalent elastic modulus. R^* is the equivalent particle radius. α is the amount of normal overlap. m^* is the equivalent mass. v_n^{rel} is the value of the normal component of the relative velocity. S_n is normal stiffness. $\beta = \ln e/\sqrt{\ln^2 e + \pi^2}$. e is the coefficient of restitution.

The tangential contact force between the particles is

$$F_{tij} = F_{kt} + F_{ct} \tag{B.4}$$

and

$$F_{kn} = \frac{4}{3}E^*\sqrt{R^*\alpha^3} \qquad F_{cn} = -2\sqrt{\frac{5}{6}}\beta\sqrt{S_n m^*}v_n^{rel} \tag{B.5}$$

where S_t is tangential stiffness, δ is tangential overlap, v_t^{rel} is tangential relative velocity.

The torque generated by the tangential contact force is

$$T_{ij} = -\mu_t F_{nij} R_i \omega_i \tag{B.6}$$

where μ_t is the rolling friction coefficient, R_i is the distance between the center of mass and the point of contact, ω_i is the unit angular velocity of the object at the contact point.

3.3. Energy consumption mechanism in the compressor particle dampers

Under an external excitation, the movement of the particle damping system mainly includes collision and friction between particles themselves and between particles and the wall of the damper. Therefore, damping particles mainly consume energy by collision and friction. According to the law of momentum conservation, when the particles i and j collide, the total energy consumption is

$$\Delta E = \sum \Delta E_{collision} + \sum \Delta E_{friction} \tag{B.7}$$

and

$$\Delta E_{collision} = \frac{m_i m_j (1 - e^2)}{2(m_i + m_j)} |\Delta v|^2 \qquad \Delta E_{friction} = \mu F_{nij} \Delta S \tag{B.8}$$

where $E_{collision}$ is collision energy consumption, and $E_{friction}$ is friction energy consumption. e is the particle coefficient of restitution. Δv is the relative velocity before the collision. μ is the friction coefficient between the two particles. ΔS is the relative tangential displacement of the particles i and j.

4. Influence of different parameters on the energy consumption of dampers

4.1. Particle size

In order to make particle dampers achieve the purpose of energy dissipation and vibration reduction, it is necessary to ensure that the particles have geometrical characteristics of the rigid body and the flow state of a fluid, and the particle size is the main influencing factor.

The optimal particle size for different dampers is simulated as shown in Fig. 5. Considering the application environment of damping particles in the chiller, iron-based particles are used as the material. Material density is 7800 kg/m^3, elastic modulus is 210 GPa, Poisson's ratio is 0.3, particle recovery coefficient is 0.63, and the damper filling rate is 80%. The model is imported into DEM software, the excitation frequency is 386 Hz and the amplitude is 1 mm.

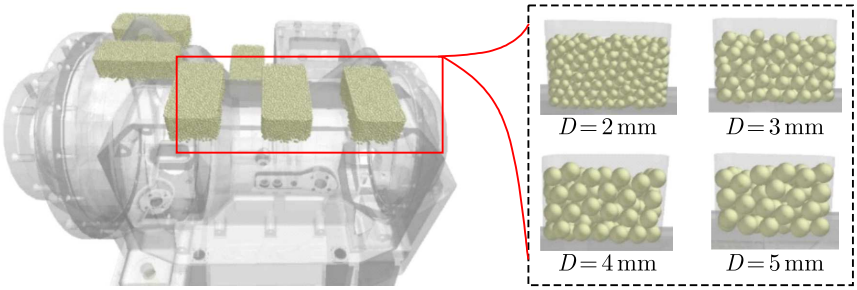

Fig. 5. Different particle sizes

The energy dissipation of each damper at different particle sizes and different times is shown in Fig. 6, and the energy dissipation trend of each damper particle is shown in Fig. 7. As can be seen from Figs. 6 and 7, when the particle size increases from 1 mm to 5 mm, the optimal particle size of different dampers varies. The optimal particle size of the top dampers of the compressor is 2 mm, for the foot dampers it is 5 mm, and for the support frame is 3 mm.

4.2. Excitation frequency and amplitude

According to the energy dissipation mechanism of particle damping, the more energy dissipated by particles, the better the effect of vibration reduction. In this paper, the influence

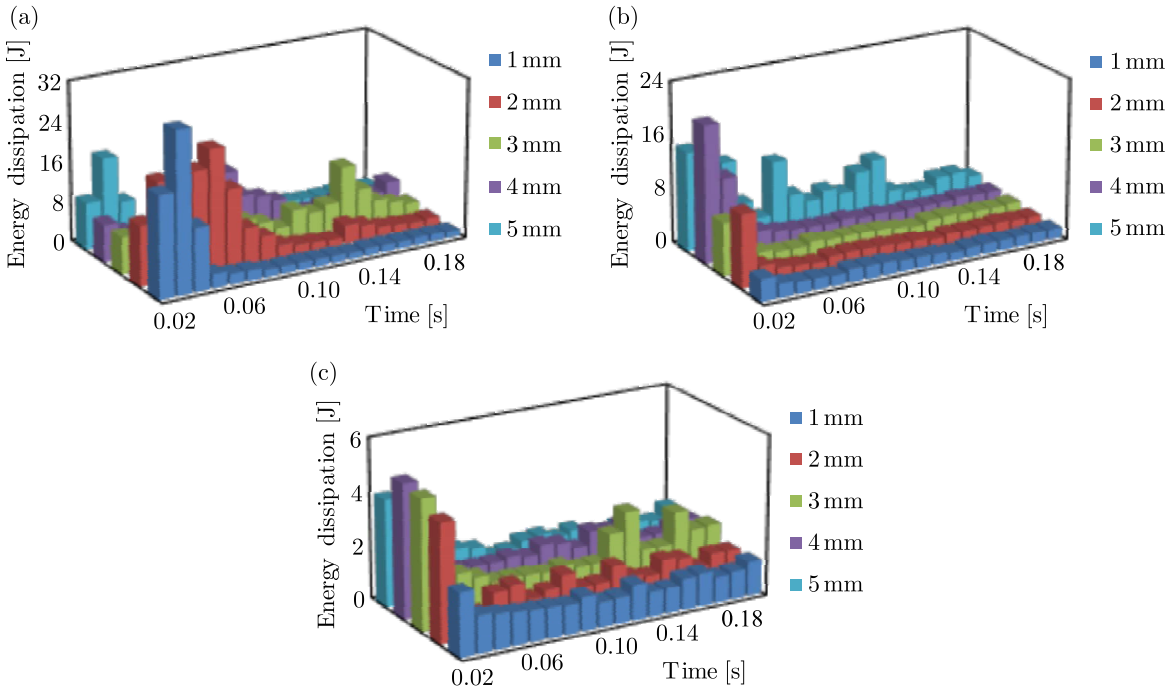

Fig. 6. Energy dissipation of dampers at different times: (a) compressor top, (b) compressor foot, (c) compressor support frame

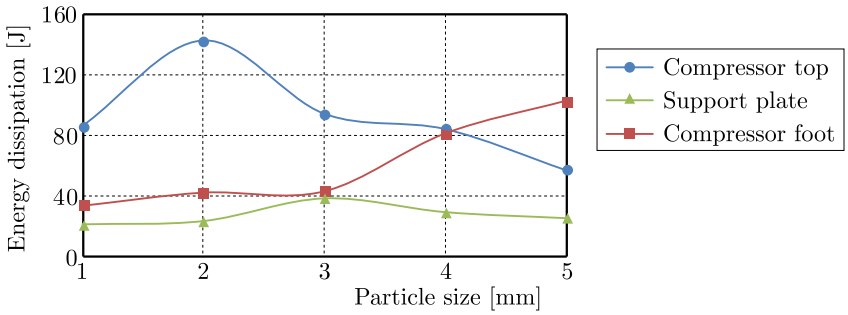

Fig. 7. Optimal particle sizes of different dampers

of excitation frequency and excitation amplitude on particle energy consumption is studied according to vibration reduction requirements of different frequency bands in practical operation. Based on DEM, the energy dissipation of dampers under different excitation frequencies and different excitation amplitudes is simulated, and the results are shown in Fig. 8.

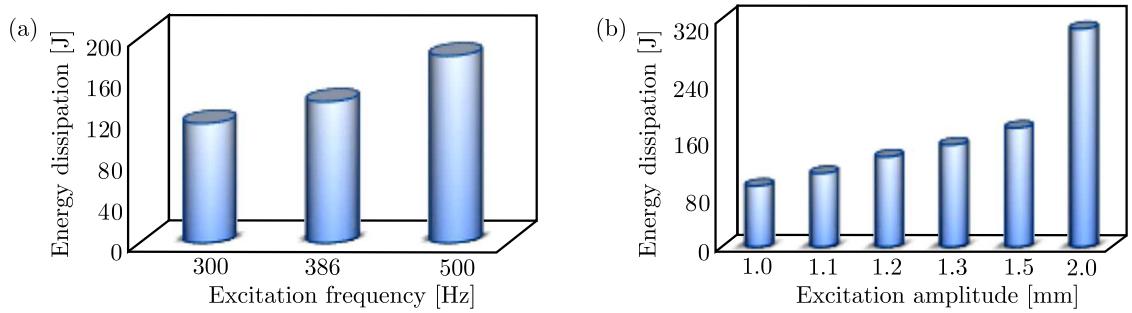

Fig. 8. Effects of different excitation frequencies and amplitudes on particle energy consumption: (a) different excitation frequencies, (b) different excitation amplitudes

It can be seen from Fig. 8 that the energy consumption of particles increases with an increase of frequency assumming that the excitation amplitude remains unchanged. Under the premise of constant excitation frequency, the energy consumption per unit time increases with growth of the amplitude, indicating that the energy dissipation effect of particles is superior for large amplitudes.

4.3. Optimal arrangement of particle dampers

According to the modal results, four installation schemes are designed, and the corresponding damper arrangement is shown in Fig. 9. The corresponding damper models and energy consumption at different excitation frequencies are shown in Table 2. The energy dissipation of particles with different damper schemes at different excitation frequencies is shown in Fig. 10.

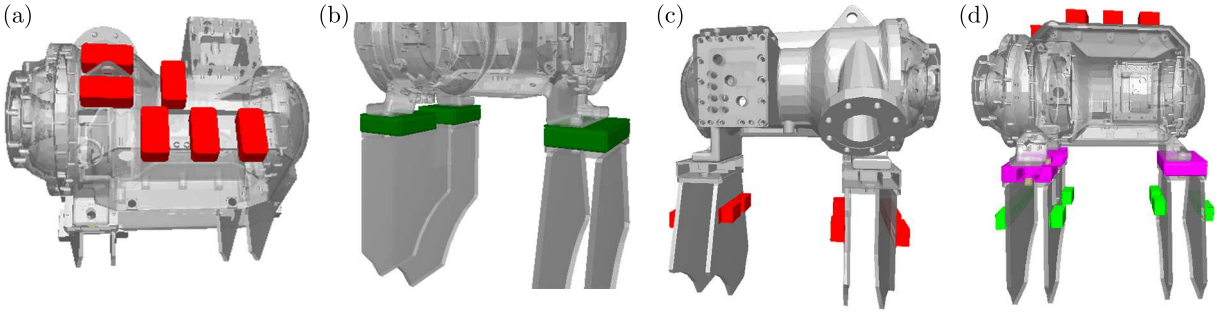

Fig. 9. Damper layout scheme: (a) scheme 1, (b) scheme 2, (c) scheme 3, (d) scheme 4

Table 2. Total energy consumption of the system in different schemes

Scheme	J1	J2	J3	J4	J5	300 Hz	386 Hz	500 Hz
1	√	√	×	×	×	43.36182	51.40913	61.16093
2	×	×	√	√	×	87.1398	105.8247	149.9172
3	×	×	×	×	√	15.74722	18.88648	21.72246
4	√	√	√	√	√	114.9274	148.2866	195.4099

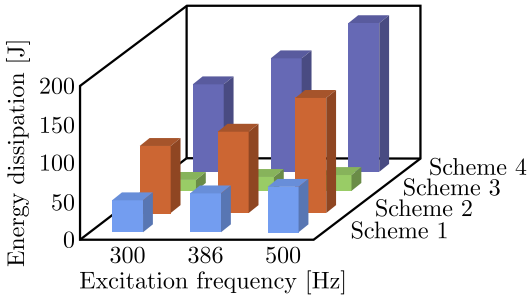

Fig. 10. Damping effect of different damper schemes

As can be seen from Table 2 and Fig. 10, particle dampers installed at different positions of the compressor have different energy dissipation levels under different excitation frequencies. The sequence from high to low is: scheme 4 > scheme 2 > scheme 1 > scheme 3. The combined installation is the optimal scheme.

5. Experimental verification of the vibration reduction effect of the centrifugal chiller

In order to verify the actual vibration reduction effect of the chiller in the optimal arrangement an experimental platform is built based on the centrifugal air-conditioning chiller, and experimental tests are carried out. The actual installation of the damper is shown in Fig. 11.

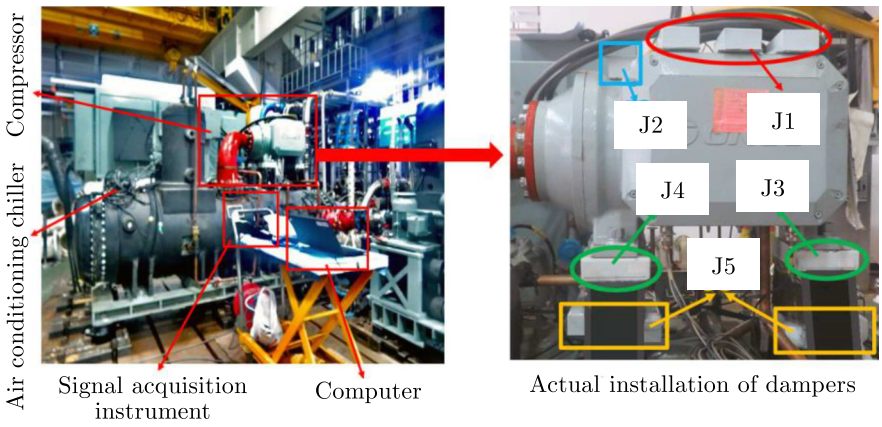

Fig. 11. Field experimentation

Acceleration sensors are arranged on the foot of the chiller compressor in the vertical direction. The particle dampers are instaled according to the optimal solution and the test system is calibrated, including the acceleration sensor and signal processing system. After setting the specified working conditions of the compressor (conversion frequency 386 Hz and 300 Hz), the data are collected at the vibration signal acquisition end, and the signal is transmitted to the computer end after being calculated and processed by the signal acquisition instrument. The waveform is displayed in the corresponding Date Acquisition & Signal Processing (DASP) software, and the signal data are recorded. The experimental data are shown in Table 3.

Table 3. Experimental data

Centrifugal air conditioner chiller (unit: dB)				
Measuring point	Excitation frequency	Without particle damper	With particle damper	Damping
Compressor foot	300 Hz	105.81	96.57	9.24
	386 Hz	107.25	96.63	10.62
	10-315 Hz (at 386 Hz)	97.74	90.81	6.93
	10-10k Hz (at 386 Hz)	125.3	118.88	6.42
	10-315 Hz (at 300 Hz)	107.63	97.16	10.47
	10-10k Hz (at 300 Hz)	117.08	110.04	7.04

The frequency spectrum of compressor acceleration in the target vibration reduction frequency band before and after installing the dampers is shown in Fig. 12. It can be seen from Table 3 and Fig. 12 that the particle dampers installed on the compressor have a significant damping effect, and the total vibration level of the compressor is reduced by 10.62 dB at 300 Hz. At 386 Hz, the total vibration level is reduced by 9.42 dB. When the compressor is running at 386 Hz, the total vibration stage value is reduced by 6.93 dB in the frequency range of 10 Hz--315 Hz. At 10 Hz-10 kHz, the total vibration stage value decreases by 6.42 dB. When the compressor runs at 300 Hz, the total vibration stage value decreases by 10.47 dB in the frequency range of 10 Hz-315 Hz. At 10 Hz-10 kHz, the total vibration stage value decreases by 7.04 dB.

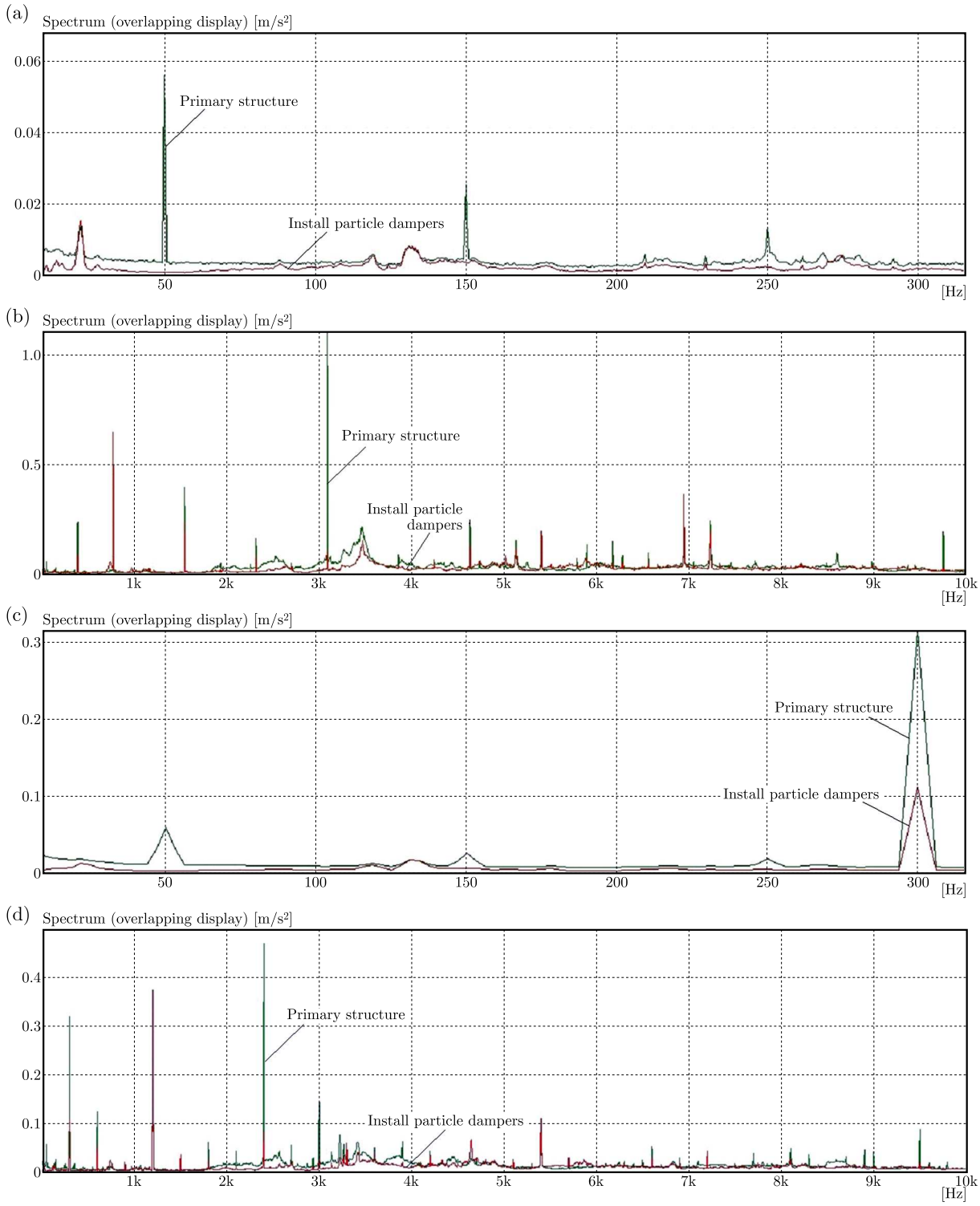

Fig. 12. Experiment effect. Vibration reduction effect diagram of: (a) 10 Hz-315 Hz unit (at 386 Hz), (b) 10 Hz-10 kHz unit (at 386 Hz), (c) of 10 Hz-315 Hz unit (at 300 Hz), (d) 10 Hz-10 kHz unit (at 300 Hz)

6. Conclusion

- Based on the dynamic model of a centrifugal air-conditioning chiller, dynamic characteristics of the chiller were analyzed, and the vibration transmission path of the chiller was obtained. Based on the finite element analysis, the vibration sensitive area of the chiller was

obtained, and the installation area of the dampers was determined. The particle dampers were installed on the top of the compressor, and installed in parallel at the support frame position and mounted rigidly in series between the compressor and the support frame.

- Based on the particle damping and DEM, the optimal particle size and the optimal installation scheme of each damper of the unit were studied. According to simulation results, the optimal particle size of the top damper was 2 mm, the optimal particle size of the foot was 5 mm, and the optimal particle size of the support frame was 3 mm. Among the four installation methods of particle dampers, the combined installation occurred to be the best one.
- The damping effect of the compressor in the optimal configuration of dampers was verified by experiments. The experimental results showed that under the optimal configuration, the total vibration level was reduced by 10.62 dB at 300 Hz and was reduced by 9.42 dB at 386 Hz. When the compressor was running at 386 Hz, the total vibration stage value was reduced by 6.93 dB in the frequency range of 10 Hz-315 Hz and was reduced by 6.42 dB in the frequency range of 10 Hz-10 kHz. When the compressor ran at 300 Hz, the total vibration stage value decreased by 10.47 dB in the frequency range of 10 Hz-315 Hz and decreased by 7.04 dB in the frequency range of 10 Hz-10 kHz.
- A vibration reduction method for centrifugal chiller based on particle damping was proposed. Based on dynamic analysis and DEM, particle dampers were introduced to reduce vibration of the chiller. Simulation calculations and experimental results verified feasibility of the particle discrete element model, and the a method was proposed for vibration control of a centrifugal air-conditioning chiller.

Acknowledgements

This work was supported by the National Natural Science Foundation of China (NO. 51875490); State Key Laboratory of Air-Conditioning Equipment and System Energy Conservation (No. ACSKL2018KT01); Fundamental Research Funds for the Central Universities (CN) (No. 20720210042).

References

1. Cheng X.K., Yang Q.L., Hu L., Yuan S., Tang Z., 2014, Study on the method of particle damping loss factor experiment, *Applied Mechanics and Materials*, **501-504**, 920-924
2. Deng J.W., Yang Q., 2020, Operation characteristics and control strategy of magnetic bearing variable frequency chillers, *Heating Ventilating and Air Conditioning*, **50**, 3, 57-62+37
3. Fang X.-D., Hu L., Hu J., 2019, Research on vibration exceeding standard for open type screw water chiller, *Refrigeration and Air Conditioning*, **19**, 8, 87-90
4. Geng X.-F., Ding H., Mao X.Y., Chen L.Q., 2021, Nonlinear energy sink with limited vibration amplitude, *Mechanical Systems and Signal Processing*, **156**, 107625
5. Hassan W., Mahmood F., Akmal M., Nasir M., 2020, Optimum operation of low voltage variable-frequency drives to improve the performance of heating, ventilation, and air conditioning chiller system, *International Transactions on Electrical Energy Systems*, **30**, 9, 12481
6. Jiang G.-F., 2015, Large marine chiller damping structural design, *Home Appliance of Science and Technology*, **2015**, 9, 60-63
7. Lei X.-F., Wu C.-J., Chen P., 2018, Optimizing parameter of particle damping based on Leidenfrost effect of particle flows, *Mechanical Systems and Signal Processing*, **104**, 60-71
8. Lu Z., Wang Z.,Masri S.F.,Lu X., 2018, Particle impact dampers: Past, present, and future, *Structural Control and Health Monitoring*, **25**, 1, 1-25

9. Mo Y.-H., Ding L., 2019, Analysis of damping effect of chiller frame, *China Mechanical Engineering*, **30**, 16, 1891-1895

10. Nallusamy S., Sujatha K, Rajan K., Vijaya Kumar K.R., 2020, Analysis of particle damping characteristics on steel vertical machining centre column with epoxy reinforced granite, *International Journal of Engineering Research in Africa*, **50**, 94-102

11. Romdhane M.B., N. Bouhaddi N., Trigui M., Foltéte E, Haddar M., 2013, The loss factor experimental characterisation of the non-obstructive particles damping approach, *Mechanical Systems and Signal Processing*, **38**, 585-600

12. Severson B.L., Keer L.M., Ottino J.M., Snurr R.Q., 2008, Mechanical damping using adhesive micro or nano powders, *Powder Technology*, **191**, 143-148

13. Wang H.-W., 2004, Vibration reduction of air conditioning equipment and pipelines, *Installation*, **2**, 21-23

14. Wang W., Li Y.Y., 2011, Experimental investigation on vibration-reduced characteristics of non-obstructive particle damping for free beam structure, *Advanced Materials Research*, **230-232**, 867-871

15. Wang Y., Lu Z., Du J., 2020, Experimental study on damping mechanism of buffered impact dampers, *Applied Acoustics*, **170**, 107492

16. Xiao W., Xu Z., Bian H., Li Z., 2021, Lightweight heavy-duty CNC horizontal lathe based on particle damping materials, *Mechanical Systems and Signal Processing*, **147**, 107127.

17. Xing H.Y., 2016, Pipe vibration control of piston type nitrogen compressor, Master Thesis, China University Of Petroleum, East China

18. Zhang R., Zhang Y., Zheng Z., Mo L., Wu C., 2020, Parametrical optimization of particle dampers based on particle swarm algorithm, *Applied Acoustics*, **160**, 107083

Manuscript received August 29, 2022; accepted for print December 3, 2022

INFORMATION FOR AUTHORS

Journal of Theoretical and Applied Mechanics (***JTAM***) is devoted to all aspects of solid mechanics, fluid mechanics, thermodynamics and applied problems of structural mechanics, mechatronics, biomechanics and robotics. Both theoretical and experimental papers as well as survey papers can be proposed.

JTAM accepts full-text articles (max. 12 pages) as well as the short communications with all the requirements concerning standard publications, except a volume that is limited to 4 pages.

We accept articles in English only. The text of JTAM paper should not exceed 12 pages of standard format A4 (11-point type size, standard margins – 2.5 cm, single line spacing) including abstract, figures, tables and references.

The material for publication should be sent to the Editorial Office via electronic journal system: http://www.editorialsystem.com/jtam

Papers are accepted for publication after the review process. Blind review model is applied, which means that the reviewers' names are kept confidential to the authors. Reviewer(s) declare that there is no interpersonal relation with the author(s) that would affect the opinion and recommendation of the article for publication in JTAM. The final decision on paper acceptance belongs to the Editorial Board.

Starting from January 1, 2020, the Publisher of *Journal of Theoretical and Applied Mechanics* introduces a fee for published articles.

This applies only to papers submitted after this date and accepted by the Editorial Board for publication.

A payment of 500 EUR will be a condition for commencing the editorial procedure for upcoming articles.

After qualifying your paper for publication we will require LaTeX or TeX or Word document file and figures.

The best preferred form of figures are files obtained by making use of editorial environments employing vector graphics.

Requirements for paper preparation

Contents of the manuscripts should appear in the following order:

- Title of the paper.
- Authors' full name, affiliation and e-mail.
- Short abstract (maximum 100 words) and 3-5 key words (1 line).
- Article text (equations should be numbered separately in each section; each reference should be cited in the text by the last name(s) of the author(s) and the publication year).
- References (maximum 25) in alphabetical order.
- Titles of references originally published not in English, should be translated into English.

All the data should be reported in SI units.

Cena 40,00 zł (VAT 8%)

Contents

Ilewicz G., Mrozowski J., Awrejcewicz J., Zagrodny B., Ludwicki M. — Biomechanical criterion of dynamic stability based on ZMP formula and Flash-Hogan principle of minimum jerk **3**

Liu Z.-Y., Song Y., Zhou F.-X., Wang L.-Y. — Analytical solution for one--dimensional consolidation of unsaturated soils under dynamic load **11**

Wang T., Xie L., Yu H., Wei X., Dong P., Zhao T. — Analysis of abnormal vibrations of crude oil efflux pumps using Ansys **23**

Wu D., Liu Z., Li D., Zhang Z., Chen J. — Study on the stress intensity factor of a compact specimen under the pre-compressed load condition **37**

Ouzandja D., Messaad M., Berrabah A.T., Belhrizi M. — Impact of material nonlinearity of dam-foundation rock system on seismic performance of concrete gravity dams **49**

Guo Q., Wang Y., Zhou B. — Analytical study on the cutting force and residual stress in whirlwind milling of a large screw **65**

Li R., Wei W., Liu H., Wang D., Ye J., Li S., Wang W., Wu H. — Comparative evaluation of wear behavior of tribo-pairs in reciprocating pumps with multiple materials under different conditions **77**

Cui C., Zhu Z., Chen S., Zheng Q., Chai J., Li X. — A tool orientation smoothing method for five-axis machining to avoid singularity problems **89**

Guo S., Xu D., Shang K., Yang S., Wang D., Li G., Zheng B., Jiao Y. — Analysis of progressive collapse of a super-long span latticed steel arch structure **103**

Zheng M. — Research on time-varying reliability of wind power gearbox with failure correlation **119**

Zhou E., Zhao Y., Zhang H. — Research on vibration evolution of a ball bearing without the cage under local variable-diameter raceway damage **129**

Romanowicz M. — Predictions of fracture resistance of spruce wood under mixed-mode loading using non-local fracture theory and numerical modelling **147**

Song Y., Fan B., Li Y.-Q., Wang H.-P. — Research on creep-fatigue model of anchored jointed rock mass **163**

Wang Y., Liu J. — On the yield surface of a typical bending-dominant periodic lattice metamaterial **175**

Xiao W., Shi J., Chen H., Liu H. — Research on optimal design of vibration reduction of centrifugal air conditioning chiller based on particle damping **189**